Theoretical Studies of Actinyl Bonding

Submitted by:

L. J. Larsson Häller

For the degree of:

Doctor of Philosophy

Supervisor:

Professor N. Kaltsoyannis

University College London, 2007

ProQuest LLC
789 East Eisenhower Parkway
P.O. Box 1346
Ann Arbor, MI 48106-1346

I, L. Jonas L. Häller, confirm that the work presented in this thesis is my own.

Where information has been derived from other sources, I can confirm that this has been indicated in this thesis.

Signed

Abstract

This thesis involves the computational study of uranium, neptunium, plutonium, and americium complexes in aqueous and non-aqueous solution. It seeks answers to specific experimental questions, to provide additional information to experiments, and to make predictions that experimentalists can use to design or abstain from new experiments.

The work mainly uses density functional theory, as this method shows good scaling with system size. This is important because actinides have a large number of electrons, and the ligands in this work are often very large.

The family of compounds with the formula $[UO_2(H_2O)_n(OH)_m]^{2-m}$ (n+m=5) are studied, to investigate how the changing equatorial ligand field affects the uranyl ion as hydroxide ligands replace water ligands. The investigation involves uranyl stretching vibrations, orbital analysis, charge analysis, and bond orders. I evaluate how solvent models affect the geometry and uranyl stretching vibrations.

The *cis* and *trans* isomers of the $UO_2Cl_2(Cy_3PNH)_2$ and $UO_2Cl_2(Cy_3PO)_2$ (Cy = cyclohexyl) exist in equilibrium, even though one expects the bulky phosphinimine and phosphine oxide ligands to show large repulsion in a *cis* configuration. It is unknown experimentally whether the *trans* or the *cis* isomer is the major species. N-donor ligands displace O-donor ligands, when added to solution of $UO_2Cl_2(Cy_3PO)_2$, i.e. the N-donor ligands form stronger bonds to uranium than the O-donor ligands. I investigate which isomer is the major species, and explain why the *cis* isomer exists at all. The origin of the stronger N-donor ligand bonds is studied by orbital analysis, energy decomposition, and electron densities. This study is extended to include all halide ligands, and uranium is substituted by neptunium, plutonium, and americium.

I use the concepts of electron localisation and electron density differences on the systems above, to further study the actinyl axial and equatorial bonding in greater detail. I compare this analysis with the results from more traditional methods, e.g. charge analysis. I also investigate if it is possible to form stable *cis*-uranyl compounds and neptunyl complexes with cation-cation interactions.

Contents

List of Tables

List of Figures

List of Abbreviations

WFM	Wave Function Methods
DFT	Density Functional Theory
AO	Atomic Orbital
MO	Molecular Orbital
HOMO	Highest Occupied Molecular Orbital
LUMO	Lowest Unoccupied Molecular Orbital
SCF	Self Consistent Field
IR	Infra Red
THF	TetraHydroFuran
SE	Schrödinger Equation
BOA	Born-Oppenheimer approximation
HF	Hartree-Fock
SD	Slater Determinant
SIC	Self Interaction Correction
CI	Configuration Interaction
CC	Coupled Cluster
CCSD	Coupled Cluster Single Doubles
MP	Møller-Plesset
CASSCF	Complete Active Space Self Consistent Field
xc	exchange-correlation
ELF	Electron Localization Function
LSDA	Local Spin Density Approximation
STO	Slater Type Orbital
GTO	Gaussian Type Orbital
ADF	Amsterdam Density Functional
G03	Gaussian 03
ZORA	Zero-Order Regular Approximation
FORA	First-Order Regular Approximation
PCM	Polarizable Continuum Model
COSMO	Conductor like Screening MOdel

GEPOL	GEnerate POLyhedra
VdW	Van der Waals
SES	Solvent Excluding Surface
SAS	Solvent Accessible Surface
OFAC	Overlapping FACtor
UATM	United Atom Topological Model
UAKS	United Atom Kohn-Sham
VVD	Voronoi Deformed Densities
MBO	Mayer Bond Order
LOL	Localized Orbital Locator
ELI	Electron Localizability Indicator
NMR	Nuclear Magnetic Resonance
TMS	TetraMethylSilane
IGLO	Individual Gauge for Localized Orbital
GIAO	Gauge Including Atomic Orbital
LAO	London Atomic Orbital
MAE	Mean Absolute Error

Acknowledgement

The person I like to thank first is my excellent supervisor Professor Nikolas Kaltsoyannis. I am grateful for all the time Nik has spent helping me and discussing this work in a very encouraging way. I have had much freedom to do what I have found interesting, but Nik has at the same time made sure that I focus on the important questions. Nik has an amazing ability to explain complicated things in a very clear and accurate way.

I also like to thank my flatmates Leif Jonasson and Zbigniew Wojnowski for being very good friends and for reading the thesis. I have been very lucky to have found such good flatmates.

I am grateful to Amy P., Amy D., Andy, Giusy, German, Matthew, Liz, Laura, Denise, Will, Stuart, and especially Chris in G19 for their help, interesting discussions and nice company.

I like to thank Dr. Iain May and his whole group, especially Michael and Stephanie who have been mostly involved in this project, for their great work and interesting discussions. Mark Sarsfield at Nexia Solutions has also been of the greatest importance for the experimental work.

I appreciate the support from my family, relatives, and friends.

Finally, warm thanks to my former supervisors, Professor Gunnar Skarnemark and Professor Lars Jacobson for helping me to get this PhD, and to Professor Christian Ekborg for showing me the PhD. I also like to acknowledge the help Professor Sven Larson provided regarding background material and Dr. Miroslav Kohout's help with the Dgrid program. John Hands taught me how to write more effectively and clearly. I believe that improved this thesis significantly, and I am sure I will benefit from it in the future.

Chapter 1

Introduction and Theory

This thesis constitutes part of a project in which researchers at the University of Manchester and University College London collaborate with the aim of studying the actinyl ion experimentally (University of Manchester) and computationally (UCL). The thesis involves the computational study of uranium, neptunium, plutonium, and americium complexes. It answers specific experimental questions, provides additional information to experiments, and makes predictions that experimentalists use to design or abstain from new experiments.

This thesis first introduces the actinides, the actinyl dication and its electronic structure, and discusses actinide chemistry in non-aqueous solution. Secondly, it provides a theoretical background to the calculations performed. I put emphasis on comparing Wave Function Methods (WFM) with Density Functional Theory (DFT) to highlight similarities and differences between the methods. I describe DFT more comprehensively than WFM, as DFT is the predominant method in this work. I discuss DFT approximations and compare calculated electron densities at different levels of each approximation to illustrate their significance. Finally, there follows a presentation of electronic structure analysis methods.

Chapter 2 treats our computational investigation of the uranyl ion in aqueous solution; in this case, uranyl coordinates water and hydroxide ligands in the equatorial plane. The electric field in the equatorial plane increases, as hydroxide ligands replace water ligands; I investigate how this increasing electric field affects uranyl. Water ligands only donate electrons through σ-donation, while hydroxide ligands have the additional ability of π-donation. I investigate if this additional mode of donation competes for the uranium 6*d* Atomic Orbitals (AOs) with the oxygen atoms in the uranyl bonds (O_{yl}).

Chapter 3 compares differences between how uranyl interacts with N-donor and O-donor ligands in its equatorial plane. Do the softer N-donor ligands form more covalent bonds with uranium than the O-donor ligands, and does this affect uranyl bonding significantly in that case? My collaborators find both *cis* and *trans* isomers of the N-donor and O-donor ligand complexes in solution; I study which of those isomers is most stable. I extend the study to include the neptunyl, plutonyl, and americyl ions, and investigate different halide and hydride ligands.

Chapter 4 investigates whether the tridentate anionic bis-iminophosphorano ligands $[CH(Ph_2PNSiMe_3)_2]^-$ (Ph = Phenyl, Me = Methyl) can disrupt the uranyl bonds to form a *cis* uranyl compound. The bis-iminophosphorano ligands constitute the last of three groups of ligands, investigated in this project. The monodentate ligands investigated in chapter 2 and 3 are members of the first group, the second group of ligands contains bidentate NCN and NPN ligands that have been studied experimentally by Sarsfield *et al.* [1], and computationally (within this project) by Ingram and Kaltsoyannis [2].

The last chapter revisits the projects in chapter 2 and 3, to apply the methods of electron localisation and electron density differences on those systems. I also apply the same methods on small symmetric uranium systems, and systems with multiple neptunium atoms of different oxidation states that show dication-dication interaction, with the goal to improve understanding of bonding in those complexes. The conclusions of this investigation are different from the conclusions in chapter 2.

The primary aim of the project is to answer the following question:

How does the bonding and electronic structure of the actinyl ion change in the presence of f-electrons and an equatorial ligand field that is strong or distorted or both?

Both fundamental scientific reasons and applications of actinides in the nuclear industry motivate this work. Understanding the chemical behaviour of actinides is important to improve the process of actinide separation from waste products and other actinides in reprocessing, and for safe storage of nuclear waste. Transmutation is another potential application where separation of actinides, and therefore the understanding of their chemical behaviour, is crucial.

The greatest problem of studying actinides experimentally is their scarcity and radioactivity. The difficulties increase with rising atomic number, because the Coulomb repulsion of the protons destabilises the nuclei, i.e. the half-life generally becomes shorter and production harder. Working with highly radioactive material requires expensive special facilities and equipment. The great variety of the actinides' oxidation numbers (discussed below) also increases the experimental difficulties. The experiments in this thesis are performed in non-aqueous solutions that enable exposure of the actinyl ion to strong equatorial ligand fields and ligands especially tailored to disrupt it. Actinide chemistry in non-aqueous solution is sensitive to moisture and air, which also makes the experimental work more difficult. Despite these difficulties, experiments are essential as they provide exact values (within measurement errors).

1.1 Actinides

The actinides fill the 5*f* AOs in the periodic table, and therefore have their own subrow. They exhibit similar chemical behaviour to lanthanides (which fill the 4*f* AOs), but there are differences. The 5*f* AOs have a radial node (4*f* have none) and are more accessible for chemical bonding in the early actinides, because they are less contracted and in closer energetic proximity to the other valence electrons than the lanthanide's 4*f* electrons. The contraction of the "core like" 5*f* electrons is more pronounced for the latter members of the

actinides, which behave more similarly to the lanthanides. The differences between actinides and lanthanides are assigned to larger relativistic effects in the actinides [3]. Relativistic effects contract the *s* orbitals (and slightly the *p* orbitals), but expand the *d* and *f* orbitals (Figure 1). The *d* and *f* orbitals expand because they experience a smaller effective charge of the nucleus, as the electrons in the contracted *s* and *p* orbitals shield it more effectively. The effects on the *s* and *p* electrons are attributable to their high speed, and are therefore direct effects of relativity, while the effects on the *d* and *f* electrons are indirect. Relativistic effects affect actinides more significantly than lanthanides, as their heavier nuclei make their inner core electrons move faster. The shielding from the 5*f* AOs, however, is not very effective, because angular nodality causes the 5*f* electrons to avoid each other and consequently feel a greater effective charge, as the actinides are traversed. This effect makes the valence AOs of the later actinides and the lanthanides contract and participate less in covalent bonding.

Table 1 compares the electronic structure of the lanthanides and actinides. It shows that the early actinides include 6*d* electrons in the electronic ground state more often than early lanthanides include a 5*d* electron, but the later members of both lanthanides and actinides only have *f* and *s* electrons in the valence shell. The close energetic proximity of the 6*d* and 5*f* AOs makes switches among them easy, and makes the early actinides exhibit properties similar to the transition metals (which also have at least one *d* electron). Actinides were first misplaced under the transition metals, but Seaborg proposed to put them under the lanthanides [4], as he noticed that the newly discovered elements, neptunium and plutonium, are more stable in lower oxidation states than their precursors. They also behave more similar to the lanthanides than to rhenium and osmium. Actinides and lanthanides are both electropositive but actinides adopt more oxidation states than lanthanides that always form trivalent ions (because the 5*f* electrons in the valence shell are easier to remove than 4*f* electrons). Table 2 presents all oxidation states of the actinides.

Table 1. *Electronic ground configuration of the lanthanide and actinide elements.*

La	[Xe] $5d^1\ 6s^2$	Ac	[Rn] $6d^1\ 7s^2$	Gd	[Xe]$4f^7\ 5d^1\ 6s^2$	Cm	[Rn]$5f^7\ 6d^1\ 7s^2$
Ce	[Xe]$4f^1\ 5d^1\ 6s^2$	Th	[Rn] $6d^2\ 7s^2$	Tb	[Xe]$4f^9\ 6s^2$	Bk	[Rn]$5f^9\ 7s^2$
Pr	[Xe]$4f^3\ 6s^2$	Pa	[Rn]$5f^2\ 6d^1\ 7s^2$	Dy	[Xe]$4f^{10}\ 6s^2$	Cf	[Rn]$5f^{10}\ 7s^2$
Nd	[Xe]$4f^4\ 6s^2$	U	[Rn]$5f^3\ 6d^1\ 7s^2$	Ho	[Xe]$4f^{11}\ 6s^2$	Es	[Rn]$5f^{11}\ 7s^2$
Pm	[Xe]$4f^5\ 6s^2$	Np	[Rn]$5f^4\ 6d^1\ 7s^2$	Er	[Xe]$4f^{12}\ 6s^2$	Fm	[Rn]$5f^{12}\ 7s^2$
Sm	[Xe]$4f^6\ 6s^2$	Pu	[Rn]$5f^6\ 7s^2$	Tm	[Xe]$4f^{13}\ 6s^2$	Md	[Rn]$5f^{13}\ 7s^2$
Eu	[Xe]$4f^7\ 6s^2$	Am	[Rn]$5f^7\ 7s^2$	Yb	[Xe]$4f^{14}\ 6s^2$	No	[Rn]$5f^{14}\ 7s^2$

Table 2. *All oxidation states found experimentally in the actinide elements [5]. The most common oxidation states are underlined and boldened, and states only formed in solids are underlined and italicised.*

Ac	**3**	Pu	3, **4**, 5, 6, 7	Es	*2*, **3**
Th	3, **4**	Am	*2*, **3**, 4, 5, 6	Fm	2, **3**
Pa	*3*, 4, **5**	Cm	**3**, 4	Md	2, **3**
U	3, 4, 5, **6**	Bk	**3**, 4	No	**2**, 3
Np	3, 4, **5**, 6, 7	Cf	*2*, **3**, *4*	Lr	**3**

Figure 1 presents the orbital radial distribution of the valence AOs for the Sm^{3+} and Pu^{3+} ions [3], from relativistic and non-relativistic calculations. It shows that relativistic effects expand the 5*f* AOs, especially in the tail region, and contract the 7*s* AOs considerably. The 7*s* and 7*p* AOs are, despite their relativistic contraction, too diffuse to participate in bonding. Figure 2 shows that the 6*s* and the 6*p* AOs have a similar spatial distribution to the 5*f* and 6*d* AOs, and it is essential to include them in the valence shell in calculations. The 6*p* AOs in uranyl, for example, cause a splitting of the σ_u and σ_g Molecular Orbitals (MOs); this is an example of the "pushing from below" effect [6-9].

Figure 1(a)-(b). *Orbital radial distribution functions from relativistic and non-relativistic calculations on the (a) Sm^{3+} and (b) Pu^{3+} ions illustrating the contraction of the s and p orbitals and the expansion of the d and f orbitals [3].*

Figure 2. *Radial wave function from relativistic calculations on the uranium atom showing the close spatial distribution of the 5f, 6s, 6p, and 6d AOs [10]. The distance to the oxygen atom in uranyl is included and shows that the 7s orbitals are much too diffuse to give a large contribution to uranyl bonding.*

1.1.1 The Actinyl Ion

Uranium, neptunium, plutonium and americium are unique among the actinides because they form the actinyl dication. Actinyls consist of the actinide and two oxygen atoms in a linear composition with two formally triple bonds between the metal and oxygen atoms. These bonds consist of a linear combination of the $2p$ AOs on the oxygen atoms and $6d$ and $5f$ AOs on the actinide, forming σ_u, σ_g and doubly degenerate π_u and π_g bonding MOs. Unlike most multiple bonds, the σ-bonds have a higher energy and a smaller overlap between the actinide and O than the π-bonds. The weakness of the σ-bonds is due to large cancellation between the $2p_\sigma$ and the $5f_\sigma$ and $6d_\sigma$ orbital in the bonding region [10]. Figure 3 shows isosurfaces of the bonding uranyl MOs, an example of the orbitals in the actinyl bond. Orbitals are usually illustrated by isosurfaces, but Figure 4 shows the electron density in a plane through the uranyl axis. This is very useful because it contains more information than the single isosurface value in Figure 3. The electron density (the square of the MO) is also the physical observable. The figure illustrates that the uranyl bond is very

polar, with most of its electron density at the oxygen atoms, and some donation to the uranium AOs. The bonding in the actinyl ion gets more ionic as the actinide gets heavier, following the general trend of contracting AOs as the actinides are traversed.

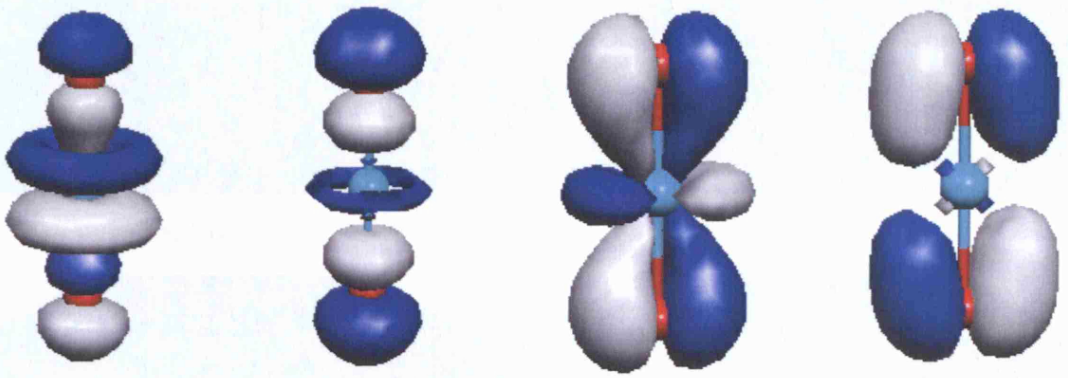

(a) σ_u **(b)** σ_g **(c)** π_u **(d)** π_g

Figure 3(a)-(d). *Isosurfaces of the (a)* σ_u*, (b)* σ_g*, (c)* π_u *and (d)* π_g *MOs in* UO_2^{2+} *from DFT calculations with TZ2P all electron basis sets and the PBE xc-functional. The isosurface value is 0.05.*

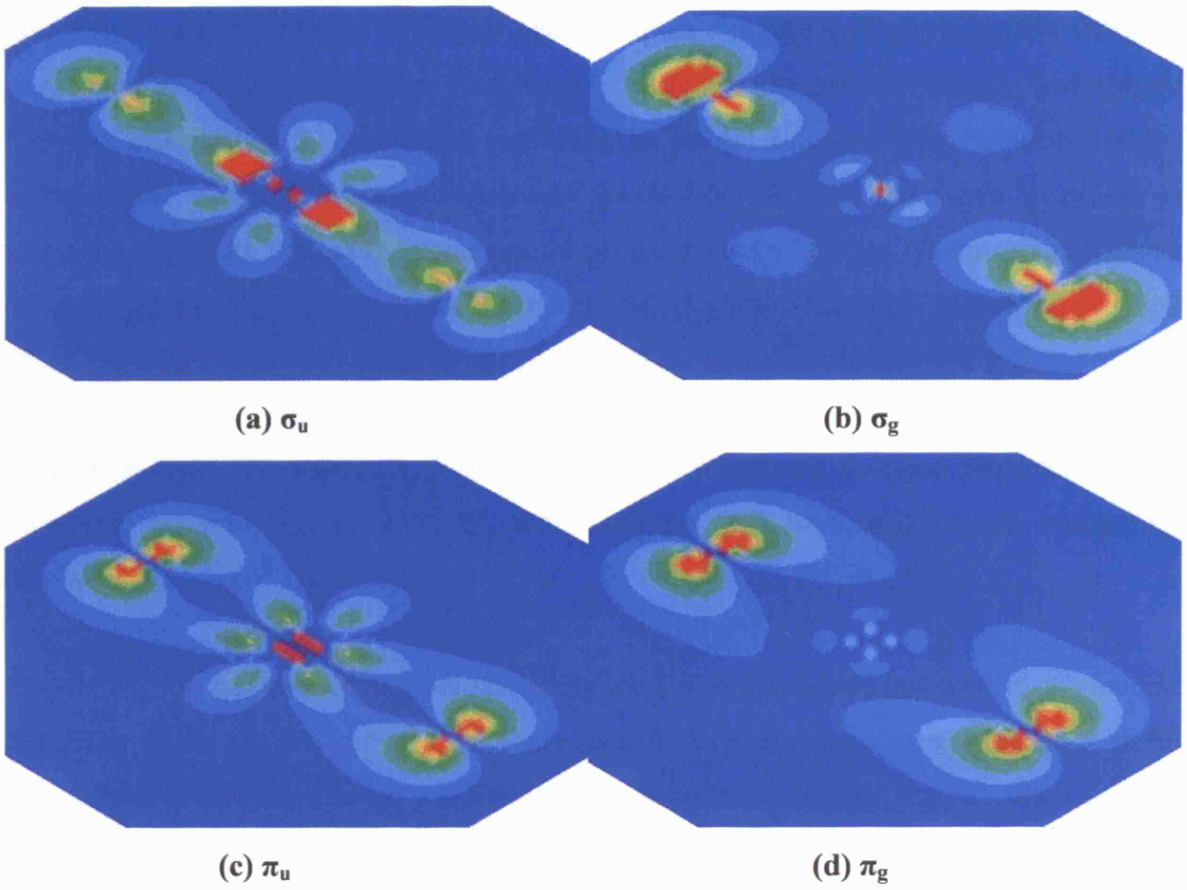

Figure 4(a)-(d). *Electron densities ($e^-/Bohr^3$) of the (a) σ_u, (b) σ_g, (c) π_u, and (d) π_g MOs in UO_2^{2+} from DFT calculations with TZ2P all electron basis sets and the PBE xc-functional. The maximum values for the electron density is 0.3 (red) and the minimum value 0 (blue).*

The actinyl ion coordinates ligands in its equatorial plane, perpendicular to the actinyl axis. The number of coordinated equatorial ligands ranges from 3 to 6, depending on the steric and electronic properties of the ligands. Coordination of 5 ligands, arranged in bipyramidal geometry, is by far the most common. The bonding in the equatorial plane is generally considered very ionic with a small component of covalence.

The experimental difficulties make computational methods very interesting for actinides, but calculations produce their own problems, arising from the large number of electrons and relativistic effects. The number of unpaired electrons also increases as the actinides get

heavier, to complicate and increase the computational demand of the calculations. The uranyl ion has a closed shell electronic configuration, but neptunyl, plutonyl, and americyl have open shells with one, two, and three unpaired electrons respectively, and should therefore be treated with unrestricted methods. The actinyl ions have many states of similar energies that give rise to near degeneracy correlation. A multi reference treatment is therefore important for many properties, although the coordination of equatorial ligands often increases the energetic gap between the Highest Occupied Molecular Orbital (HOMO) and the Lowest Unoccupied Molecular Orbital (LUMO), making these effects less severe. The close energetic proximity of the states in the actinyl ion makes the Self Consistent Field (SCF) (section 1.2.6.4) hard to converge and electrons often have to be "smeared" over several orbitals, i.e. many orbitals will have non integer occupation numbers.

The actinyl ion has two vibrational stretching modes, a symmetric and an anti symmetric translation of the oxygen atoms (O_{yl}). These modes of vibrations are good indicators of the actinyl bond strength; a large wavenumber corresponds to strong bonds, which usually corresponds to short Ac-O_{yl} distances. Raman spectroscopy measures the symmetric stretch, while Infra Red (IR) spectroscopy measures the anti symmetric. I use uranyl vibrational frequencies in chapter 2 to probe uranyl bond strengths.

1.1.2 Uranium

Martin Heinrich Klaproth discovered uranium in 1789 [11] and named it after the newly discovered planet Uranus. Klaproth thought he had discovered pure uranium metal, but Eugene Melchior Peligot later showed that Klaproth had only obtained UO_2, (by reducing UO_3 with hydrogen) [12]. Peligot reduced UO_2 to the metal by letting UCl_4 react with potassium [13-16]. Uranium was for a long time thought to be the heaviest element in the periodic table [17].

Natural uranium consists of a mixture of the isotopes ^{234}U (0.0055%), ^{235}U (0.72%) and ^{238}U (99.27%). The ^{233}U and ^{235}U isotopes are fissile, and ^{238}U is fertile, materials in nuclear reactors, but ^{235}U is mainly used today. Enrichment of ^{235}U is necessary for use in

reactors and atomic bombs; the atomic bomb that detonated over Hiroshima at the end of world war two used ^{235}U. ^{238}U and ^{235}U are parents of the $4N+2$ and $4N+3$ decay chains; they, like ^{234}U, decay by alpha particle emission accompanied by gamma decay, with a half-life of $2.4x10^5$ (^{234}U), $7.0x10^8$ (^{235}U), and $4{,}5x10^9$ (^{238}U) years respectively.

Uranium forms the linear uranyl ion, UO_2^{2+}, in aqueous solutions; hence the oxidation number of the uranium atom in the uranyl ion is VI. A study involving the experimental exchange of $^{17}O/^{16}O$ for UO_2^{2+} in aqueous solution [18] demonstrates the stability of uranyl with $t_{1/2} > 40\,000$ h ($t_{1/2}$ is the time to exchange half of the O_{yl} atoms). The exchange rate of O_{yl}, however, increases to $t_{1/2} = 0.015$s under highly alkaline conditions. Uranyl coordinates four hydroxide ligands, to form $[UO_2(OH)_4]^{2-}$, under those conditions. The destabilisation of uranyl in $[UO_2(OH)_4]^{2-}$ is one of the motives to study the $[UO_2(H_2O)_m(OH)_n]^{2-n}$ (m+n = 5) complexes in chapter 2.

The magnitude of the vibrational frequencies decrease linearly as the uranyl ion coordinates negative ligands. Strong coordination of the ligands leads to weakening of the uranyl bonds (and a smaller wavenumber of the vibrations), Raman and IR spectra therefore measure the relative bond strength of equatorial ligands [19]. Nguyen *et al.* [19] obtained the following order of bond strength for some organic and inorganic ligands: OH^- > CO_3^{2-} > $C_2O_4^{2-}$ > F^- > SO_4^{2-} and $CH_3CO_2^-$ > Cl^- > Br^- , NO_3^-, ClO_4^-, and HSO_4^- by measuring uranyl stretching frequencies.

1.1.3 Neptunium

Neptunium, named after the planet Neptune, was discovered in 1940 by McMillan and Abelson [20] by bombarding uranium with neutrons from a cyclotron. They discovered a new mode of decay with a half life of 2.3 days, in addition to the already known decay mode of ^{239}U (with a half life of 23 minutes). The product of the 2.3 day activity precipitates with HF when a reducing agent is present, but not with an oxidising agent, this behaviour is different from the rare earths. The unknown product exists in lower oxidation states than uranium and is the new element ^{239}Np. Based on these findings, McMillan and Abelson suggested that "there may be a second "rare earth" group of similar elements

starting with uranium", similar to Seaborg's correct suggestion of a new subrow, that started with actinium. McMillan and Abelson also tried to identify element 94 by studying the decay product of their new element, which was expected to be alpha active. They did not, however, find any alpha decay, and concluded that the alpha decay of element 94 must have a very long half life – if it was created at all. ^{239}Np actually decays to ^{239}Pu, but this was not established by McMillan and Abelson at this point.

Neptunium does not exist in nature, because the half lives of the longest lived isotopes of neptunium are much shorter than the lifetime of the earth. It is, however, possible to find small amounts of neptunium in uranium ore, because uranium absorbs neutrons from self fission and decays to neptunium.

1.1.4 Plutonium

Plutonium was discovered during the Manhattan project in world war two, but the publication of the discovery was withheld until the end of the war, to prevent other countries from producing nuclear bombs. Plutonium, named after the planetoid Pluto, was discovered by Seaborg, McMillan, Wahl and Kennedy from bombardment of uranium with 16 MeV deuterons [21]. The separated reaction product was beta active, with increasing alpha activity in the sample. The alpha emitter has different chemical properties than any other elements and is element 94 (already named plutonium before its discovery) [22].

1.1.5 Americium

Americium is (together with curium) the only element whose discovery was announced on a children's radio show, in this case "Quiz Kids". Seaborg appeared as a guest on "Quiz Kids" just after the war and a child asked him if they had found any more new elements than neptunium and plutonium during the war. The discovery information had just been declassified for an upcoming conference so Seaborg answered that two additional elements (95 and 96) had also been found: "So now you'll have to tell your teachers to change the 92 elements in your schoolbook to 96 elements," he added [23]. Americium got its name

after listeners on another radio show where Seaborg appeared just after the announcement had been able to suggest names. "Americium" was chosen because it is under the lanthanide europium in the periodic table and Seaborg therefore found the name appropriate.

Americium was discovered by Seaborg, James, Morgan and Giorso [24] by letting ^{239}Pu absorbing neutrons:

$$^{239}Pu(n,\gamma)^{240}Pu(n,\gamma)^{241}Pu \xrightarrow{\beta^-} {}^{241}Am$$

i.e. ^{239}Pu captures two neutrons while emitting γ-radiation and finally emits an electron to form ^{241}Am.

1.1.6 Actinyl Chemistry in non-Aqueous Solution

Actinide chemistry is dominated by complexes in aqueous solution, but recent synthesis of starting materials like $UO_2Cl_2(THF)_3$ and $UO_2(OTf)_2$ (OTf = O_3SCF_3 THF = TetraHydroFuran) opens the field to chemistry in non-aqueous solution. Ligands in aqueous solutions, like OH^-, form stronger bonds to uranium in the equatorial plane than the ligands of interest in non-aqueous solutions. Experiments in non-aqueous solutions are therefore very sensitive to moisture. Non-aqueous chemistry often involves donor ligands softer than oxygen donor ligands. As soft donor ligands are less resistant to charge transfer, they often form more covalent equatorial bonds with uranium, compared with bonds formed between uranium and hard donor ligands. In chapter 3, I investigate if soft donor ligands perturb the actinyl ion in a different way than hard donor ligands.

1.2 Quantum Mechanics and Computational Methods

1.2.1 The Schrödinger Equation

Finite quanta are the building blocks of energy; a classical continuous theory is therefore unable to describe accurately processes on a very small scale. The duality between wave and particle properties of matter, where wave characteristics are more pronounced at lower energies, requires the description of a wave function for the small energies on the atomic scale. Niels Bohr's attempt to model the atom by applying quantum theory to a classical model [25-27], did not produce a stable atom. Quantum mechanics remedies all these problems through the time independent, non-relativistic Schrödinger Equation (SE) [28-33].

$$\mathbf{H}\Psi = E\Psi \tag{1.1}$$

Equation (1.1) is an eigenvalue equation, **H** is the non-relativistic Hamiltonian operator that consists of the kinetic energy (**T**) and the potential energy (**V**) operators, the eigenvalue E is the total energy of the system, and Ψ is the wave function. It is possible to break the potential energy operator down into nuclear-nuclear, nuclear-electron, and electron-electron terms, and the kinetic energy into a nuclear and an electron contribution.

$$\mathbf{H} = \mathbf{T}_N + \mathbf{V}_{NN} + \mathbf{T}_E + \mathbf{V}_{NE} + \mathbf{V}_{EE} \tag{1.2}$$

1.2.2 The Born-Oppenheimer Approximation

A transformation of (1.2) to a centre of mass system produces a mass-polarization operator $\mathbf{H}_{MP}$. I collect the last four terms of (1.2) in an electronic Hamiltonian operator $\mathbf{H}_E$ (notice that $\mathbf{V}_{NN}$ is part of $\mathbf{H}_E$ due to the coupling between the nuclear and electron motion):

$$\mathbf{H} = \mathbf{T}_N + \mathbf{H}_E + \mathbf{H}_{MP} \tag{1.3}$$

The wave function is, without making any approximation, expanded in an infinite set of electron functions (states) where the coefficients ($\Psi_{N,i}(\mathbf{R})$) depend only on the positions of the nuclei (**R**). Combining (1.1) and (1.3) together with the expanded wavefunction gives:

$$\sum_{i=1}^{\infty}(\mathbf{T}_N + \mathbf{H}_E + \mathbf{H}_{MP})\Psi_{N,i}(\mathbf{R})\Psi_i(\mathbf{R},\mathbf{r}) = E\sum_{i=1}^{\infty}\Psi_{N,i}(\mathbf{R})\Psi_i(\mathbf{R},\mathbf{r}) \tag{1.4}$$

where **r** is the coordinate of the electron. The expression for the kinetic energy of the nuclei ($\mathbf{T}_N$) is:

$$\mathbf{T}_N = \sum_a \frac{1}{2M_a}\nabla_a^2 = \nabla_N^2 \tag{1.5}$$

where M_a is the mass of nucleus a. Neglecting the $\mathbf{H}_{MP}$ term and using equation (1.5) turns (1.4) into:

$$\begin{aligned}
&\sum_{i=1}^{\infty}\nabla_N^2\Psi_{N,j}\Psi_i + \mathbf{H}_E\Psi_{N,j}\Psi_i = E\sum_{i=1}^{\infty}\Psi_{N,j}\Psi_i \\
&\sum_{i=1}^{\infty}\nabla_N[\Psi_{N,j}\nabla_N\Psi_i + \Psi_i\nabla_N\Psi_{N,j}] + \Psi_{N,j}\mathbf{H}_E\Psi_i = E\sum_{i=1}^{\infty}\Psi_{N,j}\Psi_i \\
&\sum_{i=1}^{\infty}\Psi_{N,j}\nabla_N^2\Psi_i + 2\nabla_N\Psi_{N,j}\nabla_N\Psi_i + \Psi_i\nabla_N^2\Psi_{N,j} + \Psi_{N,j}E_i\Psi_i = E\sum_{i=1}^{\infty}\Psi_{N,j}\Psi_i
\end{aligned} \tag{1.6}$$

(the dependency of the electron and nuclei coordinates in the wave function is not written explicitly). Multiplying (1.6) from the left with a specific basis function (Ψ_j) orthonormal to Ψ_i gives:

$$\nabla_N^2\Psi_{N,j} + E_j\Psi_{N,j} + \sum_{i=1}^{\infty}(2\Psi_j\nabla_N\Psi_i\nabla_N\Psi_{N,i} + \Psi_{N,i}\Psi_j\nabla_N^2\Psi_i) = E\Psi_{N,j} \tag{1.7}$$

The terms in the infinite sum for which $i \neq j$ characterise coupling between electronic states, are usually very small, and are neglected when the adiabatic approximation is used. The term with $j = i$ in is usually zero, except for spatially degenerate wave functions. The last term in the sum is very small compared with the second term and corresponds to coupling between the nuclei and the electronic motion. A classical theoretical study by Born and Oppenheimer [34] regarding spectroscopic contributions in diatomic molecules concludes that the coupling term is of higher order than 4 for κ, which is defined as:

$$\kappa = (m/M)^{1/4} \tag{1.8}$$

where m is the electron mass and M is the average of the nuclear masses. This had previously been done using old quantum theory, which involved classical mechanics, but Born and Oppenheimer used quantum mechanics and their results corresponded more accurately to experiments. The general case was later solved by Slater [35], but neglecting the fourth term in (1.7) with $j = i$ is still known as the Born-Oppenheimer approximation (BOA).

A way of imaging the BOA is to consider the nuclei fixed, because they move much slower than electrons, which therefore almost instantaneously respond to the movement of the nuclei, hence, the nuclear kinetic energy is neglected. The $\mathbf{V}_{NN}$ term in (1.2) is independent of the electrons when the BOA is applied, and therefore constant for a given geometry. $\mathbf{H}_E$ will not include $\mathbf{V}_{NN}$, since the BOA is applied from now on.

1.2.3 A General Approach to Electronic Structure Calculations

The main purpose of this section is to introduce the equations for the energy terms of the SE, and to use this notation to write both the equations of WFM and DFT. This will highlight the similarities and differences between the methods. DFT has been used far more than WFM in this work, but I still present WFM because it is useful to explain hybrid functionals and some of the problems with DFT. This section partly follows Peter Gill's approach to DFT and the Hartree-Fock (HF) method in reference [36].

The three terms included in $\mathbf{H}_E$ have various complexity, because the components of $\mathbf{T}_E$ and $\mathbf{V}_{NE}$ depend on one electron coordinate, while the components of $\mathbf{V}_{EE}$ depend on two. Electron-electron repulsion is therefore more complicated and computationally expensive to evaluate. The major difference between the WFM and DFT approaches is the way they approximate the electron-electron term.

The components of the total energy are:

$$E_{tot} = E_T + E_V + E_J + E_X + E_C \tag{1.9}$$

in both WFM and DFT. The first three terms on the right hand side are: the kinetic energy of the electrons (E_T), the potential energy of the electrons due to their interaction with the nuclei (E_V), and the average Coulomb interaction between the electrons (E_J) (E_J includes electron self interaction). The expressions of these terms are:

$$E_T = -\frac{1}{2}\sum_{i=1}^{n} \int \psi_i(\mathbf{r}) \nabla^2 \psi_i(\mathbf{r}) d\mathbf{r} \tag{1.10}$$

$$E_V = -\sum_{a=1}^{m} \sum_{i=1}^{n} \int \frac{Z_a}{\mathbf{R}_a - \mathbf{r}_i} d\mathbf{r} \tag{1.11}$$

$$E_J = -\frac{1}{2}\sum_{i=1}^{n} \sum_{j=1}^{n} \int\int \frac{\psi_i(\mathbf{r})\psi_i(\mathbf{r})\psi_j(\mathbf{r}')\psi_j(\mathbf{r}')}{|\mathbf{r} - \mathbf{r}'|} d\mathbf{r} d\mathbf{r}' \tag{1.12}$$

where m is the number of the nuclei. The 1/2 factor is necessary to avoid double counting of the electrons and Z_a is the atomic number of the nucleus. Notice that the terms in which $i = j$ in (1.12) correspond to interaction of an electron with itself and have no physical relevance. Equation (1.10) – (1.12) are identical in WFM and DFT, with the exception that different orbitals are used. The last two terms in (1.9), however, differentiate DFT from WFM; I will show their different expressions in the sections about WFM and DFT respectively.

The exchange term (E_X) corrects for the fact that electrons are fermions and have an anti symmetric wave function (i.e. electrons with the same spin repel each other). This non-Coulomb repulsion between same spin electrons is often called "Fermi correlation" or "Fermi repulsion". Fermi correlation makes electrons of opposite spin form electron pairs, because it makes electrons with parallel spin repel each other – but it does not affect electrons with opposite spin. The exchange term also corrects for electron self interaction.

The orbitals in both WFM and DFT are products of a spin function and a spatial function (spin orbitals). Antisymmetrised products of spin orbitals, Slater Determinants (SDs), are the building blocks of the wavefunction in HF and post HF methods:

$$\Phi_{\mathrm{SD}} = \frac{1}{\sqrt{N!}} \begin{vmatrix} \psi_1(\mathbf{x}_1) & \psi_2(\mathbf{x}_1) & \dots & \psi_N(\mathbf{x}_1) \\ \psi_1(\mathbf{x}_2) & \psi_2(\mathbf{x}_2) & \dots & \psi_N(\mathbf{x}_2) \\ \dots & \dots & \dots & \dots \\ \psi_1(\mathbf{x}_N) & \psi_2(\mathbf{x}_N) & \dots & \psi_N(\mathbf{x}_N) \end{vmatrix} \tag{1.13}$$

$$\psi_i(\mathbf{x}) = \varphi(\mathbf{r}) \times \chi(s) \tag{1.14}$$

where $\mathbf{x}$ represents both the spatial and the spin coordinates, φ is the spatial part of the orbital, χ is the spin part (which can be either α or β), and N is the number of electrons. The columns in the Slater determinant each represent different orbitals and the rows electron coordinates. The Slater determinant fulfils the Pauli principle as the exchange of two electrons results in a sign change of the determinant.

Spin orbitals in closed shell molecules are paired; both spin orbitals in such a pair share the same spatial distribution. It is possible to reduce the computational cost of a calculation by only calculating one spatial distribution for each pair and occupying it with two electrons of opposite spin – this is called a restricted calculation. The spatial part of the spin orbitals in open shell molecules, however, all have different distributions, because unpaired electrons affect electrons with parallel spin differently than electrons with opposite spin. It is possible to use restricted methods on open shell molecules, although it is more accurate

to treat all orbitals individually. This is called unrestricted and is more computationally expensive.

1.2.4 Wave Function Methods

In 1928, Hartree introduced the SCF method [37]; he used a Self Interaction Correction (SIC) formula for the exchange term:

$$E_X^{\text{Hartree}} = -\frac{1}{2}\sum_{i=1}^{n}\int\int\frac{\psi_i^2(\mathbf{r})\psi_i^2(\mathbf{r}')}{|\mathbf{r}-\mathbf{r}'|}\mathbf{dr}\mathbf{dr}' \tag{1.15}$$

This correction is not invariant under unitary transformations and does not make the wave function anti symmetric. Fock corrected these problems in 1930 [38]; he suggested the following exchange functional:

$$E_X^{\text{Fock}} = -\frac{1}{2}\sum_{j=1}^{n}\sum_{i=1}^{n}\int\int\frac{\psi_i(\mathbf{r})\psi_j(\mathbf{r})\psi_i(\mathbf{r}')\psi_j(\mathbf{r}')}{|\mathbf{r}-\mathbf{r}'|}\mathbf{dr}\mathbf{dr}' \tag{1.16}$$

This functional has Hartree's SIC formula embedded (the terms in which $i=j$); the additional terms ensure that the wave function is anti symmetric and invariant to unitary transformations. Fock exchange provides the exact exchange of a system. It is a non-local functional since the value at point **r** depends on all values in space (integration over **r**'). Hence, exchange is a non-local property.

The obvious problem with the HF approach is that it neglects electron correlation. Correlation is often divided into dynamic and near-degeneracy correlation (near-degeneracy correlation is also called non-dynamic or static correlation), but there is no clear distinction between the two. Dynamic correlation originates from the difference between the *instantaneous* Coulomb repulsion and the *average* repulsion between electrons (E_J). It is therefore much more important at short electron-electron distances. Near-degeneracy correlation, which is due to the fact that an accurate description of the wave

function needs to consider multiple electronic states if the energy of one or many electronic state/states are close to the ground state, is a long range effect. The latter situation is common for dissociation of atoms in molecules, excited states, and in compounds with very heavy metals, but atoms do not have any near-degeneracy correlation at all [39]. A good example of dynamic correlation effects on molecular properties is the electrons in the hydrogen molecule. Assume that one of the electrons, e_a^-, is located at one of the hydrogen nuclei at the equilibrium geometry. Given this, the probability for finding the other electron, e_b^-, at the other nucleus is very high, but HF theory predicts the probability of finding e_b^- to be the same at both nuclei (because it only accounts for the average position, not the instantaneous position of e_a^-). Hence, HF theory screens e_a^- too much from the nucleus, and the energy is consequently too high. Near-degeneracy correlation is also a problem for the hydrogen molecule, because the energy of the anti-bonding sigma MO approaches the energy of the bonding sigma MO at large bond distances. One needs both of these MOs to describe the electronic structure when the molecule dissociates. Otherwise, the probability of forming two ions, and consequently the energy, is much too high.

Several methods add correlation to the HF method; these include various excitations of the wave function. Examples of methods to include dynamic correlation are Configuration Interaction (CI), Coupled Cluster (CC), and perturbation methods like Møller-Plesset (MP) (all these methods also include some near-degeneracy correlation). Multi-reference methods like Complete Active Space SCF (CASSCF) include near-degeneracy correlation; CI (MRCI) or perturbation theory (CASPT2) are often grafted onto CASSCF to account for the dynamic correlation. It is correct to consider these methods as "correlation functionals"; nevertheless, the correlation energy is not only due to pure correlation effects. The correlation energy also contains contributions to the kinetic energy, and changes in the nuclear-electron and the Coulomb part of the electron-electron potential energy, because inclusion of correlation effects changes the electron density. The formal definition of correlation energy is:

$$E_c^{HF} = E_{exact} - E_{HF} \tag{1.17}$$

or equivalent:

$$E_c^{HF} = \mathbf{T}_c^{HF} + E_{V,c}(\Delta\rho) + E_{J,c}(\Delta\rho) + E_{pure,c}^{HF} \tag{1.18}$$

The exchange energy is generally much higher than the correlation energy, the exchange energy for a neon atom is -12.11 a.u. and the correlation energy -0.39 a.u. using WFM [40].

1.2.4.1 The Reduced Density Matrix

The wavefunction provides information on all expectation values of a corresponding operator for a system at the expense of being very complicated. One obtains the density matrix of order k by integrating over $N - k$ of the wavefunction's variables:

$$\begin{aligned}&\gamma_k(\mathbf{r}_1', \mathbf{r}_2', ..., \mathbf{r}_k', \mathbf{r}_1, \mathbf{r}_2, ..., \mathbf{r}_k) \\ &= \binom{N}{k} \int \Psi^*(\mathbf{r}_1, \mathbf{r}_2, ..., \mathbf{r}_k, \mathbf{r}_{k+1}, ..., \mathbf{r}_N) \Psi(\mathbf{r}_1', \mathbf{r}_2', ..., \mathbf{r}_k', \mathbf{r}_{k+1}, ..., \mathbf{r}_N) d\mathbf{r}_{k+1} ... d\mathbf{r}_N\end{aligned} \tag{1.19}$$

Notice that the first k variables of Ψ^* and Ψ in (1.19) are different. The reduced density matrices of first and second order are of particular interest since the Hamiltonian only involves one- and two-electron operators. The diagonal elements of the first and second order density matrices are the electron density and the electron pair density respectively. Many analysis tools (presented below) use the reduced electron density matrices of first and second order.

1.2.5 Density Functional Theory

The major difference between DFT and WFM is that the electron density (ρ) is the basis of the exchange-correlation (xc) functionals in DFT, compared with the orbitals in WFM. Post HF methods can include correlation systematically because they treat electrons individually, but this also makes the methods computationally expensive. The electron density only depends on the three spatial coordinates (compared with $3N$ for WFM, where

N is the number of electrons); DFT therefore scales favourable with the size of the system in comparison with WFM. DFT has traditionally been used mainly by solid state physicists, but the improved accuracy of the calculated energies of functionals that depend on the reduced gradient of the electron density, and exact exchange, has made DFT more popular among computational chemists. As a result, the number of publications involving DFT increased exponentially from year 1990 to 1999 [41]. Xc-functionals are under rapid development and DFT's popularity is therefore likely to continue.

The history of DFT starts with the Thomas–Fermi model [42, 43] from 1927, which does not use a SCF or orbitals, but only the electron density explicitly. It is based on the uniform electron gas (section 1.2.5.1), and is derived from the particle in a box [36]. The Thomas-Fermi model expresses the kinetic energy of the spin density:

$$E_{\mathrm{T}}^{\mathrm{Thomas-Fermi}} = \frac{3}{10}(6\pi^2)^{2/3}\int \rho_{\alpha}^{3/5}(\mathbf{r})\mathbf{dr} \tag{1.20}$$

Dirac later came up with a correction for exchange [44], also based on the uniform electron gas:

$$E_{\mathrm{X}}^{\mathrm{Dirac}} = -\frac{3}{2}(\frac{3}{4\pi})^{1/3}\int \rho_{\alpha}^{4/3}(\mathbf{r})\mathbf{dr} \tag{1.21}$$

Despite this and the additional corrections of von Weizsäcker regarding gradients of the electron density [45], the non-SCF Thomas-Fermi-Dirac model is not accurate enough, but it is still under development [46].

The justification for using DFT is the two theorems of Hohenberg and Kohn [47] that consider a non-degenerate ground state. The Hamiltonian in these theorems consists of the kinetic energy of non-interacting electrons, the average coulomb interaction, and a potential term. The kinetic energy and coulomb average interaction are given by (1.10) and (1.12) and the potential is given by:

$$\mathbf{V} \equiv \int \mathbf{v}(\mathbf{r})\psi(\mathbf{r})\psi^*(\mathbf{r})d\mathbf{r} \tag{1.22}$$

where $\mathbf{v}(\mathbf{r})$ is an external potential. The first theorem states that the external potential is (to within a constant) a unique functional of the electron density; hence, the electronic ground state is a unique functional of the electron density. It is therefore possible to calculate the exact electron density by considering non-interacting electrons moving in a unique external potential. The proof that the external potential is unique is based on two potentials which differ by more than a constant. The assumption that these potentials give rise to the same electron density leads to an inconsistency. The conclusion is that this assumption is wrong: the potential is a unique functional of the electron density. The second theorem provides an energy variational principle for DFT; a trial density ρ_{trial} yields an energy equal to or higher than the exact electron ground state density ρ ($E(\rho_{\text{trial}}) \geq E(\rho)$). If Hohenberg and Kohn's theorems are the fundamental justification for using DFT, then the practical breakthrough was the introduction of the SCF and orbitals by Kohn and Sham [48]:

$$\mathbf{h}_{\text{KS}}\psi_i = \varepsilon_i\psi_i \tag{1.23}$$

$$\mathbf{h}_{\text{KS}} = -\frac{1}{2}\nabla^2 + \mathbf{v}_{\text{eff}} \tag{1.24}$$

$\mathbf{v}_{\text{eff}}$ is the effective potential. Notice that the expression does not include an electron-electron operator – only an effective potential that yields the exact electron density (if the potential is exact). The wavefunction is written as a single determinant (Ψ_S) of the Kohn-Sham orbitals; this wavefunction corresponds to non-interacting electrons, because of the absence of the electron-electron operator. Ψ_S is not the exact wavefunction, even if the effective potential that yields the exact electron density is used [49, 50], because this potential yields the non-interacting kinetic energy ($\mathbf{T}_S$) that differs from the exact kinetic energy. The kinetic energy is only dependent on the orbitals; wrong kinetic energy is therefore equivalent to wrong orbitals – even for the exact effective potential. It is therefore evident that there are fundamental differences between Hartree-Fock orbitals and Kohn-Sham orbitals.

The effective potential is written as:

$$\mathbf{v}_{\text{eff}} = \mathbf{v}_{\text{ne}} + \int \frac{\rho(\mathbf{r})}{|\mathbf{r}-\mathbf{r}'|} d\mathbf{r} + \mathbf{v}_{\text{xc}} \tag{1.25}$$

The first term is the potential from the nuclei, the second the average potential from the electrons, and the last the exchange-correlation potential. The exchange-correlation potential will always include some kinetic energy, even for the exact exchange-correlation potential, because the difference between the exact and non-interacting kinetic energy is collected in the exchange-correlation potential. Trying to find a good approximation for the exchange-correlation potential is crucial, as DFT with the exact exchange-correlation potential is a formally exact theory. It is, however, useful to introduce some simple models and concepts of DFT that xc-functionals are based upon, before a discussion of those functionals.

1.2.5.1 The Uniform Electron Gas Model

The uniform gas is a volume (V) with n electrons uniformly distributed, which consequently has an electron density $\rho = n/V$. It is obtained when n and V approach infinity, and has uniformly distributed positive charges, which neutralise the system. The uniform gas resembles a metal of a perfect crystal where the cores are smeared out, and is also known as "jellium".

1.2.5.2 The Adiabatic Connection Formula

The adiabatic connection formula provides an alternative way of writing the xc-energy:

$$E_{\text{XC}} = \int_0^1 \mathbf{U}_{\text{XC}}^{\lambda} d\lambda \tag{1.26}$$

The integral is over an "interelectronic coupling strength" parameter (λ) that "switches on/off" Coulomb repulsion between electrons, and $\mathbf{U}_{\text{XC}}^{\lambda}$ is the potential energy for

coupling strength λ. This formula connects the non-interacting Kohn-Sham reference system (λ=0) with the interacting system (λ=1) and is among other things a theoretical justification for including exact exchange in hybrid functionals.

1.2.5.3 The Pair Density and Electron Holes

The electron-electron term is the most difficult term to evaluate in equation (1.2). Useful properties in approximating this term include the pair density and the electron hole function (based on the pair density). The pair density is the probability of finding two electrons at position r_1 and r_2 at the same time:

$$\rho_2(\mathbf{r}_1,\mathbf{r}_2) = N(N-1)\int\ldots\int\left|\Psi(\mathbf{r}_1,\mathbf{r}_2,\mathbf{r}_3,\mathbf{r}_4\ldots\mathbf{r}_n)\right|^2 \mathbf{dr}_3\mathbf{dr}_4\ldots\mathbf{dr}_n \qquad (1.27)$$

The factor of $N(N\text{-}1)$ is due to the N ways of choosing the first electron and (N-1) ways of choosing the second. One often divides the pair density into two terms, to show the dependence on exchange and correlation more explicitly:

$$\rho_2(\mathbf{r}_1,\mathbf{r}_2) = \rho(\mathbf{r}_1)\rho(\mathbf{r}_2)(1+f(\mathbf{r}_1,\mathbf{r}_2)) \qquad (1.28)$$

$f(\mathbf{r}_1,\mathbf{r}_2)$ is the correlation factor (which includes exchange and correlation). It is evident that $f(\mathbf{r}_1,\mathbf{r}_2)$ includes the SIC, because a double integration over space gives N^2 electron pairs if $f(\mathbf{r}_1,\mathbf{r}_2) = 0$. A property related to the pair density is the conditional probability:

$$\Omega(\mathbf{r}_2;\mathbf{r}_1) = \frac{\rho_2(\mathbf{r}_1,\mathbf{r}_2)}{\rho(\mathbf{r}_1)} \qquad (1.29)$$

Ω is the probability of finding an electron at $\mathbf{r}_2$, *given* that another electron is located at $\mathbf{r}_1$. (1.28) shows that the difference between the conditional and the unconditional probability of finding an electron in $\mathbf{r}_2$ is:

$$h_{XC}(\mathbf{r}_2;\mathbf{r}_1)=\frac{\rho_2(\mathbf{r}_1,\mathbf{r}_2)}{\rho(\mathbf{r}_1)}-\rho(\mathbf{r}_2)=\rho(\mathbf{r}_2)f(\mathbf{r}_2;\mathbf{r}_1) \tag{1.30}$$

h_{XC} is known as the exchange-correlation hole. It illustrates how the motion of electrons is correlated, for instance how the probability of finding an electron close to the reference electron in r_1 is reduced. Integration of the xc-hole over all space results in the removal of one electron charge:

$$\int h_{XC}(\mathbf{r}_2;\mathbf{r}_1)\mathbf{dr}_2=-1 \tag{1.31}$$

This is because the first term in (1.30) corresponds to the probability of finding an electron *other* than the reference electron. As the system consists of N electrons (including the reference electron), integration over the first term in (1.30) yields N-1 electron charges, i.e. the number of electrons in the system minus the reference electron.

The electron pair density is very important for evaluating the electron-electron interaction. It is possible to write the electron-electron interaction in terms of the pair density:

$$E_{EE}=\frac{1}{2}\int\int\frac{\rho_2(\mathbf{r}_1,\mathbf{r}_2)}{\mathbf{r}_{12}}\mathbf{dr}_1\mathbf{dr}_2=\frac{1}{2}\int\int\frac{\rho(\mathbf{r}_1)}{\mathbf{r}_{12}}(\rho(\mathbf{r}_2)+h_{XC}(\mathbf{r}_2;\mathbf{r}_1))\mathbf{dr}_1\mathbf{dr}_2 \tag{1.32}$$

The first term is the average Coulomb energy, which includes electron self interaction, and the second is the correction to this term by the exchange-correlation hole, which includes SIC, other classical corrections, and quantum effects. It is possible to divide the xc-hole into an exchange (Fermi), and a correlation contribution:

$$h_{XC}(\mathbf{r}_1;\mathbf{r}_2)=h_X(\mathbf{r}_1;\mathbf{r}_2)+h_C(\mathbf{r}_1;\mathbf{r}_2) \tag{1.33}$$

$$h_X(\mathbf{r}_2;\mathbf{r}_1)=\rho(\mathbf{r}_2)f_X(\mathbf{r}_1;\mathbf{r}_2) \tag{1.34}$$

$$h_C(\mathbf{r}_2;\mathbf{r}_1)=\rho(\mathbf{r}_2)f_C(\mathbf{r}_1;\mathbf{r}_2) \tag{1.35}$$

As in WFM, exchange is responsible for removing self interaction and hence the integral over the exchange hole equals minus the charge of an electron. The integral of the correlation hole over the entire space therefore equals zero.

$$\int h_X(\mathbf{r}_2;\mathbf{r}_1)\mathbf{dr}_2 = -1 \tag{1.36}$$

$$\int h_C(\mathbf{r}_2;\mathbf{r}_1)\mathbf{dr}_2 = 0 \tag{1.37}$$

The Pauli principle states that all electron density with the same spin as the reference electron must be removed from the reference point:

$$h_X(\mathbf{r}_1;\mathbf{r}_1) = -\rho_\alpha(\mathbf{r}_1) \tag{1.38}$$

The exchange hole is negative everywhere and usually attains its lowest value at the reference electron (if the electron density has a large magnitude at the reference electron). Bader and co-workers interpret the exchange hole as a "spreading out of the same-spin density originating from the position $\mathbf{r}_1$" [51] ($\mathbf{r}_1$ is the position of the reference electron). They continue: "Pictorially, one can imaging that as an electron moves through space it carries with it a Fermi hole of ever changing shape, the density of the electron being spread out in the manner described by its Fermi hole and excluding density equivalent to one same-spin electron".

The correlation hole is negative close to the reference electron and positive far away from it. The zero charge of its integral illustrates that the Coulomb force only transfers electron density away from the reference electron to other regions. The conditions that the exchange- and correlation-hole integrals equal -1 and 0 constitutes constraints when developing exchange-correlation functionals; certain functionals also use more detailed information about the xc-holes [52]. The exchange hole is also the basis for the Electron Localization Function (ELF) [53], which has been used in this work (section 1.2.10.1).

1.2.5.4 Jacob's Ladder of DFT

DFT generally provides better results than WFM for calculations of similar computational cost, but it has the fundamental problem that it is hard to improve systematically. The accuracy of xc-functionals depends on the property and type of molecule, and it is often unclear which functional to use for a specific problem. Perdew therefore introduced the concept of a Jacob's ladder of density functional approximations [54], to provide a systematic way of improvement. The Book of Genesis states that Jacob's ladder leads from earth to heaven, with angels ascending and descending on it. In DFT, Jacob's ladder reaches from the Hartree world to the heaven of chemical accuracy and has five rungs of xc-functional approximations. Every rung provides a better approximation, and a specific rung includes all lower ones, like a Russian doll. Functionals optimised according to these principles systematically increase the accuracy of the calculation, as one moves to a higher rung. A description of the first four rungs is provided below, since they are relevant to the calculations in this work. The fifth rung is the generalised random phase approximation, but the large basis sets needed for this method make it "not yet practical" for general use.

One way to optimise xc-functionals is to use expressions for the xc-potential that contain empirical parameters optimised on a set of molecules; another way is to design them to be exact for different simplified models (like the uniform electron gas in section 1.2.5.1). It is also possible to combine the two methods. Functionals designed to be exact for simple models generally have fewer parameters and Perdew argues [54] that these parameters are more fundamental. As one climbs up the ladder, more variables are available to make the functional exact for a greater number of simple models ("satisfying constraints" in the words of Perdew). Functionals with many fitting parameters often have problems in satisfying even the most fundamental models, and therefore do not satisfy the requirement of embedding previous rungs.

1.2.5.5 The Local Spin Density Approximation

The Local Spin Density Approximation (LSDA) uses the Dirac formula for exchange (1.16) in combination with a correlation functional. The most commonly used correlation functional in LSDA is Vosko, Wilk and Nusair's functional (VWN) which is based on fitting of data obtained by Monte Carlo simulations [55]. I do not include the expression of the VWN correlation energy because it is complicated and does not improve understanding of DFT. A more recent, and probably more accurate, LSDA correlation functional [41] is the correlation functional of Perdew and Wang [56].

The LSDA is exact for a uniform electron gas; the energy of a (small) volume element in a molecule is identical to the energy of a volume element with the same volume and density in a uniform electron gas. The LSDA produces accurate results for solid state physics problems, since the electron density varies slowly there, but gives worse results in molecules, where the density varies more rapidly. The LSDA generally provides better geometries and vibrational frequencies than HF [41], but often produces problems with overbinding. Becke argues that the source of this error is that the exchange hole of the non-interacting system follows the reference electron. It therefore simulates near degeneracy correlation, which is not desirable in a non-interacting system [57]. One usually tests the quality of xc-functionals on a set of atoms and molecules, the G2 test set [58], and extensions of this set [59]. The mean absolute error of atomization energies with the LSDA method, using the correlation functional of Perdew and Wang, is 83.8 kcal/mol [60] for the G2 set of molecules.

1.2.5.6 The Generalized Gradient Approximation

Since it is possible to describe a uniform electron gas exactly, all that is needed for a precise description of a molecule are corrections for its inhomogeneous electron density. The gradient of the electron density is a relevant variable to describe such an inhomogeneous electron density, but this does not work. Random phase approximation calculations on a jellium surface reveal that the xc-energy for small wave vectors is too

large when only the electron density gradient is included [61]. The reduced density gradient gives better results, and the general expression for the Generalized Gradient Approximation (GGA) energy is:

$$E_{XC}^{GGA} = \int f(\rho_\alpha, \frac{\nabla \rho_\alpha}{\rho_\alpha^{4/3}}) \mathbf{dr} \tag{1.39}$$

It is also possible to explain the failure of the simple gradient expansion in terms of xc-holes. The exchange hole of the gradient expansion violates the constraints that the exchange hole should be negative everywhere, and that its integral should equal minus one electron charge (1.31) [54]. GGA functionals fulfil those constraints.

Including the reduced density gradient improves the accuracy of the calculations significantly. It also removes some of the LSDA's overbinding (although the reason for overbinding in the LSDA is similar in the GGA; Becke argues that exact exchange is needed to correct this problem [57]). The GGA functional PBE [62, 63], which has been used in most calculations in this work, is developed by a non-empirical approach and has the LSDA embedded. PBE is optimised to satisfy the constraints on the xc-holes and the xc-energy. It gives a mean absolute error for atomization energies of 17.1 kcal/mol [60], for the G2 set of molecules.

1.2.5.7 Meta-GGA

The third rung of the ladder contains the meta-GGA functionals, which apart from the reduced gradient density also employ the kinetic energy (τ) and the Laplacian of the electron density, to account for the fact that the electron density of a molecule is inhomogeneous.

$$\tau_\sigma = \frac{1}{2} \sum_i^{occ.} |\nabla \psi_{i\sigma}|^2 \tag{1.40}$$

The kinetic energy (1.40) appears in the expansion of the electron exchange hole, and is more important than the Laplacian (which appears in the fourth-order gradient expansion) in terms of satisfying more constraints. The TPSS [60] functional is the meta-GGA development of PBE. TPSS shows mean absolute atomization energy errors of only 6.2 kcal/mol [60], for the G2 test set.

1.2.5.8 Hybrid Functionals and Hyper-GGAs

As exchange is exact in WFM, it seems reasonable to use Fock's exchange functional in DFT, but that does not work well at all. The local functionals for exchange and correlation in DFT contain a great deal of error cancellation and kinetic energy corrections. Becke argues [64]: "the splitting of E_{XC} into separate exchange and correlation parts ... is artificial and misleading. Only exchange and correlation *together* has ultimate physical meaning". An example: many of the most common correlation functionals have a positive slope of the correlation energy with respect to the bond distance in H_2 – opposite to what it is in reality – but the negative slope of the exchange functional compensates for this [65]. Exact exchange does not contain this cancellation of errors, and therefore shows worse results. The bad description of correlation in H_2 (and other molecules) is a consequence of correlation being a non-local effect described by a local functional. The use of exact exchange therefore requires a non-local description of correlation.

The series of articles by Becke [57, 66-69] in which he proposes a hybrid scheme that includes exact exchange was a great breakthrough for DFT. Exact exchange is similar to HF exchange, but it is based on Kohn-Sham orbitals; hence, exact exchange – and not HF exchange – is the correct term. Becke's first suggestion for a hybrid functional is a linear interpolation of the function in the adiabatic connection integral. The starting point (λ=0) in this approximation corresponds to exact exchange, and the finishing point (λ=1) corresponds to the LSDA xc-functional (this functional is referred to as "half-and-half"). He probes various combinations of functionals in the series of papers; the final hybrid functional is B3PW91. This functional contains contributions from the LSDA xc-functional (using the electron gas parameterization of Perdew and Wang [56]), the

difference between exact and LSDA exchange, Becke's gradient correction for exchange [52], and the PW91 correlation functional [70]:

$$E_{XC}^{B3PW91} = E_{XC}^{LSDA} + a_0(E_X^{exact} - E_X^{LSDA}) + a_X E_X^{B88} + a_C E_C^{PW91} \quad (1.41)$$

Fitting to experimental data determines the weighting parameters. Becke obtained the following values: $a_0 = 0.20$, $a_X = 0.72$, and $a_C = 0.81$. The hybrid functional B3LYP [71, 72] is the most widely used functional today, probably because it achieves great accuracy for the G2 test set of molecules.

The difference between hyper-GGA and hybrid functionals is that hyper-GGA functionals are based on all parameters of the meta-GGA *plus* exact exchange, and that they are developed in non-empirical ways.

1.2.6 Other Approximations and Comparisons between Them

Solving the SE requires several approximations; some of the most important ones are presented below. The magnitudes of electron density differences ($\Delta\rho$) between different levels of the approximation illustrate its relative importance. The $\Delta\rho$ calculations are performed on uranyl, because this is the most important molecule in this thesis. Section 1.2.11 presents how to calculate $\Delta\rho$ between a molecule and its fragments; here, I consider the $\Delta\rho$ between two calculations on UO_2^{2+} with the same geometry, but different options for a certain approximation. ρ is fundamental for molecules, as Kohn and Sham's theorems state that one only needs ρ to calculate all ground state properties. It is therefore suitable to use the magnitude of $\Delta\rho$, to illustrate to what extent different approximations affect the result of the calculations.

I consider only the magnitude of $\Delta\rho$ in this section, because the purpose is to illustrate how important a certain approximation is. There are other conclusions to draw from $\Delta\rho$, but they are not considered here.

1.2.6.1 The Basis Set

The SE is impossible to solve for atoms and molecules with more than one electron, without making the basis set approximation (the wave function must be expanded in an infinite sum of basis functions (1.4) to obtain the exact solution). The basis functions are called AOs, because of their resemblance to the orbitals in isolated atoms. MOs are obtained from optimized linear combinations of AOs. It is possible to simplify the wave function by separating its angular and radial contributions:

$$\Psi = \sum_{\infty} \chi(\mathbf{r},\theta,\varphi) = \sum_{\infty} R(\mathbf{r}) * \Theta(\theta) * \Phi(\varphi) \tag{1.42}$$

$\Theta(\theta)$ have solutions in terms of Legendre polynomials and $\Phi(\varphi) = (2\pi)^{-0.5} * e^{im\varphi}$. The two angular contributions are described by the spherical harmonics $Y_{l,m}(\theta, \varphi)$ [73]. There are two common ways of expressing the radial part:

$$R(\mathbf{r}) = N \times \mathbf{r}^{n-1} \times e^{-\zeta \mathbf{r}} \tag{1.43}$$

or

$$R(\mathbf{r}) = N \times \mathbf{r}^{(2n-2-l)} \times e^{-\zeta \mathbf{r}^2} \tag{1.44}$$

N is a normalisation constant and n and l are quantum numbers. The $\chi(\mathbf{r}, \theta, \varphi)$ functions are Slater Type Orbitals (STO), expressed as (1.43), and Gaussian Type Orbitals (GTO), expressed as (1.44). STOs have the advantage of describing the wave function better, i.e. fewer STOs are required to get the same quality of the wave function compared with GTOs. This is because the derivative of an STO is discontinuous at the nucleus and the STO falls off less rapidly at large distances from the nucleus. The drawback with STOs is that integrals only have numerical solutions; whereas GTOs have analytical solutions [40].

Different methods of basis set design result in different types of basis sets. The programs used in this work, for example, employ different types of basis sets. The smallest basis set

is the minimum basis set that only includes the essential AOs for each row i.e. 1*s* for the first row, and 1*s*, 2*s*, 2*p* for the second row etc. Including more AOs with different values of ζ (zeta) improves the quality of the basis set. Large values of ζ correspond to tight basis functions, small values to diffuse ones. A basis set that uses basis functions with two different values of zeta has Double Zeta (DZ) quality, three functions with different zeta values is known as Triple Zeta (TZ) etc. It is also possible to add functions of higher angular momentum (*l*-values) than those occupied in the ground valence configuration, these are polarisation functions. Hence, a basis set with two basis functions of different zeta values augmented with a polarisation function is called DZ plus polarisation (DZP), two extra polarisation functions DZ2P etc. This is, however, not a very efficient way to build a basis set, because a very precise description of the inner core orbitals is not necessary since chemistry is determined by the valence electrons. Hence, it is more effective to use a lower quality for the inner core orbitals. For instance, a basis set with TZ quality in the valence region might have only DZ quality for the inner core. A basis set of this type is called a split valence basis set.

The basis sets in the Amsterdam Density Functional (ADF) suite of programs [74] are STO split valence basis sets. The basis sets in the Gaussian03 (G03) code [75] are of GTOs type, designed by using "primitive" orbitals which are "contracted". The reason for contracting orbitals is, again, that the inner core orbitals do not change very much in a molecule, compared with an atom, and do not have to be described as accurately. ADF has the option of using "the frozen core approximation", where the inner core are calculated very accurately with relativistic effects in the beginning of the calculation, and are thereafter fixed.

The basis sets of the non-actinide atoms used in G03 have the notation 6-311G**, which means that the core orbitals are one contraction of six primitive GTOs and that the valence orbitals are made up of three contracted GTOs which contain three, one, and one primitive GTOs respectively. The stars represent polarisation, the first one additional *d* functions for second row atoms and the second additional *p* functions for hydrogen. The actinide basis set employed in G03 is also contracted; the notation is (14*s* 13*p* 10*d* 8*f* 6*g*)/[6*s* 6*p* 5*d* 4*f* 3*g*] [76]. The numbers within parentheses are the number of primitive functions and those within brackets signify the number of contracted functions. The actinide basis sets also

replace the inner core electrons with a relativistic effective core potential, to speed up the calculation.

It is important to evaluate how much the accuracy of the calculation improves as the number of basis functions increase, because the computational demand of the calculation is strongly dependent on the basis set. Figure 5 compares $\Delta\rho$ between different basis sets for uranyl.

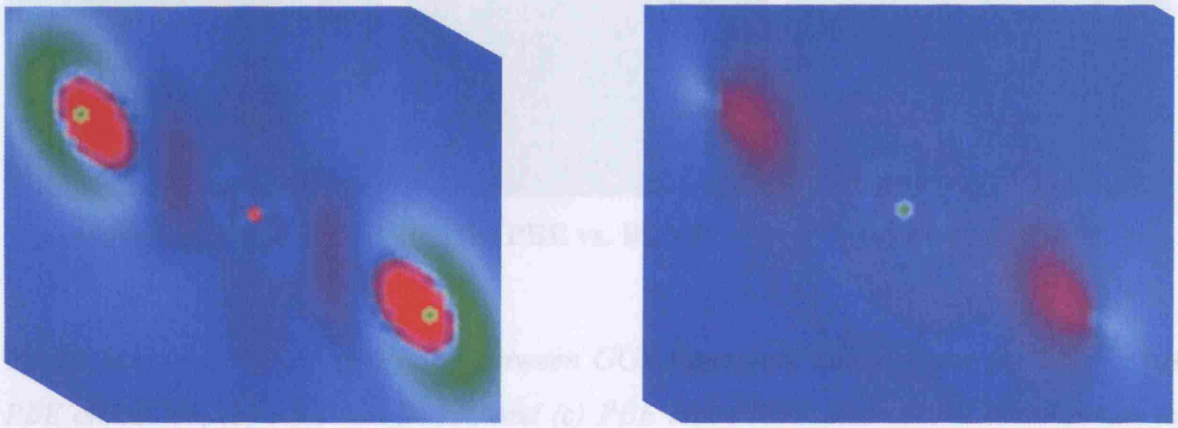

(a) oxygen SZ vs. DZ **(b) TZP vs. TZ2P**

Figure 5(a)-(b). *$\Delta\rho$ ($e^-/Bohr^3$) between calculations with different basis sets for UO_2^{2+}. (a) compares a DZ basis set for uranium and a SZ for oxygen with DZ basis sets for all atoms. (b) compares TZP basis sets for all atoms with TZ2P basis sets for all atoms. Red colour corresponds to higher ρ of the molecule with the larger basis set and green to higher ρ of the molecule with the smaller basis set. The maximum and minimum values are $\pm$ 0.1.*

$\Delta\rho$ between the Single Zeta (SZ) and DZ basis set for oxygen is much larger than $\Delta\rho$ between TZP and TZ2P for both the U and O atoms.

1.2.6.2 Comparison of xc-Functionals

Figure 6 shows $\Delta\rho$ between the PBE and the (a) BP86, (b) BLYP, and (c) PW91 xc-functionals for uranyl, as an illustration of the importance of the xc-functional

approximation. The largest $\Delta\rho$ is between PBE and BLYP; $\Delta\rho$ between PBE and BP86, and PBE and PW91 are small. PBE is developed from PW91, which is developed from the P86 correlation functional; this explains the small $\Delta\rho$.

The magnitude of $\Delta\rho$ is larger between different basis sets than between xc-functionals.

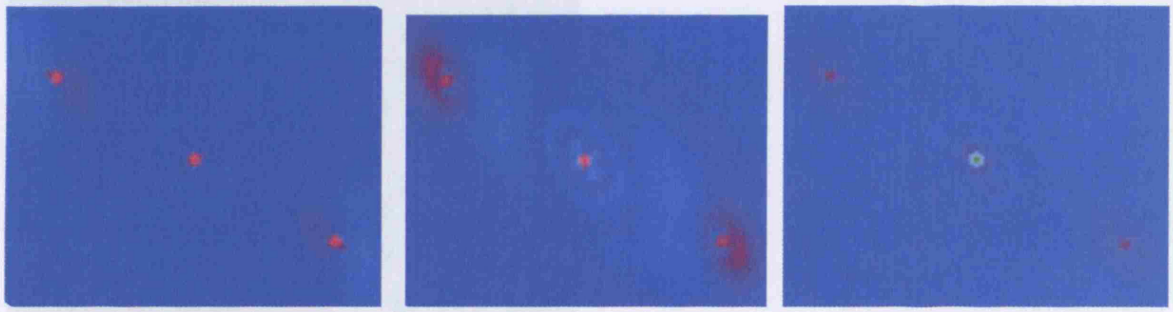

(a) PBE vs. BP86 **(b) PBE vs. BLYP** **(c) PBE vs. PW91**

Figure 6(a)-(c). *$\Delta\rho$ (e^-/Bohr^3) between GGA-functional calculations for UO_2^{2+}: (a) PBE and BP86, (b) PBE and BLYP, and (c) PBE and PW91. Red colour corresponds to higher ρ of the molecule with a non-PBE functional and green to higher ρ of the molecule with the PBE functional. The maximum and minimum values of the scale are ± 0.1.*

1.2.6.3 The Integration Grid

ADF evaluates all integrals by numerical integration; hence, there is an error due to discretisation. ADF controls the number of grid points by an integration parameter ranging from 0.5 to 12, increasing this parameter by 1.0 approximately doubles the number of grid points. The integration grid is denser at chemically important locations (pruned) in ADF and G03. The integration grid used with G03 has 99 radial shells and a maximum of 590 angular points per shell. This corresponds to the keyword "ultrafine".

Figure 7 shows $\Delta\rho$ between calculations with different integration parameters for uranyl, to illustrate how the integration parameter in ADF influences the result. The magnitude of the $\Delta\rho$ between these calculations is smaller than the $\Delta\rho$ obtained by changing the basis set from TZP to TZ2P, and similar to the $\Delta\rho$ between the BP86 and PBE xc-functionals. The

comparison is made between a low value of the integration grid parameter (3.0) and the recommended value for geometry optimization (5.0). Increasing the value further will probably have less effect on ρ than changing it from 3.0 to 5.0, as ρ reaches saturation.

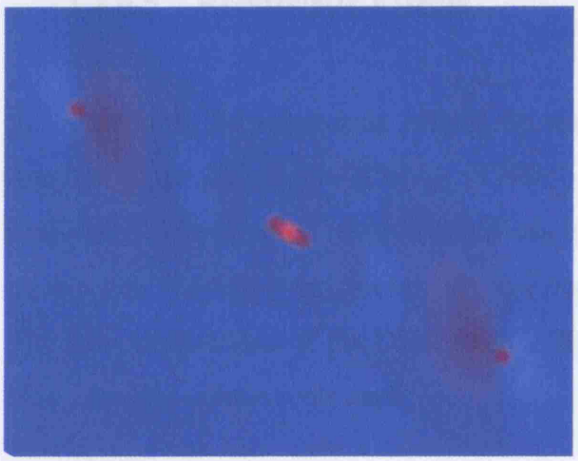

Figure 7. *$\Delta\rho$ (e^-/Bohr^3) between ADF calculations with integration grid parameters 3 and 5 for UO_2^{2+}. Red colour corresponds to a higher ρ for the molecule with the higher value of the integration grid parameter and green to a higher ρ for the molecule with the lower value. The maximum and minimum values are ± 0.1.*

1.2.6.4 The Self Consistent Field

The values of the potentials and operators in equation (1.24) depend on the orbitals, which are obtained by solving Kohn and Sham's equation (1.23); one therefore needs an iterative method to calculate the orbitals. The first step in solving equation (1.23) is to guess the orbitals. These orbitals are used to solve the equation and thereby obtain new orbitals. This procedure continues until the difference between the old and the new orbitals is smaller than a specified criterion. The ADF program has two different criteria: the norm and the maximum element of the difference between the $\mathbf{h}_{KS}$ operators of the two most recent cycles. The criterion that the maximum element between the two most recent cycles is less than 10^{-7} is usually used in this work. $\Delta\rho$ between uranyl calculations with the SCF criterion set to 10^{-4} and 10^{-5} (not shown) is so small that it is impossible to see except at the

uranium nucleus. Hence, setting the convergence criterion to 10^{-7} is a very good approximation in terms of $\Delta\rho$ for uranyl.

1.2.6.5 Relativistic Effects

ADF accounts for relativistic effects by either the Pauli formalism or the Zeroth-Order Regular Approximation (ZORA) [77-81], and G03 by the relativistic effective core potentials. Incorporating relativistic effects into the SE turns it into the Dirac equation [82]. Its solution has four components, the electron and the positron with two spin options each. The four components of the Dirac time independent equation are written in two equations with two spin components each:

$$c(\boldsymbol{\alpha}\cdot\boldsymbol{\pi})\Psi_{\text{Small}} + \mathbf{V}\Psi_{\text{Large}} = E\Psi_{\text{Large}} \tag{1.45}$$

$$c(\boldsymbol{\alpha}\cdot\boldsymbol{\pi})\Psi_{\text{Large}} + (-2mc^2 + \mathbf{V})\Psi_{\text{Small}} = E\Psi_{\text{Small}} \tag{1.46}$$

where $\boldsymbol{\alpha}$ is a spin function, $\boldsymbol{\pi}$ is the generalized momentum operator, and $\mathbf{V}$ is the electrostatic potential. Solving for Ψ_{Small} results in a relation between the electron (Ψ_{Large}) and positron (Ψ_{Small}) :

$$\Psi_{\text{Small}} = (E + 2mc^2 - \mathbf{V})^{-1} c(\boldsymbol{\sigma}\cdot\boldsymbol{\pi})\Psi_{\text{Large}} \tag{1.47}$$

Factorising the first factor on the right hand side gives:

$$(E + 2mc^2 - \mathbf{V})^{-1} = (2mc^2)^{-1}(1 + \frac{E - \mathbf{V}}{2mc^2})^{-1} = (2mc^2)^{-1}\mathbf{K} \tag{1.48}$$

It is possible to expand the **K**-factor:

$$(1 + \frac{E - \mathbf{V}}{2mc^2})^{-1} = 1 - \frac{E - \mathbf{V}}{2mc^2} + \ldots \tag{1.49}$$

Inserting (1.48) and (1.49) in (1.47), which is inserted in (1.46), results in the Pauli equation. The problem with this expansion is that $(E\text{-}\mathbf{V})/2mc^2$ must be small, or equivalent, $2mc^2 >> E\text{-}\mathbf{V}$, for the expansion to be valid. This is not true close to the nucleus where $\mathbf{V}$ approaches minus infinity. The ZORA method avoids this by factorizing (1.48) in a slightly different way:

$$(E + 2mc^2 - \mathbf{V})^{-1} = (2mc^2 - \mathbf{V})^{-1}(1 + \frac{E}{2mc^2 - \mathbf{V}})^{-1} = (2mc^2 - \mathbf{V})^{-1}\mathbf{K}' \qquad (1.50)$$

$E/(2mc^2\text{-}\mathbf{V})$ is much smaller than 1 everywhere, so expansion of the $\mathbf{K}'$-factor is a better approximation than expansion of the $\mathbf{K}$-factor. One obtains different orders of the regular approximation by keeping different numbers of terms in the expression: to keep no terms corresponds to the ZORA, and to keep one term corresponds to the First-Order Regular Approximation (FORA) etc. ADF recommends the ZORA, since it describes relativistic effects more accurately than the Pauli formalism, and avoids the divergence of the expansion problem close to the nucleus.

1.2.6.6 Solvent Models

Including solvent effects is important in theoretical calculations, as experimentalists often conduct experiments in solution, and the effect of solvent on the solute is often significant. Quantum chemists usually consider the following approaches: explicit inclusion of solvent molecules in the calculation or modelling of the solvent by a charge distribution around the solute. Using explicit solvent molecules has the advantage of modeling direct interactions, although the large number of solvent molecules needed to mimic the solvent increases the computational cost of the calculation dramatically. Ideal screening models provide a less expensive alternative that is accurate for most properties. The Polarizable Continuum Model (PCM) [83, 84], and the COnductor like Screening MOdel (COSMO) [85-87] are the best known screening models, and are used in this work.

Ideal screening dielectric continuum models incorporate solvent effects by building a cavity around the solute and distributing point charges on the cavity surface. PCM and

COSMO use an algorithm called GEnerate POLyhedra [88] (GEPOL) to build the cavity. The cavity is built by placing spheres around the atoms of the solute. The algorithm discards the overlapping surfaces of the spheres and smoothes the remaining surface.
Figure 8 shows different options for the smoothing of the surface. The Van der Waals (VdW) surface is generated without smoothing; the path traced by rolling the solvent about the VdW surface defines the Solvent Excluding Surface (SES), and the path traced by the centre of the solvent when rolling about the VdW surface generates the Solvent Accessible Surface (SAS).

Figure 8(a)-(c). *The (a) VdW surface, (b) SES, and (c) SAS [89].*

The cavity is created by filling the spaces not accessible to the solvent with spheres and computing the surface of interlocking spheres. This is done by dividing each sphere into 60 triangular areas called tesserae, by projecting the surface of a pentakisdodecahedron, which is placed in the middle of the sphere, on the surface. The tesserae found at the intersection volume of the spheres are eliminated. The creation of new spheres are controlled by different parameters, the most impotant parameter for this work is p_i^r, the Overlapping FACtor (OFAC). A high value of OFAC corresponds to high overlap between the spheres. New spheres are discarded if the value of OFAC is higher than a certain criteria. Figure 9 shows how OFAC is defined.

Figure 9. *Description of the OFAC parameter (p_i^r) [88].*

Figure 10 illustrates how the choice of cavity surface influences solvent effects by showing $\Delta\rho$ between calculations in the gas phase, with the SAS model, and with the SES model (in this thesis, the term "gas phase" is used to describe an isolated molecule). The larger size of the cavity in the SAS model reduces the solvent effects to yield similar ρ as in the gas phase. The SAS model's appropriate use is to calculate the non electrostatic contribution to the total energy [90].

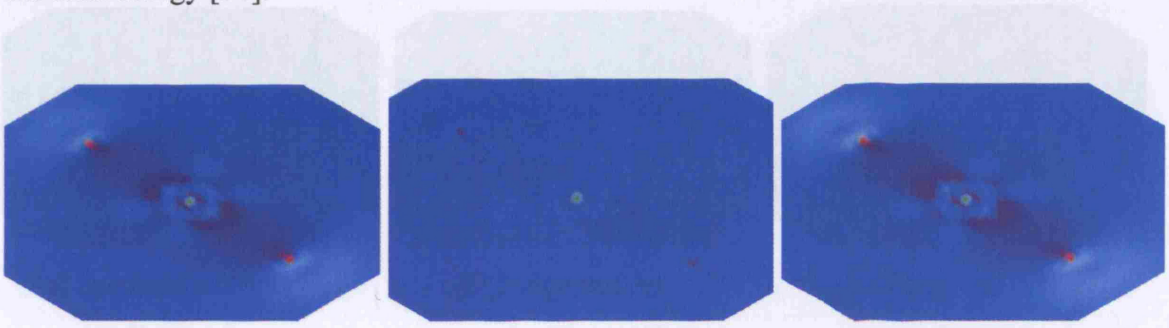

(a) SAS vs. SES **(b) SAS vs. gas phase** **(c) SES vs. gas phase**

Figure 10(a)-(c). *$\Delta\rho$ ($e^-/Bohr^3$) between calculations with the (a) SAS and SES, (b) SAS and gas phase, and (c) SES and the gas phase for UO_2^{2+}. Red colour corresponds to a higher ρ for the molecule with the SAS model and green to a higher ρ for the molecule with the SES model. The maximum and minimum values are ± 0.1.*

The volume of the cavity is crucial when modelling solvent effects; the radii of the spheres used to build the cavity are therefore important parameters for the solvent model. The radii of the spheres are determined by the United Atom Topological Model (UATM) [91] in G03, and set by the user in ADF. The UATM calculates the radius of a sphere around an atom X as:

$$R(X) = R^0(X) + \gamma(X) \cdot (n_H + \frac{n_{act}}{2} + \partial_{sp^2} + \frac{3\partial_{sp}}{2}) \quad (1.51)$$

$R^0(X)$ is a "basic radius", $\gamma(X)$ is a parameter that depends on X's row in the periodic table, n_H is the number of linked hydrogen atoms, n_{act} is the number of linking atoms with the same atomic number and hybridization as X and bonded to C and H atoms only. δ_{sp2} and δ_{sp} equal 1 if X is sp^2 or sp hybridized and 0 otherwise. Some special cases regarding sp^3 hybridized carbon atoms and ions have some further corrections.

Figure 11 shows ρ's dependence on the cavity volume for ADF calculations with the COSMO. It is clear that the cavity volume is an important parameter for the solvent model; solvent effects decrease with increasing radii of the spheres around the atoms.

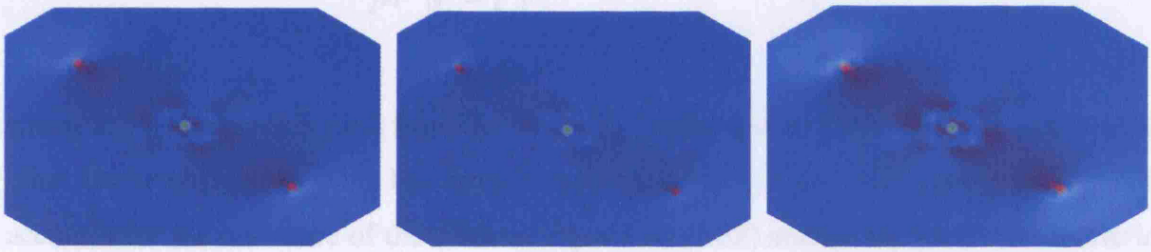

(a) medium volume vs. small volume **(b) large vol. vs. medium volume** **(c) large vol. vs. small volume**

Figure 11(a)-(c). *$\Delta\rho$ (e^-/Bohr^3) between calculations with the radii of the sphere around the U and O atom set to (a) U = 2.0 Å and O = 1.6 Å, and U = 1.8 Å and O = 1.4 Å, (b) U = 2.2 Å and O = 1.8 Å, and U = 2.0 Å and O = 1.6 Å, and (c) U = 2.2 Å and O = 1.8 Å, and U = 1.8 Å and O = 1.4 Å for UO_2^{2+}. Red colour corresponds to higher ρ for the molecule with larger cavity volume and green to higher ρ for the molecule with the smaller volume of the cavity. The maximum and minimum values are ± 0.1.*

The charge density on the surface of the cavity (σ) relates to the electric field:

$$\sigma = -\frac{\varepsilon - 1}{4\pi} E(\rho_{\text{sol}}, \sigma) \cdot n \tag{1.52}$$

where ε is the dielectric constant of the solvent, E is the electric field, ρ_{sol} is the electron density of the solute, and n is a vector perpendicular to the cavity surface. (1.52) does not have analytical solutions for complicated geometries (non-spherical and non-elliptical) of the cavity, and solving it requires numerical methods. All tesserae are therefore assigned point charges:

$$q_i = \sigma(\mathbf{r}_i) a_i \tag{1.53}$$

where a_i is the area of the tesserae. It is possible to calculate the component of the electric field perpendicular to the cavity surface:

$$E(\mathbf{r}_i) \cdot n = E(\mathbf{r}_i)_{\text{sol}} \cdot n + \sum_{j \neq i}^{\text{tesserae}} \frac{q_i}{\left|\mathbf{r}_i - \mathbf{r}_j\right|^3} (\mathbf{r}_i - \mathbf{r}_j) \cdot n + 2\pi \frac{q_i}{a_i} (1 - \eta) \tag{1.54}$$

where E_{sol} is the electric field from the solute, the second term is the contribution from the other cavity charges, and the last term is the field from q_i itself. The correction factor (η) accounts for the curvature of the surface. Equations (1.52) and (1.54) have only numerical solutions, because of the coupling between the cavity charges and the electric field.

Figure 12 shows how the dielectric constant and the radius of the solvent affect ρ in uranyl. ρ changes only slightly after the dielectric constant has reached a certain level.

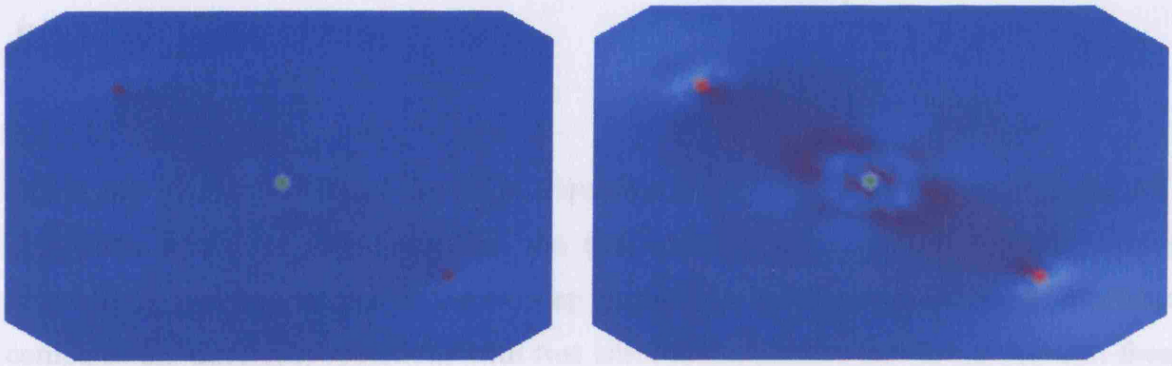

(a) water vs. THF **(b) THF vs. gas phase**

Figure 12(a)-(b). *$\Delta\rho$ ($e^-/Bohr^3$) between calculations with different parameters of the dielectric constant (ε) and radius (r) of the solvent corresponding to (a) water (ε= 78.39 and r = 1.385 Å) and THF (ε = 7.58 and r = 2.56 Å) and (b) THF and gas phase for UO_2^{2+}. Red colour corresponds to higher ρ of the molecule with smaller dielectric constant of the solvent and green to higher ρ of the molecule with higher dielectric constant of the solvent. The maximum and minimum values are ± 0.1.*

1.2.7 Charge Analysis

Three methods of charge analysis are available in ADF: Mulliken population analysis [92, 93], Voronoi Deformed Densities [94-96] (VDD), and the Hirshfeld scheme [97, 98].

1.2.7.1 Mulliken Population Analysis

Mulliken population analysis is an old and well known method that has the disadvantage of strong basis set dependence. It is convenient to explain Mulliken population analysis on a diatomic molecule with MOs (ψ_i) of occupation number $N(i)$, made from linear combinations of all orthonormal AOs (χ) on atom A and B:

$$\psi_i = c_{A,i}\chi_A + c_{B,i}\chi_B \tag{1.55}$$

$$N(i)\psi_i^2 = N(i) = N(i)c_{A,i}^2 + 2N(i)c_{A,i}c_{B,i}S_{AB} + N(i)c_{B,i}^2 \tag{1.56}$$

$$S_{AB} = \int_{\infty} \chi_A \chi_B dr \tag{1.57}$$

S_{AB} is the overlap matrix of the AOs. Equation (1.56) shows the division of the MO population into three subpopulations, the first and the last terms are the net atomic populations, and the second is the overlap population. In his original paper, Mulliken compares the three subpopulations with two cities and a joint suburb lying between them [92], but notes that the three molecular distributions are: "not entirely mutually non-overlapping". The Mulliken charge of atom A in a diatomic molecule is the difference between the atomic number of A, and the sum of the atomic population of atom A and half of the joint population shared by atom A and B (summed over all MOs):

$$Q_{A,\text{Mulliken}} = Z_A - \sum_{i}^{\text{all\_MOs}} N(i)(c_{A,i}^2 + c_{A,i}c_{B,i}S_{AB}) \tag{1.58}$$

The general case of a polyatomic molecule follows the same principles, but a sum over all atoms replaces equation (1.55) and (1.56):

$$\psi_i = \sum_{r}^{\text{all\_atoms}} c_{r,i}\chi_r \tag{1.59}$$

$$N(i) = N(i) \sum_{r}^{\text{all\_atoms}} c_{r,i}^2 + N(i) \sum_{r,s}^{\text{all\_atoms}} c_{r,i}c_{s,i}S_{rs} \tag{1.60}$$

Let us now introduce the P_{rs} matrix:

$$P_{rs} = N(i) \sum_{i}^{\text{all\_MOs}} c_{r,i}c_{s,i} \tag{1.61}$$

It is possible to write the total population of the molecule as:

$$N = \sum_{i}^{\text{all\_MOs}} N(i) = \sum_{r,s}^{\text{all\_atoms}} P_{rs}S_{rs} \tag{1.62}$$

Mulliken population analysis provides the opportunity to break down bonds in terms of AOs, as AOs construct the P_{rs} matrix. This is used to analyse how AOs are involved in bonding.

1.2.7.2 Voronoi Deformed Densities

The Voronoi deformed density method integrates the $\Delta\rho$ between the free atom and the molecule over a Voronoi cell. The Voronoi cell of an atom (A) is the volume that is closer to A than any other atom. The method can be thought of as the charge in/out-flow from the Voronoi cell, when chemical interactions are "switched on". It is similar to the method of $\Delta\rho$ (section 1.2.11), although the $\Delta\rho$ is usually calculated with respect to fragments instead of atoms. The mathematical formula for the Voronoi charge of an atom A is:

$$Q_A^{\mathrm{VDD}} = -\int_{\substack{\text{Voronoi}\\ \text{cell}-A}} (\rho(\mathbf{r}) - \sum_{B}^{\text{all\_atoms}} \rho_B(\mathbf{r}))\mathrm{d}\mathbf{r} \qquad (1.63)$$

$\rho(\mathbf{r})$ is the total electron density in the molecule and $\rho_B(\mathbf{r})$ is the electron density in the isolated atom.

1.2.7.3 The Hirshfeld Scheme

The Hirshfeld charge of an atom (A) is calculated from the integral of the total electron density, weighted by the ratio between the electron density of the neutral atom A at its position in the molecule and the total electron density, when the chemical interaction is "switched off". An interpretation of this is that only electron density that "belongs" to an atom is integrated [99].

$$Q_A^{\mathrm{Hirshfeld}} = Z_A - \int \rho(\mathbf{r}) \frac{\rho_A(\mathbf{r})}{\sum_B \rho_B(\mathbf{r})} \mathrm{d}\mathbf{r} \qquad (1.64)$$

Bultinck argues [100] that it is wrong to use Hirshfeld charges on ions, because the total charge of the neutral atoms are zero and the weight factor in (1.64) is therefore not properly normalised. ADF's authors recommend dividing ions into fragments instead of atoms, i.e. replace an atom or a group of atoms by a fragment, which contains one or many atoms. The denominator then becomes the sum of the electron density over all charged fragments, and the method works properly.

1.2.8 Mayer Bond Orders

Mayer Bond Orders (MBOs) [101] are useful for large compounds with little or no symmetry, because MOs in such compounds are often delocalised, and it is therefore difficult to estimate their contributions [102]. A MBO between two atoms A and B is calculated by:

$$B_{AB}^{\text{Mayer}} = \sum_{s}^{A}\sum_{t}^{B}(\mathbf{PS})_{st}(\mathbf{PS})_{ts} \tag{1.65}$$

s and t are the AOs of atoms A and B. The similarity to Mulliken overlap population in equation (1.62) and (1.65) is evident.

MBOs are, as Mulliken analysis, basis set dependent, and comparison between different basis sets are not valid.

1.2.9 Energy Decomposition

ADF provides the opportunity to study the chemical bond between two or more fragments in detail by breaking its energy down into three components [49]:

$$E_{\text{Bond}} = E_{\text{Stat}} + E_{\text{Pauli}} + E_{\text{Orb.Int.}} \tag{1.66}$$

where E_{Stat} is the electrostatic interaction, E_{Pauli} is the Pauli repulsion, and $E_{Orb.\ Int.}$ is the orbital interaction. ADF defines the electrostatic interaction between two fragments as the change in energy when the unperturbed fragments are brought from infinite separation to their equilibrium position in the molecule. The Pauli repulsion energy is the energy required to make the wavefunction anti-symmetric, and the orbital interaction energy is obtained by letting the wavefunction relax to its optimized composition in the molecule. One needs to divide the molecule of interest into a number of fragments, which are either atoms or groups of atoms, to perform an energy decomposition. Single point calculations at the optimised geometry provide the electronic structures of the fragments. Finally, a single point calculation for the whole molecule is performed, but the fragments are now the building blocks of the molecule, instead of individual atoms. The steric repulsion energy is the sum of the electrostatic and Pauli repulsion energies.

1.2.10 Electron Localisation

1.2.10.1 The Electron Localization Function

The ELF, developed by Becke and Edgecombe [53], is based on the Taylor expansion of the Hartree-Fock spherically averaged conditional pair probability:

$$\Omega_{HF}^{\sigma}(\mathbf{r};s) = \frac{1}{3} D_{\sigma} s^2 + \ldots \tag{1.67}$$

$$D_{\sigma} = \tau_{\sigma} - \frac{1}{4}\frac{(\nabla \rho_{\sigma})^2}{\rho_{\sigma}} \tag{1.68}$$

where $\mathbf{r}$ is the coordinate of the reference electron, s is the radius of a sphere around $\mathbf{r}$, σ denotes the spin, and τ_{σ} is given by (1.40), although it only includes the σ spin. A large coefficient of s^2 is equivalent to a steep curvature of $\Omega_{HF}{}^{\sigma}$, and therefore a higher probability of finding another parallel spin electron close to the reference electron. A large value of D_{σ} therefore implies delocalisation, and small value implies localisation.

Dividing (1.68) with its comparison in a uniform electron gas (D_σ^0) gives a dimensionless indicator of localisation χ_σ:

$$D_\sigma^0 = \frac{3}{5}(6\pi^2)^{2/3}\rho_\sigma^{5/3} \tag{1.69}$$

$$\chi_\sigma = \frac{D_\sigma}{D_\sigma^0} \tag{1.70}$$

Finally, a Lorentz transformation of χ_σ is convenient since that bounds it from above, and "inverts" the relationship between localisation and the ELF – a high value of ELF corresponds to high localization:

$$ELF = \frac{1}{1+\chi_\sigma^2} \tag{1.71}$$

This definition of ELF confines its values between 0 and 1, a value of 1 corresponding to perfect localization and a value of ½ to an electron gas like pair probability. Notice that the definition of ELF is in terms of the electron density matrix, and therefore has no direct orbital dependency.

ELF reveals the shell structure in atoms, and covalent bonding and lone pairs in molecules of light atoms, but has the unfortunate artefact of approaching 1 far away from the nucleus in atoms with *s* electrons in the outer shells [53]. ELF is derived from HF theory and should be therefore only be used for HF calculations. ELF for DFT is derived by Savin *et al.* [103].

1.2.10.2 The Localized Orbital Locator

Becke uses the dimensionless variable t_σ to develop xc-functionals, and a model that attempts to explain how local approximations simulate non-local exchange [104]:

$$t_\sigma = \frac{\tau_\sigma^{LSDA}}{\tau_\sigma^{exact}} \tag{1.72}$$

τ_σ^{LSDA} equals D_σ^0 above, and τ_σ^{exact} is the non-interacting Kohn-Sham kinetic energy. Plots of t_σ reveal that it contains chemical information, for example location and size of atomic shells, bonding and electron lone pairs, and non-covalent interactions [105]. t_σ is transformed to the Localized Orbital Locator (LOL) to confine LOL between 0 and 1:

$$LOL = \frac{t_\sigma}{1+t_\sigma} \tag{1.73}$$

A LOL value of ½ corresponds to electrons with the same kinetic energy as the uniform electron gas and smaller values to higher kinetic energy than the uniform electron gas. LOL is independent of the choice of orbitals, but localised orbitals provide an opportunity to explain why LOL yields higher values for bonding and lone pair electrons. Localised orbitals have their stationary points in areas of electron pairs and shells. There are no gradients of the orbitals in these points and this makes τ_σ^{exact} small and hence gives a large value for LOL. The regions where the localised orbitals overlap have larger gradients of the localised orbitals and hence smaller values of LOL.

LOL provides a simpler function than ELF, its graphs are somewhat cleaner, and it does not have the problem of not vanishing in regions of very low electron density, far away form the molecule. It is also possible to use the LOL on single MOs, because it is based on the kinetic energy instead of the density matrix.

1.2.10.3 The Electron Localizability Indicator

This section only presents the main ideas of the Electron Localizability Indicator (ELI) [106-108]; reference [107] contains the complete theory. The ELI is defined in terms of the second order density matrix. The average number of σ-spin pairs in a region is calculated by:

$$D_2^{\sigma\sigma}(\Omega) = \int_{\Omega} d\mathbf{r}_1 \int_{\Omega} \gamma_2^{\sigma\sigma}(\mathbf{r}_1, \mathbf{r}_2) d\mathbf{r}_2 \qquad (1.74)$$

where $\gamma_2^{\sigma\sigma}$ is the second order density matrix (section 1.2.4.1). The integration regions in (1.74) all contain the same σ-spin charge q_σ. A region that contains no electron pairs ($D_2^{\sigma\sigma} = 0$), i.e. a region that contains only a single electron, corresponds to maximum localisation; the localisation decreases as $D_2^{\sigma\sigma}$ increases. The expression for the ELI therefore needs to be inversed, so that an increased value of ELI corresponds to increased localisation. $D_2^{\sigma\sigma}$ is therefore transformed with a Lorentz transformation to yield the ELI:

$$ELI = \frac{1}{1 + (c_q D_2^{\sigma\sigma})^2} \qquad (1.75)$$

where c_q compensates for the charge dependence of $D_2^{\sigma\sigma}$, to make ELI independent of q_σ. Equation (1.74) can be simplified by using Taylor expansions, if q_σ is chosen to be small enough. This is, however, relatively complicated. I therefore refer to reference [107] for the details.

1.2.11 Electron Density Differences

One obtains $\Delta\rho$ between a molecule and its fragments by calculating ρ of the molecule and the fragments, and then subtracting ρ of the fragments from ρ of the molecule. One can also calculate $\Delta\rho$ between calculations of different methods; many examples of this are given in previous sections. In that case, $\Delta\rho$ is calculated as the difference between the ρ of the molecule with the first approximation, and ρ of the second approximation. It is important to use the same geometry in both calculations. $\Delta\rho$ between molecules and fragments are given in chapter 5.

The interpretation of $\Delta\rho$ between the ρ of the molecule and its fragments is that the electrons move from regions with negative values of $\Delta\rho$ to regions of positive values, as the fragments start to interact.

I perform all calculations of electron density and localisation index with the small but powerful program DGrid [109], provided and written by Dr M. Kohout; I visualise the results with the OpenDX program [110]. I perform these calculations by extracting information about the MOs from the binary files of a previous QM calculation, and calculate the different properties on a three dimensional grid.

1.2.12 Nuclear Magnetic Resonance

1.2.12.1 General

Nuclear Magnetic Resonance (NMR) exploits the behaviour of the total spin of a nucleus ($I \neq 0$), under the influence of a magnetic field. The spins of the nuclei have random directions in the absence of a magnetic field, but they direct either against or in line with a magnetic field. The two spin directions exist in equilibrium, as their energies are of similar magnitude. A nucleus with spin in the opposite direction of the magnetic field has a slightly higher energy than one with parallel spin; hence, a spin flip from opposite to parallel spin will result in emission of radiation. NMR is measured by detecting this radiation, i.e. the energy required to go from the lower energy to the higher. The energy difference between parallel and opposite spin of the nuclei is very small, but increases directly in proportion to the magnetic field. The measurement error is generally small compared with the total energy difference in a very strong magnetic field.

The nuclear environment, i.e. the electrons around the nucleus, modifies the external magnetic field. The electrons induce a magnetic field in the opposite direction to the applied field, a phenomenon called electron shielding. The magnetic response to the applied field therefore contains information about the electrons; this information is used to investigate the electronic structure.

NMR signals are called isotropic shielding constants. These are compared with NMR signals for reference compounds; the resulting quantity is the chemical shift:

$$\partial_X = \sigma_{ref} - \sigma_X \tag{1.76}$$

where X is the atom of interest, σ_{ref} is the isotropic shielding constant of X in the reference compound, and σ_X is the isotropic shielding constant of X in the compound studied. The standard reference compound for carbon and hydrogen is TetraMethylSilane (TMS, $Si(CH_3)_4$). Other references used in this work are phosphoric acid (H_3PO_4) for P and $Fe(CO)_5$ for Fe.

1.2.12.2 NMR Calculations

Calculation of NMR parameters is a relatively new application, especially for DFT. This is because the calculations are sensitive to the quality of the wave function; large basis sets and advanced xc-functionals that include the electronic gradient are therefore needed to achieve high accuracy (in ADF, the recommended minimum requirement is to use a TZ2P all electron basis set and to set the integration grid parameter to 6). Hybrid functionals generally provide more accurate NMR results than GGA functionals [111]. Calculations for complexes including very heavy atoms are obviously even more demanding, and are still relatively scarce [112]. The number of NMR calculations on lighter atoms, however, has increased rapidly during the last 5 years.

1.2.12.3 Theoretical Background

The shielding constant σ_{ij} of an atom A (a tensor as indicated by the index) is the second derivative of the total energy with respect to the static external magnetic field and the nuclear magnetic moment of the atom A (μ_A):

$$\sigma_{ij}^{A} = \frac{\partial^2 E}{\partial B \partial \mu_A} \tag{1.77}$$

One obtains the following uncoupled expression for the shielding tensor with the approximation of no orbital- and current-dependence [113]:

$$\sigma_{\alpha\beta}^{A} = \sum_{j} \left(j\left|(\mathbf{r}\cdot\mathbf{r}_A\delta^{\alpha\beta} - \mathbf{r}^{\alpha}\mathbf{r}_A^{\beta})\mathbf{r}_A^{-3}\right|j\right) -$$

$$\sum_{j,b} \frac{(b|l^{\alpha}|j)(j|l_A^{\beta}\mathbf{r}_A^{-3}|b) + (b|l_A^{\alpha}\mathbf{r}_A^{-3}|j)(j|l^{\beta}|b)}{\varepsilon_b - \varepsilon_j} \qquad (1.78)$$

$\mathbf{r}_A$ is the distance between the nucleus and the electron, l^{α} and l^{β} are angular momentum operators, and b and j represent occupied and unoccupied MOs with eigenvalues ε_b and ε_j. The trace of $\sigma_{\alpha\beta}{}^{A}$ divided by 3 is the isotropic shielding constant.

The sums in (1.78) are the diamagnetic and paramagnetic contribution to the shielding tensor respectively. Discrepancies from experiment in DFT NMR calculations are often deduced from the denominator in the paramagnetic sum. The energy difference between occupied and virtual MOs is in general too small in DFT; hence, the magnitude of the paramagnetic contribution is overestimated. Wrong asymptotic behaviour of the exchange-correlation potential is an important factor behind this.

In NMR calculations, the gauge dependence, that is the result's dependence on the origin of the coordinate system, is a consequence of the basis set approximation; a calculation with a complete basis set has no gauge dependence. Gauge dependence is not a problem for very large basis sets, but calculations that use small or medium sized basis sets must be gauge dependence corrected. Different methods are available to make the calculations, at least approximately, gauge independent. The Individual Gauge for Localized Orbital (IGLO) and the Gauge Including Atomic Orbital (GIAO) methods both introduce complex phase factors in the orbitals [114], GIAO in the AOs and IGLO in the MOs. GIAO is also known as the Gauge Invariant Atomic Orbital or the London Atomic Orbital (LAO) method. GIAO is superior to IGLO [115] and one of the most widely applied methods.

Exchange-correlation functionals are seldom designed for situations when magnetic fields are present. The magnetic field induces a current density; hence, the exchange-correlation functional should take this into account. Current density functionals have been developed both for LSDA [114] and GGA [116], but the results are disappointing. The contribution from current density is small and can be neglected [114], at least for the present exchange-

correlation functionals. Neglect of the current density dependence leads to uncoupled NMR equations in DFT. The NMR equations for WFM are coupled and therefore more computationally expensive.

The following chapters contain the results of my computational investigations of actinide complexes.

Chapter 2

Density Functional Theory Investigation of the Geometry and Electronic Structure of $[UO_2(H_2O)_m(OH)_n]^{2-n}$ (m+n=5)

2.1 Introduction

The uranyl ion coordinates water or hydroxide ligands in its equatorial plane in aqueous solution, depending on the pH level. EXAFS [117] and computational investigations suggest coordination of five water ligands at low pH levels [118, 119], three hydroxide ligands in the pH range 8.8 – 10 [120], and four or five hydroxide ligands at higher pH levels [117, 121, 122]. There is, however, disagreement whether $[UO_2(OH)_3]^-$ exists at all [117, 121].

The symmetric and anti-symmetric stretching vibrations (ν_{sym} and ν_{asym}) of the uranyl oxygen atoms (O_{yl}), indicators of the uranyl bond strength, are available from experiment [19, 121, 123-126]. The uranium-equatorial ligand bond length, the axial bond length (r(U-O_{yl})), ν_{sym}, and ν_{asym} show strong correlation; a short r(U-O_{yl}) and large ν_{sym} and ν_{asym} correspond to strong uranyl bonds and long equatorial bonds, and vice versa. The symmetric structure of $[UO_2(OH)_n]^{2-n}$ (n = 4,5) and the large difference in r(U-O_{yl}), ν_{sym}, and ν_{asym} between $[UO_2(H_2O)_5]^{2+}$ (**5W**, Figure 13(a)) and $[UO_2(OH)_4]^{2-}$/$[UO_2(OH)_5]^{3-}$ (**4OH/5OH** Figure 13(e),(f)), made Clark *et al.* [121] speculate that the uranyl bond in

4OH/5OH weakens because the hydroxide ligands are competing with O_{yl} to donate electrons to the 6*d* AOs. Water and hydroxide ligands both donate electrons by forming σ-bonds to uranium, but hydroxide ligands also use π-donation. An alternative explanation to the increased $r(U\text{-}O_{yl})$ is destabilization of the uranyl MOs, through charge build-up in the equatorial plane [127]. This work uses charge and MO analysis on all compounds with the formula $[UO_2(H_2O)_m(OH)_n]^{2-n}$ ($m+n=5$), to probe why the uranyl bond weakens as water ligands are substituted for hydroxide ligands. It investigates Clark's hypothesis in particular.

Several articles report studies of individual complexes of the $[UO_2(H_2O)_m(OH)_n]^{2-n}$ family, but none systematically examine all members with the same methods, compare the computational and experimental trends of vibrational frequencies, atomic charges, MOs, and bond lengths. This study does so, and also provides an opportunity to investigate the influence of the COSMO and PCM solvent models.

This study, made in collaboration with Kieran Ingram, is reported in reference [128] and [129].

2.2 Computational Details

2.2.1 ADF

This study used the BP86 [52, 130], PW91 [70], and PBE [62, 63] xc-functionals with a TZP ZORA basis set on uranium and DZP ZORA basis sets on oxygen and hydrogen; these basis sets archive saturation for structural and vibrational data. The uranium and oxygen basis sets used the frozen core approximation, leaving the uranium 5*f*, 6*s*, 6*p*, 6*d*, and 7*s* AOs, and the oxygen 2*s* and 2*p* AOs in the valence shell. The integration parameter was set to 5 for geometry optimisations and 6 for frequency calculations, the geometry and SCF convergence criteria are 0.00045 a.u. $Å^{-1}$ and 10^{-7} respectively. Solvent effects were modelled by the COSMO, using the asurf keyword and the following atomic radii; U = 2.0 Å, O = 1.4 Å, and H = 1.2 Å.

2.2.2 *Gaussian 03*

Calculations in G03 employed the same xc-functionals as ADF, and in some instances additionally the hybrid functional B3LYP. 6-31G** basis sets were assigned to all atoms except uranium, which used a (14*s* 13*p* 10*d* 8*f* 6*g*) [10*s* 9*p* 5*d* 4*f* 3g] segmented valence basis set with a relativistic pseudo potential of the Stuttgart-Bonn variety [76]. The integration grid assigned (keyword "ultrafine") is pruned with 99 radial shells and a maximum of 590 angular points each (section 1.2.6.3) for all atoms from H to Kr (but not pruned for heavier element). The Conductor PCM (CPCM) with the UAKS equation for the atomic radii accounted for solvent effects (section 1.2.6.6). The tesserae parameters had the default values in all calculations, except the calculation on $UO_2(H_2O)_2(OH)_2$ that used the values TSARE = 0.4 and OFAC = 0.96, due to problems with the default values.

2.3 Geometries

2.3.1 *Overview*

All geometries of the target molecules were optimised in both ADF and G03 for all xc-functionals, with and without solvent models and from a large number of starting structures, to ensure a global energy minimum ligand arrangement. Figure 13 presents the final structures of the ADF/PBE/gas phase calculations, Table 3, Table 4, and Table 5 provide structural data. Complexes with two or more hydroxide ligands are not stable in pentagonal arrangements; geometry optimisations of those complexes eject a water ligand. This ligand is therefore removed from those complexes.

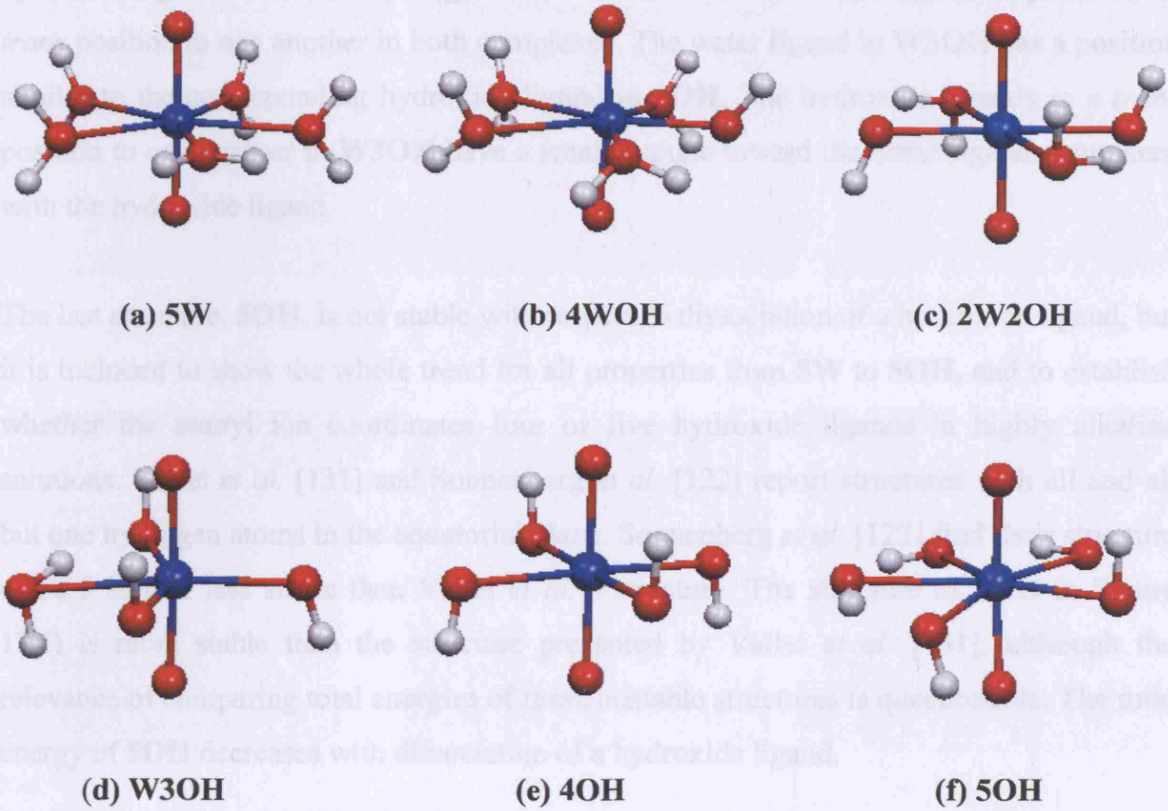

(a) 5W (b) 4WOH (c) 2W2OH

(d) W3OH (e) 4OH (f) 5OH

Figure 13(a)-(f). *Geometries of (a) **5W**, (b) **4WOH**, (c) **2W2OH**, (d) **W3OH**, (e) **4OH**, and (f) **5OH** from gas phase calculations with the PBE xc-functional.*

5W and $[UO_2(H_2O)_4(OH)]^+$ (**4WOH**, Figure 13(b)) have similar structures with one water ligand perpendicular to the uranyl axis, the rest of the water ligands are rotated 90° from this position, to become co-planar to the uranyl axis. The hydroxide ligand in **4WOH** adopts a similar position as the water ligand it replaces in the **5W** complex. Wahlgren *et al.* [117] have also found the above structure of **5W** more stable than the one with all water ligands co-planar to the uranyl axis. The same study calculates a rotational barrier of the water ligand with both hydrogen atoms in the equatorial plane of only 1.5 kJ/mol.

$[UO_2(H_2O)_2(OH)_2]$ (**2W2OH**, Figure 13(c)) has the water and hydroxide ligands in a *trans* arrangement, with the ligands rotated 180° to one another. The hydrogen atoms of the hydroxide ligands are located above and below the equatorial plane.

$[UO_2(H_2O)(OH)_3]^-$ (**W3OH**, Figure 13(d)) and **4OH** also have a similar structure, the hydroxide ligands with their hydrogen atoms on the same side of the equatorial plane are in *trans* position to one another in both complexes. The water ligand in **W3OH** has a position similar to the corresponding hydroxide ligand in **4OH**. The hydroxide ligands in a *trans* position to one another in **W3OH** have a smaller angle toward the water ligand, compared with the hydroxide ligand.

The last structure, **5OH**, is not stable with respect to dissociation of a hydroxide ligand, but it is included to show the whole trend for all properties from **5W** to **5OH**, and to establish whether the uranyl ion coordinates four or five hydroxide ligands in highly alkaline solutions. Vallet *et al.* [131] and Sonnenberg *et al.* [122] report structures with all and all but one hydrogen atoms in the equatorial plane. Sonnenberg *et al.* [122] find their structure to be 5 kJ/mol less stable than Vallet *et al.*'s structure. The structure of **5OH** in Figure 13(f) is more stable than the structure presented by Vallet *et al.* [131], although the relevance of comparing total energies of these unstable structures is questionable. The total energy of **5OH** decreases with dissociation of a hydroxide ligand.

Table 3. *Calculated r(U-O_{yl}) (Å) for all target complexes and previous experimental and theoretical results. The results in reference [132] consider $UO_2(H_2O)_3(OH)_2$, compared with **2W2OH** in this work, and are for the ortho and meta isomers respectively.*

Code	Functional	**5W**	**4WOH**	**2W2OH**	**W3OH**	**4OH**	**5OH**
ADF gas phase	PBE	1.768	1.797	1.822	1.839	1.875	1.879
	BP86	1.771	1.800	1.826	1.841	1.878	1.883
G03 gas phase	PBE	1.765	1.794	1.809	1.835	1.873	1.884
	BP86	1.768	-	1.812	-	1.877	-
	PW91	1.766	-	1.810	-	1.874	-
ADF COSMO (SAS)	PBE	1.770	1.798	1.825	1.836	1.873	1.881
	BP86	1.773	1.801	1.828	1.840	1.878	1.886
	PW91	1.770	-	-	-	1.876	-
G03 CPCM (SES)	PBE	1.779	1.807	1.829	1.844	1.878	not conv.
Exp. result							
Ref. [117]: EXAFS		1.780					
Ref. [131]: EXAFS		1.770					
Ref. [133]: XRD (solid)		1.710					
Ref. [134]: XRD (soln.)		1.700					
Ref. [135]: EXAFS		1.760					
Ref. [121]: XRD						1.820	
Ref. [121]: EXAFS (solid)						1.810	
Ref. [121]: EXAFS (soln.)						1.790	
Ref. [136]: EXAFS						1.830	
Prev. theoretical result							
Ref. [117]: B3LYP		1.780				1.800	
Ref. [137]: MP2		1.770					
Ref. [138]: BLYP (gas)		1.746					
Ref. [138]: BLYP (solv.)		1.748					
Ref. [119]: HF		1.694					
Ref. [119]: LDA		1.778					
Ref. [119]: BLYP		1.803					
Ref. [119]: B3LYP		1.756	1.783				
Ref. [139]: B3LYP		1.752	1.786	1.795			
Ref. [132]: B3LYP (ortho)				1.800			
Ref. [132]: B3LYP (meta)				1.800			
Ref. [131]: AIMP (solv.)						1.760	
Ref. [131]: AIMP (gas)						1.770	
Ref. [140]: B3LYP						1.842	
Ref. [122]: B3LYP						1.841	1.835

Table 4. *Calculated r(U-O_{water}) (Å) for all target complexes with water ligands and previous experimental and theoretical results. The results in reference [132] consider $UO_2(H_2O)_3(OH)_2$, compared with **2W2OH** in this work, and are for the ortho and meta isomers respectively.*

Code	Functional	**5W**	**4WOH**	**2W2OH**	**W3OH**
ADF gas phase	PBE	2.499	2.595	2.610	2.803
	BP86	2.499	2.592	2.604	2.797
G03 gas phase	PBE	2.474	2.562	2.583	2.735
	BP86	2.474	-	2.582	-
	PW91	2.469	-	2.576	-
ADF COSMO (SAS)	PBE	2.476	2.584	2.593	2.750
	BP86	2.475	2.586	2.591	2.744
	PW91	2.471	-	-	-
G03 CPCM (SES)	PBE	2.432	2.524	2.520	2.638
Exp. result					
Ref. [117]: EXAFS		2.410			
Ref. [131]: EXAFS		2.410			
Ref. [133]: XRD (solid)		2.450			
Ref. [134]: XRD (soln.)		2.420			
Ref. [135]: EXAFS		2.410			
Prev. theoretical result					
Ref. [117]: B3LYP		2.570			
Ref. [141]: MP2 (solv.)		2.470			
Ref. [141]: MP2 (gas)		2.530			
Ref. [137]: MP2		2.460			
Ref. [119]: HF		2.545			
Ref. [119]: LDA		2.423			
Ref. [119]: BLYP		2.516			
Ref. [119]: B3LYP		2.516			
Ref. [138]: BLYP (gas)		2.550			
Ref. [138]: BLYP (solv.)		2.500			
Ref. [139]: B3LYP		2.522	2.577	2.620	
Ref. [132]: B3LYP (ortho)				2.669	
Ref. [132]: B3LYP (meta)				2.651	

Table 5. *Calculated r(U-$O_{hydroxide}$) (Å) for all target complexes with hydroxide ligands and previous experimental and theoretical results. The results in reference [132] consider $UO_2(H_2O)_3(OH)_2$, compared with **2W2OH** in this work, and are for the ortho and meta isomers respectively.*

Code	Functional	**4WOH**	**2W2OH**	**W3OH**	**4OH**	**5OH**
ADF gas phase	PBE	2.113	2.164	2.252	2.309	2.465
	BP86	2.116	2.165	2.256	2.311	2.465
G03 gas phase	PBE	2.109	2.177	2.235	2.283	2.415
	BP86	-	-	-	2.285	-
	PW91	-	-	-	2.280	-
ADF COSMO (SAS)	PBE	2.116	2.163	2.255	2.294	2.421
	BP86	2.123	2.165	2.255	2.311	2.424
	PW91	-	-	-	2.290	-
G03 CPCM (SES)	PBE	2.118	2.152	2.216	2.251	not conv.
Exp. result						
Ref. [121]: XRD					2.260	
Ref. [121]: EXAFS (solid)					2.210	
Ref. [121]: EXAFS (soln.)					2.220	
Ref. [136]: EXAFS					2.260	
prev. theoretical result						
Ref. [131]: AIMP (solv.)					2.300	
Ref. [131]: AIMP (gas)					2.336	
Ref. [140]: B3LYP					2.334	
Ref. [122]: B3LYP					2.309	2.462
Ref. [119]: B3LYP		2.162				
Ref. [132]: B3LYP (ortho)			2.231			
Ref. [132]: B3LYP (meta)			2.250			

Table 6 compares the stability of **5OH** and **4OH** by subtracting the sum of the total energies of **4OH** and OH^- from the total energy of **5OH**. As this energy difference is a massive 507 kJ/mol, I draw the same conclusion as Vallet *et al.* that coordination of four hydroxide ligands is more stable than five.

Table 6. *Total bonding energy difference (kJ/mol) between **5OH** and **4OH** + OH^-.*

Species	Total bonding energy
$[OH]^-$	-847
$[UO_2(OH)_4]^{2-}$ (**4OH**)	-6787
$[UO_2(OH)_5]^{3-}$ (**5OH**)	-7127
ΔE (**5OH** – (**4OH** + $[OH]^-$))	507

2.3.2 *Trends in Bond Lengths*

Figure 14 shows that $r(U\text{-}O_{yl})$ increases as water ligands are substituted by hydroxides. Calculations agree excellently with experiment for **5W**, but significantly worse for **4OH**; these calculations overestimate $r(U\text{-}O_{yl})$ by about 0.06 Å. I therefore optimised the geometry of **4OH** with B3LYP; previous studies show more accurate results with this functional. $r(U\text{-}O_{yl})$ with B3LYP is 1.846 Å in the gas phase and 1.854 Å with the solvent model (SES), an improvement of about 0.03 Å compared with PBE. Calculations with the SES show slightly longer axial bond lengths, and therefore worsen agreement with experiment. Calculations with the SAS and in the gas phase show almost identical $r(U\text{-}O_{yl})$.

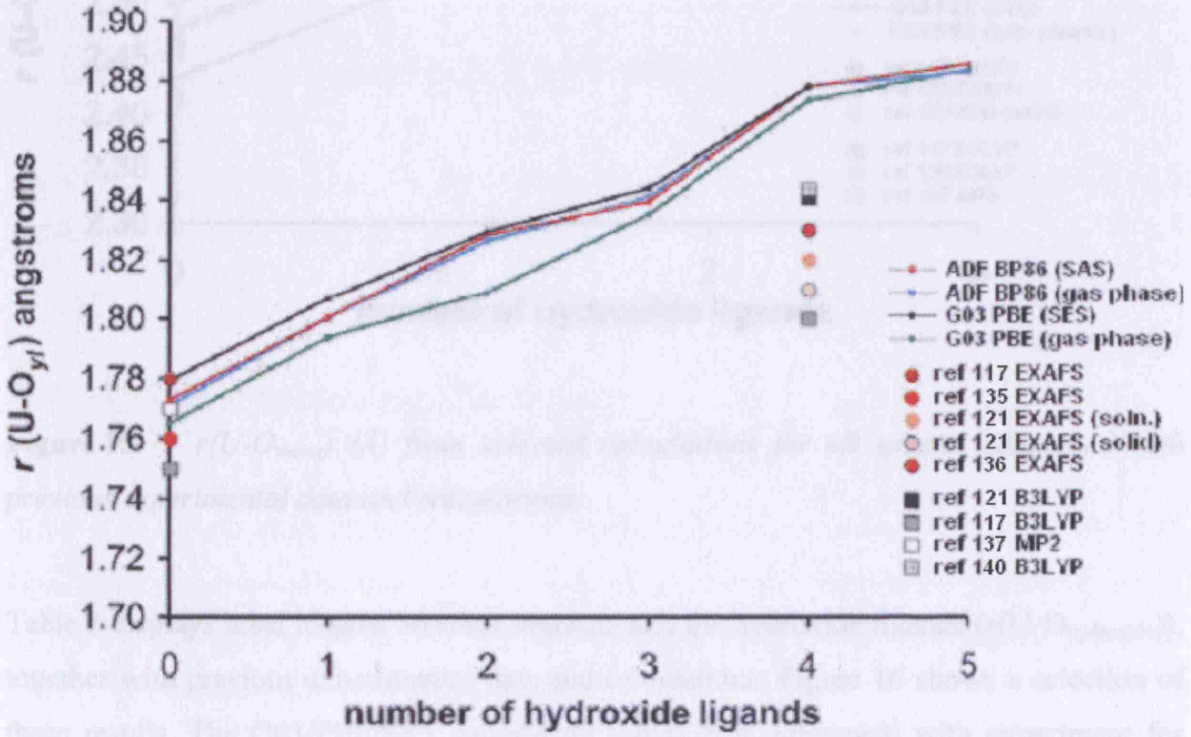

Figure 14. *r(U-Oyl) (Å) from selected calculations for all species compared with previous experimental data and calculations.*

Table 4 gives calculated $r(U\text{-}O_{water})$ along with previous experimental and theoretical results, Figure 15 shows a selection of them. $r(U\text{-}O_{water})$ increases with increasing number of hydroxide ligands; calculations for **5W** in this work agree better with experiment than

previous calculations do. The G03/PBE/SES calculation for **5W** shows a particularly good agreement with experiment. All calculations show the same trend when the number of hydroxide ligands increases, although calculations with the SES show shorter r(U-O_{water}). This is consistent with the longer r(U-O_{yl}) of the SES in Table 3.

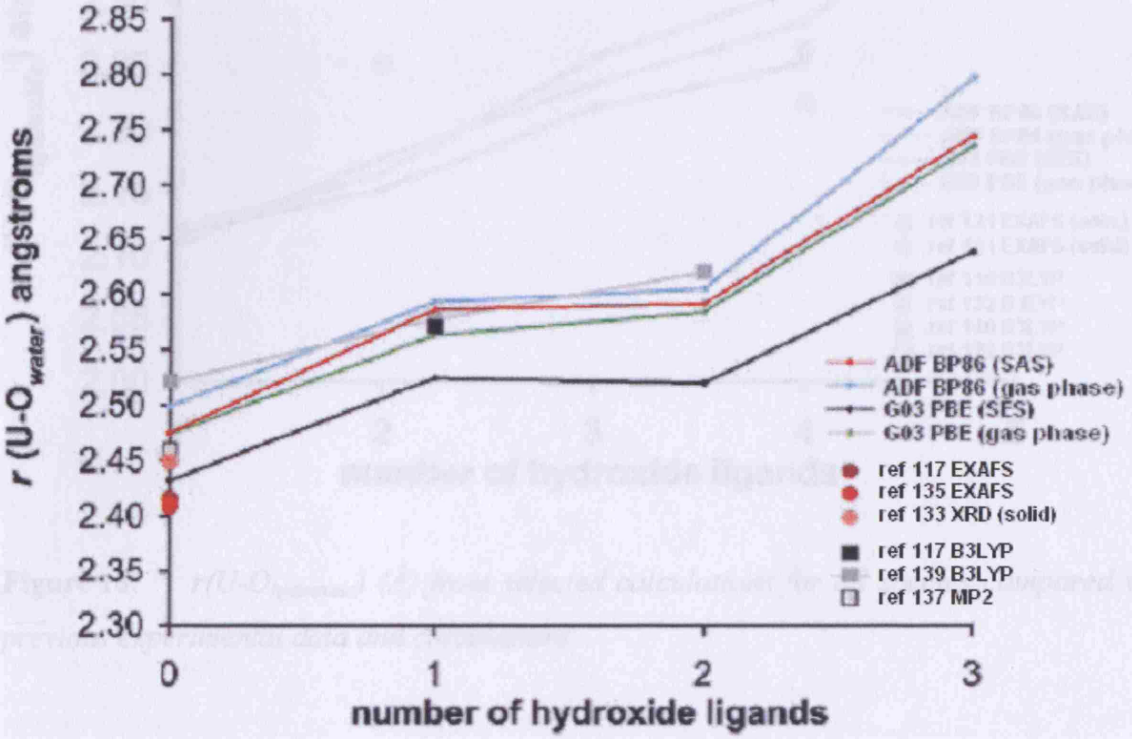

Figure 15. *r(U-O_{water}) (Å) from selected calculations for all species compared with previous experimental data and calculations.*

Table 5 displays bond lengths between uranium and the hydroxide ligands (r(U-$O_{hydroxide}$)), together with previous experimental data and calculations; Figure 16 shows a selection of these results. The G03/PBE/SES calculation shows best agreement with experiment for **4OH**, the only complex with experimental data available. r(U-$O_{hydroxide}$) in this work are generally shorter than previous calculations that are performed with the B3LYP functional; the present results agree better with the experimental results for **4OH** than previous studies. r(U-$O_{hydroxide}$) increases as the number of hydroxide ligands increases, faster in the gas phase and with the SAS compared with the SES.

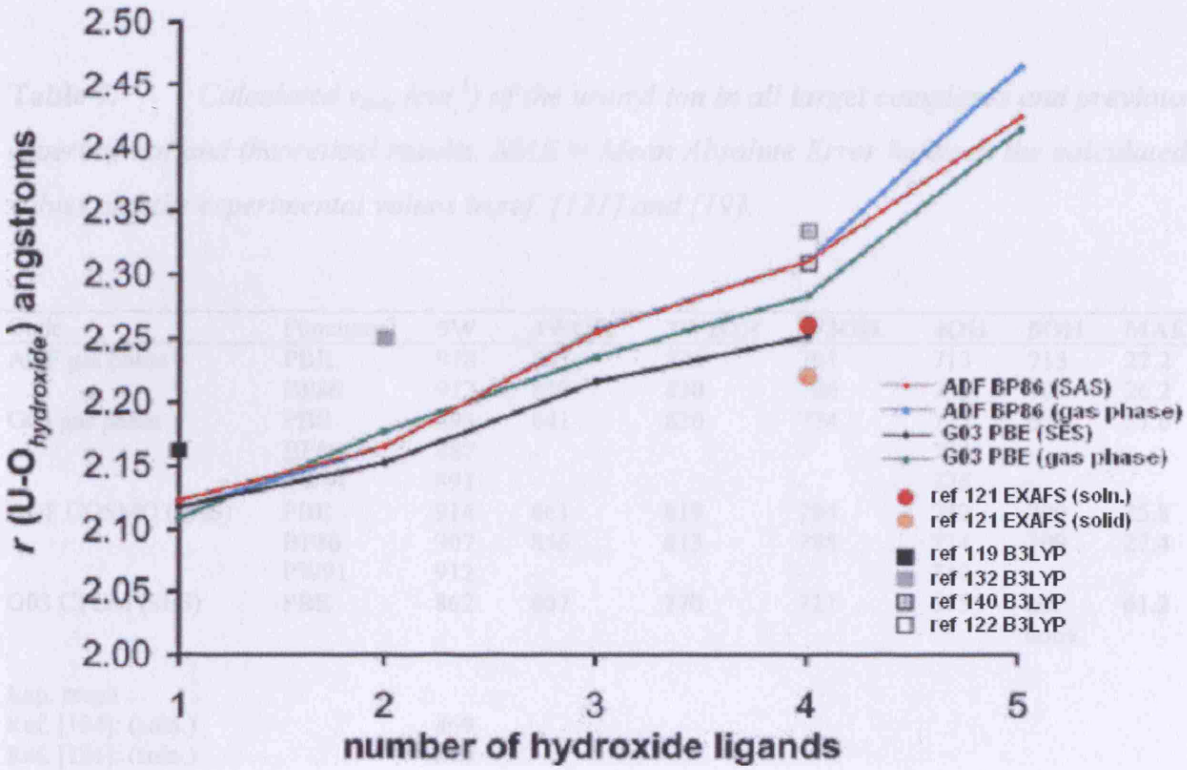

Figure 16. *$r(U\text{-}O_{hydroxide})$ (Å) from selected calculations for all species compared with previous experimental data and calculations.*

2.4 Uranyl Stretching Vibrations

ν_{sym} and ν_{asym}, indicators of the uranyl bond strength, provide a useful comparison between experiment and calculations, in addition to $r(U\text{-}O_{yl})$. Table 7 and Table 8 present ν_{sym} and ν_{asym} for all calculations, along with experimental data and previous calculations; Figure 17 and Figure 18 show a selection of these data.

Table 7. *Calculated v_{sym} (cm^{-1}) of the uranyl ion in all target complexes and previous experimental and theoretical results. MAE = Mean Absolute Error between the calculated values and the experimental values in ref. [121] and [19].*

Code	Functional	5W	4WOH	2W2OH	W3OH	4OH	5OH	MAE
ADF gas phase	PBE	918	865	825	791	713	713	27.2
	BP86	912	859	830	786	733	707	26.2
G03 gas phase	PBE	893	841	820	774	727	677	27.6
	BP86	887	-	-	-	724	-	
	PW91	891	-	-	-	726	-	
ADF COSMO (SAS)	PBE	914	861	819	794	742	709	25.8
	BP86	907	856	813	788	734	709	27.4
	PW91	912	-	-	-	740	-	
G03 CPCM (SES)	PBE	862	807	770	727	675	not conv.	61.2
Exp. result								
Ref. [124]: (soln.)		869						
Ref. [125]: (soln.)		870						
Ref. [126]: (soln.)		874						
Ref. [19]: (soln.)		870	849	837	805			
Ref. [121]: (solid)						796		
Ref. [121]: (soln.)						786		
Prev. theoretical result								
Ref. [119]: HF		1091						
Ref. [119]: LDA		854						
Ref. [119]: BLYP		787						
Ref. [119]: B3LYP		910						
Ref. [139]: B3LYP		902	848					
Ref. [140]: B3LYP						739		
Ref. [122]: B3LYP						762	750	

Table 8. *Calculated v_{asym} (cm^{-1}) of the uranyl ion in all target complexes and previous experimental and theoretical results.*

Code	Functional	5W	4WOH	2W2OH	W3OH	4OH	5OH
ADF gas phase	PBE	1011	948	904	871	814	789
	BP86	1004	941	900	867	809	785
G03 gas phase	PBE	981	921	898	853	809	-
	BP86	976	-	-	-	807	-
	PW91	980	-	-	-	808	-
ADF COSMO (SAS)	PBE	997	942	888	867	810	789
	BP86	991	931	883	860	809	784
	PW91	997	-	-	-	809	-
G03 CPCM (SES)	PBE	929	862	818	776	708	not conv.
Exp. result							
Ref. [125]: (soln.)		961					
Ref. [126]: (soln.)		962					
Prev. theoretical result							
Ref. [119]: HF		1149					
Ref. [119]: LDA		945					
Ref. [119]: BLYP		893					
Ref. [119]: B3LYP		1003					
Ref. [140]: B3LYP						823	
Ref. [122]: B3LYP						833	822

The decrease of v_{sym} and v_{asym}, and increase of r(U-O_{yl}) in all calculations, illustrates the weakening of the uranyl bond as water ligands are replaced by hydroxides. The Mean Absolute Errors (MAEs) of v_{sym} in Table 7 are similar for all calculations in the gas phase and with the SAS cavity, while the MAE for the SES is rather disappointing. Figure 17 shows that the trend of decreasing v_{sym} as hydroxide ligands are added is similar for all calculations. The gas phase calculations overestimate the magnitude of v_{sym} for **5W**, are very close to experiment for **4WOH** and **2W2OH**, and underestimate v_{sym} for **4OH**. The G03/PBE/SES calculation for **5W** is very close to experiment, but underestimates v_{sym} for all other species, in particular for **4OH**. A comparison of Figure 14 and Figure 17 reveals that the trends of the errors for the calculated v_{sym} and r(U-O_{yl}) with G03/PBE/SES are very similar (i.e. small errors for **5W** that increase as the series is traversed). The trends of the errors in the gas phase and the SAS calculations between v_{sym} and r(U-O_{yl}), however, are not quite as similar. The magnitudes of v_{sym} are larger in the gas phase than expected when it is considered that r(U-O_{yl}) are overestimated in all calculations except **5W** (if one assumes that r(U-O_{yl}) increases linearly as one adds $[OH]^-$ ligands). I therefore argue that

the small MAE in the gas phase is a consequence of error cancellation between neglecting solvent effects and calculating uranyl bonds that are too weak (in all species except **5W**).

The solvent model weakens the uranyl bond and increases $r(U\text{-}O_{yl})$, as it transfers electron density from the bonding region to the volume of space located around O_{yl} but oriented away from uranium (Figure 12 in chapter 1). The inclusion of explicit solvent molecules in the equatorial plane also results in a longer $r(U\text{-}O_{yl})$ (i.e. **5W** have larger $r(U\text{-}O_{yl})$ than $[UO_2]^{2+}$). The solvent model therefore (at least qualitatively) includes the effect of solvation, and should be used in calculations despite that it shows worse agreement with experimental results than gas phase calculations.

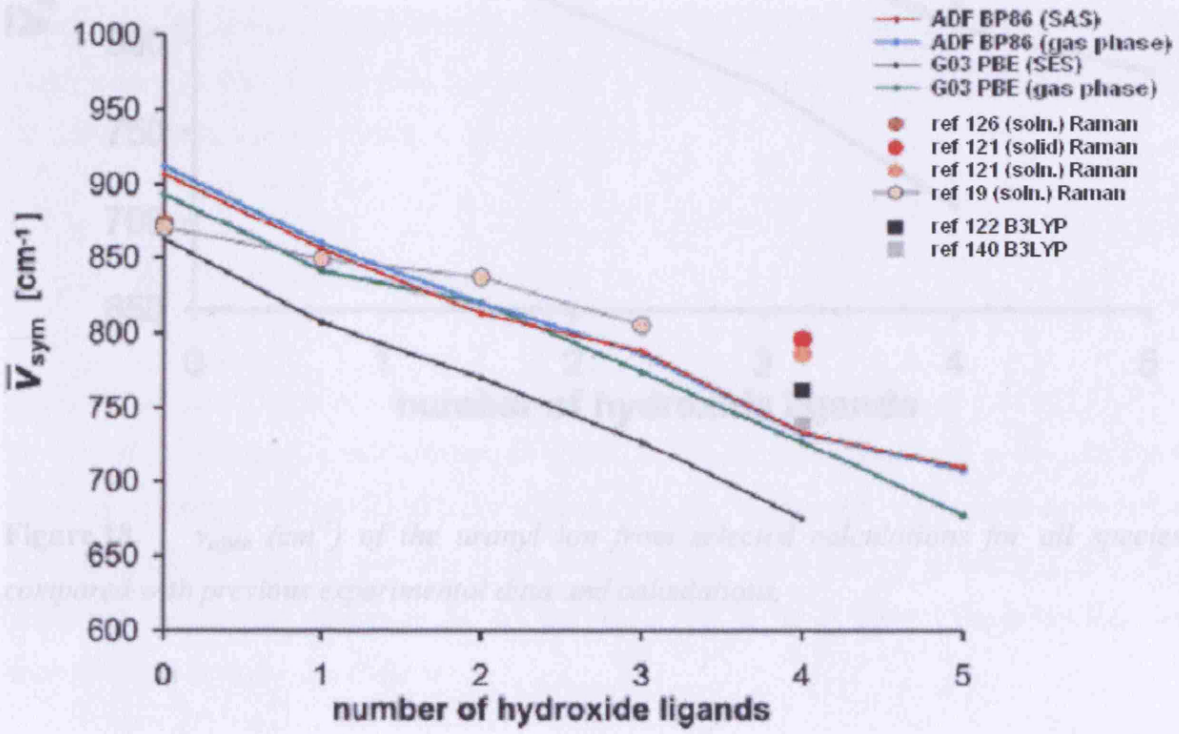

Figure 17. *ν_{sym} (cm^{-1}) of the uranyl ion from selected calculations for all species compared with previous experimental data and calculations.*

ν_{asym} shows a similar trend to ν_{sym} of decreasing wavenumbers as the number of hydroxides increase, but the agreement between experiment and the G03/PBE/SES calculation is slightly worse for **5W**. The similarity of ν_{asym} and ν_{sym} suggests that calculations probably

underestimate v_{asym} for the anionic species, but it is impossible to confirm this in the absence of experimental results.

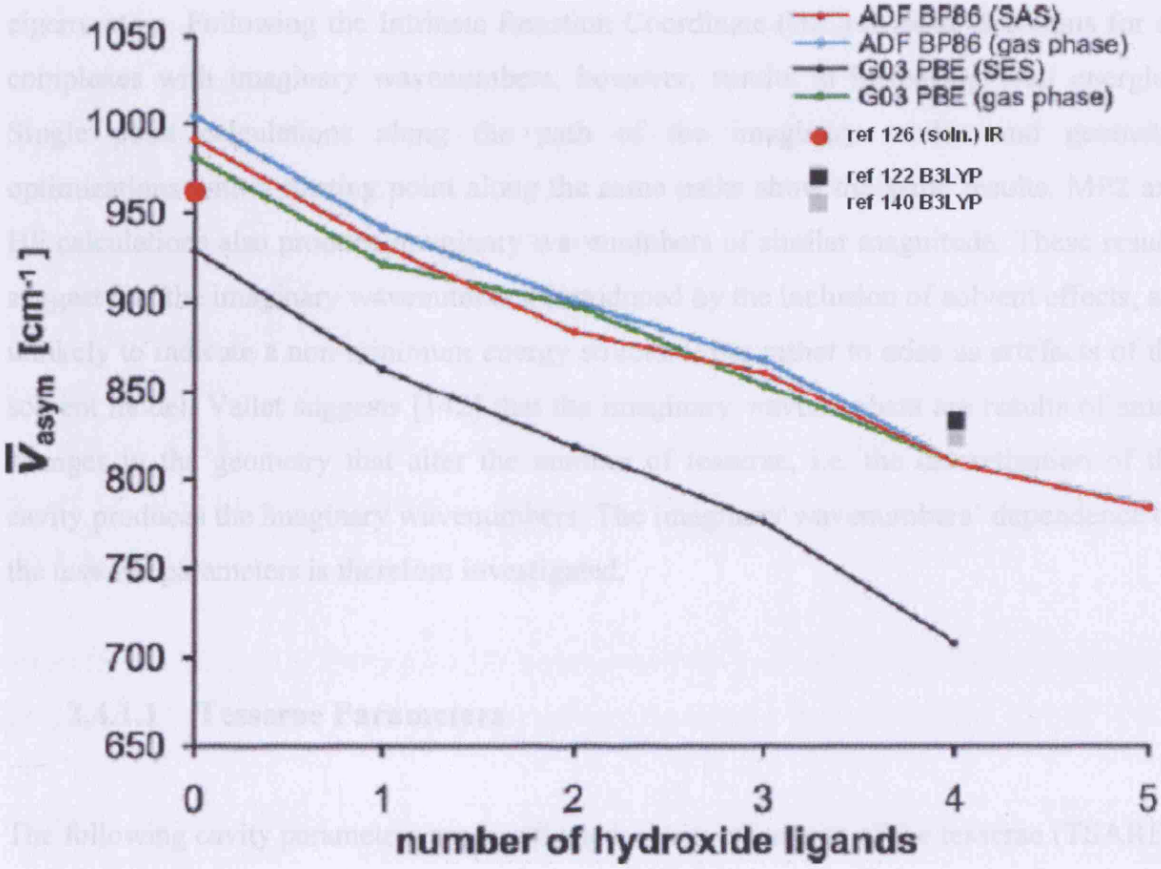

Figure 18. *v_{asym} (cm^{-1}) of the uranyl ion from selected calculations for all species compared with previous experimental data and calculations.*

2.4.1 Imaginary Wavenumbers

Calculations with the SES in G03 and ADF produce a few imaginary wavenumbers of small magnitude. Adjusting the solvent model parameters in ADF does not eliminate these modes, but the SAS calculations show no imaginary wavenumbers, or greatly reduced ones. The decision to use the SAS in ADF was based on the elimination or reduction of the imaginary wavenumbers. Calculations produce imaginary wavenumbers for the cationic and neutral complexes with the SES and the default solvent model parameters in G03.

Imaginary wavenumbers normally correspond to saddle points on a potential energy surface. If the calculated imaginary wavenumbers in this study correspond to saddle points, it should be possible to reach minima on the potential energy surface by following their eigenvectors. Following the Intrinsic Reaction Coordinate (IRC) in both directions for all complexes with imaginary wavenumbers, however, results in increasing total energies. Single point calculations along the path of the imaginary modes and geometry optimizations with a starting point along the same paths show the same results. MP2 and HF calculations also produce imaginary wavenumbers of similar magnitude. These results suggest that the imaginary wavenumbers, introduced by the inclusion of solvent effects, are unlikely to indicate a non-minimum energy structure, but rather to arise as artefacts of the solvent model. Vallet suggests [142] that the imaginary wavenumbers are results of small changes in the geometry that alter the number of tesserae, i.e. the discretisation of the cavity produces the imaginary wavenumbers. The imaginary wavenumbers' dependence on the tesserae parameters is therefore investigated.

2.4.1.1 Tesserae Parameters

The following cavity parameters are invetigated: the average area of the tesserae (TSARE), the threshold to discard small tesserae (SMALLTESSERA), the threshold to discard short edges in a tessera (SHORTEDGE), the minimum radius for the spheres used to smooth the surface (RMIN), and the overlap index between two interlocking spheres (OFAC). I perform geometry optimisations for all values of the tesserae parameters and calculate wavenumbers on those geometries.

Changing the SMALLTESSERA, SHORTEDGE, and RMIN parameters has small effects on the imaginary wavenumbers, the default values of these parameters are used subsequently. Table 9 shows the imaginary wavenumbers, ν_{sym}, ν_{asym}, and different cavity properties from calculations with values of the TSARE parameter between 0.1 and 0.8. The imaginary wavenumbers do not follow any specific trend, although the calculations with the TSARE parameter set to 0.4 produces the smallest magnitude. The average areas of the tesserae are different from the TSARE parameters. The volume and surface area of the cavity are almost independent of the TSARE parameter.

The OFAC parameter controls the smoothing of the cavity surface, a high value of OFAC results in a smooth surface (section 1.2.6.6). I studied the effect of the OFAC parameter on the imaginary wavenumbers with a fixed value of 0.4 for the TSARE parameter. Table 10 shows that the cavity volume is almost constant and the cavity area decreases, as OFAC increases; this indicates that the cavity gets smoother, as OFAC increases. A smoother surface should reduce or give no imaginary wavenumbers, because a change in geometry generally affects a smooth cavity less than a rough one.

The calculation with OFAC=0.94 results in a significantly different geometry, and a magnitude of the imaginary wavenumbers very different from the other calculations. If this calculation is disregarded, the magnitude of the wavenumbers generally decreases slightly, as the OFAC parameter increases. The uranyl vibrations do not change as much as the imaginary modes.

Table 9. *Cavity properties and wavenumbers (cm^{-1}) for different values of the TSARE parameters (all the other cavity parameters have the default value). Default: TSARE=0.2*

TSARE	Freq. 1 / cm^{-1}	Freq. 2 / cm^{-1}	Uranyl sym stretch / cm^{-1}	Uranyl antisym stretch cm^{-1}	Number of tesserae	Average tesserae area / $Å^2$	Cavity area / $Å^2$	Cavity volume / $Å^2$
0.1	74 i	58 i	863	930	2685	0.07	180.9	189.9
0.2	73 i	56 i	862	929	1590	0.11	180.9	190.0
0.4	67 i	53 i	862	928	911	0.20	181.2	189.2
0.6	91 i	78 i	860	926	610	0.30	181.2	189.1
0.8	68 i	54 i	861	927	570	0.32	181.2	188.9

Table 10. *Cavity properties and wavenumbers (cm^{-1}) for different values of the OFAC parameter (the TSARE parameter has a value of 0.4 in all calculations). Default: OFAC=0.89*

OFAC	Freq. 1 / cm^{-1}	Freq. 2 / cm^{-1}	Uranyl sym stretch / cm^{-1}	Uranyl antisym stretch cm^{-1}	Number of tesserae	Average tesserae area / $Å^2$	Cavity area / $Å^2$	Cavity volume / $Å^3$
0.86	66 i	49 i	862	929	744	0.24	181.9	188.8
0.88	65 i	53 i	862	928	854	0.21	181.5	188.9
0.90	67 i	49 i	861	928	917	0.20	181.2	189.2
0.92	63 i	47 i	861	928	981	0.18	180.9	189.4
0.93	69 i	51 i	861	928	1051	0.17	180.6	189.4
0.94	1970 i	313 i	859	928	1250	0.14	179.8	190.5
0.96	60 i	41 i	860	927	1523	0.12	178.8	190.3
0.97	59 i	56 i	859	927	1691	0.10	177.2	189.7

Since I obtain the lowest magnitude of the imaginary wavenumber with OFAC=0.96, I varied the TSARE parameter while keeping the OFAC parameter constant at that level. Table 11 shows the result.

Table 11. *Cavity properties and wavenumbers (cm^{-1}) for different values of the TSARE parameters and OFAC=0.96 (all the other cavity parameters have the default value). Default: TSARE=0.2, OFAC=0.89*

TSARE	Freq. 1 / cm^{-1}	Freq. 2 / cm^{-1}	Uranyl sym stretch / cm^{-1}	Uranyl antisym stretch cm^{-1}	Number of tesserae	Average tesserae area / $Å^2$	Cavity area / $Å^2$	Cavity volume / $Å^2$
0.2	74i	57i	861	928	2311	0.08	179	191
0.4	60i	41i	860	927	1523	0.12	179	190
0.6	117i	79i	861	928	1269	0.14	179	190
0.8	180i	143i	861	928	1071	0.17	179	190

The cavity parameter combination of TSARE=0.4 and OFAC=0.96 obtains the smallest magnitudes of the imaginary wavenumbers. I tried this combination in geometry optimisations for all other compounds, but encountered convergence problems and therefore used the default values. The only compound that uses this combination of parameters is **2W2OH**, since the geometry optimisation for that compound does not work properly with the default settings.

2.4.1.2 Other Solvents

The parameters in the solvent effects including calculations are the dielectric constant and the radius of the solvent. I wanted to probe the effect of changing the solvent, and thus performed calculations for solvents with dielectric constants over a broad range. I performed the calculations on **5W**, Table 12 collects the results.

I divide the results into four groups, depending on the solvent parameters. Water and ethanol have the smallest radii and large dielectric constants; these calculations correspond to the largest imaginary modes. The cavities for water and ethanol have similar area and volume. The other extreme is benzene that has a large radius and the smallest dielectric

constant of the solvents in this study. The calculation with the solvent parameters of benzene has no imaginary modes. Ether is put in a third, separate group, because its cavity area and volume is different from all the other solvents. The imaginary wavenumbers from the calculation with the solvent model parameters of ether are between the first group and the rest of the solvents. The last group consists of the rest of the solvents that have similar cavity areas and volumes to benzene. They have only one imaginary mode of small magnitude.

The imaginary wavenumbers are correlated with the geometry change between the gas and the solvent phase. The further below the plane the hydrogen atoms are in the water ligand that is rotated 90 degrees, compared with the other ligands, the higher the magnitude of the imaginary wavenumbers.

The magnitude of the uranyl stretching vibrations increases as the dielectric constant decreases, although not as much as the imaginary modes decrease. This increase is expected, as a decrease of the dielectric constant and increase of the cavity volume make the calculations more similar to gas phase calculations.

I argue that the imaginary modes are artefacts of the solvent model according to Vallet's suggestion, because they increase with the dielectric constant, are affected by the tesserae parameters, and do not correspond to saddle points on the potential energy surface.

Table 12. *Cavity properties and wavenumbers (cm^{-1}) for calculations with dielectric constant and radius parameters of different solvents.*

Solvent	di-electric constant	Solvent radius / Å	Freq. 1 / cm^{-1}	Freq. 2 / cm^{-1}	Uranyl sym stretch / cm^{-1}	Uranyl antisym stretch /cm^{-1}	Cavity area / $Å^2$	Cavity volume / $Å^3$
Water	78.39	1.385	67 i	53 i	862	928	181.2	189.2
ethanol	24.55	2.18	65 i	50 i	862	930	181.4	189.9
dimethylsulfoxide	46.7	2.455	24 i	27	877	950	216.7	255.4
quinoline	9.03	3.5	22 i	27	879	954	217.3	257.9
tetrahydrofuran	7.58	2.56	22 i	27	879	955	216.0	255.3
chlorobenzen	5.621	2.805	11 i	33	880	957	216.1	255.2
chloroform	4.9	2.48	13 i	28	881	957	216.2	255.1
ether	4.335	2.785	26 i	19	876	952	198.7	220.1
benzene	2.247	2.63	11	32	885	965	216.1	255.2

2.5 Mayer Bond Orders

I used Bridgeman's Mayer code [143] to calculate MBOs for all species; Figure 19 and Table 13 present the results. Cavigliasso and Bridgeman calculate an MBO of 2.11 for the **5W** complex [144]; this higher value is explained by the use of different basis sets. MBOs are particularly useful for the $[UO_2(H_2O)_m(OH)_n]^{2-n}$ family of compounds, because the varying charge of the ligands makes the heavily charge dependent Ziegler-Rauk energy decomposition scheme unsatisfactory.

The MBOs of the uranyl bond decrease as the number of hydroxide ligands increases, consistent with a longer $r(U\text{-}O_{yl})$ and decreasing uranyl stretching vibrations. The decrease in MBOs from **5W** to **2W2OH** is small, but accelerates from **2W2OH** to **5OH**. The MBOs of **4WOH** and **2W2OH** are very similar, most likely a cancelling effect between a decreasing coordination number, and an extra $[OH]^-$ ligand in **2W2OH**. The MBO differences between the SAS and the gas phase, and between the different xc-functionals, are very small.

Table 13. *Calculated $U\text{-}O_{yl}$ MBOs in all target complexes.*

Code	Functional	5W	4WOH	2W2OH	W3OH	4OH	5OH
ADF gas phase	PBE	1.68	1.67	1.66	1.64	1.61	1.59
	BP86	1.70	1.69	1.68	1.66	1.63	1.61
ADF COSMO (SAS)	PBE	1.67	1.66	1.66	1.65	1.61	1.59
	BP86	1.69	1.68	1.68	1.67	1.63	1.61

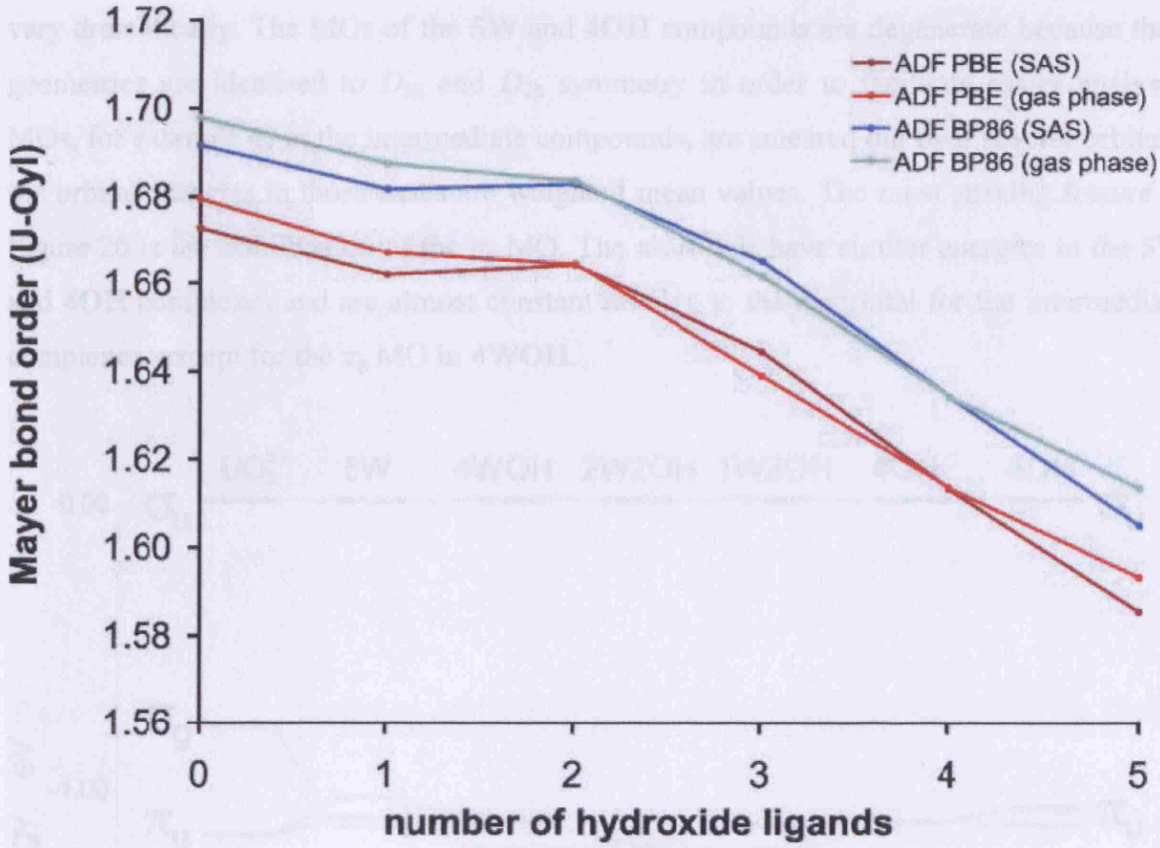

Figure 19. *Calculated U-O_{yl} MBOs for all target complexes.*

2.6 Molecular Orbital Analysis

The previous results in this work strongly suggest that the uranyl bond weakens as hydroxide ligands replace water ligands; this section provides an explanation for this behaviour. Clark *et al.* present a hypothesis regarding the origin of the uranyl bond weakening [121]. They suggest that the weakening is partially due to the strong σ-donor ability of the $[OH]^-$ ligands, but also that the hydroxide ligands' π-donor ability makes it possible for $[OH]^-$ ligands to compete with O_{yl}, to form π-bonds with the 6*d* AOs. This hypothesis is investigated below by studying the π_g, π_u, σ_g, and σ_u MOs of the uranyl unit.

Figure 20 shows the relative energy of the π_g, π_u, σ_g, and σ_u MOs for all species, with the energy of the σ_u MO set to 0 as a reference to the other MOs. This is necessary because of the charge difference between the compounds that makes the absolute energy of the MOs

vary dramatically. The MOs of the **5W** and **4OH** compounds are degenerate because their geometries are idealised to D_{5h} and D_{2h} symmetry in order to facilitate easier analysis. MOs, for example σ_g in the intermediate compounds, are smeared out over several orbitals; the orbital energies in those cases are weighted mean values. The most striking feature of Figure 20 is the stabilization of the σ_g MO. The π-orbitals have similar energies in the **5W** and **4OH** complexes and are almost constant relative to the σ_u orbital for the intermediate complexes, except for the π_g MO in **4WOH**.

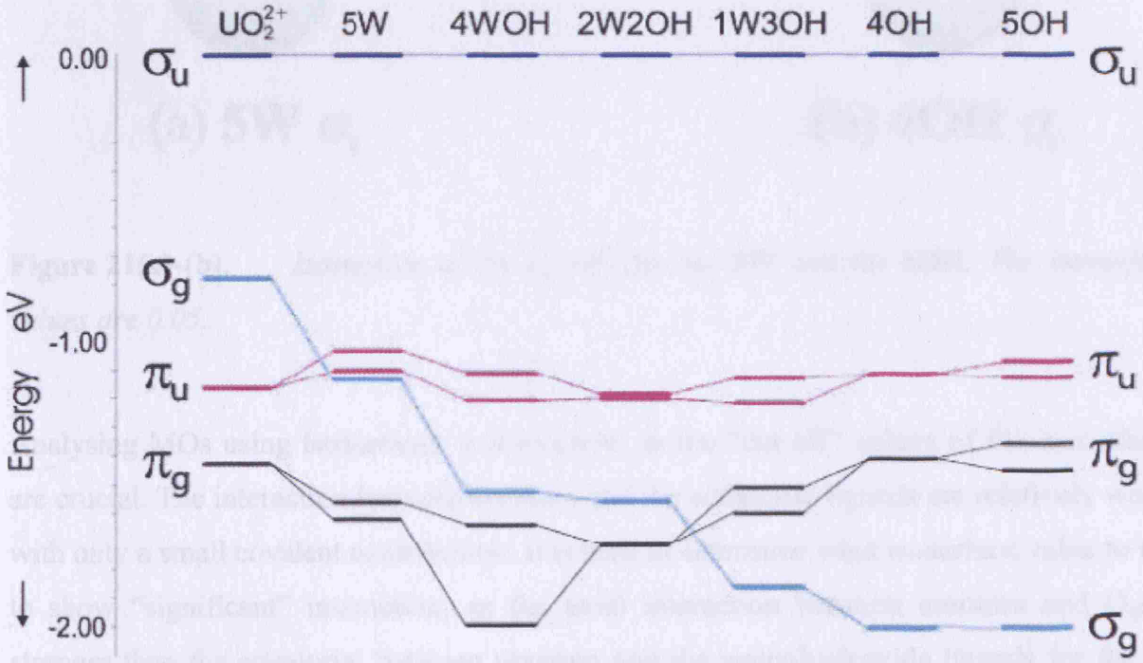

Figure 20. *MO energies for UO_2^{2+},* **5W**, **4WOH**, **2W2OH**, **W3OH**, **4OH**, *and* **5OH**. *The energy of σ_u has been set to zero, and the other MO energies are given relative to σ_u.*

Figure 21 shows the σ_g MO for **5W** and **4OH**; these MOs provide an explanation for the stabilisation of the σ_g MO. The σ_g MO in **4OH** spreads out to the bonding region in the equatorial plane, where it forms bonding combinations with the hydroxide ligands. By contrast, the electron density of the σ_g MO for **5W** is almost exclusively located along the uranyl vector and the insignificant interactions with the water ligands are anti bonding.

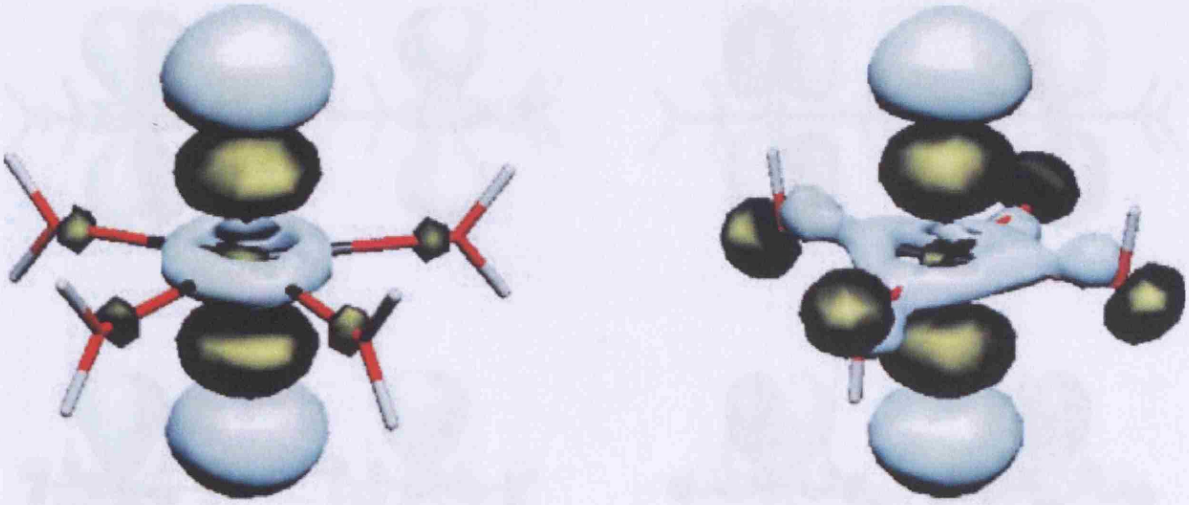

(a) **5W** σ_g (b) **4OH** σ_g

Figure 21(a)-(b). *Isosurface of the σ_g MO for (a)* **5W** *and (b)* **4OH**. *The isosurface values are 0.05.*

Analysing MOs using isosurfaces is subjective, as the "cut off" values of the isosurfaces are crucial. The interaction between uranium and the equatorial ligands are relatively weak, with only a small covalent contribution. It is hard to determine what isosurface value to use to show "significant" interaction, as the axial interaction between uranium and O_{yl} is stronger than the equatorial between uranium and the water/hydroxide ligands for the σ_g, σ_u, π_g, and π_u orbitals. It is often more relevant to compare similar orbitals of different species with the same "cut off" value, however, the question of what isosurface value that will correspond to significant interaction still remains.

Figure 22 shows the π_g and π_u MOs of **5W** and **4OH** respectively. The interaction in the equatorial plane is greater for **4OH** than **5W**, but the interaction between uranium and the hydroxide ligands in the π_g MO consists of σ-donations from the hydroxide ligands, and no π-bonding. There is therefore little evidence of any "π-loading" in the equatorial plane to compete for 6*d* AOs in the π_g MO.

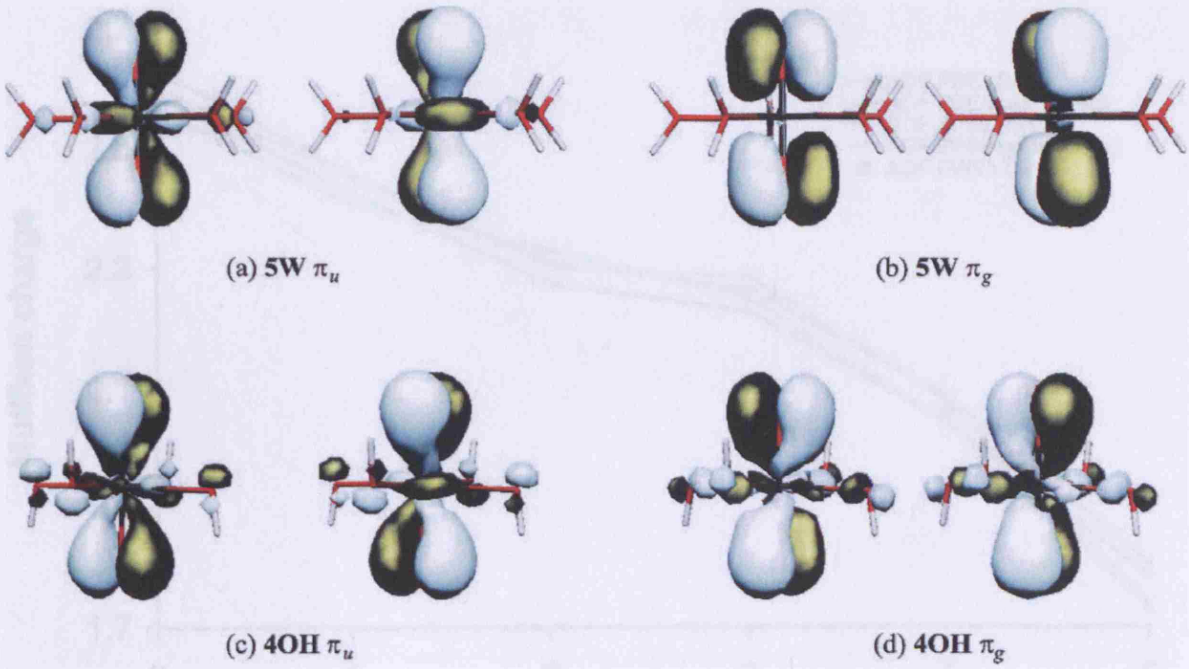

Figure 22(a)-(d). *Isosurface of the π_u MO for (a)* **5W** *and (c)* **4OH**, *and the π_g MO for (b)* **5W** *and (d)* **4OH**. *The isosurface values are 0.05.*

2.7 Charge Analysis

Figure 23 and Figure 25 show Mulliken and Hirshfeld U charges, and Figure 24 and Figure 26 show Mulliken and Hirshfeld O_{yl} charges, for different xc-functionals in the gas phase and with solvent models. It is clear that the dependence on the xc-functionals and on the solvent models is small and that both the charges of U and O_{yl} become more negative, as the number of hydroxide ligands increases. The magnitude of the uranium charge decreases faster than the rates at which the O_{yl} charge becomes more negative for both Mulliken charges and the Hirshfeld scheme. Our published paper on this study [128] concludes that the weakening of the uranyl bond is due to a decreased ionic interaction as the charge difference between uranium and O_{yl} decreases. The density difference analysis in chapter 5, however, suggests that this might not the case (more details of this are given in chapter 5).

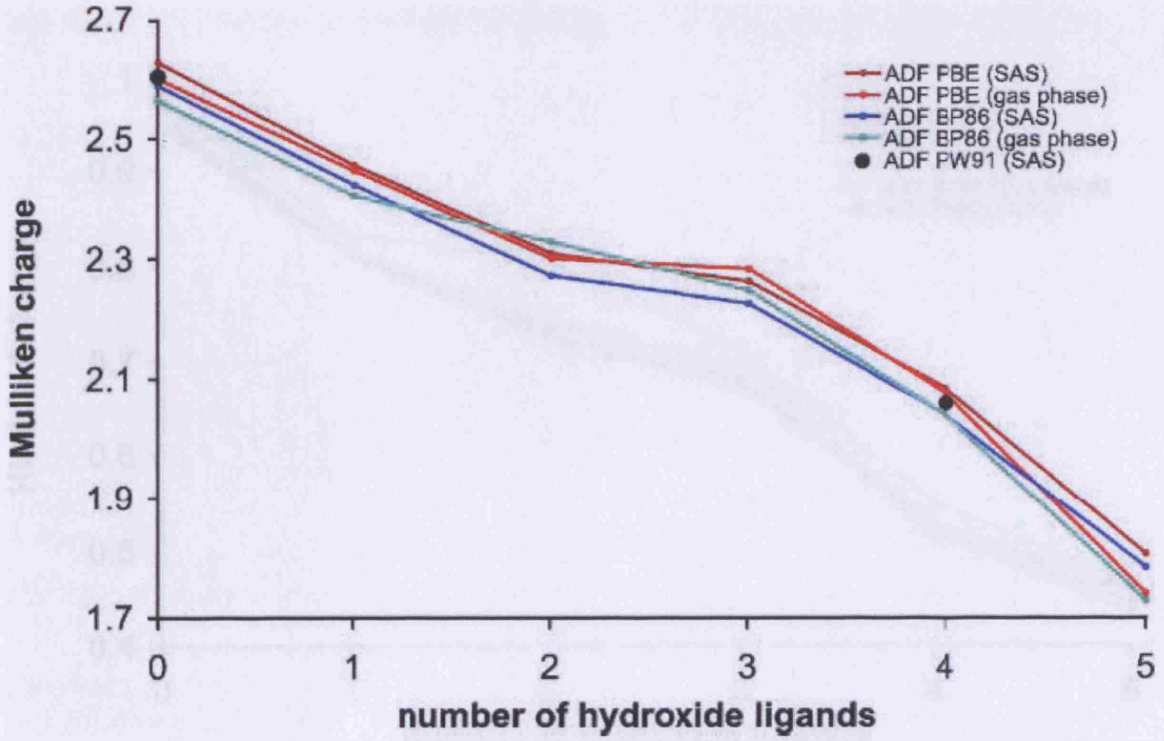

Figure 23. *Mulliken charges (e^-) of the uranium atoms for all species.*

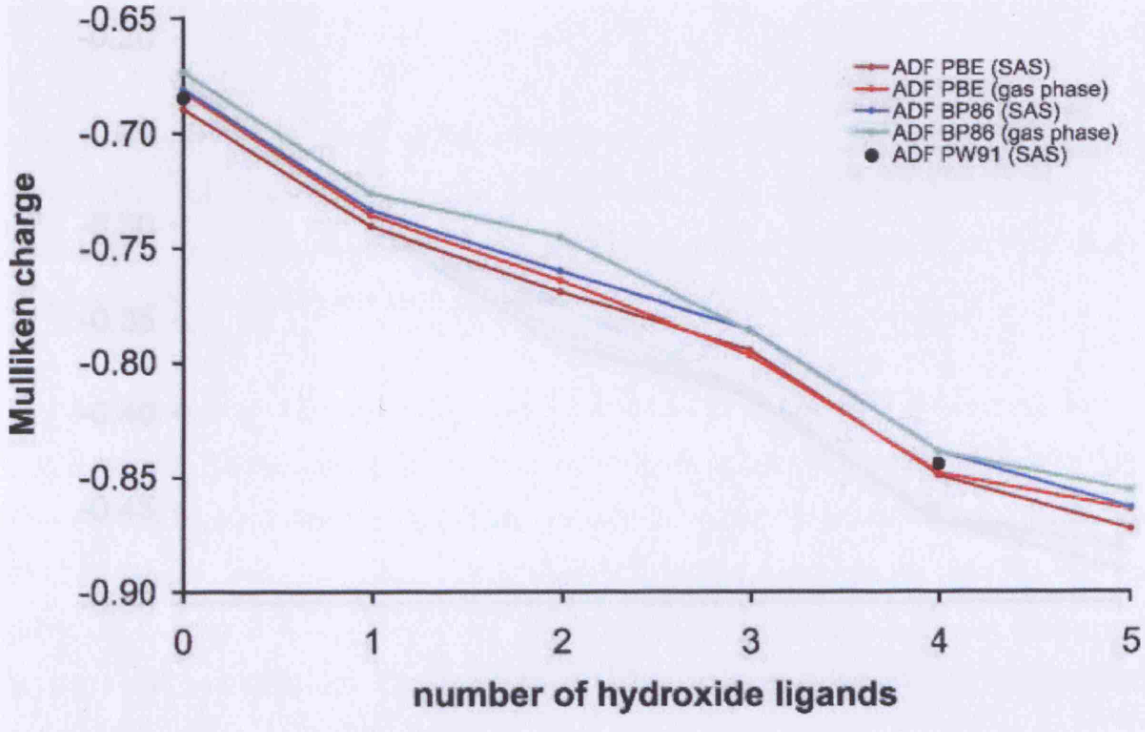

Figure 24. *Mulliken charges (e^-) of O_{yl} for all species.*

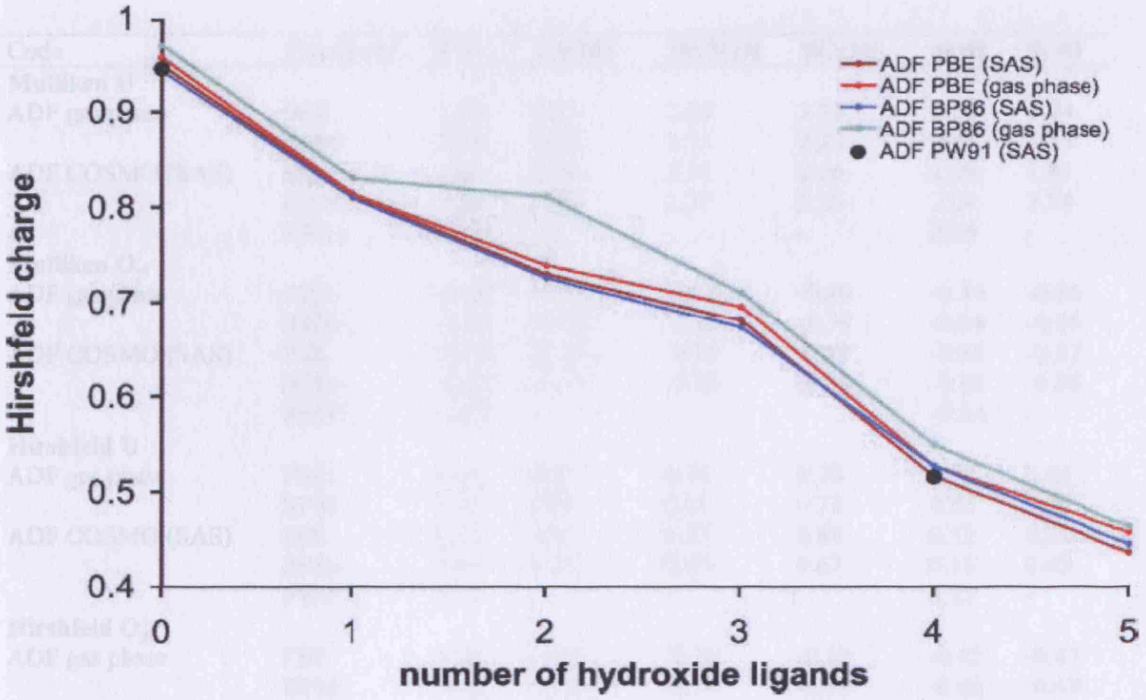

Figure 25. *Hirshfeld charges (e^-) of the uranium atoms for all species.*

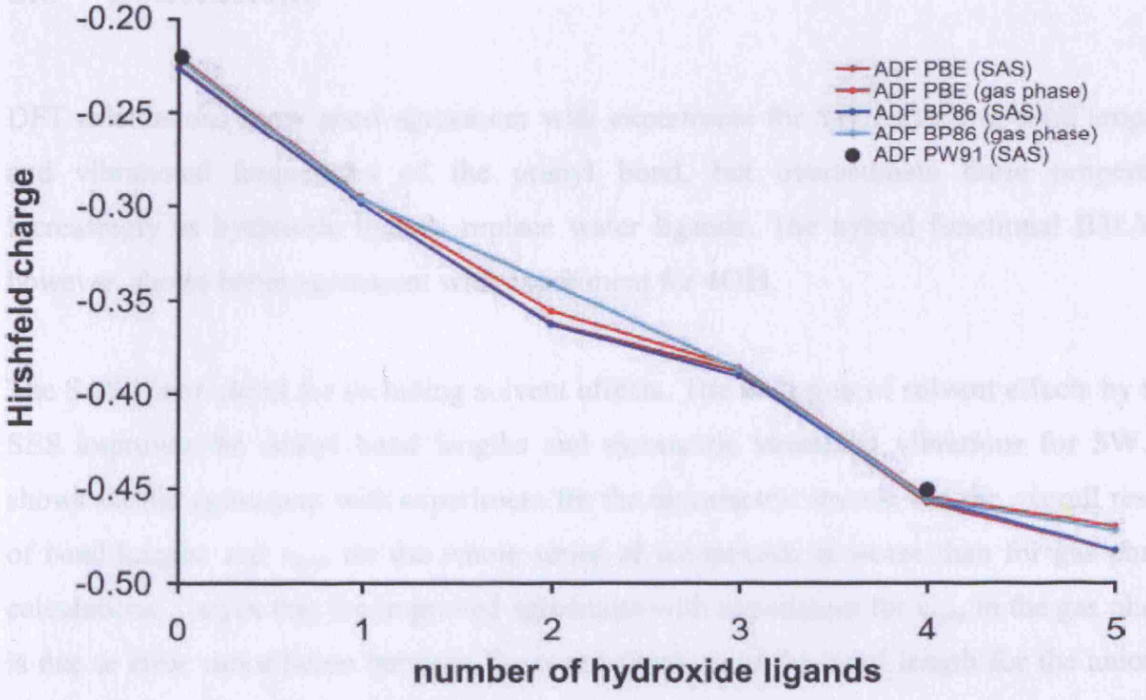

Figure 26. *Hirshfeld charges (e^-) of O_{yl} for all species.*

Table 14. *Mulliken and Hirshfeld charges (e^-) of uranium and O_{yl} for all species.*

Code	Functional	5W	4WOH	2W2OH	W3OH	4OH	5OH
Mulliken U							
ADF gas phase	PBE	2.60	2.45	2.30	2.28	2.08	1.74
	BP86	2.56	2.40	2.33	2.25	2.04	1.73
ADF COSMO (SAS)	PBE	2.63	2.46	2.31	2.26	2.08	1.81
	BP86	2.59	2.42	2.27	2.23	2.04	1.78
	PW91	2.60	-	-	-	2.06	-
Mulliken O_{yl}							
ADF gas phase	PBE	-0.68	-0.74	-0.76	-0.80	-0.85	-0.86
	BP86	-0.67	-0.73	-0.75	-0.79	-0.84	-0.86
ADF COSMO (SAS)	PBE	-0.69	-0.74	-0.77	-0.79	-0.85	-0.87
	BP86	-0.68	-0.73	-0.76	-0.79	-0.84	-0.86
	PW91	-0.68	-	-	-	-0.84	-
Hirshfeld U							
ADF gas phase	PBE	0.96	0.81	0.74	0.70	0.53	0.46
	BP86	0.97	0.83	0.81	0.71	0.55	0.46
ADF COSMO (SAS)	PBE	0.95	0.81	0.73	0.68	0.52	0.44
	BP86	0.94	0.81	0.73	0.67	0.53	0.45
	PW91	0.95	-	-	-	0.52	-
Hirshfeld O_{yl}							
ADF gas phase	PBE	-0.22	-0.30	-0.36	-0.39	-0.45	-0.47
	BP86	-0.22	-0.30	-0.34	-0.39	-0.46	-0.47
ADF COSMO (SAS)	PBE	-0.23	-0.30	-0.36	-0.39	-0.46	-0.48
	BP86	-0.23	-0.30	-0.36	-0.39	-0.46	-0.48
	PW91	-0.23	-	-	-	-0.46	-

2.8 Conclusions

DFT calculations show good agreement with experiment for **5W** regarding bond lengths and vibrational frequencies of the uranyl bond, but overestimate these properties increasingly as hydroxide ligands replace water ligands. The hybrid functional B3LYP, however, shows better agreement with experiment for **4OH**.

The SAS is not useful for including solvent effects. The inclusion of solvent effects by the SES improves the uranyl bond lengths and symmetric stretching vibrations for **5W**. It shows similar agreement with experiment for the asymmetric stretch, but the overall result of bond lengths and ν_{sym} for the whole series of compounds is worse than for gas phase calculations. I argue that the improved agreement with experiment for ν_{sym} in the gas phase is due to error cancellation between the overestimation of the bond length for the anionic species and neglect of solvent effects.

Calculated bond lengths and vibrational data strongly suggest that the uranyl bond weakens as the number of hydroxide ligands increases; this is confirmed by MBOs. Charge analysis shows that the increased negative charge in the **5W** → **4OH** series is distributed on both uranium and O_{yl}, with the major part on uranium. This suggests a reduction in the ionic interaction, which will be investigated further in chapter 5. The hypothesis of Clark *et al.* [121] that the hydroxide ligands in **4OH** compete with O_{yl} for 6*d* uranium AOs through π-bonding is not confirmed by investigation of the π_g MO in **4OH**.

Chapter 3

Theoretical Investigations of Equatorial *cis* and *trans* Actinyl Phosphinimine and Phosphine Oxide Complexes $AnO_2Z_2(Cy_3PX)_2$ (An = U, Np, Pu, or Am; Z = H, F, Cl, Br, or I; Cy = Cyclohexyl; X = O or NH).

3.1 Introduction

The work in section 3.3 – 3.5 has been published in a combined experimental and computational article [145].

The newly synthesised complexes $UO_2Cl_2(Cy_3PNH)_2$ (**1**) and $UO_2Cl_2(Cy_3PO)_2$ (**2**) (Cy=cyclohexyl) surprised my collaborators in Manchester. Firstly, Cy_3PNH ligands in a solution of **2** displace Cy_3PO ligands to form **1**. $UO_2Cl_2(Cy_3PNH)(Cy_3PO)$ (**3**) is an intermediate in the reaction (Scheme 1) – adding Cy_3PO ligands to a solution of **1** causes no reaction. The displacement of the Cy_3PO ligands strongly suggests that the U-N bond in **1** is stronger than the equatorial U-O bond in **2**. N-donor ligands are softer donors than O-donor ligands; it is therefore likely that the U-N bonds are more covalent than the equatorial U-O bonds. Does this explain why the U-N bonds are stronger than the U-O bonds? It is also possible that Cy_3PO is more stable in solution than Cy_3PNH, although that is not investigated here.

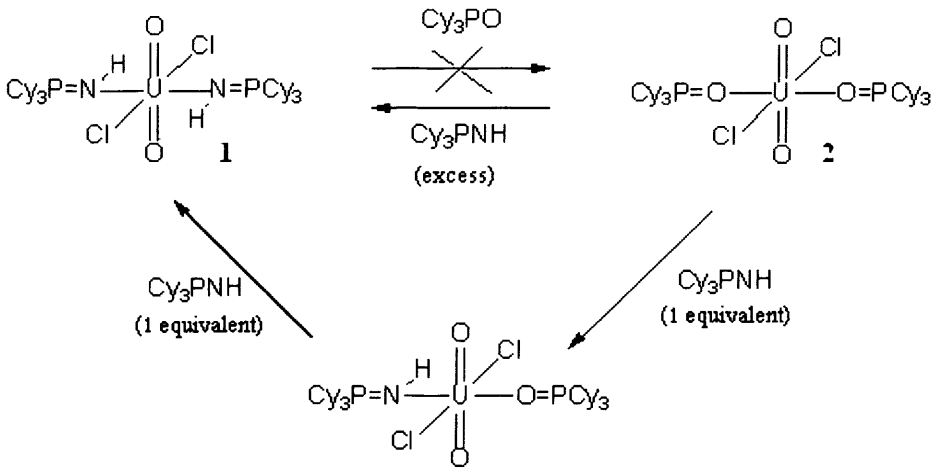

Scheme 1. *Comparison of the ligand substituting ability of Cy_3PO and Cy_3PNH.*

Secondly, my collaborators detect a major and a minor isomer of **1** and **2** that they interpret as *cis* and *trans* isomers. They find a major/minor ratio of 0.88/0.12 for **1** and 0.93/0.07 for **2**, although they are unable to determine the dominant isomer. A *cis* configuration must have considerably higher steric repulsion between the large and bulky phosphinimine and phosphine oxide ligands than a *trans*. Something stabilises the *cis* isomer – I seek to find out what that is. Comparison between Raman spectra in solution and in the solid state gives a tentative indication that the *cis* isomer is the major isomer in solution. Experimental NMR data are available for both the minor and major isomer of **1**; calculating NMR chemical shifts for both isomers of **1** and comparing them with the experimental data will therefore indicate which the major species is, provided that the calculated data are accurate enough.

Two central questions in this investigation are:

1) Why does Cy_3PNH displace Cy_3PO?
2) Which isomer is most stable?

I use the energy decomposition scheme, electron densities, and orbital analysis to address the former question; I calculate total bond energies, dipole moments, NMR chemical shifts, and study solvent effects, to address the latter. I also study the geometry, Hirshfeld charges, and extend the study to other actinides, halide, and hydride ligands.

3.2 Computational Details

This study used the ADF suit of programmes to perform DFT calculations with the PBE xc-functional on all compounds. TZP ZORA all electron basis sets were employed for all atoms except C and H for which DZP ZORA all electron basis sets were employed. The integration parameter was set to 5, the geometry optimisation convergence criterion was 0.001 a.u. $Å^{-1}$, and the SCF convergence criterion was 10^{-7}. The ZORA accounted for scalar relativistic effects and spin-orbit coupling. Only the NMR calculations included spin orbit coupling (the total bonding energies, dipole moments, and Hirshfeld charges of **1** and **2** were obtained from those calculations; these properties therefore include spin orbit effects). The ADF NMR property programme [146, 147] calculated isotropic shielding constants and chemical shifts; these calculations used all relativistic effects available, i.e. the mass-velocity, Darwin, and spin-Zeeman terms. The COSMO with the SES (esurf is the keyword in ADF) accounted for solvent effects. The following values of the atomic radii were used: U = 2.0 Å, O = 1.6 Å, F = 1.4 Å, Cl = 1.8 Å, Br = 2.0 Å, I = 2.2 Å, N = 1.6 Å, P = 2.0 Å, C = 1.8 Å, and H = 1.2 Å. The following values for the solvent radii and dielectric constants were used: $CHCl_3$, r = 2.48 Å, ε = 4.9; CH_2Cl_2, r = 2.27 Å, ε = 8.93; CH_3Cl, r = 2.00 Å, ε = 12.9; THF, r = 2.56 Å, ε = 7.58; H_2O, r = 1.385 Å, ε = 78.39.

3.3 Geometries

Figure 27 shows the geometries of the *cis* and *trans* isomers of **1** ($\mathbf{1}_{cis}$ and $\mathbf{1}_{trans}$) and **2** ($\mathbf{2}_{cis}$ and $\mathbf{2}_{trans}$); Table 15 provides bond distances and bond angles from the experimental crystal structures of $\mathbf{1}_{cis}$, $\mathbf{1}_{trans}$, and $\mathbf{2}_{trans}$ (my collaborators have been unable to grow crystals of $\mathbf{2}_{cis}$), and bond lengths and bond angles calculated in the gas phase for complexes $\mathbf{1}_{cis}$, $\mathbf{1}_{trans}$, $\mathbf{2}_{cis}$, $\mathbf{2}_{trans}$, $\mathbf{3}_{cis}$, and $\mathbf{3}_{trans}$.

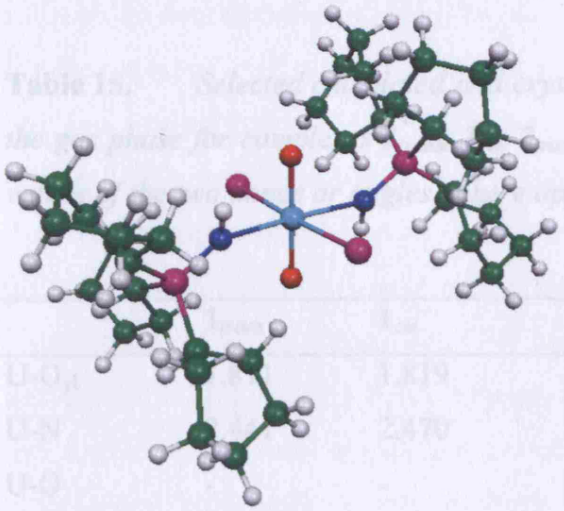

(a) $\mathbf{1}_{trans}$

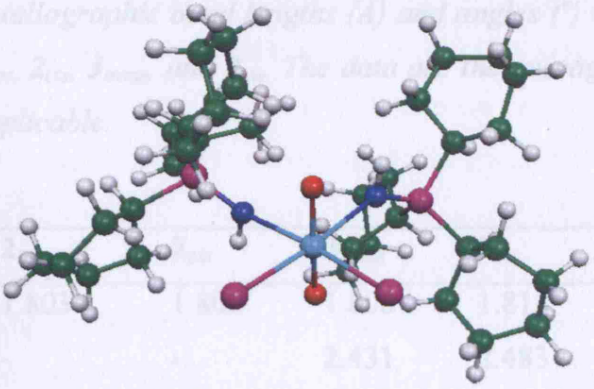

(b) $\mathbf{1}_{cis}$

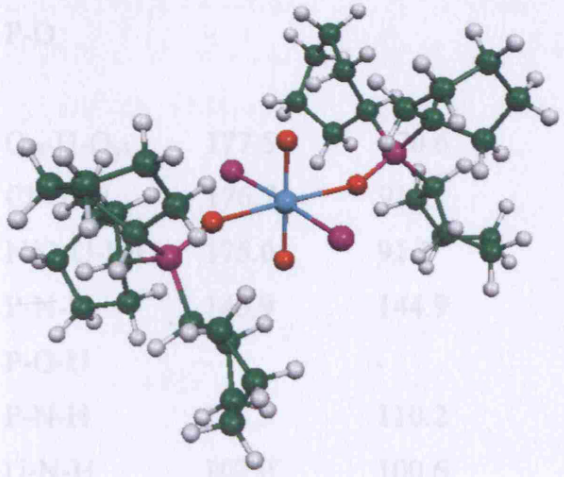

(c) $\mathbf{2}_{trans}$

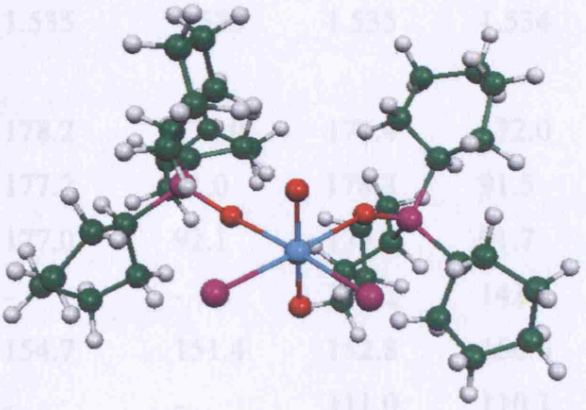

(d) $\mathbf{2}_{cis}$

Figure 27(a)-(d). *Ball-and-stick-representations of (a) $\mathbf{1}_{trans}$, (b) $\mathbf{1}_{cis}$, (c) $\mathbf{2}_{trans}$, and (d) $\mathbf{2}_{cis}$ calculated in the gas phase.*

Both isomers of **1** have one N-*H* hydrogen atom above and one below the equatorial plane; this minimises the steric repulsion between the phosphinimine ligands. Both isomers of **2** adopt very similar geometries to **1**.

Table 15. *Selected calculated and crystallographic bond lengths (Å) and angles (°) in the gas phase for complexes $\mathbf{1}_{trans}$, $\mathbf{1}_{cis}$, $\mathbf{2}_{trans}$, $\mathbf{2}_{cis}$, $\mathbf{3}_{trans}$, and $\mathbf{3}_{cis}$. The data are the average values of the two bonds or angles, where applicable.*

	$\mathbf{1}_{trans}$	$\mathbf{1}_{cis}$	$\mathbf{2}_{trans}$	$\mathbf{2}_{cis}$	$\mathbf{3}_{trans}$	$\mathbf{3}_{cis}$
U-O_{yl}	1.811	1.819	1.803	1.808	1.808	1.813
U-N	2.441	2.470	-	-	2.431	2.483
U-O	-	-	2.393	2.432	2.400	2.422
U-Cl	2.676	2.642	2.663	2.629	2.670	2.636
P-N	1.619	1.621	-	-	1.620	1.625
P-O	-	-	1.535	1.535	1.535	1.534
O_{yl}-U-O_{yl}	177.5	170.6	178.2	174.0	177.4	172.0
Cl-U-Cl	176.7	91.1	177.2	91.0	178.3	91.5
N/O-U-N/O	175.0	91.8	177.0	92.1	173.9	91.7
P-N-U	145.9	144.9	-	-	147.2	143.8
P-O-U	-	-	154.7	151.4	152.8	150.6
P-N-H	111.3	110.2	-	-	111.0	110.1
U-N-H	102.0	100.6	-	-	100.8	99.8
experimental						
U-O_{yl}	1.792(4)	1.781(2)	1.778(5)	-	-	-
U-N/O	2.392(5)	2.350(2)	2.278(5)	-	-	-
U-Cl	2.704(2)	2.6861(7)	2.667(2)	-	-	-
P-N/O	1.622(5)	1.625(3)	1.535(5)	-	-	-
O-U-O	180.000(2)	174.24(13)	179.6(3)	-	-	-
Cl-U-Cl	180.0	89.75(3)	179.89(7)	-	-	-
N-U-N	180.000(1)	96.04(13)	-	-	-	-
P-N/O-U	139.8(3)	140.93(15)	167.3(3)	-	-	-
P-N-H	112(6)	114(3)	-	-	-	-
U-N-H	107(6)	102(3)	-	-	-	-

Calculation overestimates r(U-O_{yl}) for all species and **2** yields the shortest r(U-O_{yl}). These results compare well with the calculations on the neutral complex **2W2OH** in chapter 2 that also overestimate r(U-O_{yl}) (based on interpolation of experimental result). The longer r(U-O_{yl}) in **1**, compared with **2**, is a tentative indication that the U-N bonds are stronger than the equatorial U-O bonds. Calculation overestimates r(U-N) of **1** and r(U-O) of **2**, the difference between experiment and calculations is about 0.12 Å for $\mathbf{1}_{cis}$ and $\mathbf{2}_{trans}$. Calculations in the gas phase for the **5W** complex in chapter 2 (and references therein) also overestimate the equatorial bond distance between uranium and the neutral water ligands (no experimental bond lengths are available for **2W2OH**, which is otherwise a better comparison). Calculations yields shorter r(U-N) in $\mathbf{1}_{trans}$ than in $\mathbf{1}_{cis}$, opposite to experiment. r(U-N) is slightly shorter and r(U-O) slightly longer in **3** compared with **1** and **2**; this indicates competition between the N-donor and O-donor ligands for uranium AOs. r(U-Cl) is slightly underestimated; this is probably related to the overestimation of r(U-N) and r(U-O). r(P-N) and r(P-O) show excellent agreement with experiment.

Both calculated and experimental O_{yl}-U-O_{yl} bond angles are smaller in the *cis* than in the *trans* isomers. This most likely reflects the charge distribution in the *cis* isomer; the O_{yl} atoms bend away from the negatively charged Cl-ligands. The calculated O_{yl}-U-O_{yl} bond angle is smaller in $\mathbf{1}_{cis}$ than in $\mathbf{2}_{cis}$.

3.4 Relative Stability of the Isomers

3.4.1 Total Bonding Energies and Dipole Moments

I have calculated the total bonding energies of **1** and **2** in the gas phase and in CH_2Cl_2 by using the COSMO; Table 16 presents the energy differences between the *cis* and *trans* isomers (ΔE) of **1** and **2**. $\Delta E = E_{cis} - E_{trans}$. A positive value of ΔE therefore corresponds to greater stability of the *trans* isomer.

Table 16. *ΔE (kJ/mol) calculated in the gas phase and in CH_2Cl_2 for complexes 1 and 2. A positive ΔE value corresponds to the trans isomer being more stable.*

		1	**2**
Gas:	$E_{cis} - E_{trans}$	24.7	15.5
CH_2Cl_2:	$E_{cis} - E_{trans}$	8.8	7.1

It is evident from Table 16 that including solvent effects is essential to calculate accurate relative total bonding energies; ΔE decreases markedly when I include solvent effects. The *trans* isomers are more stable than the *cis* in all calculations – a strong indication that the *trans* isomers are the major species in solution. ΔE of **1** is larger than of **2** in both gas phase and solution, although the difference decreases when I use the solvent model. Other calculations with slightly smaller basis sets and with frozen core basis sets (not shown) yield smaller ΔE values for **1** than **2**.

A Boltzmann distribution relates the experimental ratios of the isomers to ΔE values:

$$\frac{C_{trans}}{C_{cis}} = e^{-\Delta E / kT} \tag{1.79}$$

C_{trans} and C_{cis} are the relative numbers of the *cis* and *trans* forms, k is the Boltzmann constant, and T is the absolute temperature. This formula yields an energy difference of 4.9 kJ/mol for **1** and 6.4 kJ/mol for **2**. The calculated values are in very good agreement with experiment, although calculations predict the energy difference to be smaller between the isomers of **1** than between the isomers of **2** – opposite to experiment.

The stabilisation of the *cis* isomer in solution reflects the fact that its charge distribution is quite different from the *trans* isomer, as the dipole moments in Table 17 show.

Table 17. *Calculated dipole moments (Debye) in the gas phase and in CH_2Cl_2 for complexes $\mathbf{1}_{trans}$, $\mathbf{1}_{cis}$, $\mathbf{2}_{trans}$, and $\mathbf{2}_{cis}$.*

	$\mathbf{1}_{trans}$	$\mathbf{1}_{cis}$	$\mathbf{2}_{trans}$	$\mathbf{2}_{cis}$
Gas:	0.84	13.83	0.58	12.64
CH_2Cl_2:	0.66	24.25	0.54	21.61

The *cis* isomer has much larger dipole moments than the *trans* isomer in all calculations; the inclusion of solvent effects increases this difference. This difference in dipole moments explains the stabilisation of the *cis* isomer in solution. The dipole moments are larger in **1** compared with **2** in all calculations, consistent with the smaller experimental ΔE value of **1**.

3.4.2 Total Bonding Energies in Other Solvents

Table 18 and Figure 28 present calculated ΔE values of **1** and **2** in the gas phase and in solution with model parameters of a variety of solvents. I have performed these calculations with the same approximations as in the computational details section, with the exception that I used frozen core basis sets (although I calculated the gas phase and CH_2Cl_2 data with all electron basis sets). Calculations for **1** and **2** in the gas phase and in CH_2Cl_2 (not shown) confirm that this does not affect the results significantly in comparison with the all electron calculations. The reason for this is that differences between the basis sets are often similar for both isomers and therefore cancel out.

Table 18. *Calculated ΔE (kJ/mol) in different solvents for complexes 1_{trans}, 1_{cis}, 2_{trans}, and 2_{cis}. A positive ΔE value corresponds to the trans isomer being more stable.*

	1	2
$CHCl_3$: ΔE	10.9	15.1
THF: ΔE	5.1	7.0
CH_3Cl: ΔE	6.1	12.3
Water: ΔE	3.2	8.1

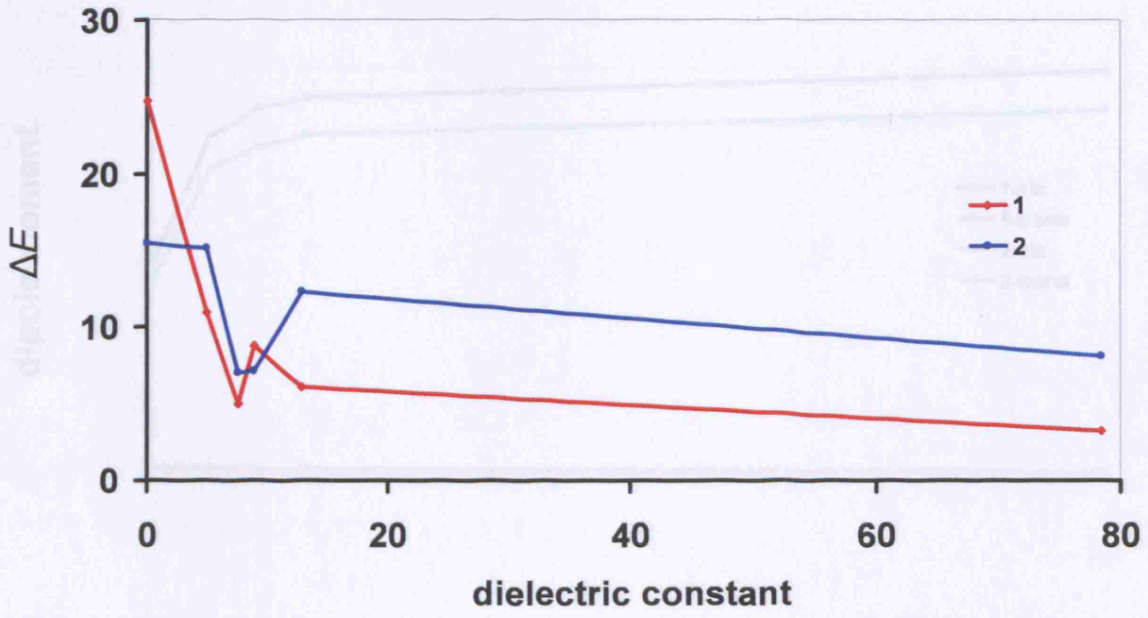

Figure 28. *Calculated ΔE (kJ/mol) in the gas phase and in different solvents for complexes 1_{trans}, 1_{cis}, 2_{trans}, and 2_{cis}, versus the dielectric constant.*

Table 19. *Calculated dipole moments (Debye) in different solvents for complexes* $\mathbf{1}_{trans}$, $\mathbf{1}_{cis}$, $\mathbf{2}_{trans}$, *and* $\mathbf{2}_{cis}$.

	$\mathbf{1}_{trans}$	$\mathbf{1}_{cis}$	$\mathbf{2}_{trans}$	$\mathbf{2}_{cis}$
$CHCl_3$:	0.73	22.35	0.60	20.31
CH_3Cl:	0.64	24.93	0.52	22.46
THF:	0.74	23.52	0.61	21.18
Water:	0.57	26.73	0.58	24.15

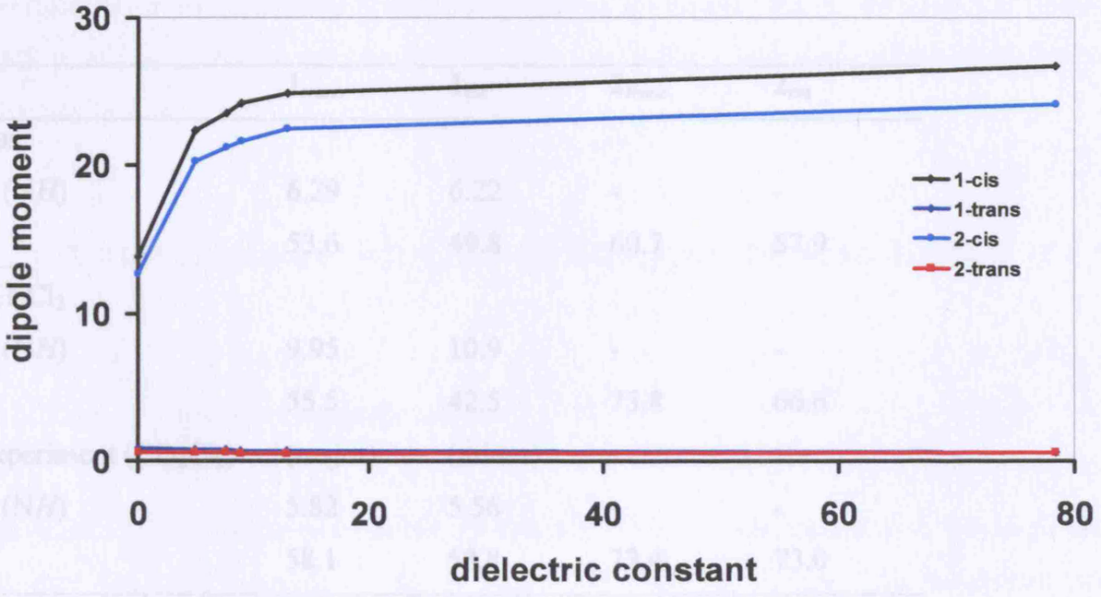

Figure 29. *Calculated dipole moments (Debye) in the gas phase and in different solvents for complexes* $\mathbf{1}_{trans}$, $\mathbf{1}_{cis}$, $\mathbf{2}_{trans}$, *and* $\mathbf{2}_{cis}$.

Table 18 and Figure 28 show that increasing the dielectric constant of the solvent (see section 3.2 for solvent parameters) stabilises the *cis* isomers relative to the *trans*, and Table 19 and Figure 29 that it also increases the dipole moments of the *cis* isomers. The *trans* isomers, however, do not show any clear correlation between the magnitudes of their dipole moments and the dielectric constant of the solvent. This indicates that the

stabilisation of the *cis* isomers, as the dielectric constant increases, is due to the increased magnitude of their dipole moments. ΔE of **1** is smaller than between the isomers of **2** in all calculations, except in the gas phase and CH_2Cl_2 calculations.

3.4.3 NMR Chemical Shifts

Table 20 presents calculated NMR chemical shifts of **1** and **2**.

Table 20. *Calculated NMR chemical shifts in the gas phase and CH_2Cl_2 solution, and experimental NMR chemical shifts for complexes $\mathbf{1}_{trans}$, $\mathbf{1}_{cis}$, $\mathbf{2}_{trans}$, and $\mathbf{2}_{cis}$.*

	$\mathbf{1}_{trans}$	$\mathbf{1}_{cis}$	$\mathbf{2}_{trans}$	$\mathbf{2}_{cis}$
Gas				
H (N*H*)	6.29	6.22	-	-
P	53.6	49.8	60.7	57.9
CH_2Cl_2				
H (N*H*)	9.95	10.9	-	-
P	55.5	42.5	75.8	66.6
Experiment (CD_2Cl_2)	(major)	(minor)		
H (N*H*)	5.82	5.56	-	-
P	58.1	58.8	73.4	73.0

Agreement between experiment and theory for the N*H* chemical shift is satisfying in the gas phase, but solvent model calculations overestimate the chemical shift. The calculated N*H* chemical shift of the *trans* isomer in the gas phase is slightly larger than of the *cis*, while the solvent model calculations show a larger chemical shift for the *cis* isomer. The calculated chemical shifts in the gas phase seem more reliable than those calculated with the solvent model; their absolute values and the difference between the isomers agree much better with experiment than the solvent model calculations do. The experimental N*H* chemical shift of the major isomer is slightly larger than the minor isomer (in agreement with the gas phase calculations); this is tentative evidence that the *trans* isomer is the major species. The solvent effect including calculations of the P chemical shifts show better

agreement with experiment than the gas phase calculations in all species except $\mathbf{1}_{cis}$. The difference between the calculated P chemical shifts of the isomers in the gas phase, however, agree better with experiment than the same property calculated with the solvent model. The calculated P chemical shifts are larger in $\mathbf{1}_{trans}$ compared with $\mathbf{1}_{cis}$, opposite to experiment. Calculations, however, reproduce the larger experimental shift of the *trans* isomer of **2** correctly, although the calculated differences between the isomers are too large.

In conclusion, calculations find the *trans* isomer to be more stable than the *cis*, although the *cis* isomer is stabilised by the inclusion of the solvent model; the higher the dielectric constant, the smaller the difference in energy between the isomers. The relative stabilisation of the *cis* isomer is probably due to its higher dipole moment. Calculated NMR chemical shifts are not accurate enough to draw any conclusions of which isomer is more stable in solution.

3.5 Comparison of U-N/O Bond Strength between 1 and 2

3.5.1 Energy Decomposition

I have divided all the compounds into two neutral, closed shell fragments to calculate and compare the bond strength of the N-donor and O-donor ligands. The fragments are Cy_3PNH and $UO_2Cl_2Cy_3PNH$ for **1**, and Cy_3PO and $UO_2Cl_2Cy_3PO$ for **2**. Table 21 shows calculated bond strengths for both U-N and U-O bonds at the optimised geometries; the results are the average values of the bond strengths. I have calculated bond strengths of the U-N and U-O bonds in $\mathbf{3}_{trans}$ in the same way as I have in **1** and **2**.

Table 21. *Energy decomposition of the U-N and U-O bonds (kJ/mol) in the gas phase for complexes $\mathbf{1}_{trans}$, $\mathbf{1}_{cis}$, $\mathbf{2}_{trans}$, $\mathbf{2}_{cis}$, and $\mathbf{3}_{trans}$. The bond strength and their decomposition are average values of the two bonds.*

	$\mathbf{1}_{trans}$	$\mathbf{1}_{cis}$	$\mathbf{2}_{trans}$	$\mathbf{2}_{cis}$	U-N in $\mathbf{3}_{trans}$	U-O in $\mathbf{3}_{trans}$
Electrostatic interaction	-304.3	-299.9	-217.3	-221.8	-305.9	-222.4
Pauli repulsion	315.2	316.8	217.3	227.6	313.5	230.9
Steric repulsion	10.9	16.9	0.0	5.8	7.6	8.5
Orbital interaction	-174.1	-174.4	-144.4	-145.7	-178.0	-146.2
Bond strength	-163.2	-157.5	-144.4	-139.9	-170.5	-137.7

Table 21 clearly shows that the U-N bonds are stronger than the U-O bonds; this is even more evident in the $\mathbf{3}_{trans}$ complex. The competition between the N-donor and O-donor ligands in $\mathbf{3}_{trans}$ favours the N-donor ligand; the U-N bond in $\mathbf{3}_{trans}$ is stronger than the average strength of the U-N bonds in $\mathbf{1}_{trans}$, and the U-O bond in $\mathbf{3}_{trans}$ is weaker than the average strength of the U-O bonds in $\mathbf{2}_{trans}$. The bonds in the *trans* isomers are about 5 kJ/mol stronger than the bonds in the *cis* isomers. The increased strength of the *trans* isomer seems to originate from a less repulsive steric interaction term, while the orbital interaction term is almost identical between the isomers. The magnitudes of the electrostatic interaction and the Pauli repulsion differ significantly between **1** and **2** as well as between the bonds in $\mathbf{3}_{trans}$. These differences, however, cancel out almost completely when the electrostatic interaction and the Pauli repulsion are added to yield the steric repulsion. The steric repulsion is therefore only approximately 10 kJ/mol larger in **1** for both isomers in comparison with **2**. The cancellation between electrostatic interaction and Pauli repulsion in $\mathbf{3}_{trans}$ is almost identical between the bonds; hence, the steric repulsions are similar. The significant stabilisation of the U-N bonds, in comparison with the U-O bonds, is due to the orbital interaction term. The difference in orbital interaction energy between $\mathbf{1}_{trans}$ and $\mathbf{2}_{trans}$ is similar to the same quantity for the U-N and U-O bonds in $\mathbf{3}_{trans}$. The increased difference in bond strength between the U-N and U-O bonds in $\mathbf{3}_{trans}$, compared with the difference between **1** and **2**, is therefore due to a smaller difference in steric repulsion – not increased orbital interaction in the U-N bond.

3.5.2 Mayer Bond Orders

Table 22 collects MBOs for all uranium bonds in **1** and **2**.

Table 22. *MBOs of the bonds to uranium, calculated in the gas phase for complexes* $\mathbf{1}_{trans}$, $\mathbf{1}_{cis}$, $\mathbf{2}_{trans}$, *and* $\mathbf{2}_{cis}$. *The MBOs are average values of the two bonds.*

	$\mathbf{1}_{trans}$	$\mathbf{1}_{cis}$	$\mathbf{2}_{trans}$	$\mathbf{2}_{cis}$
U-O_{yl}	2.03	2.04	2.06	2.04
U-N/O	0.47	0.43	0.39	0.36
U-Cl	0.88	0.96	0.91	0.97

The most striking result in Table 22 is that the U-N bonds have higher bond orders than the U-O bonds. The other bonds in **1** have slightly lower MBOs in comparison with **2**, it therefore appears that the U-O_{yl} and U-Cl bonds in **1** weaken slightly because of the stronger U-N bond. The U-N/O bonds have higher MBOs in the *trans* isomers compared with the *cis*, but the U-Cl bonds have higher MBOs in the *cis* isomer. The MBOs of the U-O_{yl} are higher in the *trans* than in the *cis* isomer for **2**, but the opposite is true for **1**. The differences between the U-O_{yl} bonds are, however, very small.

3.5.3 Molecular Orbital and Electron Density Analysis

MO analysis on large molecules without symmetry is often difficult because all AOs can, in principle, contribute to all MOs. Figure 30 shows the MOs with the greatest contributions to the U-N and U-O bonds in **1** and **2** respectively.

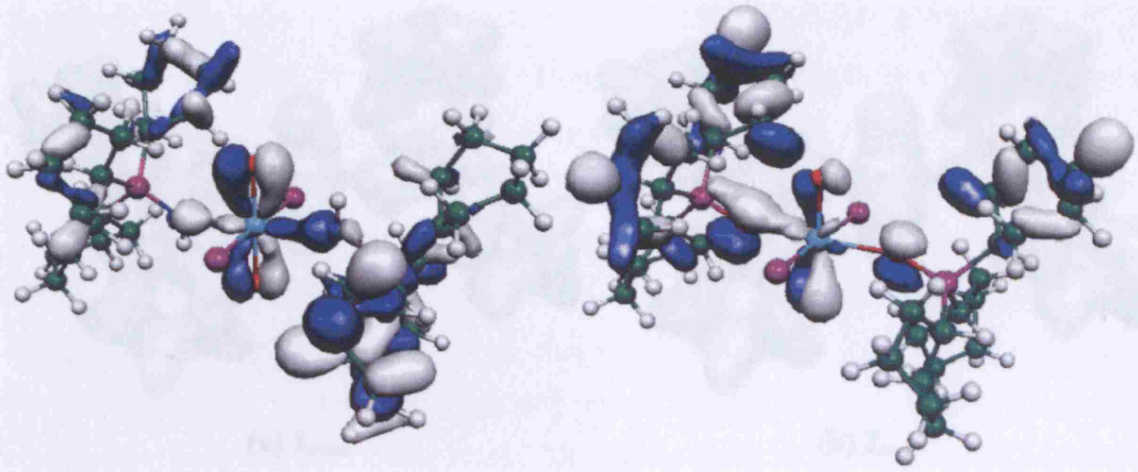

(a) HOMO-22 $\mathbf{1}_{trans}$ **(b) HOMO-28 $\mathbf{2}_{trans}$**

Figure 30(a)-(b). *(a) HOMO-22 for $\mathbf{1}_{trans}$, and (b) HOMO-28 for $\mathbf{2}_{trans}$, both calculated in the gas phase. The cutoff values are 0.03 for both MOs.*

The HOMO-22 of $\mathbf{1}_{trans}$ shows more interaction between U and the N-donor ligands, compared with the interaction between U and the O-donor ligands in HOMO-28 of $\mathbf{2}_{trans}$; the interaction between U and N in the HOMO-22 in $\mathbf{1}_{trans}$ has σ-character, while the HOMO-28 for $\mathbf{2}_{trans}$ has more π-character between U and the O-donor ligands. σ-bonds are, in general, more stable than π-bonds. Greater sigma donation from the N-donor ligands, in comparison with the O-donor ligands, is therefore a likely explanation for the greater orbital interaction contribution to the bond strength of U-N in **1**, although I do not find conclusive evidence for this.

Figure 31 shows isosurfaces with the same cutoff values of ρ for $\mathbf{1}_{trans}$ and $\mathbf{2}_{trans}$.

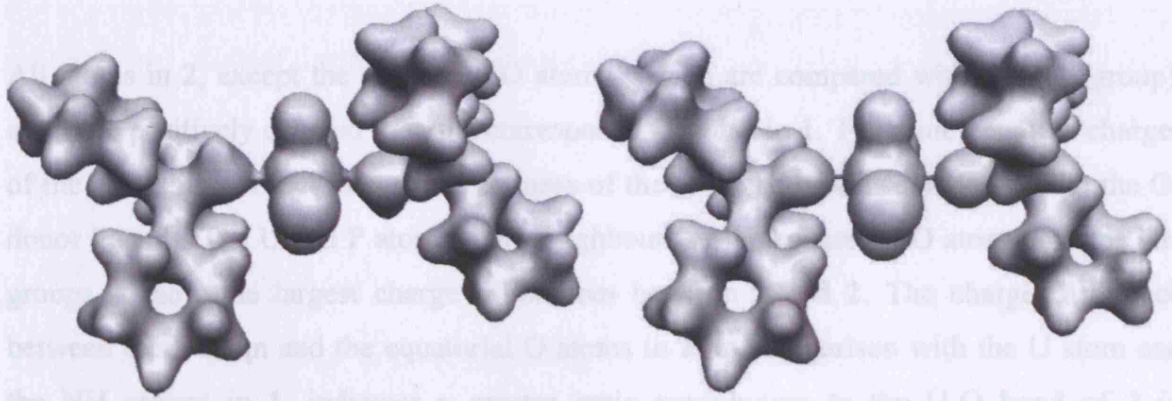

(a) $\mathbf{1}_{trans}$ (b) $\mathbf{2}_{trans}$

Figure 31(a)-(b). *Isosurface of ρ for (a) $\mathbf{1}_{trans}$, and (b) $\mathbf{2}_{trans}$, both calculated in the gas phase. The cutoff values are 0.07 for both species.*

It is evident that ρ is greater in the bonding region of $\mathbf{1}_{trans}$ in comparison with $\mathbf{2}_{trans}$, despite r(U-O) in $\mathbf{2}_{trans}$ being shorter than r(U-N) in $\mathbf{1}_{trans}$.

3.5.4 Hirshfeld Charges

Table 23 presents Hirshfeld charges for **1** and **2** in the gas phase. I have merged the atomic charges of the N and H atoms in **1**, to provide more relevant comparison to the equatorial O atoms in **2**.

Table 23. *Atomic charges (e^-) in the gas phase for complexes $\mathbf{1}_{trans}$, $\mathbf{1}_{cis}$, $\mathbf{2}_{trans}$, and $\mathbf{2}_{cis}$, calculated with the Hirshfeld scheme.*

	$\mathbf{1}_{trans}$	$\mathbf{1}_{cis}$	$\mathbf{2}_{trans}$	$\mathbf{2}_{cis}$
U:	0.59	0.59	0.63	0.63
O_{yl}:	-0.32	-0.31	-0.31	-0.30
NH/O:	-0.18	-0.18	-0.26	-0.26
Cl:	-0.26	-0.24	-0.24	-0.22
P	0.43	0.43	0.45	0.45

All atoms in **2**, except the equatorial O atoms (which are compared with the NH group), are more positively charged than the corresponding atoms in **1**. The more negative charges of the atoms in **1** reflect the greater softness of the N-donor ligands compared with the O-donor ligands. The U and P atoms – the neighbours of the equatorial O atoms and the NH groups – show the largest charge differences between **1** and **2**. The charge difference between the U atom and the equatorial O atoms in **2**, in comparison with the U atom and the NH groups in **1**, indicates a greater ionic contribution to the U-O bond of **2** in comparison with the U-N bond of **1**. The atoms with the greatest charge difference between the isomers are the Cl ligands; the *cis* isomer has a smaller magnitude of the charge. This is probably due to the increased repulsion between the chlorine ligands in the *cis* configuration. The reduced charges in the *cis* isomer correlate with higher MBOs of the U-Cl bond.

3.6 Extension to Other Halide Ligands and Hydride Ligands

I have extended the study of **1** and **2** to $UO_2Z_2(Cy_3PNH)_2$ and $UO_2Z_2(Cy_3PO)_2$ (Z = H, F, Br, or I) complexes, and an analogous experimental investigation is in progress in Manchester. I will refer to all these Z ligands as halide ligands for convenience, even though hydride ligands are not halides. The central questions in this section are:

1) How does the change of halide ligand affect the relative stabilities of the isomers?
2) How does the change of halide ligand affect the U-N and U-O bond strengths?

I introduce the notation $\mathbf{1}_{hal}$ and $\mathbf{2}_{hal}$ as a general description of complexes with the formula $UO_2Z_2(Cy_3PX)_2$ (Z = H, F, Cl, Br, or I; Cy = cyclohexyl; X = NH or O). I use the notation $\mathbf{1}_H$, $\mathbf{2}_H$, $\mathbf{1}_F$, $\mathbf{2}_F$, $\mathbf{1}_{Br}$, $\mathbf{2}_{Br}$, $\mathbf{1}_I$, and $\mathbf{2}_I$ for the specific complexes.

3.6.1 Bond Lengths and Bond Angles

Table 24 provides selected bond lengths and bond angles for both isomers of $\mathbf{1}_{hal}$ and $\mathbf{2}_{hal}$ in the gas phase.

Table 24. *Selected calculated bond lengths (Å) and angles (°) in the gas phase for complexes $\mathbf{1}_{hal,trans}$, $\mathbf{1}_{hal,cis}$, $\mathbf{2}_{hal,trans}$, and $\mathbf{2}_{hal,cis}$. The bond distances and bond angles are average values of the two bonds/bond angles (where applicable).*

	$\mathbf{1}_{hal,trans}$	$\mathbf{1}_{hal,cis}$	$\mathbf{2}_{hal,trans}$	$\mathbf{2}_{hal,cis}$
H-ligands				
U-O_{yl}	1.831	1.832	1.822	1.822
U-N/O	2.463	2.478	2.427	2.441
U-H	2.084	2.072	2.080	2.061
P-N/O	1.612	1.616	1.531	1.533
O_{yl}-U-O_{yl}	177.7	177.1	177.1	177.7
H-U-H	180.0	95.2	172.0	93.6
P-N/O-U	144.9	142.6	150.9	147.5
F-ligands				
U-O_{yl}	1.829	1.836	1.821	1.823
U-N/O	2.483	2.492	2.431	2.444
U-F	2.155	2.145	2.149	2.143
P-N/O	1.611	1.614	1.529	1.531
O_{yl}-U-O_{yl}	178.1	171.1	178.2	174.8
F-U-F	179.7	95.1	178.8	98.6
P-N/O-U	144.2	143.0	152.8	148.8

	$\mathbf{1}_{hal,trans}$	$\mathbf{1}_{hal,cis}$	$\mathbf{2}_{hal,trans}$	$\mathbf{2}_{hal,cis}$
Br-ligands				
U-O_{yl}	1.809	1.816	1.802	1.805
U-N/O	2.429	2.460	2.382	2.427
U-Br	2.855	2.821	2.840	2.804
P-N/O	1.622	1.623	1.538	1.537
O_{yl}-U-O_{yl}	177.2	171.0	178.2	174.2
Br-U-Br	175.6	89.0	176.6	88.3
P-N/O-U	145.9	145.0	155.9	152.4
I-ligands				
U-O_{yl}	1.807	1.813	1.799	1.804
U-N/O	2.417	2.448	2.370	2.421
U-I	3.104	3.071	3.084	3.048
P-N/O	1.627	1.626	1.539	1.540
O_{yl}-U-O_{yl}	176.9	171.8	179.1	175.0
I-U-I	174.7	85.3	177.0	85.2
P-N/O-U	147.5	145.5	160.4	153.4

The major trend as one traverses $\mathbf{1}_{hal}$ and $\mathbf{2}_{hal}$ is that *r*(U-halide) increases, and that *r*(U-O_{yl}) and *r*(U-N/O) decrease. I expect longer *r*(U-halide), because the size of the halides increases with increasing atomic number. The decreasing *r*(U-O_{yl}) and *r*(U-N/O) indicates strengthening of these bonds, probably at the expense of weaker U-halide bonds. $\mathbf{1}_{hal}$ have longer *r*(U-O_{yl}) and *r*(U-halide) than $\mathbf{2}_{hal}$ for all species; this indicates that the U-N bonds are stronger than the U-O bonds in all complexes.

Each *cis* isomer has longer *r*(U-O_{yl}) than the *trans* isomer, except the isomers of $\mathbf{2}_{H}$ which have identical *r*(U-O_{yl}); the differences between the isomers are slightly smaller in $\mathbf{2}_{hal}$ compared with $\mathbf{1}_{hal}$. All *cis* isomers have longer *r*(U-N) and shorter *r*(U-halide) than the *trans* isomers. Longer bond lengths decrease steric repulsion between the ligands; this is most likely the main reason *r*(U-N) is longer in the *cis* isomers.

The O_{yl}-U-O_{yl} bond angles are smaller in the *cis* isomers than in the *trans* isomers in all halide complexes, except $\mathbf{1}_H$ and $\mathbf{2}_H$. The small size (compared with Cl, Br, and I), and the low electronegativity (compared with F) of the hydride ligands are possible explanations for this. The halide-U-halide bond angles in the *cis* isomers decrease rapidly as the halide series is traversed; this is most likely because the F- and the H-ligands are small enough to get close to the N- and O-donor ligands, thereby reducing the steric repulsion between them. It is possible that $\mathbf{1}_H$, $\mathbf{2}_H$, $\mathbf{1}_F$, and $\mathbf{2}_F$ can coordinate more than four ligands, but I have investigated coordination of only four ligands, because this is a better comparison with the other halide complexes.

3.6.2 Total Bonding Energies and Dipole Moments

Table 25 and Figure 32 show ΔE values, and Table 26, Figure 33, and Figure 34 show dipole moments of $\mathbf{1}_{hal}$ and $\mathbf{2}_{hal}$; I include the data of **1** and **2** for comparison.

Table 25. *Calculated ΔE (kJ/mol) in the gas phase and with the solvent model for complexes $\mathbf{1}_{hal,trans}$, $\mathbf{1}_{hal,cis}$, $\mathbf{2}_{hal,trans}$, and $\mathbf{2}_{hal,cis}$. Positive ΔE values correspond to the trans isomer being more stable.*

	$\mathbf{1}_{hal}$	$\mathbf{2}_{hal}$
H-ligands		
Gas: ΔE	18.6	22.6
CH_2Cl_2: ΔE	9.8	18.0
F-ligands		
Gas: ΔE	6.6	11.3
CH_2Cl_2: ΔE	2.6	10.0
Cl-ligands		
Gas: ΔE	24.7	15.5
CH_2Cl_2: ΔE	8.8	7.1
Br-ligands		
Gas: ΔE	28.7	30.4
CH_2Cl_2: ΔE	11.0	17.9
I-ligands		
Gas: ΔE	35.0	38.2
CH_2Cl_2: ΔE	14.3	20.6

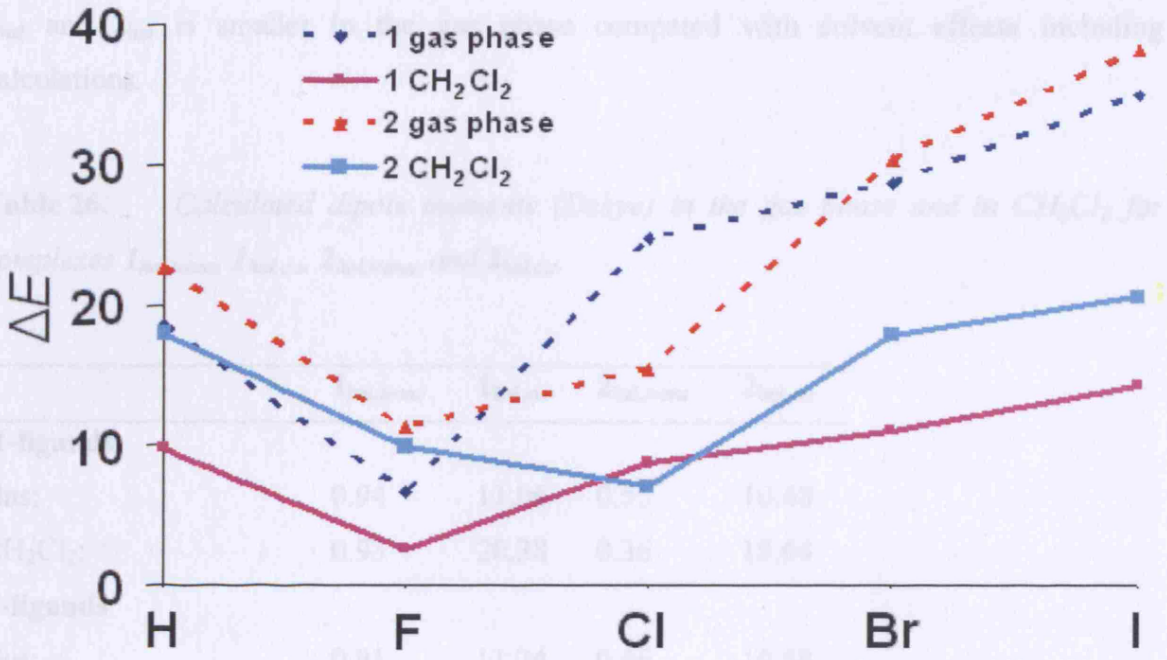

Figure 32. *Calculated ΔE (kJ/mol) in the gas phase and with the solvent model for complexes* $\mathbf{1}_{hal,trans}$, $\mathbf{1}_{hal,cis}$, $\mathbf{2}_{hal,trans}$ *and* $\mathbf{2}_{hal,cis}$. *Positive ΔE values correspond to the trans isomer being more stable.*

The *trans* isomer is more stable than the *cis* isomer in all complexes; $\mathbf{1}_F$ and $\mathbf{2}_F$ show the smallest ΔE values; ΔE increases as the halide ligands become heavier. A likely reason for the relative stabilisation of the *cis* isomer of $\mathbf{1}_F$ and $\mathbf{2}_F$ is that fluorine is the smallest of the halide ligands. The relative destabilisation of the *cis* isomer in the complexes with heavier halide ligands is likely to originate from their larger size.

Inclusion of solvent effects stabilises the *cis* isomer in all complexes; the stabilisation is greater in the complexes with heavier halides, and $\mathbf{1}_H$ and $\mathbf{2}_H$ stabilise more than $\mathbf{1}_F$ and $\mathbf{2}_F$. The high electronegativity of $\mathbf{1}_F$ and $\mathbf{2}_F$ should increase the solvent model's stabilising effects for the *cis* isomer. It is not clear why the solvent model stabilises the *cis* isomer of $\mathbf{1}_F$ and $\mathbf{2}_F$ less than the other halide compounds. The inclusion of the solvent model stabilises $\mathbf{1}_{hal}$ more than $\mathbf{2}_{hal}$.

ΔE is smaller in $\mathbf{1}_{hal}$ than $\mathbf{2}_{hal}$ in all complexes except **1** and **2**. The ΔE difference between $\mathbf{1}_{hal}$ and $\mathbf{2}_{hal}$ is smaller in the gas phase compared with solvent effects including calculations.

Table 26. *Calculated dipole moments (Debye) in the gas phase and in CH_2Cl_2 for complexes $\mathbf{1}_{hal,trans}$, $\mathbf{1}_{hal,cis}$, $\mathbf{2}_{hal,trans}$, and $\mathbf{2}_{hal,cis}$.*

	$\mathbf{1}_{hal,trans}$	$\mathbf{1}_{hal,cis}$	$\mathbf{2}_{hal,trans}$	$\mathbf{2}_{hal,cis}$
H-ligands				
Gas:	0.94	11.06	0.55	10.48
CH_2Cl_2:	0.93	20.38	0.36	18.64
F-ligands				
Gas:	0.91	11.24	0.46	10.58
CH_2Cl_2:	0.68	20.11	0.29	18.25
Cl-ligands				
Gas:	0.84	13.83	0.58	12.64
CH_2Cl_2:	0.66	24.25	0.54	21.61
Br-ligands				
Gas:	0.91	14.53	0.62	13.52
CH_2Cl_2:	0.85	25.01	0.63	22.91
I-ligands				
Gas:	0.99	16.20	0.64	14.59
CH_2Cl_2:	0.97	27.01	0.81	24.48

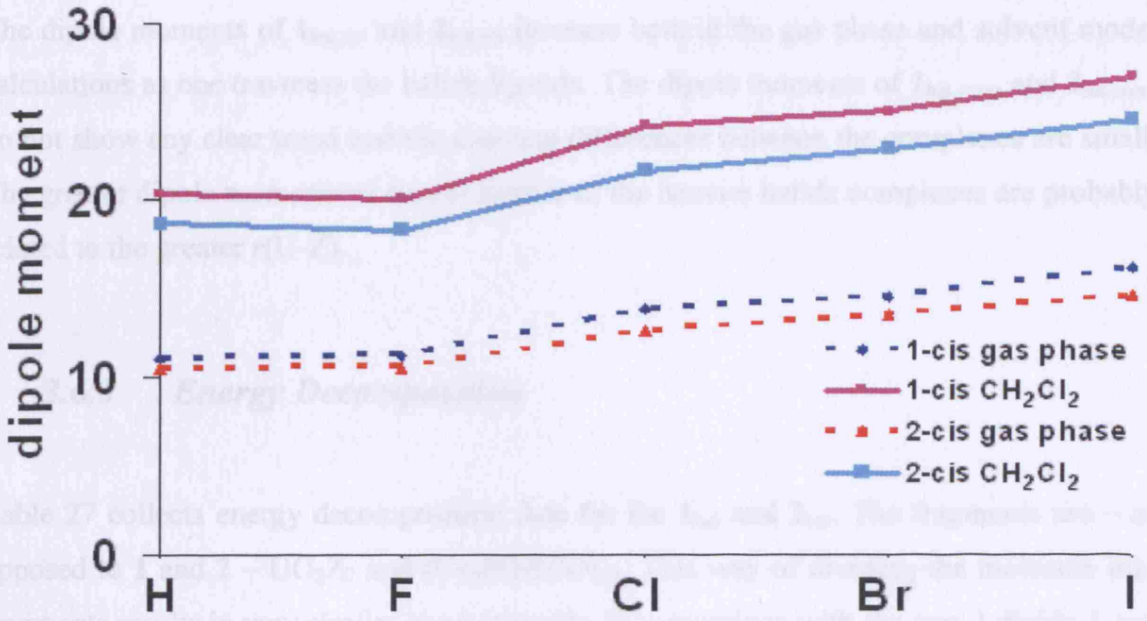

Figure 33. *Calculated dipole moments (Debye) in the gas phase and in CH_2Cl_2 for complexes $1_{hal,cis}$ and $2_{hal,cis}$.*

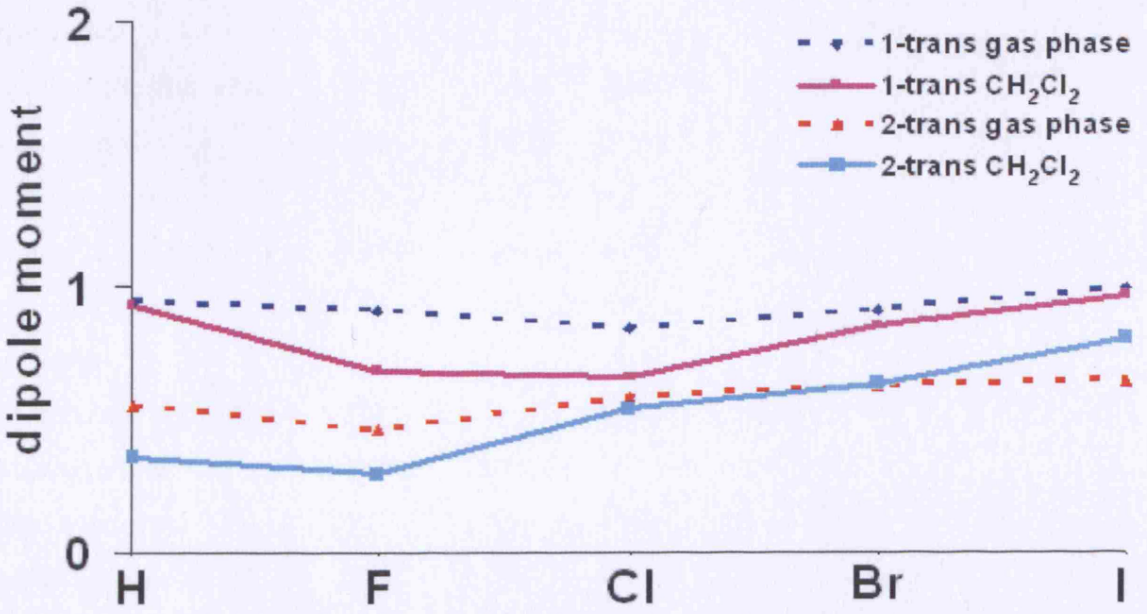

Figure 34. *Calculated dipole moments (Debye) in the gas phase and in CH_2Cl_2 for complexes $1_{hal,trans}$ and $2_{hal,trans}$.*

The dipole moments of $\mathbf{1}_{hal,cis}$ and $\mathbf{2}_{hal,cis}$ increase both in the gas phase and solvent model calculations as one traverses the halide ligands. The dipole moments of $\mathbf{1}_{hal,trans}$ and $\mathbf{2}_{hal,trans}$ do not show any clear trend and the absolute differences between the complexes are small. The greater dipole moments of the *cis* isomer of the heavier halide complexes are probably related to the greater r(U-Z).

3.6.3 Energy Decomposition

Table 27 collects energy decomposition data for the $\mathbf{1}_{hal}$ and $\mathbf{2}_{hal}$. The fragments are – as opposed to **1** and **2** – UO_2Z_2 and $(Cy_3P(NH/O))_2$. This way of dividing the molecule into fragments results in very similar bond strengths in comparison with the way I divide **1** and **2**.

Table 27. *Energy decomposition of the U-N and U-O bonds (kJ/mol) in the gas phase for complexes $\mathbf{1}_{hal,trans}$, $\mathbf{1}_{hal,cis}$, $\mathbf{2}_{hal,trans}$, and $\mathbf{2}_{hal,cis}$. The bond strengths and their decomposition are average values of the two bonds.*

	$\mathbf{1}_{hal,trans}$	$\mathbf{1}_{hal,cis}$	$\mathbf{2}_{hal,trans}$	$\mathbf{2}_{hal,cis}$
H-ligands				
Electrostatic interaction	-277.2	-291.6	-200.9	-221.5
Pauli repulsion	255.3	305.2	177.5	228.1
Steric repulsion	-21.9	13.6	-23.3	6.7
Orbital interaction	-148.7	-181.1	-121.9	-147.4
Bond strength	-170.6	-167.5	-145.2	-140.8
F-ligands				
Electrostatic interaction	-260.7	-275.4	-186.6	-203.7
Pauli repulsion	264.1	288.4	181.9	205.4
Steric repulsion	3.4	13.0	-4.7	1.8
Orbital interaction	-145.9	-161.7	-124.8	-137.3
Bond strength	-142.4	-148.7	-129.5	-135.5
Br-ligands				
Electrostatic interaction	-315.7	-309.0	-226.7	-224.6
Pauli repulsion	336.6	333.7	236.4	235.5
Steric repulsion	20.9	24.7	9.7	10.9
Orbital interaction	-195.0	-194.1	-165.3	-161.7
Bond strength	-174.2	-169.4	-155.6	-150.8
I-ligands				
Electrostatic interaction	-327.3	-319.8	-232.2	-230.5
Pauli repulsion	352.9	349.5	242.6	244.3
Steric repulsion	25.5	29.7	10.4	13.8
Orbital interaction	-207.2	-204.5	-172.5	-167.6
Bond strength	-180.9	-174.7	-162.1	-153.9

$\mathbf{1}_F$ and $\mathbf{2}_F$ show the weakest U-N and U-O bonds; the strength of these bonds increases with the size of the halide ligands. This increasing bond strength of the U-N and U-O bonds in

the complexes with heavier halides is due to their greater orbital interaction term. These bonds also show increased steric repulsion, although this term does not increase as much as the orbital interaction.

The U-N bonds of $\mathbf{1}_{hal}$ are stronger than the U-O bonds of $\mathbf{2}_{hal}$ in all complexes; the difference is smallest between the bonds of $\mathbf{1}_F$ and $\mathbf{2}_F$, and increases with the mass of the halide ligands. The greater strength of the U-N bond in comparison with the U-O bond is due to its greater orbital interaction. The steric repulsion is similar in $\mathbf{1}_H$ and $\mathbf{2}_H$, but increases faster for $\mathbf{1}_{hal}$ than $\mathbf{2}_{hal}$ as one traverses the halide complexes.

All *trans* isomers have stronger U-N and U-O bonds than the *cis* isomer, except in the $\mathbf{1}_F$ and $\mathbf{2}_F$ complexes. The explanation for the greater bond strength of the *cis* isomer, in comparison with the *trans* isomer, in $\mathbf{1}_F$ and $\mathbf{2}_F$ is the *cis* isomer's greater orbital interaction; the greater bond strength in the *cis* isomer partially explains the small ΔE value of $\mathbf{1}_F$ and $\mathbf{2}_F$. The bond strength differences between the isomers of the U-N and U-O bonds are largest in $\mathbf{1}_I$ and $\mathbf{2}_I$; the relative stabilisation of the bonds in the *trans* isomers is due to a relative increase of the orbital interaction term, compared with the *cis* isomer.

3.6.4 Mayer Bond Orders

Table 28 and Figure 35 present MBOs of the U-O_{yl}, U-halide, U-N, and U-O bonds for $\mathbf{1}_{hal,trans}$ and $\mathbf{2}_{hal,trans}$.

Table 28. *MBOs of the uranium bonds calculated in the gas phase for complexes $\mathbf{1}_{hal,trans}$ and $\mathbf{2}_{hal,trans}$. The MBOs are average values of the two bonds.*

	$\mathbf{1}_{hal,trans}$	$\mathbf{2}_{hal,trans}$
H-ligands		
U-O_{yl}	1.98	2.01
U-N/O	0.40	0.35
U-H	0.81	0.81
F-ligands		
U-O_{yl}	1.97	2.00
U-N/O	0.36	0.32
U-F	0.66	0.66
Cl-ligands		
U-O_{yl}	2.03	2.06
U-N/O	0.47	0.39
U-Cl	0.88	0.91
Br-ligands		
U-O_{yl}	2.04	2.07
U-N/O	0.49	0.41
U-Br	0.76	0.79
I-ligands		
U-O_{yl}	2.07	2.10
U-N/O	0.55	0.44
U-I	0.94	0.99

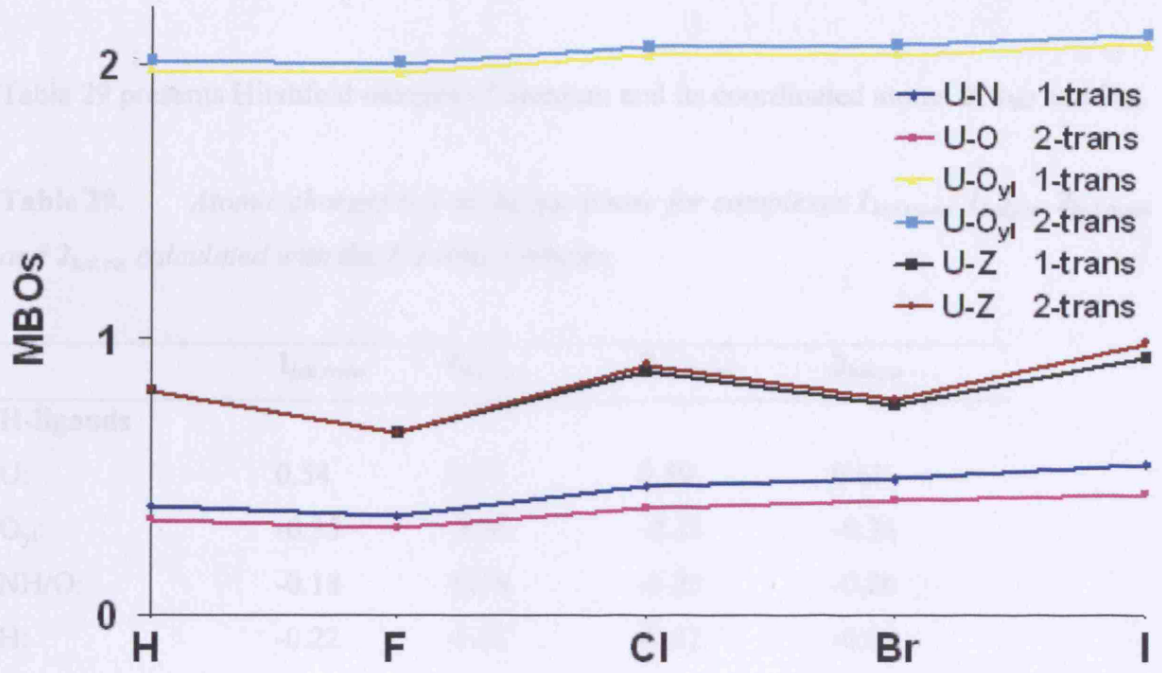

Figure 35. *MBOs of the uranium bonds calculated in the gas phase for complexes* $\mathbf{1}_{hal,trans}$ *and* $\mathbf{2}_{hal,trans}$. *The MBOs are average values of the two bonds.*

$\mathbf{1}_F$ and $\mathbf{2}_F$ show the lowest MBOs in all bonds for all complexes in Table 28; the MBOs increase as one traverses the series of halide complexes. The increase of the MBOs in the U-O_{yl} and U-N/O bonds, as one traverses the halide complexes, reflects that the heavier halide ligands are less electronegative. The increase of the MBOs in the U-halide bond is probably due to the increasing covalent contribution in the U-halide bond as one traverses the halide series – the covalent contribution increases despite the decrease in total bond strength. The MBOs of the U-N and U-O bonds are consistent with the bond lengths and energy decomposition that suggest stronger U-N and U-O bonds in the heavier halide complexes.

$\mathbf{2}_{hal,trans}$ have higher MBOs than $\mathbf{1}_{hal,trans}$ for the U-O_{yl} and U-halide bonds, and smaller MBOs for the U-O bonds (compared with the U-N bonds). This reflects the fact that the U-N bonds are stronger than the U-O bonds. The U-O_{yl} and U-halide bonds are weaker in $\mathbf{1}_{hal,trans}$, because they have more competition from the U-N bond than the same bonds have from the equatorial U-O bond in $\mathbf{2}_{hal,trans}$.

3.6.5 Hirshfeld Charges

Table 29 presents Hirshfeld charges of uranium and its coordinated atoms in $\mathbf{1}_{hal}$ and $\mathbf{2}_{hal}$.

Table 29. *Atomic charges (e^-) in the gas phase for complexes $1_{hal,trans}$, $1_{hal,cis}$, $2_{hal,trans}$, and $2_{hal,cis}$ calculated with the Hirshfeld scheme.*

	$\mathbf{1}_{hal,trans}$	$\mathbf{1}_{hal,cis}$	$\mathbf{2}_{hal,trans}$	$\mathbf{2}_{hal,cis}$
H-ligands				
U:	0.54	0.57	0.59	0.61
O_{yl}:	-0.35	-0.34	-0.35	-0.33
NH/O:	-0.18	-0.18	-0.25	-0.26
H:	-0.22	-0.21	-0.22	-0.21
F-ligands				
U:	0.67	0.70	0.71	0.73
O_{yl}:	-0.34	-0.33	-0.34	-0.33
NH/O:	-0.18	-0.19	-0.26	-0.26
F:	-0.30	-0.29	-0.30	-0.29
Cl-ligands				
U:	0.59	0.59	0.63	0.63
O_{yl}:	-0.32	-0.31	-0.31	-0.30
NH/O:	-0.18	-0.18	-0.26	-0.26
Cl:	-0.26	-0.24	-0.24	-0.22
Br-ligands				
U:	0.58	0.57	0.62	0.61
O_{yl}:	-0.32	-0.31	-0.31	-0.31
NH/O:	-0.18	-0.19	-0.26	-0.26
Br:	-0.24	-0.23	-0.23	-0.21
I-ligands				
U:	0.54	0.54	0.59	0.58
O_{yl}:	-0.31	-0.31	-0.31	-0.31
NH/O:	-0.18	-0.19	-0.26	-0.26
I:	-0.22	-0.22	-0.19	-0.18

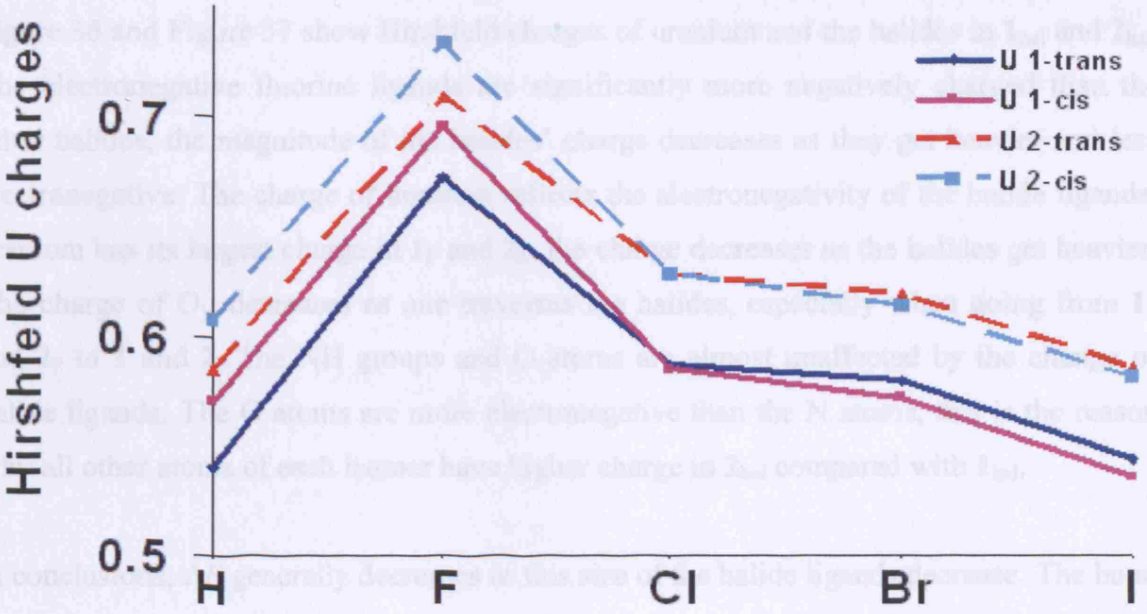

Figure 36. *Uranium atomic charges (e^-) in the gas phase for complexes $\mathbf{1}_{hal,trans}$, $\mathbf{1}_{hal,cis}$, $\mathbf{2}_{hal,trans}$, and $\mathbf{2}_{hal,cis}$ calculated with the Hirshfeld scheme.*

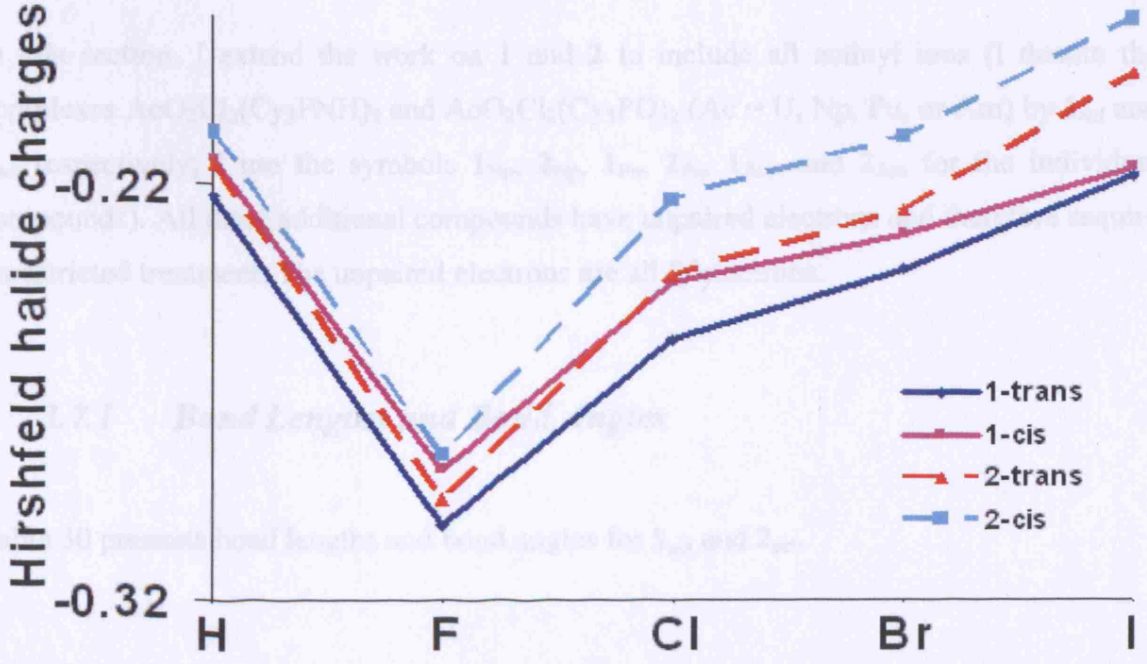

Figure 37. *Halide atomic charges (e^-) in the gas phase for complexes $\mathbf{1}_{hal,trans}$, $\mathbf{1}_{hal,cis}$, $\mathbf{2}_{hal,trans}$, and $\mathbf{2}_{hal,cis}$ calculated with the Hirshfeld scheme.*

Figure 36 and Figure 37 show Hirshfeld charges of uranium and the halides in $\mathbf{1}_{hal}$ and $\mathbf{2}_{hal}$. The electronegative fluorine ligands are significantly more negatively charged than the other halides, the magnitude of the halides' charge decreases as they get heavier and less electronegative. The charge of uranium reflects the electronegativity of the halide ligands; uranium has its largest charge in $\mathbf{1}_F$ and $\mathbf{2}_F$, the charge decreases as the halides get heavier. The charge of O_{yl} decreases as one traverses the halides, especially when going from $\mathbf{1}_F$ and $\mathbf{2}_F$ to **1** and **2**. The NH groups and O atoms are almost unaffected by the change of halide ligands. The O atoms are more electronegative than the N atoms; this is the reason why all other atoms of each isomer have higher charge in $\mathbf{2}_{hal}$ compared with $\mathbf{1}_{hal}$.

In conclusions, ΔE generally decreases as this size of the halide ligands decrease. The bond strengths between the U-N and the equatorial U-O bonds generally increase with the size of the halide ligands.

3.7 Extension to Np, Pu, and Am

In this section, I extend the work on **1** and **2** to include all actinyl ions (I denote the complexes $AcO_2Cl_2(Cy_3PNH)_2$ and $AcO_2Cl_2(Cy_3PO)_2$ (Ac = U, Np, Pu, or Am) by $\mathbf{1}_{act}$ and $\mathbf{2}_{act}$ respectively; I use the symbols $\mathbf{1}_{Np}$, $\mathbf{2}_{Np}$, $\mathbf{1}_{Pu}$, $\mathbf{2}_{Pu}$, $\mathbf{1}_{Am}$, and $\mathbf{2}_{Am}$ for the individual compounds). All these additional compounds have unpaired electrons and therefore require unrestricted treatment. The unpaired electrons are all 5*f* electrons.

3.7.1 Bond Lengths and Bond Angles

Table 30 presents bond lengths and bond angles for $\mathbf{1}_{act}$ and $\mathbf{2}_{act}$.

Table 30. *Selected calculated bond lengths (Å) and angles (°) in the gas phase for complexes* $\mathbf{1}_{act,trans}$, $\mathbf{1}_{act,cis}$, $\mathbf{2}_{act,trans}$, *and* $\mathbf{2}_{act,cis}$. *The bond distances and bond angles are average values of the two bonds/angles.*

	$\mathbf{1}_{act,trans}$	$\mathbf{1}_{act,cis}$	$\mathbf{2}_{act,trans}$	$\mathbf{2}_{act,cis}$
Np				
Np-O_{yl}	1.793	1.800	1.785	1.789
Np-N/O	2.429	2.453	2.373	2.417
Np-Cl	2.655	2.625	2.643	2.612
P-N/O	1.618	1.620	1.534	1.535
O_{yl}-Np-O_{yl}	178.5	173.8	179.0	176.5
Cl-Np-Cl	177.4	90.9	177.6	90.3
P-N/O-Np	146.3	145.0	155.6	151.3
Pu				
Pu-O_{yl}	1.780	1.786	1.771	1.775
Pu-N/O	2.412	2.433	2.377	2.405
Pu-Cl	2.656	2.633	2.638	2.618
P-N/O	1.619	1.621	1.532	1.534
O_{yl}-Pu-O_{yl}	178.7	176.6	179.1	178.4
Cl-Pu-Cl	177.1	91.3	177.5	89.9
P-N/O-Pu	145.9	144.4	154.6	150.8
Am				
Am-O_{yl}	1.780	1.786	1.773	1.776
Am-N/O	2.446	2.454	2.390	2.406
Am-Cl	2.671	2.656	2.644	2.642
P-N/O	1.618	1.621	1.533	1.530
O_{yl}-Am-O_{yl}	179.2	177.8	179.2	179.6
Cl-Am-Cl	171.6	93.4	177.7	94.4
P-N/O-Am	144.4	144.6	155.6	152.5

r(Ac-O_{yl}) decrease as the atomic number of the actinides increases, although the differences between the plutonium and americium complexes are small; the decrease of r(Ac-O_{yl}) is most likely due to the actinide contraction. r(Ac-N/O) and r(Ac-Cl) are almost constant over the actinide series, the difference between **1** and **2**, and $\mathbf{1}_{Am}$ and $\mathbf{2}_{Am}$ is within 0.03 Ångström.

The *cis* isomers have longer r(Ac-O_{yl}) and r(Ac-N/O), and shorter r(Ac-Cl) than the *trans* isomer in all complexes. This is also the case in $\mathbf{1}_{hal}$ and $\mathbf{2}_{hal}$; reduced steric repulsion between the N- and O-donor ligands in the *cis* isomer is probably the reason for this.

All metal bonds in $\mathbf{2}_{act}$ are shorter than in $\mathbf{1}_{act}$, similar to $\mathbf{1}_{hal}$ and $\mathbf{2}_{hal}$. This indicates that the N-donor ligands form stronger bonds than the O-donor ligands.

3.7.2 Total Bonding Energies and Dipole Moments

Table 31 and Figure 38 show ΔE values, and Table 32, Figure 39, and Figure 40 dipole moments of $\mathbf{1}_{act}$ and $\mathbf{2}_{act}$. The solvent effect including calculations use frozen core basis sets, because of SCF convergence problems with the all electron basis sets.

Table 31. *Calculated ΔE values (kJ/mol) in the gas phase and with the solvent model for complexes $\mathbf{1}_{act}$ and $\mathbf{2}_{act}$. Positive ΔE values correspond to the trans isomer being more stable.*

		$\mathbf{1}_{act}$	$\mathbf{2}_{act}$
Np			
Gas:	ΔE	25.9	27.4
CH_2Cl_2:	ΔE	12.4	12.7
Pu			
Gas:	ΔE	29.2	28.8
CH_2Cl_2:	ΔE	13.2	15.5
Am			
Gas:	ΔE	30.4	30.1
CH_2Cl_2:	ΔE	13.9	14.4

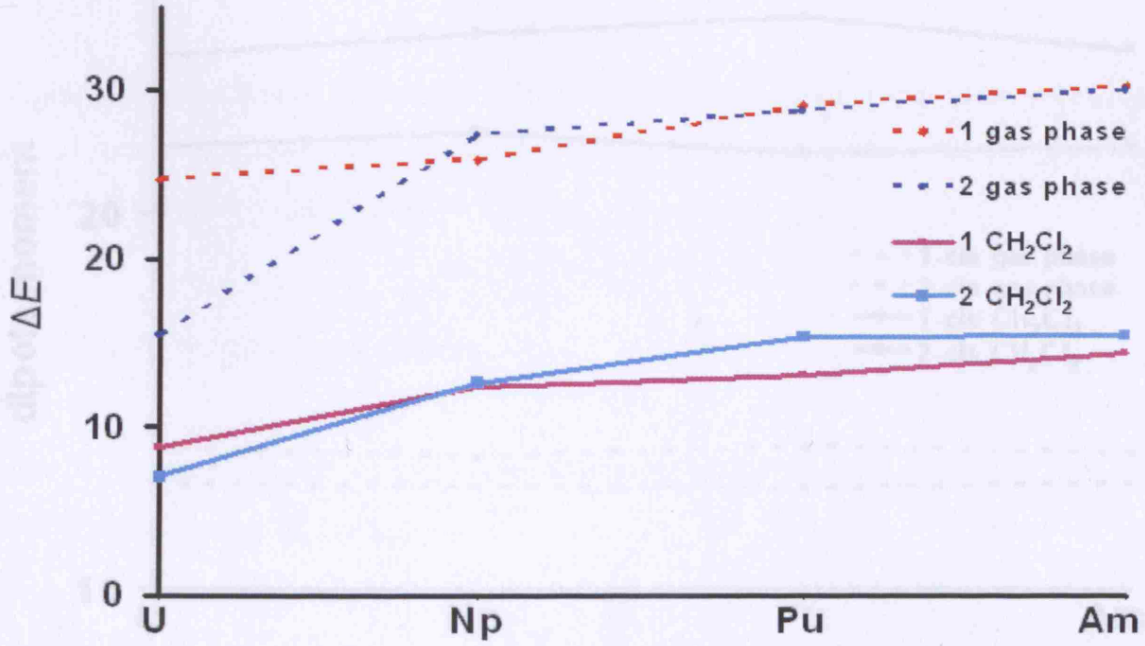

Figure 38. *Calculated ΔE values (kJ/mol) in the gas phase and with the solvent model for complexes $\mathbf{1}_{act}$ and $\mathbf{2}_{act}$. Positive ΔE values correspond to the trans isomer being more stable.*

Table 32. *Calculated dipole moments (Debye) in the gas phase and in CH_2Cl_2 for complexes $\mathbf{1}_{act,trans}$, $\mathbf{1}_{act,cis}$, $\mathbf{2}_{act,trans}$, and $\mathbf{2}_{act,cis}$.*

	$\mathbf{1}_{act,trans}$	$\mathbf{1}_{act,cis}$	$\mathbf{2}_{act,trans}$	$\mathbf{2}_{act,cis}$
Np				
Gas:	0.77	13.56	0.53	13.08
CH_2Cl_2:	0.73	24.83	0.56	22.16
Pu				
Gas:	0.75	13.82	0.52	12.72
CH_2Cl_2:	0.65	25.26	0.50	21.65
Am				
Gas:	1.01	13.62	0.55	12.83
CH_2Cl_2:	0.63	24.40	0.67	21.84

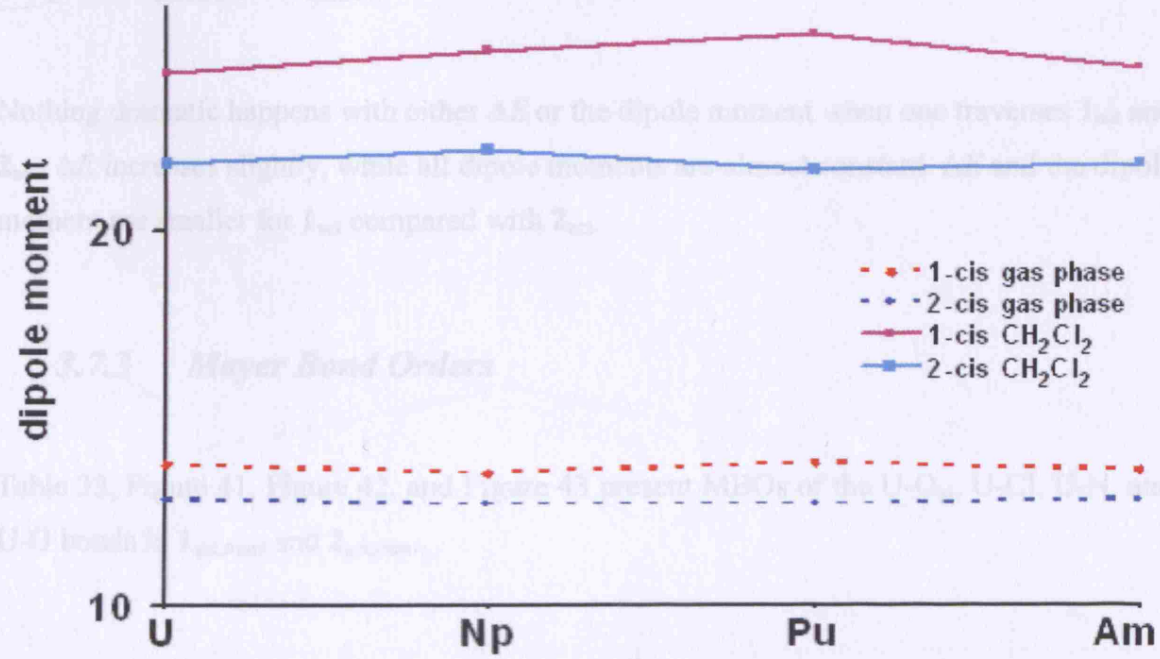

Figure 39. *Calculated dipole moments (Debye) in the gas phase and in CH_2Cl_2 for complexes $\mathbf{1}_{act,cis}$ and $\mathbf{2}_{act,cis}$.*

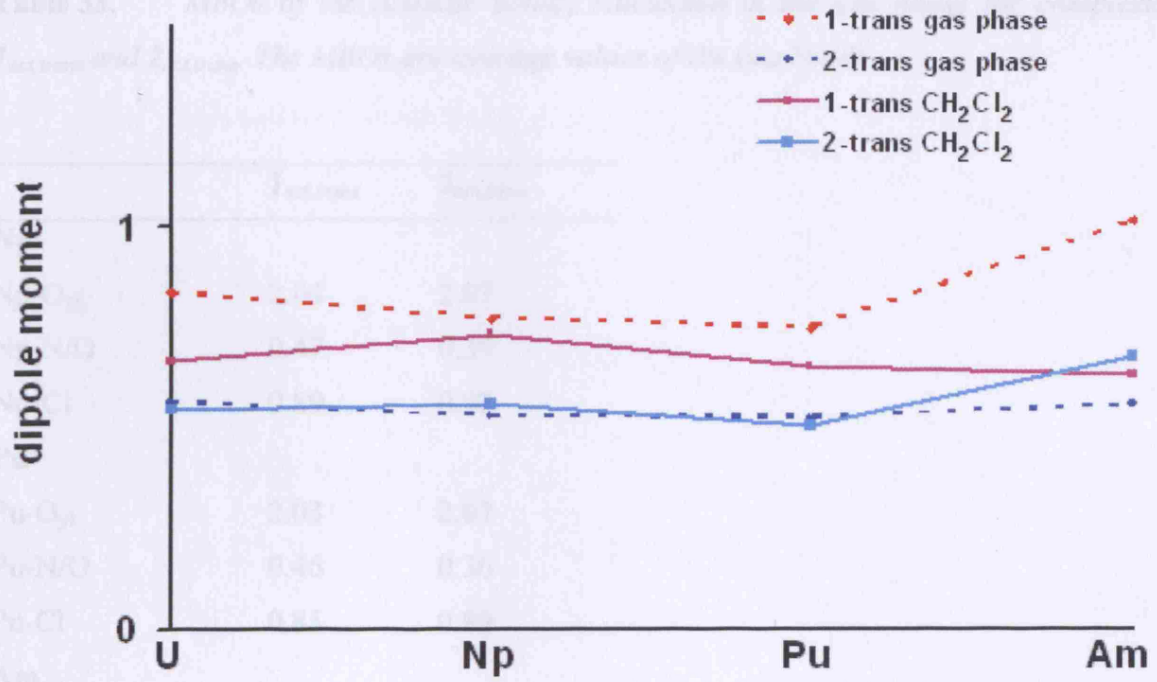

Figure 40. *Calculated dipole moments (Debye) in the gas phase and in CH_2Cl_2 for complexes $\mathbf{1}_{act,trans}$ and $\mathbf{2}_{act,trans}$.*

Nothing dramatic happens with either ΔE or the dipole moment when one traverses $\mathbf{1}_{act}$ and $\mathbf{2}_{act}$; ΔE increases slightly, while all dipole moments are almost constant. ΔE and the dipole moment are smaller for $\mathbf{1}_{act}$ compared with $\mathbf{2}_{act}$.

3.7.3 Mayer Bond Orders

Table 33, Figure 41, Figure 42, and Figure 43 present MBOs of the U-O_{yl}, U-Cl, U-N, and U-O bonds in $\mathbf{1}_{act,trans}$ and $\mathbf{2}_{act,trans}$.

Table 33. *MBOs of the actinide bonds, calculated in the gas phase for complexes* $\mathbf{1}_{act,trans}$ *and* $\mathbf{2}_{act,trans}$. *The MBOs are average values of the two bonds.*

	$\mathbf{1}_{act,trans}$	$\mathbf{2}_{act,trans}$
Np		
Np-O_{yl}	2.04	2.07
Np-N/O	0.47	0.39
Np-Cl	0.89	0.92
Pu		
Pu-O_{yl}	2.03	2.07
Pu-N/O	0.46	0.36
Pu-Cl	0.85	0.89
Am		
Am-O_{yl}	2.00	2.03
Am-N/O	0.42	0.33
Am-Cl	0.78	0.83

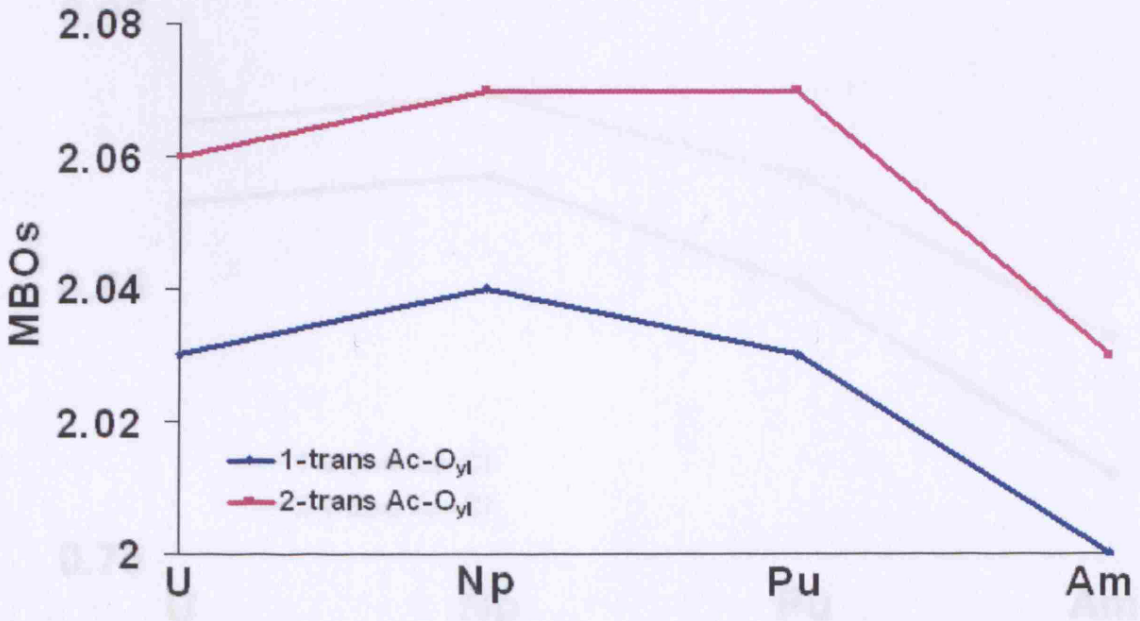

Figure 41. *MBOs of the actinyl bonds, calculated in the gas phase for complexes* $\mathbf{1}_{act,trans}$ *and* $\mathbf{2}_{act,trans}$. *The MBOs are average values of the two bonds.*

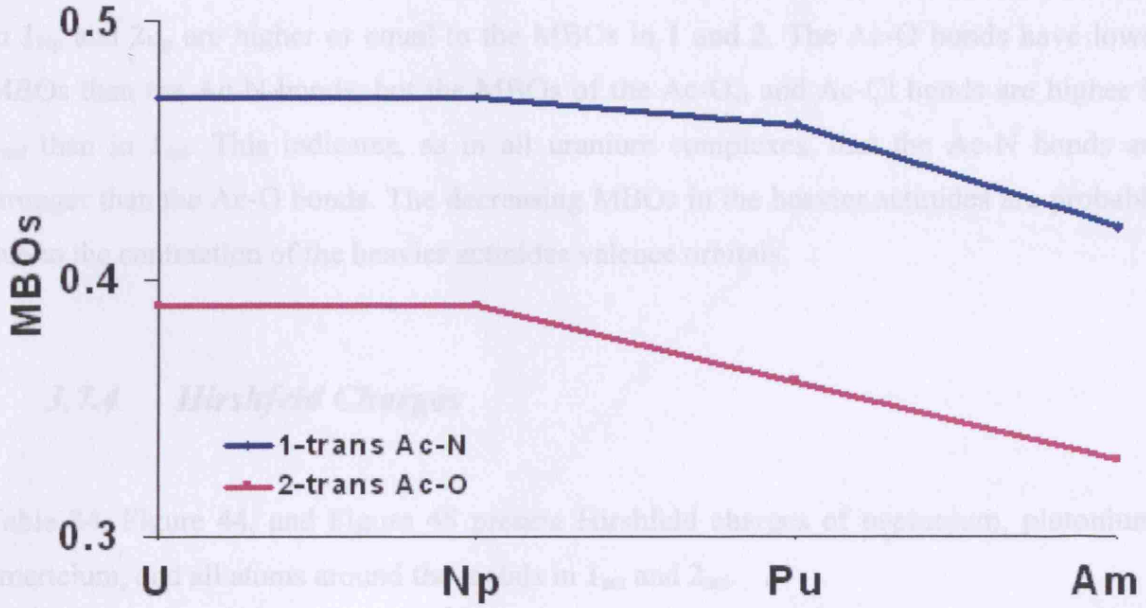

Figure 42. *MBOs of the actinyl bonds, calculated in the gas phase for complexes $1_{act,trans}$ and $2_{act,trans}$. The MBOs are average values of the two bonds.*

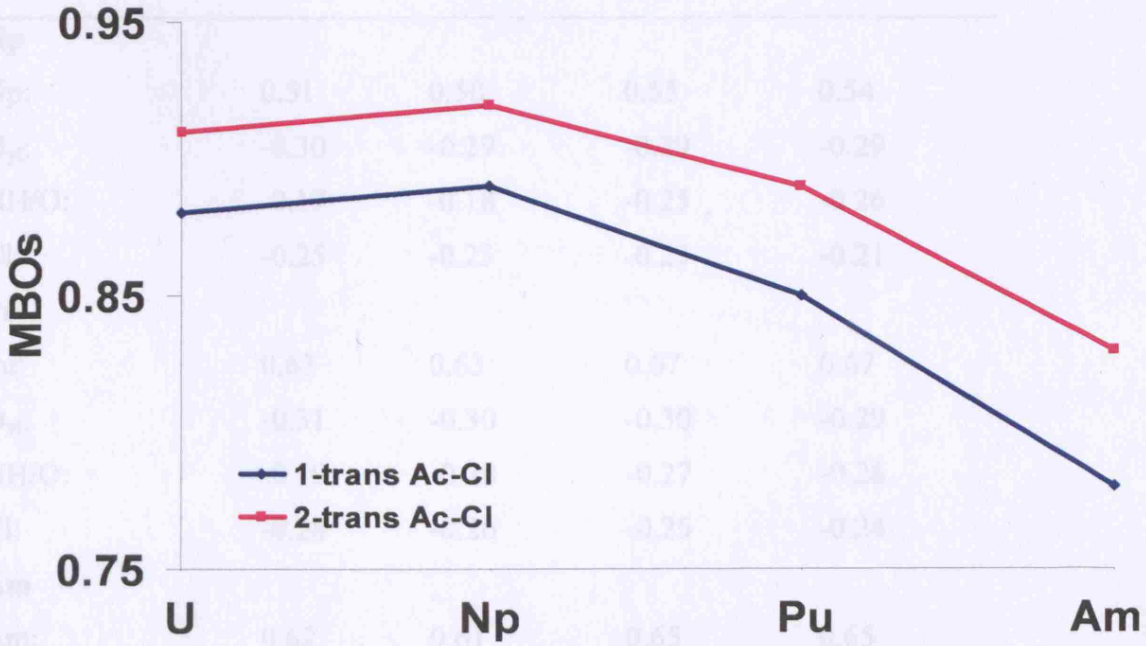

Figure 43. *MBOs of the actinyl bonds, calculated in the gas phase for complexes $1_{act,trans}$ and $2_{act,trans}$. The MBOs are average values of the two bonds.*

The MBOs of all bonds decrease when going from neptunium to americium, but the MBOs in $\mathbf{1}_{Np}$ and $\mathbf{2}_{Np}$ are higher or equal to the MBOs in **1** and **2**. The Ac-O bonds have lower MBOs than the Ac-N bonds, but the MBOs of the Ac-O_{yl} and Ac-Cl bonds are higher in $\mathbf{2}_{act}$ than in $\mathbf{1}_{act}$. This indicates, as in all uranium complexes, that the Ac-N bonds are stronger than the Ac-O bonds. The decreasing MBOs in the heavier actinides are probably due to the contraction of the heavier actinides valence orbitals.

3.7.4 Hirshfeld Charges

Table 34, Figure 44, and Figure 45 present Hirshfeld charges of neptunium, plutonium, americium, and all atoms around the metals in $\mathbf{1}_{act}$ and $\mathbf{2}_{act}$.

Table 34. *Atomic charges (e^-) in the gas phase for complexes $\mathbf{1}_{act,trans}$, $\mathbf{1}_{act,cis}$, $\mathbf{2}_{act,trans}$, and $\mathbf{2}_{act,cis}$ calculated with the Hirshfeld scheme. The charges are average values of the two atoms (where applicable).*

	$\mathbf{1}_{act,trans}$	$\mathbf{1}_{act,cis}$	$\mathbf{2}_{act,trans}$	$\mathbf{2}_{act,cis}$
Np				
Np:	0.51	0.50	0.55	0.54
O_{yl}:	-0.30	-0.29	-0.29	-0.29
NH/O:	-0.17	-0.18	-0.25	-0.26
Cl:	-0.25	-0.23	-0.23	-0.21
Pu				
Pu:	0.63	0.63	0.67	0.67
O_{yl}:	-0.31	-0.30	-0.30	-0.29
NH/O:	-0.19	-0.20	-0.27	-0.28
Cl:	-0.28	-0.26	-0.25	-0.24
Am				
Am:	0.62	0.61	0.65	0.65
O_{yl}:	-0.27	-0.26	-0.26	-0.25
NH/O:	-0.20	-0.20	-0.27	-0.28
Cl:	-0.28	-0.27	-0.27	-0.25

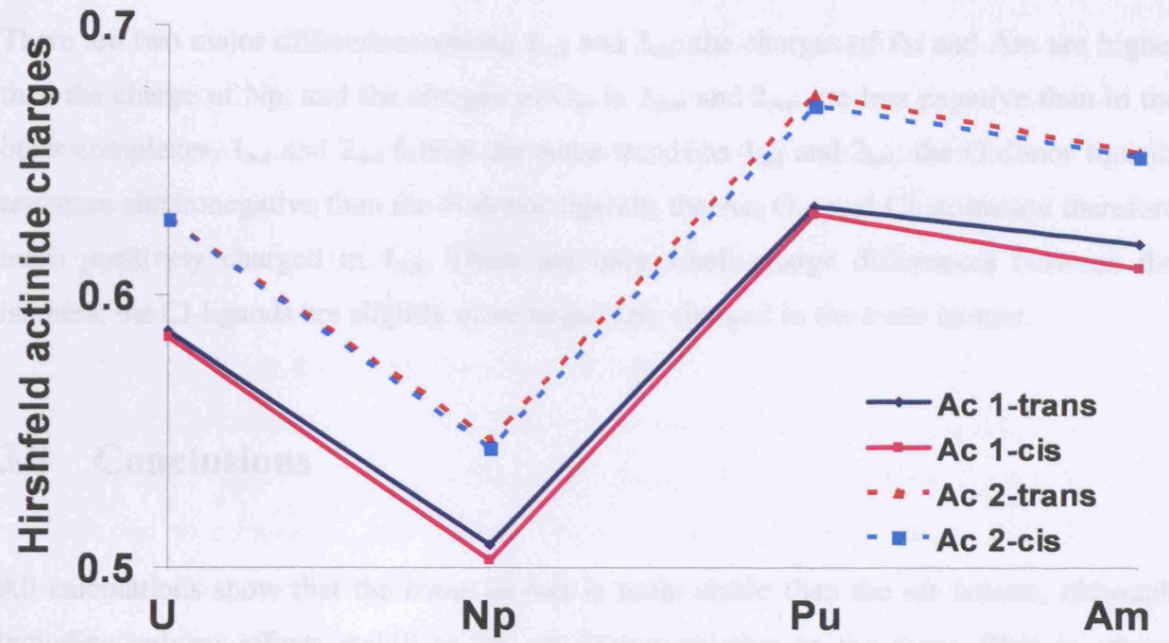

Figure 44. *Actinide atomic charges (e^-) in the gas phase for complexes $1_{act,trans}$, $1_{act,cis}$, $2_{act,trans}$, and $2_{act,cis}$ calculated with the Hirshfeld scheme.*

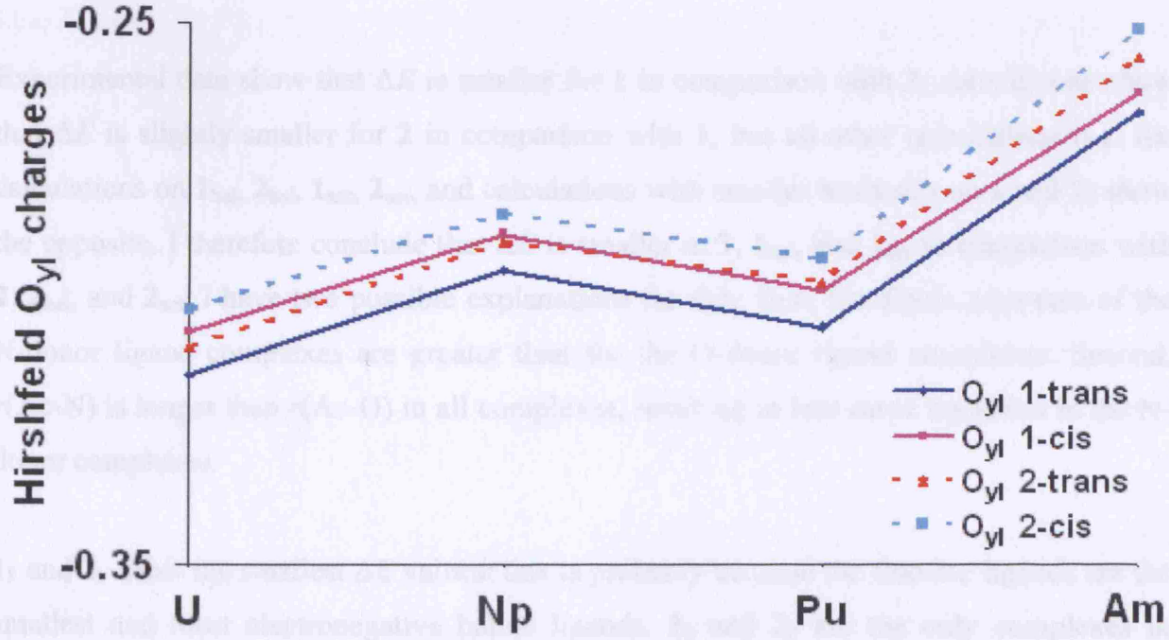

Figure 45. *O_{yl} atomic charges (e^-) in the gas phase for complexes $1_{act,trans}$, $1_{act,cis}$, $2_{act,trans}$, and $2_{act,cis}$ calculated with the Hirshfeld scheme.*

There are two major differences among $\mathbf{1}_{act}$ and $\mathbf{2}_{act}$: the charges of Pu and Am are higher than the charge of Np, and the charges of O_{yl} in $\mathbf{1}_{Am}$ and $\mathbf{2}_{Am}$ are less negative than in the other complexes. $\mathbf{1}_{act}$ and $\mathbf{2}_{act}$ follow the same trends as $\mathbf{1}_{hal}$ and $\mathbf{2}_{hal}$; the O-donor ligands are more electronegative than the N-donor ligands, the Ac, O_{yl}, and Cl atoms are therefore more positively charged in $\mathbf{1}_{act}$. There are only small charge differences between the isomers; the Cl-ligands are slightly more negatively charged in the *trans* isomer.

3.8 Conclusions

All calculations show that the *trans* isomer is more stable than the *cis* isomer, although including solvent effects stabilises the *cis* isomer relative to the *trans*. This is strong evidence that the *trans* isomers of **1** and **2** are the major isomers in solution. The greater dipole moment of the *cis* isomer explains why the solvent model stabilises it. It also explains why the *cis* isomer exists at all in solution, despite the anticipated increased repulsion between the large and bulky phosphine oxide and phosphinimine ligands in a *cis* configuration.

Experimental data show that ΔE is smaller for **1** in comparison with **2**; calculations show that ΔE is slightly smaller for **2** in comparison with **1**, but all other calculations (i.e. the calculations on $\mathbf{1}_{hal}$, $\mathbf{2}_{hal}$, $\mathbf{1}_{act}$, $\mathbf{2}_{act}$, and calculations with smaller basis sets on **1** and **2**) show the opposite. I therefore conclude that ΔE is smaller in **1**, $\mathbf{1}_{hal}$, and $\mathbf{1}_{act}$ in comparison with **2**, $\mathbf{2}_{hal}$, and $\mathbf{2}_{act}$. I have two possible explanations for this: first, the dipole moments of the N-donor ligand complexes are greater than for the O-donor ligand complexes. Second, r(Ac-N) is longer than r(Ac-O) in all complexes, resulting in less steric repulsion in the N-donor complexes.

$\mathbf{1}_F$ and $\mathbf{2}_F$ show the smallest ΔE values; this is probably because the fluorine ligands are the smallest and most electronegative halide ligands. $\mathbf{1}_F$ and $\mathbf{2}_F$ are the only complexes in which the U-N and U-O bonds are stronger in the *cis* isomer. The stabilisation of the *cis* isomer when the solvent model is included, however, is less significant in $\mathbf{1}_F$ and $\mathbf{2}_F$ in comparison with the other complexes, despite their high electronegativity.

The phosphinimine ligands form stronger bonds to uranium in comparison with phosphine oxide ligands; these stronger U-N bonds have larger covalent contributions than the U-O bonds. I support this conclusion with geometrical evidence, MBOs, and energy decomposition for all complexes, and additional MO analysis and total electron densities for **1** and **2**. I will consider further potential evidence in chapter 5.

The differences in bond strength between the U-N and U-O bonds are smallest between $\mathbf{1}_F$ and $\mathbf{2}_F$, and largest between $\mathbf{1}_H$ and $\mathbf{2}_H$. The most striking features between the components of the bond strength are that the difference in steric repulsion between $\mathbf{1}_H$ and $\mathbf{2}_H$ is the smallest for all complexes, and that the orbital interaction term does not stabilise $\mathbf{1}_F$ as much as the other complexes of $\mathbf{1}_{hal}$ in comparison with $\mathbf{2}_F$ and $\mathbf{2}_{hal}$ respectively. The large electronegativity of the fluorine ligands probably decreases the covalent part of the U-N bond in $\mathbf{1}_F$ more than the equatorial U-O bond in $\mathbf{2}_F$. The U-N and U-O bond strengths increase as one traverses the halide complexes; this is due to the weaker U-halide bonds in the heavier halide complexes.

Replacing U with Np, Pu, and Am does not produce any dramatic changes; $r(\text{Ac-O}_{yl})$ decreases slightly due to the actinide contraction, and ΔE increases slightly, as the actinide target complexes are traversed. $\mathbf{1}_{Np}$ and $\mathbf{2}_{Np}$ show the highest MBOs of $\mathbf{1}_{act}$ and $\mathbf{2}_{act}$.

Chapter 4

Is it Possible to Synthesise a *cis*-Uranyl Complex by Using $[C((CR_2)(CH_2)_2)(NHSi(CH_3)_3)(Ph_2PESiMe_3)_2]^-$ (R = H, CH_3, or $Si(CH_3)_3$; E = $NSi(CH_3)_3$, O, or S) Ligands?

4.1 Introduction

Sarsfield *et al.* [148] investigated uranium complexes with rare U-ligand bonding modes experimentally and computationally. The ligands in these complexes are anionic bis-iminophosphorano ligands $[CH(Ph_2PNSiMe_3)_2]^-$; these ligands form two U-N bonds and a U-C bond. This, however, requires the N atoms to form out-of-plane equatorial bonds (Figure 46). Both out-of-plane coordination and U-C bonds are rare in uranyl complexes.

Figure 46. *Boat conformation of the six membered chelate ring in the complexes investigated by Sarsfield et al. [148].*

This chapter considers whether the type of ligands shown in Figure 47 can force uranyl into a *cis* configuration. The ligands studied are similar to bis-iminophosphorano ligands, but have an additional carbon chain with a $NSiMe_3$ group at the end attached to the U-coordinating C atom. I investigate if this group can force one of the O_{yl} atoms from its position at the uranyl axis to the equatorial plane, thereby forming a *cis*-uranyl complex. The N atom at the end of the carbon chain will take the O_{yl} atom's place.

I will investigate how changing the equatorially coordinating $NSiMe_3$ groups of atoms to O and S atoms affects the stability of the *trans* uranyl complexes in comparison with the *cis* uranyl complexes. The type of ligands I investigate have the formula $C((CH_2)_3)NHSiMe_3)(Ph_2PESiMe_3)_2$ (E = $NSiMe_3$ ($\mathbf{I}_{L,N}$), O ($\mathbf{I}_{L,O}$), S ($\mathbf{I}_{L,S}$)). Figure 47 shows ball and stick representations of the ligands.

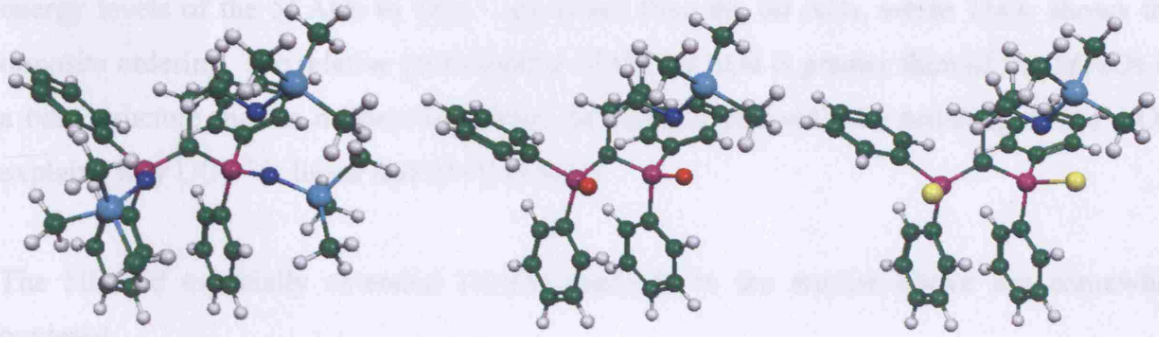

Figure 47. *Ball and stick representation of the following ligands: (a) $\mathbf{I}_{L,N}$, (b) $\mathbf{I}_{L,O}$, and (c) $\mathbf{I}_{L,S}$. The atoms have the following colours: N = dark blue, O = red, S = yellow, P = purple, Si = cyan, C = green, and H = white.*

There is room to coordinate one or two small ligands in addition to $\mathbf{I}_{L,N}$, $\mathbf{I}_{L,O}$, and $\mathbf{I}_{L,S}$ in the equatorial plane, depending on uranyl's conformation (*cis* or *trans*). Halide ligands coordinate that space in this work.

As mentioned in chapter 1, the uranyl ion is linear and very stable. The question why it adopts a linear *trans* arrangement – and not a bent *cis*, as many transition metal dioxo ions and ThO_2, has been the topic of several studies over the years. Tatsumi and Hoffmann [9]

compare MoO_2^{2+}, WO_2^{2+}, and VO_2^{+} (*cis* arrangements) with UO_2^{2+} by carrying out extended Hückel calculations. They conclude that the energies of linear and bent UO_2^{2+} are similar when the 6*p* AOs are treated in the core potential, but also that the linear configuration is clearly favoured when the 6*p* AOs are treated in the valence set. The corresponding 4*p* electrons in the transition metals, however, are more "core like" and do not show the same dramatic effect of stabilising the linear structure when they are included in the valence shell.

The extent of the effect of including the 6*p* AOs in the valence shell has, however, been questioned by Wadt [149]. He compares HF calculations on UO_2^{2+} with the isoelectronic ThO_2; the effects of the 6*p* AOs should be even more significant in ThO_2 than in UO_2^{2+}, because the energy of the 6*p* AOs are higher in ThO_2 than in UO_2^{2+} and should therefore show stronger interaction with the O_{yl} 2*p* AOs. ThO_2, however, is bent; Wadt suggests that the energy levels of the 5*f* and 6*d* AOs explain why UO_2^{2+} is linear and ThO_2 is bent. The energy levels of the 5*f* AOs in UO_2^{2+} are lower than the 6*d* AOs, while ThO_2 shows the opposite ordering. The relative participation of the 6*d* AOs is greater than of the 5*f* AOs in a bent structure than in a linear one. This, in combination with the ordering of the AOs, explains why UO_2^{2+} is linear and ThO_2 is bent.

The HF and especially extended Hückel methods in the studies above are somewhat outdated.

Schreckenbach *et al.* [140] compare *cis*- and *trans*-uranyl isomers of $[UO_2(OH)_4]^{2-}$, and conclude that the *cis*-uranyl isomers can play a role as intermediates in the ligand exchange process (chapter 1). The *cis*-uranyl structures are 18-19 kcal/mol (~75-80 kJ/mol) higher in energy than the *trans*-uranyl structures. The article also suggests that the inclusion of a solvent model can stabilise the *cis*-uranyl isomer further.

Until very recently, no *cis*-uranyl compound had been synthesised; the closest attempt was the oxo-imido complexes in references [150, 151]. These complexes have the general formula $(\eta^5\text{-}C_5(Me_3)_5)_2U(NR)O$ (R = 2,4,6-$Me_3C_6H_2$, 2,6-i-$Pr_2C_6H_3$, or 2,6-t-$Bu_2C_6H_3$; Me = methyl; Pr = propyl; Bu = butyl). In July of 2007, however, a communication by Vaughn *et al.* was published on the web [152]. The content of this communication is the synthesis

of a polymer that contains the uranyl unit in a *cis* configuration. The polymer is produced by letting uranyl acetate react with two equivalent of ferrocenecarboxylic acid (fccH) and add either THF or 2-methylTHF (Scheme 2). The polymer has the formula $[UO_2(fcdc)(THF)\cdot(Fc)]_n$ (fcdc = ferrocenedicarboxylate, Fc = ferrocene, and THF = tetrahydrofuran).

Scheme 2. *Formation of the cis-uranyl polymer [152].*

The O_{yl}-U-O_{yl} bond angle in the polymer is only 69.5(6)°, considerably smaller than observed computationally in the *cis*-uranyl transition states of $[UO_2(OH)_4]^{2-}$, and experimentally in transition metal dioxo compounds.

4.2 Computational Details

The ADF suit of programmes was employed to perform DFT calculations with the PBE xc-functional on all compounds. TZP ZORA frozen core basis sets were employed for all atoms except C and H for which DZP ZORA frozen core were employed. The 1*s* AOs were frozen in the C, N, O, and F basis sets, all AOs up to 2*p* for S and P, and the U basis set had all AOs up to 5*d* frozen. The integration parameter was set to 5, the geometry optimisation convergence criterion was 0.001 a.u. $Å^{-1}$, and the SCF convergence criterion was 10^{-7}. The ZORA accounted for scalar relativistic effects. The COSMO with the SES accounted for solvent effects with the same values of the atomic radii as in chapter 3 (the atomic radius of Si = 2.2 Å). The values for the solvent radius and dielectric constant (of CH_2Cl_2) are: r = 2.27 Å and ε = 8.93.

4.3 Geometries of the Complexes with a Single Carbon Chain

Figure 48 presents the optimised geometries of $UO_2F_2C((CH_2)_3NHSiMe_3)(Ph_2PESiMe_3)_2$ ($\mathbf{I}_{trans}$) (E = $NSiMe_3$ ($\mathbf{I}_{N,trans}$), O ($\mathbf{I}_{O,trans}$), or S ($\mathbf{I}_{S,trans}$)) and $UO_2FC((CH_2)_3NSiMe_3)(Ph_2PESiMe_3)_2$ ($\mathbf{I}_{cis}$) (E = $NSiMe_3$ ($\mathbf{I}_{N,cis}$), O ($\mathbf{I}_{O,cis}$), or S ($\mathbf{I}_{S,cis}$)).

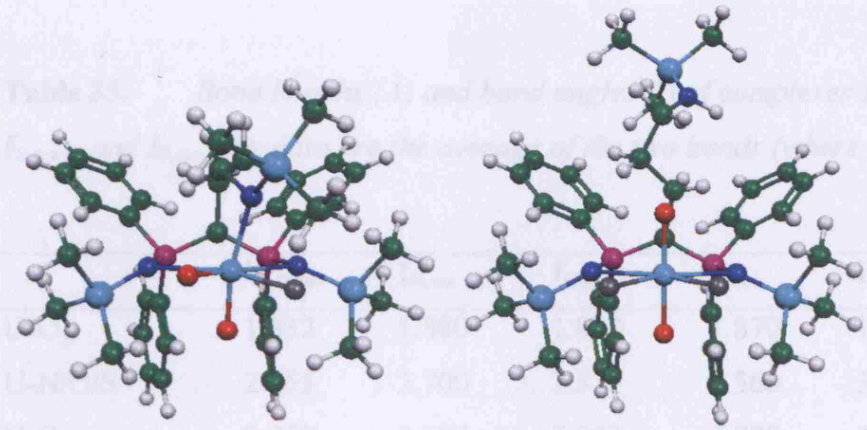

(a) $I_{N,cis}$ (b) $I_{N,trans}$

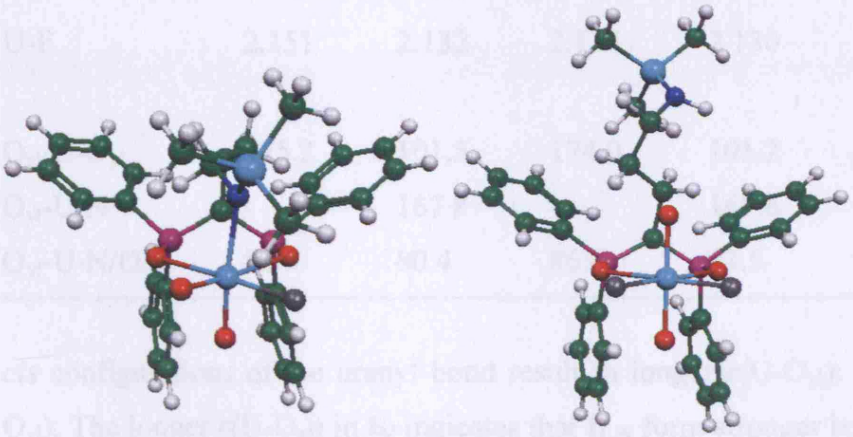

(c) $I_{O,cis}$ (d) $I_{O,trans}$

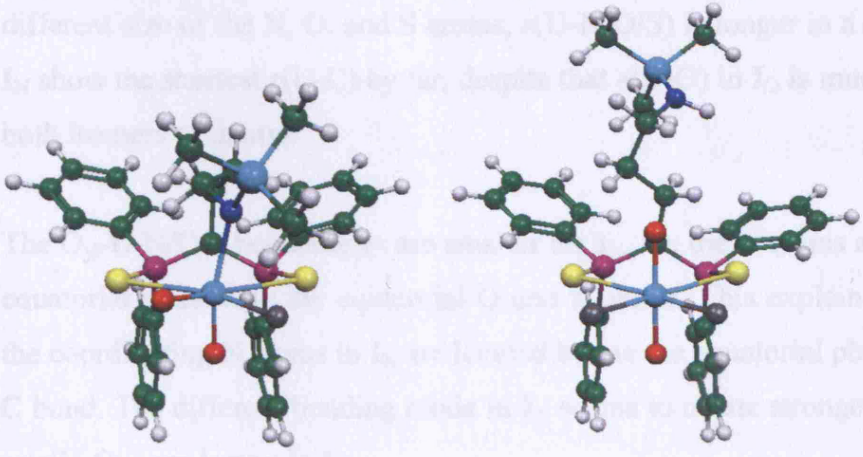

(e) $I_{S,cis}$ (f) $I_{S,trans}$

Figure 48(a)-(f). *Ball and stick representation of complexes (a) $I_{N,cis}$, (b) $I_{N,trans}$, (c) $I_{O,cis}$, (d) $I_{O,trans}$, (e) $I_{S,cis}$, and (f) $I_{S,trans}$ in the gas phase.*

Table 35 provides bond lengths and bond angles for $\mathbf{I}_N$, $\mathbf{I}_O$, and $\mathbf{I}_S$.

Table 35. *Bond lengths (Å) and bond angles (°) of complexes $I_{N,trans}$, $I_{N,cis}$, $I_{O,trans}$, $I_{O,cis}$, $I_{S,trans}$, and $I_{S,cis}$. The data are the average of the two bonds (where applicable).*

	$\mathbf{I}_{N,trans}$	$\mathbf{I}_{N,cis}$	$\mathbf{I}_{O,trans}$	$\mathbf{I}_{O,cis}$	$\mathbf{I}_{S,trans}$	$\mathbf{I}_{S,cis}$
U-O_{yl}	1.832	1.880	1.828	1.870	1.823	1.869
U-N/O/S	2.655	2.700	2.511	2.560	3.008	3.051
U-C	3.053	3.189	3.953	3.887	4.261	3.578
U-N	-	2.261	-	2.266	-	2.256
U-F	2.151	2.132	2.134	2.130	2.124	2.120
O_{yl}-U-O_{yl}	175.2	101.5	174.0	101.2	173.5	105.5
O_{yl}-U-N	-	167.8	-	169.6	-	162.8
O_{yl}-U-N/O/S	82.6	80.4	86.6	83.5	86.9	81.3

cis configurations of the uranyl bond result in longer r(U-O_{yl}); $\mathbf{I}_N$ have the longest r(U-O_{yl}). The longer r(U-O_{yl}) in $\mathbf{I}_N$ indicates that $\mathbf{I}_{L,N}$ form stronger bonds with uranyl than $\mathbf{I}_{L,O}$ and $\mathbf{I}_{L,S}$. The r(U-N/O/S) differences between $\mathbf{I}_N$, $\mathbf{I}_O$, and $\mathbf{I}_S$ are most likely due to the different size of the N, O, and S atoms, r(U-N/O/S) is longer in a *cis*-uranyl configuration. $\mathbf{I}_N$ show the shortest r(U-C) by far, despite that r(U-O) in $\mathbf{I}_O$ is much shorter than r(U-N) in both isomers of uranyl.

The O_{yl}-U-N/O/S bond angles are smaller for $\mathbf{I}_N$, i.e. the N atoms are further away from the equatorial plane than the equatorial O and S atoms. This explains the short r(U-C) in $\mathbf{I}_N$; the coordinating N atoms in $\mathbf{I}_N$ are located below the equatorial plane to form a stronger U-C bond. The different bonding mode in $\mathbf{I}_N$ seems to create stronger bonds than in $\mathbf{I}_O$ and $\mathbf{I}_S$ as r(U-O_{yl}) are longer in $\mathbf{I}_N$.

I have also optimised complexes of $\mathbf{I}_O$ and $\mathbf{I}_S$ with other halide ligands, but I do not show the geometries or provide the bond distances and bond angles of those compounds.

4.4 Energy Differences between the Isomers in the Complexes with Single Carbon Chains

$\mathbf{I}_{cis}$ is not an isomer of $\mathbf{I}_{trans}$, because $\mathbf{I}_{trans}$ has a fluorine and hydrogen atom more than $\mathbf{I}_{cis}$. I therefore compare the total bonding energy of $\mathbf{I}_{trans}$ (E_{trans}) with the total bonding energy of $\mathbf{I}_{cis}$ (E_{cis}) plus a HF molecule (E_{HF}), i.e. $\Delta E = E_{cis} + E_{HF} - E_{trans}$.

Table 36 shows ΔE values for $\mathbf{I}_N$, $\mathbf{I}_O$, and $\mathbf{I}_S$, and how ΔE depends on the equatorial halide ligands in $\mathbf{I}_O$ and $\mathbf{I}_S$.

Table 36. *ΔE (kJ/mol) calculated in the gas phase for complexes I_N, I_O, and I_S.*

Ligands	F	Cl	Br	I
N-donor	217.5	-	-	-
O-donor	214.7	218.2	-	-
S-donor	212.9	217.1	228.4	232.8

ΔE is very large, independent of donor type ligands. Increasing the size of the halide ligands destabilises $\mathbf{I}_{cis}$ relative to $\mathbf{I}_{trans}$.

4.5 Geometries of Complexes with CH_3 and $Si(CH_3)_3$ Groups

How can I stabilise $\mathbf{I}_{cis}$ relative to $\mathbf{I}_{trans}$? Figure 48 shows that $\mathbf{I}_{cis}$ has free space in the area where $\mathbf{I}_{trans}$ locates the carbon chain. An additional group of atoms between the phenyl rings (above the equatorial plane) is therefore likely to result in greater increase of steric repulsion in $\mathbf{I}_{trans}$ relative to $\mathbf{I}_{cis}$. I consider two additional groups: CH_3 and $Si(CH_3)_3$. I denote these complexes $\mathbf{I}_{CH3,trans}$, $\mathbf{I}_{CH3,cis}$, $\mathbf{I}_{Si(CH3)3,trans}$, and $\mathbf{I}_{Si(CH3)3,cis}$.

Figure 49 displays the geometries of $\mathbf{I}_{O,Si(CH3)3,trans}$ and $\mathbf{I}_{O,Si(CH3)3,cis}$; these complexes are selected to give an idea about the geometry of the complexes with additional CH_3 and $Si(CH_3)_3$ groups. The phenyl rings are closer to the equatorial plane in $\mathbf{I}_{O,Si(CH3)3,trans}$.

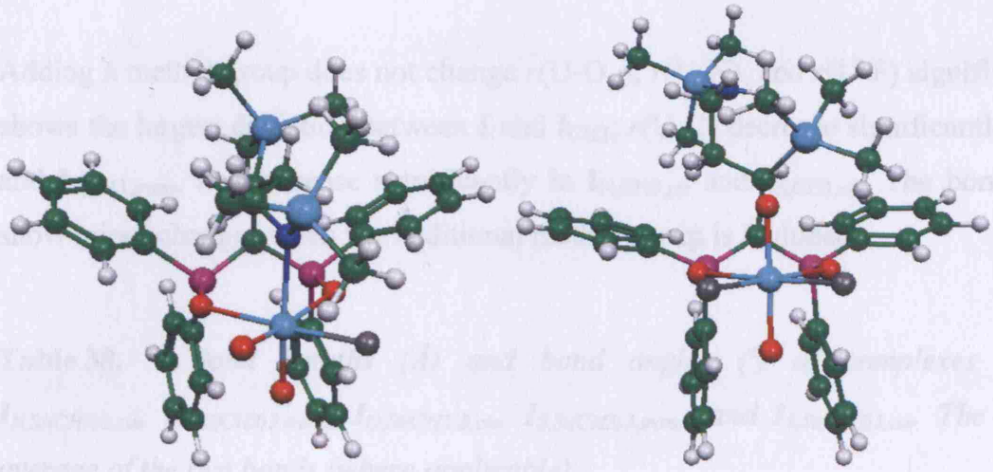

Figure 49(a)-(b). *Ball and stick representation of complexes (a) $I_{N,Si(CH3)3,cis}$ and (b) $I_{N,Si(CH3)3,trans}$ in the gas phase.*

Table 37 presents bond lengths and bond angles for $I_{N,CH3,trans}$, $I_{N,CH3,cis}$, $I_{O,CH3,trans}$, $I_{O,CH3,cis}$, $I_{S,CH3,trans}$, and $I_{S,CH3,cis}$.

Table 37. *Bond lengths (Å) and bond angles (°) of complexes $I_{N,CH3,trans}$, $I_{N,CH3,cis}$, $I_{O,CH3,trans}$, $I_{O,CH3,cis}$, $I_{S,CH3,trans}$, and $I_{S,CH3,cis}$. The data are the average of the two bonds (where applicable).*

	$I_{N,CH3}$		$I_{O,CH3}$		$I_{S,CH3}$	
	trans	*cis*	*trans*	*cis*	*trans*	*cis*
U-O_{yl}	1.830	1.878	1.826	1.871	1.827	1.868
U-N/O/S	2.714	2.683	2.629	2.532	3.031	3.071
U-C	3.005	3.370	3.510	3.984	3.622	3.761
U-N	-	2.257	-	2.271	-	2.251
U-F	2.148	2.131	2.122	2.134	2.120	2.120
O_{yl}-U-O_{yl}	175.2	101.5	176.0	101.0	174.2	105.8
O_{yl}-U-N	-	168.3	-	169.8	-	162.5
O_{yl}-U-N/O/S	81.4	81.3	84.4	83.9	84.9	82.1

Adding a methyl group does not change r(U-O_{yl}), r(U-N), and r(U-F) significantly. r(U-C) shows the largest deviation between **I** and $\mathbf{I}_{CH3}$; r(U-C) decrease significantly in $\mathbf{I}_{O,CH3,trans}$ and $\mathbf{I}_{S,CH3,trans}$, and increase significantly in $\mathbf{I}_{N,CH3,cis}$ and $\mathbf{I}_{S,CH3,cis}$. The bond angles only show minor changes when the additional methyl group is included.

Table 38. *Bond lengths (Å) and bond angles (°) of complexes* $I_{N,Si(CH3)3,trans}$, $I_{N,Si(CH3)3,cis}$, $I_{O,Si(CH3)3,trans}$, $I_{O,Si(CH3)3,cis}$, $I_{S,Si(CH3)3,trans}$, *and* $I_{S,Si(CH3)3,cis}$. *The data are the average of the two bonds (where applicable).*

	$\mathbf{I}_{N,Si(CH3)3}$		$\mathbf{I}_{O,Si(CH3)3}$		$\mathbf{I}_{S,Si(CH3)3}$	
	trans	*cis*	*trans*	*cis*	*trans*	*cis*
U-O_{yl}	1.834	1.877	1.826	1.872	1.821	1.867
U-N/O/S	2.692	2.649	2.508	2.503	3.011	3.045
U-C	2.916	3.515	4.034	4.062	4.736	3.930
U-N	-	2.265	-	2.279	-	2.256
U-F	2.150	2.134	2.135	2.139	2.125	2.120
O_{yl}-U-O_{yl}	175.6	100.8	175.5	100.4	176.8	105.1
O_{yl}-U-N	-	169.3	-	170.6	-	163.1
O_{yl}-U-N/O/S	82.6	82.3	87.9	84.5	89.3	82.4

The most striking feature of $\mathbf{I}_{Si(CH3)3}$ is the increase of r(U-C) in $\mathbf{I}_{S,Si(CH3)3,trans}$ and $\mathbf{I}_{S,Si(CH3)3,cis}$. r(U-C) in $\mathbf{I}_{O,Si(CH3)3,trans}$ is also increasing rapidly in comparison with $\mathbf{I}_{O,CH3,trans}$, but is similar to $\mathbf{I}_{O,trans}$. r(U-C) is increasing in $\mathbf{I}_{N,Si(CH3)3,cis}$, but decreasing in $\mathbf{I}_{N,Si(CH3)3,trans}$ in comparison with $\mathbf{I}_{N,CH3,cis}$ and $\mathbf{I}_{N,cis}$, and $\mathbf{I}_{N,CH3,trans}$ and $\mathbf{I}_{N,trans}$ respectively.

4.6 Energy Differences between the Isomers in Complexes with Additional CH_3, and $Si(CH_3)_3$ Groups

Table 39 presents ΔE values for $\mathbf{I}_{N,CH3}$, $\mathbf{I}_{O,CH3}$, and $\mathbf{I}_{S,CH3}$.

Table 39. *ΔE (kJ/mol) in the gas phase for complexes $I_{N,CH3}$, $I_{O,CH3}$, and $I_{S,CH3}$.*

	$\mathbf{I}_{N,CH3}$	$\mathbf{I}_{O,CH3}$	$\mathbf{I}_{S,CH3}$
ΔE	193.0	164.7	188.6

ΔE decreases, as expected, when the methyl group is added. $\mathbf{I}_{O,CH3}$, in particular, shows a small ΔE value.

Table 40 presents ΔE values for $\mathbf{I}_{N,Si(CH3)3}$, $\mathbf{I}_{O,Si(CH3)3}$, and $\mathbf{I}_{S,Si(CH3)3}$.

Table 40. *ΔE (kJ/mol) in the gas phase for complexes $I_{N,Si(CH3)3}$, $I_{O,Si(CH3)3}$, and $I_{S,Si(CH3)3}$.*

Ligands	F	Cl	Br
N-donor	145.6	-	-
O-donor	156.2	155.6	-
S-donor	157.7	155.7	162.3

The large and bulky $Si(CH_3)_3$ group decreases ΔE more than the methyl group; $\mathbf{I}_{N,Si(CH3)3}$ show the smallest ΔE value. Increased atomic weight of the halides destabilises $\mathbf{I}_{Si(CH3)3,cis}$, although not as much as heavier halides destabilise $\mathbf{I}_{cis}$.

Is it possible to stabilise $\mathbf{I}_{cis}$ even more by including a third group of atoms? I have optimised complexes with two additional groups CH_3 or $Si(CH_3)_3$ groups, or a combination of the two groups to investigate this ($\mathbf{I}_{CH3+CH3}$, $\mathbf{I}_{Si(CH3)3+CH3}$, and $\mathbf{I}_{Si(CH3)3+Si(CH3)}$). Table 41

shows ΔE values for those compounds; it shows that $\mathbf{I}_{S,Si(CH3)3,cis}$ is destabilised by 10-40 kJ/mol relative to $\mathbf{I}_{S,Si(CH3)3,trans}$ when I include an additional carbon chain. Including more additional groups therefore does not seem to be a way to find a *cis*-uranyl complex more stable than a *trans*-uranyl compound.

Table 41. *ΔE (kJ/mol) in the gas phase for complexes* $\boldsymbol{I}_{S,CH3+CH3}$, $\boldsymbol{I}_{S,Si(CH3)3+CH3}$, *and* $\boldsymbol{I}_{S,Si(CH3)3+Si(CH3)3}$.

	$CH_3 + CH_3$	$CH_3 + Si(CH_3)_3$	$Si(CH_3)_3 + Si(CH_3)_3$
S-donor	190.9	172.2	197.3

I have optimised $\mathbf{I}_N$, $\mathbf{I}_{N,CH3}$, $\mathbf{I}_{N,Si(CH3)3}$, and $\mathbf{I}_{S,Si(CH3)3}$ with the COSMO solvent model, I report the ΔE values in Table 42.

Table 42. *ΔE (kJ/mol) calculated with the COSMO solvent model for complexes* $\boldsymbol{I}_N$, $\boldsymbol{I}_{N,CH3}$, $\boldsymbol{I}_{N,Si(CH3)3}$, *and* $\boldsymbol{I}_{S,Si(CH3)3}$.

Ligands	I	I_{CH3}	$I_{Si(CH3)3}$
N-donor	223.9	189.9	145.7
S-donor	-	-	141.7

$\mathbf{I}_{S,Si(CH3)3}$ show a smaller ΔE value with the solvent model than in the gas phase, while ΔE deviate little between the gas phase and the solvent model for the N-donor complexes. ΔE is still, however, almost twice as high as in the article of Schreckenbach *et al.* It is therefore unlikely that changing the ligands more will stabilise $\mathbf{I}_{cis}$ enough to be more stable than $\mathbf{I}_{trans}$.

4.7 Conclusions

The results in this chapter strongly suggest it is not possible to synthesise *cis*-uranyl complexes by using $\mathbf{I}_{L,N}$, $\mathbf{I}_{L,O}$, and $\mathbf{I}_{L,S}$ ligands, even if they are modified with additional CH_3 and $Si(CH_3)_3$ groups. I obtain the lowest ΔE value for $\mathbf{I}_{N,Si(CH3)3}$ in the gas phase, and for $\mathbf{I}_{S,Si(CH3)3}$ with the solvent model, but both $\mathbf{I}_{N,Si(CH3)3,cis}$ and $\mathbf{I}_{S,Si(CH3)3,cis}$ are much more unstable than $\mathbf{I}_{N,Si(CH3)3,trans}$ and $\mathbf{I}_{S,Si(CH3)3,trans}$.

I do not find the combination of equatorial U-C and U-O/S out-of-plane bonds in the O- and S-donor complexes. The $\mathbf{I}_{L,O}$ and $\mathbf{I}_{L,S}$ ligands form U-O/S bonds in the equatorial plane, and r(U-C) in those complexes are longer than for the $\mathbf{I}_{L,N}$ ligands. $r(U\text{-}O_{yl})$ is longer in $\mathbf{I}_N$ than in $\mathbf{I}_O$ and $\mathbf{I}_S$; this indicates that $\mathbf{I}_{L,N}$ forms stronger bonds to U than the $\mathbf{I}_{L,O}$ and $\mathbf{I}_{L,S}$ ligands.

Chapter 5

Exploring Actinyl Bonding through Electron Localisation and Density Difference Techniques

5.1 Introduction

In this chapter, I will use $\Delta\rho$ and electron localisation indicators on the systems studied in chapters 2 and 3, mainly to provide more detail regarding covalent bonding in the equatorial plane, and how this affects actinyl bonding. I will also study some new neptunyl systems, not discussed elsewhere in this thesis. The chapter will, however, start with an investigation on some small systems, to illustrate where electrons are localised in simple light molecules, and to compare these systems with uranium complexes. I will also compare the description of localisation in DFT with CCSD calculations.

Electron localisation studies on systems that contain heavy atoms like transition metals and lanthanides are scarce [153, 154]. There is, to the best of my knowledge, only one electron localisation study on actinides [155], and that study focus mostly on actinide experiments. It is the purpose of this chapter to apply those non-standard $\Delta\rho$ and electron localisation analysis tools to *f* element systems.

5.2 Computational Details

5.2.1 Computational Details in Section 5.3 and 5.4

5.2.1.1 Density Functional Theory Calculations in ADF

The DFT calculations in section 5.3 and 5.4 used the PBE xc-functionals with a TZ2P ZORA all electron basis set on all atoms. The integration parameter was set to 5 for geometry optimisations, and the geometry and SCF convergence criteria are 0.001 a.u. $Å^{-1}$ and 10^{-7} respectively. Scalar relativistic effects are incuded by the ZORA. The fragments in the $\Delta\rho$ calculations in section 5.4 are UO_2^{2+} and the equatorial ligands respectively.

5.2.1.2 Coupled Cluster Singles and Doubles and Hartree-Fock Calculations in Gaussian 03

6-31G** basis sets were assigned to all atoms except uranium that used a (14*s* 13*p* 10*d* 8*f* 6*g*) [10*s* 9*p* 5*d* 4*f* 3g] segmented valence basis set with a relativistic pseudo potential of the Stuttgart-Bonn variety. The integration grid assigned (keyword "ultrafine") is pruned for all atoms from H to Kr (but not pruned for heavier elements) with 99 radial shells and a maximum of 590 angular points each.

5.2.2 Computational Details in Section 5.5

The DFT calculations in section 5.5 used the PBE xc-functionals with a TZP ZORA all electron basis set on all atoms except the C and H atoms that used DZP ZORA all electron basis sets. The integration parameter was set to 5 for geometry optimisations, and the geometry and SCF convergence criteria are 0.001 a.u. $Å^{-1}$ and 10^{-7} respectively. Scalar relativistic effects are incuded by the ZORA. The calculations on the systems with

unpaired electrons are treated unrestricted. The fragments in the $\Delta\rho$ calculations in section 5.5 are UO_2^{2+} and the equatorial ligands respectively.

5.2.3 Computational Details in Section 5.6

All complexes in section 5.6 used TZP all electron basis sets. All complexes were divided in neutral fragments to calculate $\Delta\rho$. $\mathbf{Np}_{tri}$ was divided into two fragments: NpO_2Cl_2 ($\mathbf{Np}_{tri,small}$) and $(NpO_2Cl_2(THF)_3)_2$ ($\mathbf{Np}_{tri,large}$); $\mathbf{Np}_{tet}$ into two fragments: $NpCl_3$ ($\mathbf{Np}_{tet,small}$) and $(NpO_2THF_2)_3Cl_4$ ($\mathbf{Np}_{tet,large}$); $\mathbf{Np}_{poly}$ into three fragments with formula $(NpO_2)Cl_2THF$. The unit in the middle of $\mathbf{Np}_{poly}$ is denoted $\mathbf{Np}_{poly,mid}$, and the units on the side $\mathbf{Np}_{poly,side}$.

The close energetic proximity of several states complicates the SCF calculations; it is necessary to use smearing in all calculations, and the SCF convergence criterion is higher than the value used in the other calculations in this thesis ($= 10^{-7}$).

Smearing is used in the following complexes and fragments: $\mathbf{Np}_{tri,large}$ (0.001), $\mathbf{Np}_{tet}$ (0.0012), $\mathbf{Np}_{tet,large}$ (0.001), and $\mathbf{Np}_{poly}$ (0.00075) (the number in parenthesis is the smearing (s) in Hartrees; electrons are smeared over the MOs with energies s over and below the Fermi level). The SCF convergence criterion is 10^{-7} except in the following complexes (the first number within parenthesis is the norm, and the second number is the maximum element of the Kohn-Sham operator (1.24) between two consecutive cycles for each complex): $\mathbf{Np}_{tet}$ (0.00035882 and -0.00020181), $\mathbf{Np}_{tet,large}$ (0.00038442 and -0.00003801), and $\mathbf{Np}_{poly}$ (0.00001151 and 0.00000097)

5.3 Probing Electron Localisation on Small and Symmetric Molecules

5.3.1 CO_2 and UO_2^{2+}

CO_2 and UO_2^{2+} both have linear structures with the oxygen atoms at the ends. CO_2 contains two double bonds, each consisting of a σ and a π MO, and uranyl has two formal triple bonds formed by a σ and two π MOs (Chapter 1).

Figure 50 shows isosurfaces of the LOL (section 1.2.10.2) and the ELI (section 1.2.10.3) that both indicate localisation of electrons at the oxygen lone pair region and around the oxygen nuclei (the lone pair region is the space located around the oxygen atoms but away from carbon and uranium respectively). CO_2 has, in addition, localised electrons in the bonding region; LOL indicates more localisation in the bonding region than in the lone pair region, while ELI shows more localisation in the lone pair region than in the bonding region.

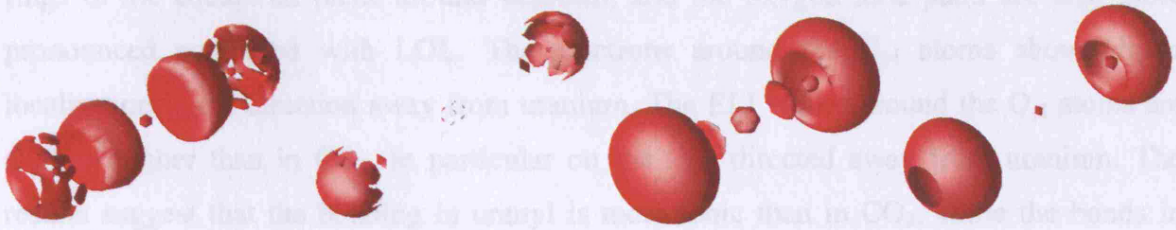

(a) CO_2 LOL **(b) UO_2^{2+} LOL** **(c) CO_2 ELI** **(d) UO_2^{2+} ELI**

Figure 50(a)-(d). *Isosurfaces of (a) LOL = 0.55 for CO_2, (b) LOL = 0.55 for UO_2^{2+}, (c) ELI = 1.75 for CO_2, and (d) ELI = 1.75 for UO_2^{2+}.*

Figure 51 shows LOL values in a plane containing the CO_2 and UO_2^{2+} axes. The LOL obtains its highest values at the nuclei and in the bonding region of CO_2. UO_2^{2+}, however,

shows low values of the LOL in the bonding region. The electrons in UO_2^{2+} are localised in spheres around the oxygen atoms, in a ring around uranium at a distance of just above 1 Å in the equatorial plane, and in a more diffuse ring in the equatorial plane, about 2 Å from uranium. The distance from the nucleus indicates that the *6p* electrons causes this localisation (Figure 2 in chapter 1), although it is unclear why they are localised.

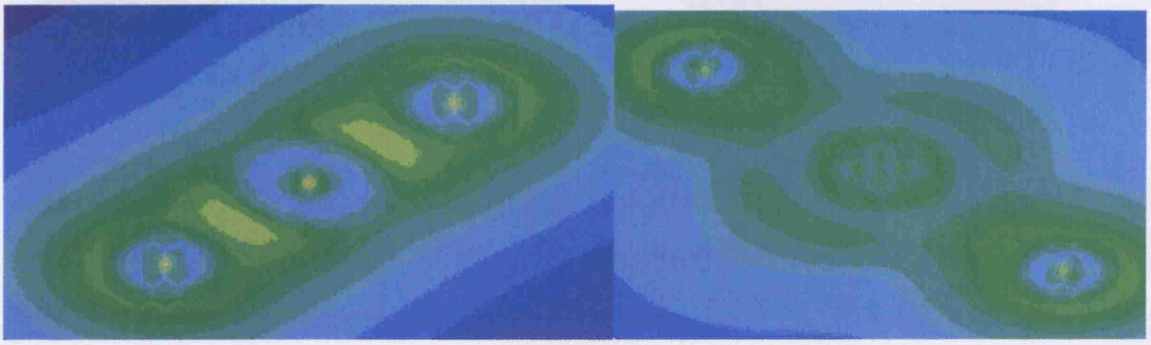

(a) CO_2 LOL **(b) UO_2^{2+} LOL**

Figure 51(a)-(b). *Electron localization in a plane through the CO_2 and UO_2^{2+} axis; (a) LOL for CO_2 and (b) LOL for UO_2^{2+}. The maximum value of the LOL is 1 (red) and the minimum value 0 (blue).*

Figure 52 shows ELI in a plane through the CO_2 and UO_2^{2+} axes. It is easier to see the rings in the equatorial plane around uranium, and the oxygen lone pairs are also more pronounced compared with LOL. The electrons around the O_{yl} atoms show higher localisation in the direction away from uranium. The ELI values around the O_{yl} atoms are slightly higher than in CO_2, in particular on the side directed away from uranium. The results suggest that the bonding in uranyl is more ionic than in CO_2, while the bonds in CO_2 are more covalent.

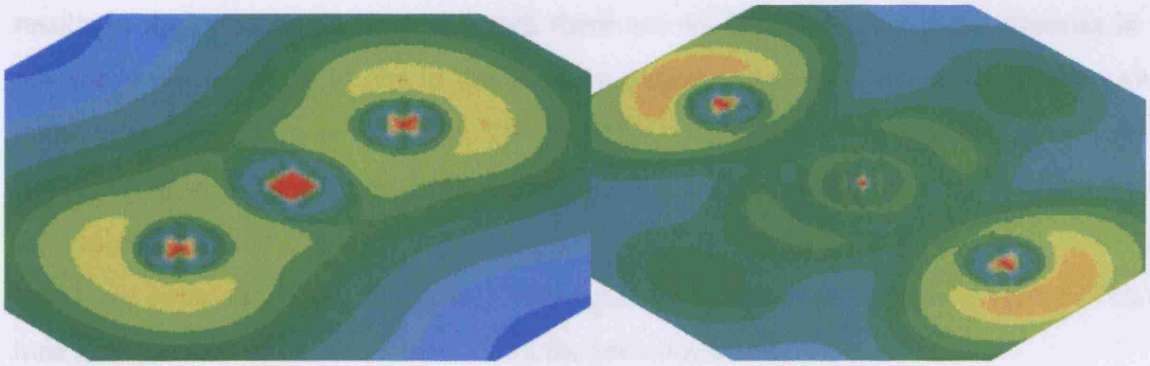

(a) CO_2 ELI **(b) UO_2^{2+} ELI**

Figure 52(a)-(b). *Electron localisation in a plane through the CO_2 and UO_2^{2+} axis; (a) ELI for CO_2 and (b) ELI for UO_2^{2+}. The maximum value of the ELI is 2.5 (red) and the minimum value 0 (blue).*

5.3.2 UO_2^{2+}, UON^+, and UN_2

It is, despite the high stability of uranyl, possible to substitute the O_{yl} atoms for N atoms; UON^+ and UN_2 are analogues of uranyl, and all three molecules are isoelectronic. The U-N bonds are more covalent than the U-O_{yl} bonds, because the oxygen atoms are more electronegative than the nitrogen atoms. Kaltsoyannis investigates this series of molecules computationally in an article that particularly focuses on the energy levels of their MOs [6]. The small size and high symmetry of these molecules allows the use of high level wave function methods (I use Coupled Cluster Singles and Doubles (CCSD) in this work). I compare these calculations with HF and DFT calculations, to probe how important the inclusion of correlation is for these molecules with respect to localisation, and whether DFT calculations are accurate enough to capture the main features of the CCSD calculations. I present only the UO_2^{2+} and UN_2 results of the CCSD and HF calculations, because the result of the DFT calculation on UON^+ is very similar to a combination of the UO_2^{2+} and UN_2 calculations. A calculation on the UON^+ molecule is also much more computationally expensive, due to the reduced symmetry of the molecule.

Figure 53 presents the LOL in a plane through the UO_2^{2+} and the UN_2 axes; the underlying QM calculations are at the CCSD level of theory. The UO_2^{2+} results are similar to the DFT

results in the previous section, although there are no diffuse rings around uranium in the equatorial plane; the electrons in the bonding region and in the first small sphere around uranium are slightly more localised. The low LOL values at the uranium nucleus are due to the effective core potentials. UN_2 shows slightly higher values of LOL in the bonding region compared with UO_2^{2+}, indicating a more covalent bond. Both the U-O_{yl} and U-N bonds are polarised. The LOL values are higher in the bonding region compared with the lone pairs, as for the DFT calculations in the previous section.

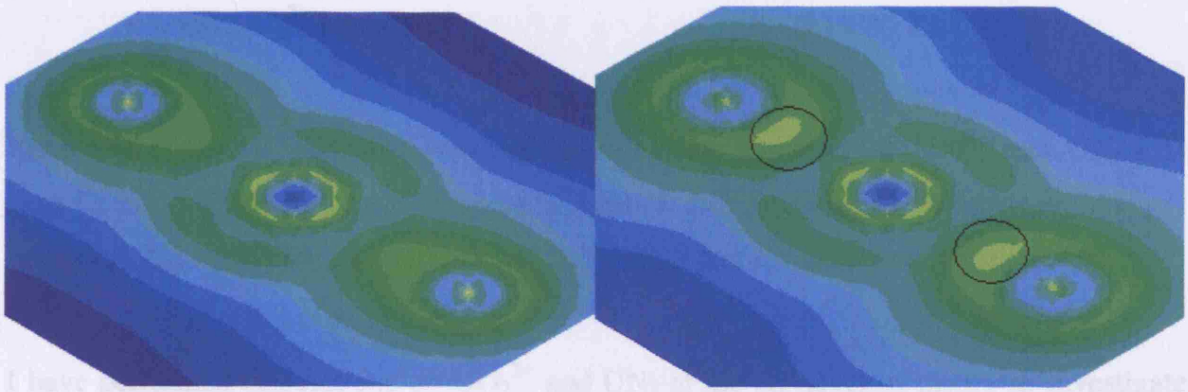

(a) UO_2^{2+} LOL **(b) UN_2 LOL**

Figure 53(a)-(b). *Electron localisation in a plane through the UO_2^{2+} and UN_2 axis from CCSD calculations; (a) LOL for UO_2^{2+} and (b) LOL for UN_2 (bonding region encircled). The maximum value of the LOL is 1 (red) and the minimum value 0 (blue).*

Figure 54 shows ELI in a plane through the UO_2^{2+} and UN_2 axis; the underlying QM calculations are at the CCSD level of theory. The ELI shows higher localisation in the lone pair regions of the O_{yl} atoms compared with in the bonding regions – opposite to the LOL of the CCSD calculations, but similar to the ELI of the DFT calculations. The differences between the ELI based on CCSD calculation and the ELI based DFT calculation are similar to the differences between the LOL at the CCSD and DFT levels. The CCSD calculations do not show the most diffuse rings in the equatorial plane around uranium and the electrons in the bonding regions and around uranium are more localised. The ELI of the CCSD calculations therefore indicates more covalent and less ionic bonds in comparison with the DFT calculations.

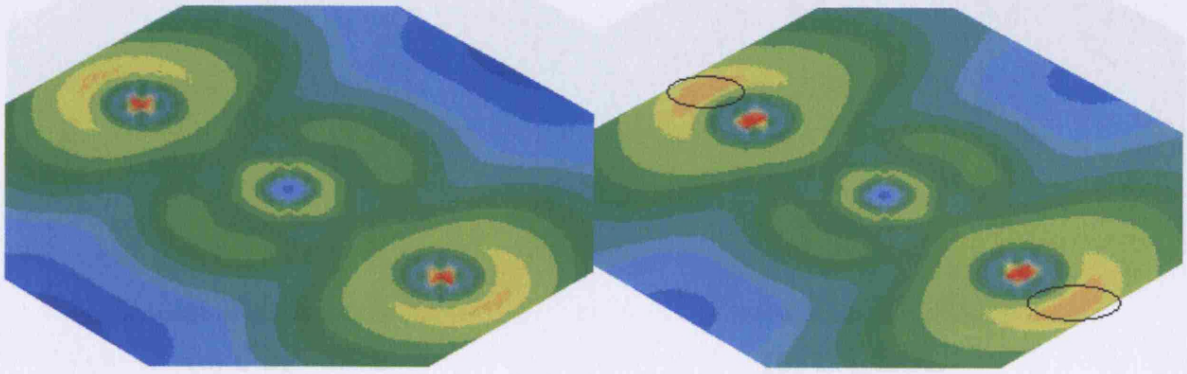

(a) UO_2^{2+} ELI **(b) UN_2 ELI**

Figure 54(a)-(b). *Electron localisation in a plane through the UO_2^{2+} and UN_2 axis from CCSD calculations; (a) ELI for UO_2^{2+} and (b) ELI for UN_2, the lone pair regions are encircled. The maximum value of the ELI is 2.5 (red) and the minimum value 0 (blue).*

I have performed calculations on UO_2^{2+} and UN_2 at the HF level of theory to investigate how localisation depends on the inclusion of correlation in the QM calculation. I also include the ELF to compare with the ELI and the LOL. I have not calculated the ELF from the DFT or CCSD calculations because ELF is only valid for HF calculations (Chapter 1). Figure 55, Figure 56, and Figure 57 present the LOL, ELI, and ELF for the UO_2^{2+} and UN_2 molecules from underlying HF calculations. The HF results are similar to the CCSD results, except that many calculations show large rings around uranium, similar to the DFT calculation on UO_2^{2+}. The high values of the ELI in UN_2 and the ELF in UO_2^{2+} in the large ring around uranium are likely to be artefacts of the QM calculation, because they occur in areas of very low electron density. High electron density does not necessarily imply high localisation, and low electron density does not necessarily imply delocalisation, although there is often a strong correlation between the electron density and its localisation. The ELF of UO_2^{2+} and UN_2 are more similar to the ELI than the LOL of the same molecules.

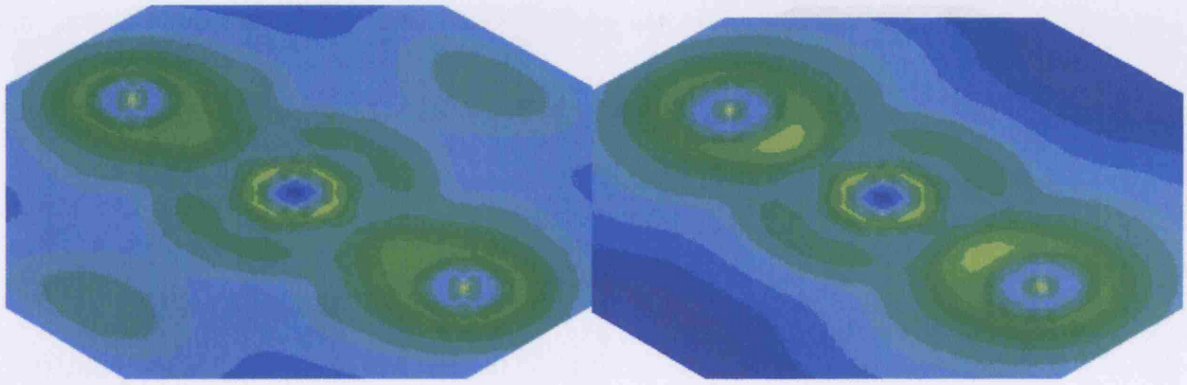

(a) UO_2^{2+} LOL **(b) UN_2 LOL**

Figure 55(a)-(b). *Electron localisation in a plane through the UO_2^{2+} and UN_2 axis from HF calculations; (a) LOL for UO_2^{2+} and (b) LOL for UN_2. The maximum value of the LOL is 1 (red) and the minimum value 0 (blue).*

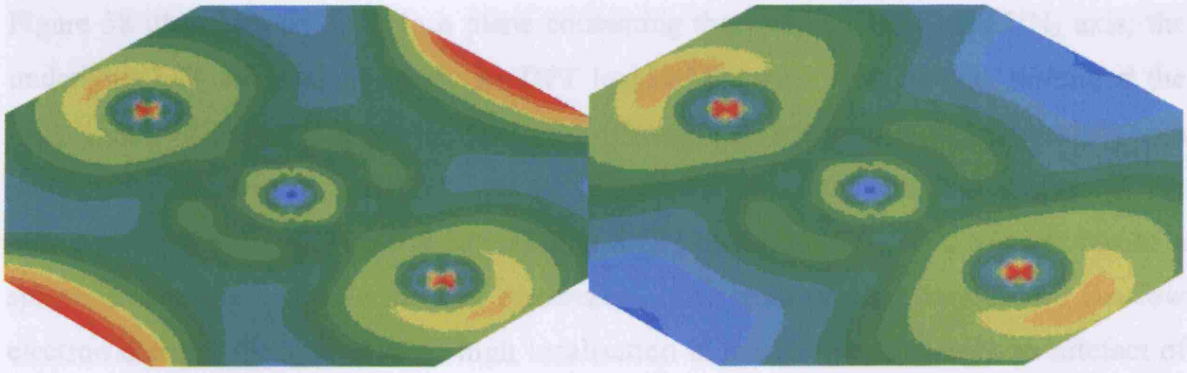

(a) UO_2 ELI **(b) UN_2 ELI**

Figure 56(a)-(b). *Electron localisation in a plane through the UO_2^{2+} and UN_2 axis from HF calculations; (a) ELI for UO_2^{2+} and (b) ELI for UN_2. The maximum value of the ELI is 2.5 (red) and the minimum value 0 (blue).*

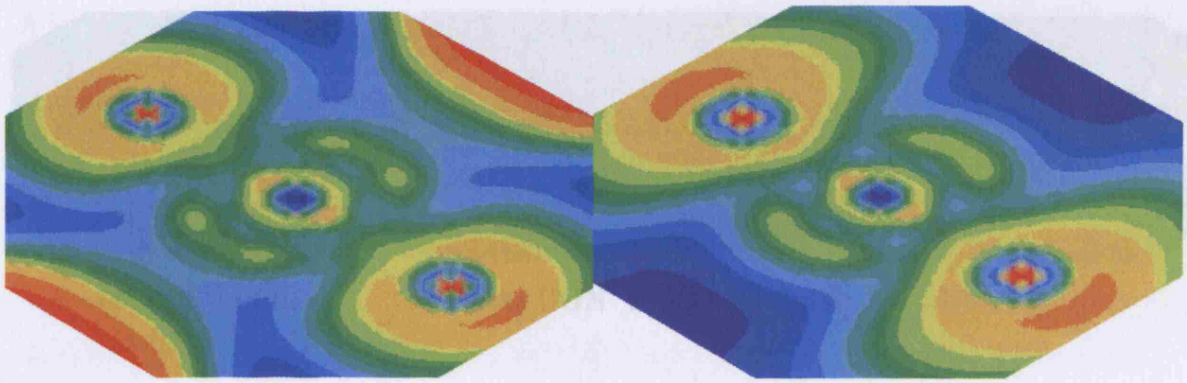

(a) UO_2^{2+} ELF **(b) UN_2 ELF**

Figure 57(a)-(b). *Electron localisation in a plane through the UO_2^{2+} and UN_2 axis from HF calculations; (a) ELF for UO_2^{2+} and (b) ELF for UN_2. The maximum values for the ELF is 1 (red) and the minimum value 0 (blue).*

Figure 58 illustrates the LOL in a plane containing the UO_2^{2+}, UON^+, and UN_2 axis; the underlying QM calculations are at the DFT level of theory. I have already discussed the LOL values of UO_2^{2+} (Figure 51(b)); UON^+ (Figure 58(b)) shows high LOL values in a large half circle around uranium, with its highest values in the lone pair region of the nitrogen atom. The half circle is extended to a full circle for UN_2; this corresponds to a sphere around the molecule in three dimensions. This area of high localisation has low electron density; the indication of high localisation is therefore most likely an artefact of DFT. The DFT calculations show smaller LOL values in the bonding region compared with the CCSD based calculations. The LOL values are similar for the U-N and U-O_{yl} bond, but it is hard to draw any conclusions because of the high localisation around UN_2.

(a) UO_2^{2+} LOL **(b) UON^+ LOL** **(c) UN_2 LOL**

Figure 58(a)-(c). *Electron localisation in a plane containing the UO_2^{2+}, UON^+, and UN_2 axis from DFT calculations; (a) LOL for UO_2^{2+}, (b) LOL for UON^+, and (c) LOL for UN_2. The maximum value of the LOL is 1 (red) and the minimum value is 0 (blue).*

Figure 59 shows ELI in a plane through the UO_2^{2+}, UON^+, and UN_2 axis; the underlying QM calculations are at the DFT level of theory. The features of the ELI are similar to the LOL: high electron localisation around the UON^+ and UN_2 molecules. The ELI suggests that localisation of the electrons around UON^+ and UN_2 is extended over a larger area than the LOL suggests.

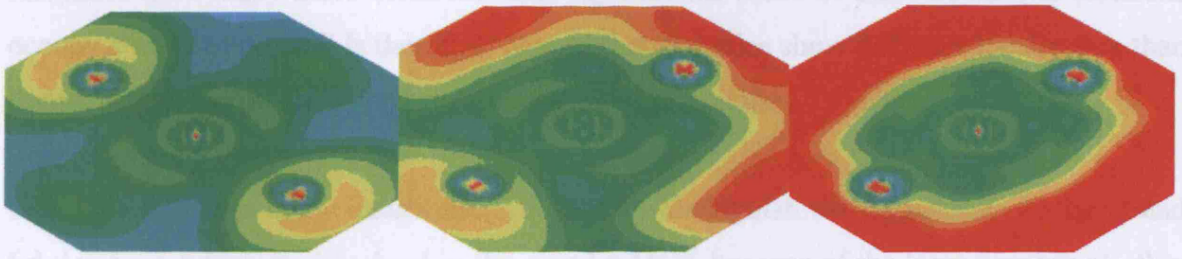

(a) UO_2^{2+} ELI **(b) UON^+ ELI** **(c) UN_2 ELI**

Figure 59(a)-(c). *Electron localisation in a plane containing the UO_2^{2+}, UON^+, and UN_2 axis from DFT calculations; (a) ELI for UO_2^{2+}, (b) ELI for UON^+, and (c) ELI for UN_2. The maximum value of the ELI is 2.5 (red) and the minimum value is 0 (blue).*

As noted in section 5.1, the main purpose of using electron localisation in this work is to compare covalence in bonds; the LOL appears more useful than ELI for this purpose, because it shows higher localisation in the bonding region. Furthermore, the LOL also

produces slightly cleaner pictures, and it can be used to calculate electron localisation in individual MOs.

I have studied electron localisation in the UOC molecule from DFT calculations (not shown); it also shows high localisation in the same area as UON. I have also investigated several small molecules containing exclusively light atoms (not shown); these molecules show chemically intuitive results regarding all indicators of electron localisation and $\Delta\rho$.

I conclude that the CCSD method gives the most chemically intuitive results for UO_2^{2+}, UON^+, and UN_2; high localisation appears in regions of low electron density for HF and DFT, these results are likely to be artefacts of the QM calculations. The problem with CCSD is its scaling with system size; it can only be used on small, symmetric systems. LOL is more valuable for detecting covalence in the systems investigated, because it is more sensitive than ELI to differences in covalent bonding between UO_2^{2+} and UN_2, although the differences are still small. ELF should only be used with HF, and is therefore not suitable for the calculations in this work.

Actinides have many more electrons than light atoms; some of these additional electrons occupy *d* and *f* orbitals. It is therefore natural that actinides show different localisation than lighter atoms, whose electrons only occupy *s* and *p* orbitals.

This section leaves many questions: Is it hard to distinguish the localisation of the 5*f* and 6*d* electrons, which are involved in the σ and π MOs, because of the large number of other electrons? Are MOs in uranium complexes less localised than MOs in lighter atoms because they involve 5*f* and 6*d* AOs, or is the delocalisation of the MOs due to polarisation of the bonds? Why are electrons localised around the UN_2 molecule in DFT calculations, and in a ring around uranium in HF calculations on UO_2^{2+}, even though these areas have low electron density?

One can investigate the contribution of individual MOs to localisation by calculating their individual LOL, although the LOL value for the total electron density does not equal the sum of LOL of the individual MOs (because of the inclusion of the uniform electron gas in LOL's definition). Calculating ELI and ELF based on single MOs is not meaningful,

because their definitions require all orbitals to yield the correct results. I therefore study the σ and π MOs individually by LOL in the following section to investigate if this can answer the above questions – in particular if they can explain the localisation of the electrons around the UN_2 molecule.

5.3.3 The Localized Orbital Locator and Electron Density of the σ and π Molecular Orbitals in UO_2^{2+} and UN_2

Chemistry textbooks usually illustrate MOs by drawing isosurfaces of their amplitude. This has the advantage of showing the MO structure in three dimensions, although it constrains the information from such a plot to only one amplitude value of the orbital. One obtains different information by plotting the amplitude of an orbital in a plane, but this also limits the information. Orbitals with rotational symmetry, however, are completely described by the amplitudes in a plane that contains the entire rotation axis. Orbital amplitudes in similar planes usually contain the most important information in molecules of high symmetry. The combination of isosurfaces and orbital amplitudes in a plane often provides a more complete picture, as the two methods of illustrating orbitals complement each other.

Pictures of the electron density of an orbital (ρ(orb) = the square of the orbital) are less common than pictures of the orbital itself, even though it is the physical observable. The only difference between isosurfaces of orbitals and isosurfaces of ρ(orb) (of the same orbital) is that they correspond to different "cutoff" values of the isosurface and that the orbital can obtain negative values. It is more interesting to compare MO amplitudes with ρ(MO) in a plane. The relative difference of ρ(orb) between regions is larger than the relative difference of the orbital amplitude between regions. The contribution to covalent bonding is also better illustrated from ρ(orb), than from the amplitude of the orbitals.

Figure 60(a) shows the amplitude of the π_u MO of UO_2^{2+} through a plane that contains the UO_2^{2+} axis, compare this with the $\rho(\pi_u)$ of UO_2^{2+} in Figure 61(a); Figure 60(b) shows an isosurface of the electron density of same MO. Figure 60(a) indicates that the $\rho(\pi_u)$ is high towards the oxygen atoms, but also that UO_2^{2+} has a relatively large covalent contribution. Figure 61(a) shows the high $\rho(\pi_u)$ around O_{yl} more clearly; it illustrates that the ionic

component provides a large contribution to the bond (although it is impossible to quantify the covalent and ionic component from this picture). The comparison between UO_2^{2+} and UN_2 in Figure 61 shows that $\rho(\pi_u)$ in UN_2 is less polarised towards the nitrogen atoms; I expect this behaviour for the less electronegative nitrogen atoms.

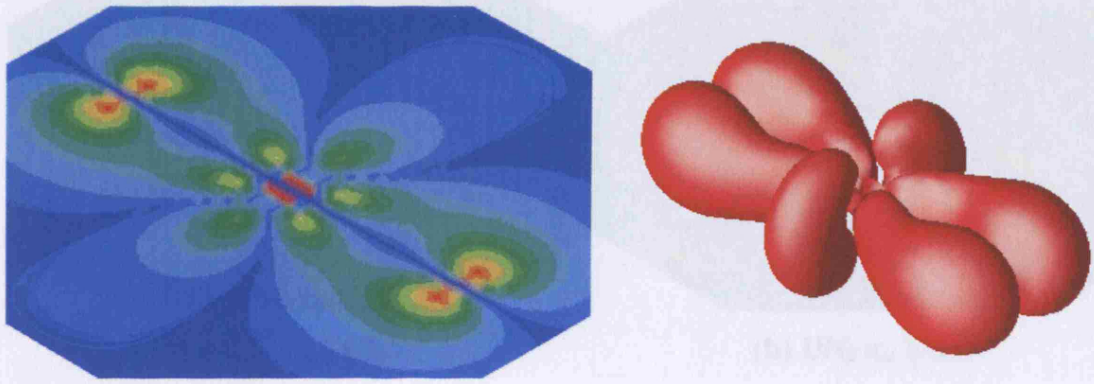

(a) UO_2^{2+} π_u **(b) UO_2^{2+} $\rho(\pi_u)$**

Figure 60(a)-(b). *(a) The amplitude of the π_u MO in a plane through the UO_2^{2+} axis from DFT calculations for UO_2^{2+}. (b) Isosurface of $\rho(\pi_u)$ from DFT calculations for UO_2^{2+}. The maximum value of the orbital amplitude in (a) is 0.6 (red) and the minimum value 0 (blue); the isosurface value in (b) is 0.01.*

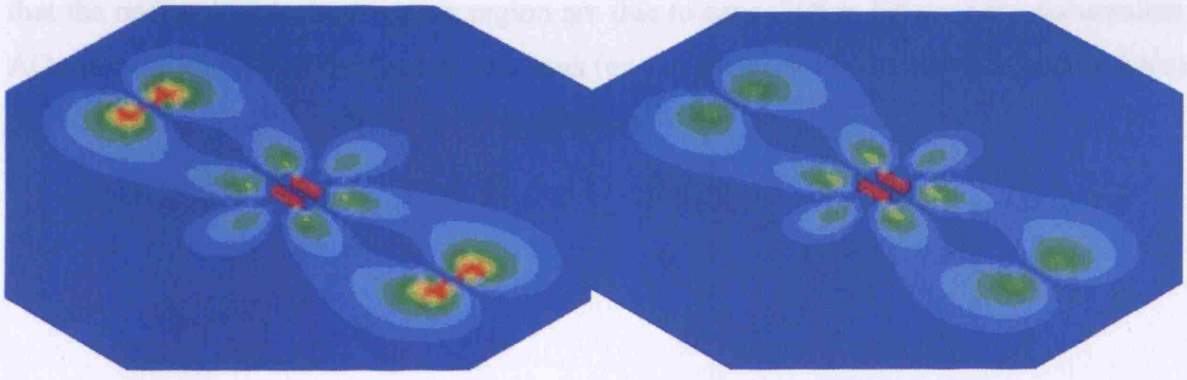

(a) UO_2^{2+} $\rho(\pi_u)$ **(b) UN_2 $\rho(\pi_u)$**

Figure 61(a)-(b). *$\rho(\pi_u)$ (e^-/Bohr^3) in a plane through the UO_2^{2+} and UN_2 axis from DFT calculations for (a) UO_2^{2+} and (b) UN_2. The maximum value of $\rho(\pi_u)$ is 0.3 (red) and the minimum value 0 (blue).*

Figure 62 provides the LOL of π_u in UO_2^{2+} and UN_2; π_u of UN_2 shows slightly more localisation in the bonding region, both bonds look like typical π bonds. Both molecules, especially UN_2, show electron localisation in regions with low values of ρ.

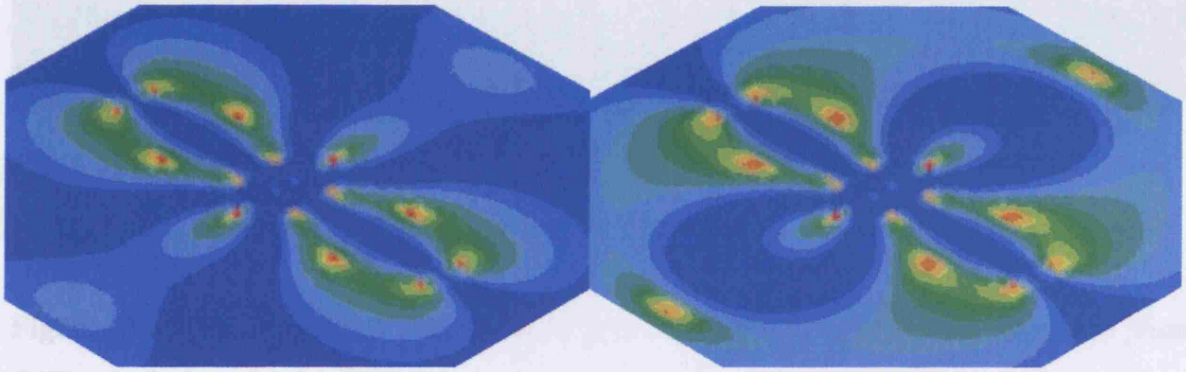

(a) UO_2^{2+} π_u LOL **(b) UN_2 π_u LOL**

Figure 62(a)-(b). *Electron localisation of the π_u MO in a plane through the UO_2^{2+} and UN_2 axis from DFT calculations; (a) LOL for UO_2^{2+} and (b) LOL for UN_2. The maximum value for the LOL is 1 (red) and the minimum value 0 (blue).*

Figure 63 illustrates $\rho(\pi_g)$ in a plane through the UO_2^{2+} and the UN_2 axis; it shows a similar trend as π_u with higher values of ρ at the oxygen atom, in comparison with nitrogen. Notice that the nodes close to the bonding region are due to cancellation between the 6*d* uranium AOs and the 2*p* AOs of the O_{yl} and N atoms (one of the nodes is encircled in Figure 63(a) and Figure 3 in chapter 1 shows the cancellation).

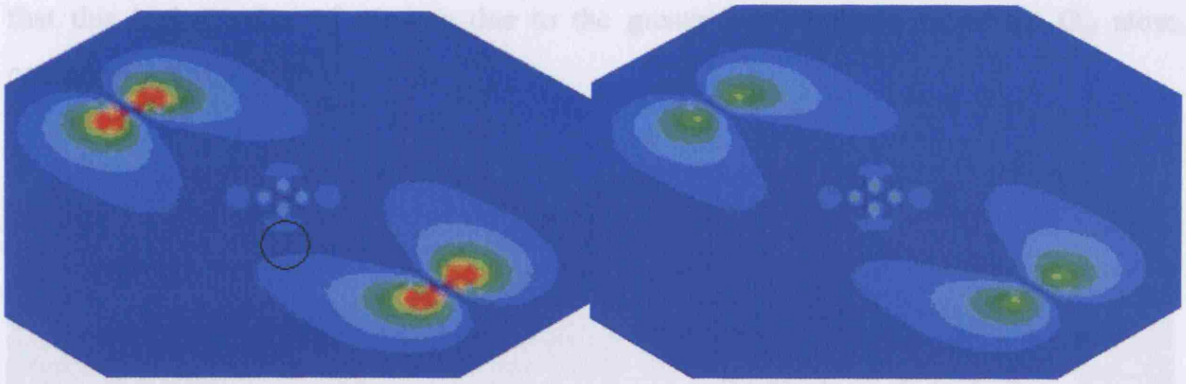

(a) UO_2^{2+} $\rho(\pi_g)$ **(b) UN_2 $\rho(\pi_g)$**

Figure 63(a)-(b). *$\rho(\pi_g)$ ($e^-/Bohr^3$) in a plane through the UO_2^{2+} and UN_2 axis from DFT calculations for (a) UO_2^{2+} and (b) UN_2. The maximum value of $\rho(\pi_g)$ is 0.3 (red) and the minimum value 0 (blue).*

Figure 64 shows the LOL of the π_g MO for UO_2^{2+} and UN_2; the π_g MO of UN_2 shows slightly more localization in the bonding region.

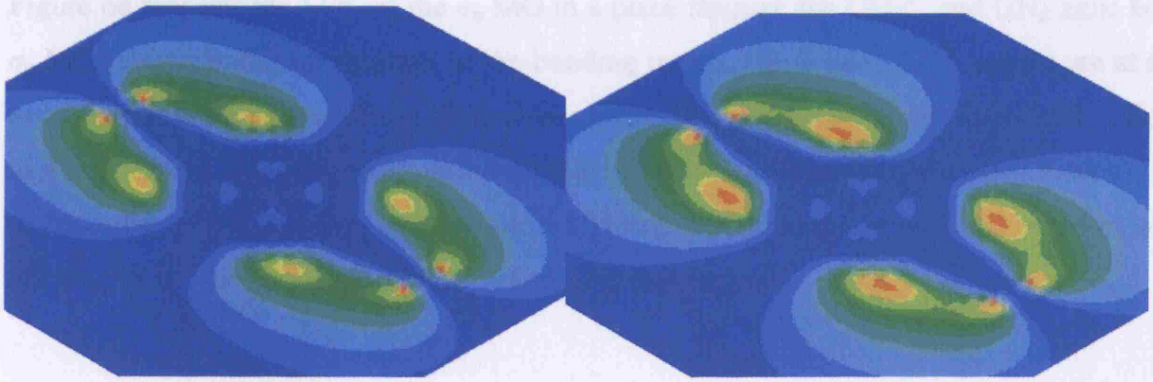

(a) UO_2^{2+} π_g LOL **(b) UN_2 π_g LOL**

Figure 64(a)-(b). *Electron localisation of the π_g MO in a plane through the UO_2^{2+} and UN_2 axis from DFT calculations; (a) LOL for UO_2^{2+} and (b) LOL for UN_2. The maximum value for the LOL is 1 (red) and the minimum value 0 (blue).*

$\rho(\sigma_u)$ of UO_2^{2+} and UN_2 in Figure 65 obtains its highest values close to the uranium atom and is higher around O_{yl} in comparison with the nitrogen atoms. $\rho(\sigma_u)$ of UO_2^{2+} is higher in the bonding region, indicating a more covalent contribution than for UN_2. It seems likely

that this higher value of $\rho(\sigma_u)$ is due to the greater electronegativity of the O_{yl} atom, compared with the N atom.

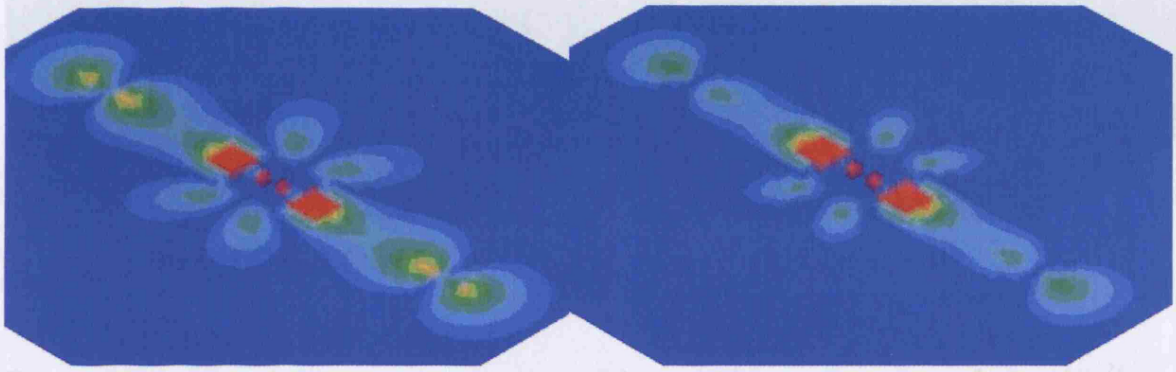

(a) UO_2^{2+} $\rho(\sigma_u)$ **(b) UN_2 $\rho(\sigma_u)$**

Figure 65(a)-(b). *$\rho(\sigma_u)$ ($e^-/Bohr^3$) in a plane through the UO_2^{2+} and UN_2 axis from DFT calculations for (a) UO_2^{2+} and (b) UN_2. The maximum value of $\rho(\sigma_u)$ is 0.3 (red) and the minimum value 0 (blue).*

Figure 66 presents the LOL of the σ_u MO in a plane through the UO_2^{2+} and UN_2 axis; both σ_u MOs show similar localisation in the bonding region, the highest LOL values are at the bond mid-points – characteristic for a sigma bond. UN_2, however, shows high LOL values in a ring around the nitrogen atoms and the UN_2 axis – a region with low $\rho(\sigma_u)$ values. The σ_u MO of UO_2^{2+} also shows localisation in this region, although not as much as the σ_u MO of UN_2; UO_2^{2+} also has higher values of $\rho(\sigma_u)$ in this region.

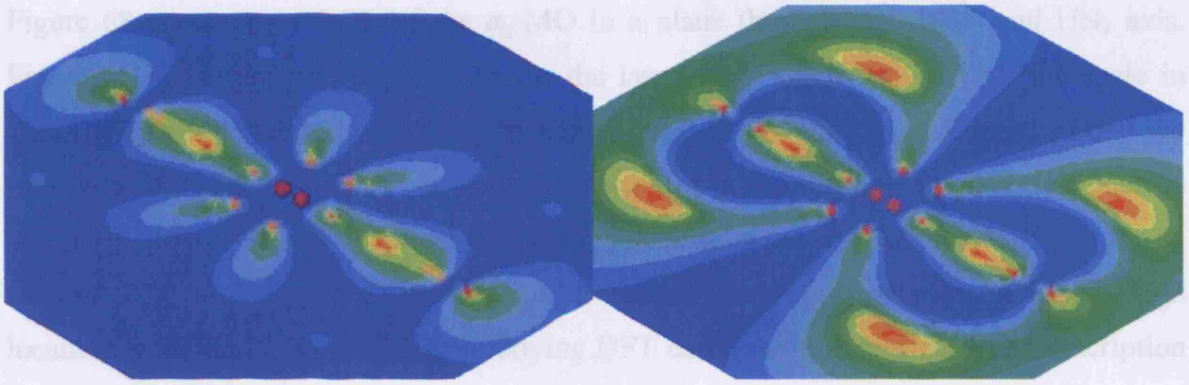

(a) UO_2^{2+} σ_u LOL **(b) UN_2 σ_u LOL**

Figure 66(a)-(b). *Electron localization of the σ_u MO in a plane through the UO_2^{2+} and UN_2 axis from DFT calculations; (a) LOL for UO_2^{2+} and (b) LOL for UN_2. The maximum value for the LOL is 1 (red) and the minimum value 0 (blue).*

Figure 67 provides $\rho(\sigma_g)$ in a plane containing the UO_2^{2+} and UN_2 axis; UN_2 has very low values of $\rho(\sigma_g)$ in the bonding region. $\rho(\sigma_g)$ shows high values around the oxygen and nitrogen atoms in each molecule, it also shows high values around the UN_2 molecule; $\rho(\sigma_g)$ of UO_2^{2+} is also significant around the molecule, although not as high as around UN_2.

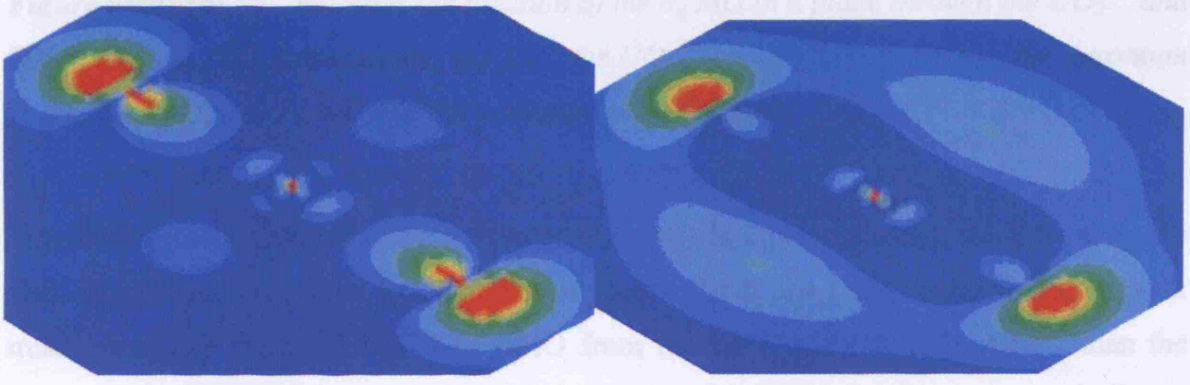

(a) UO_2^{2+} $\rho(\sigma_g)$ **(b) UN_2 $\rho(\sigma_g)$**

Figure 67(a)-(b). *$\rho(\sigma_g)$ ($e^-/Bohr^3$) in a plane through the UO_2^{2+} and UN_2 axis from DFT calculations for (a) UO_2^{2+} and (b) UN_2. The maximum value of $\rho(\sigma_g)$ is 0.3 (red) and the minimum value 0 (blue).*

Figure 68 presents the LOL of the σ_g MO in a plane through the UO_2^{2+} and UN_2 axis. Figure 68(b) provides an explanation for the large LOL values of the UN_2 molecule in Figure 58(b); the electrons of the σ_g MO show high LOL values in an ellipse around the molecule. The σ_g MO of UO_2^{2+} is also quite localised in this area, although not as much as in UN_2. I cannot see any chemical reason for localisation around the molecule, and the σ_g MO of UN_2 looks particularly strange; it seems likely that problem with the high localization around UN_2 is in the underlying DFT calculation, in particular the description of the σ_g MO.

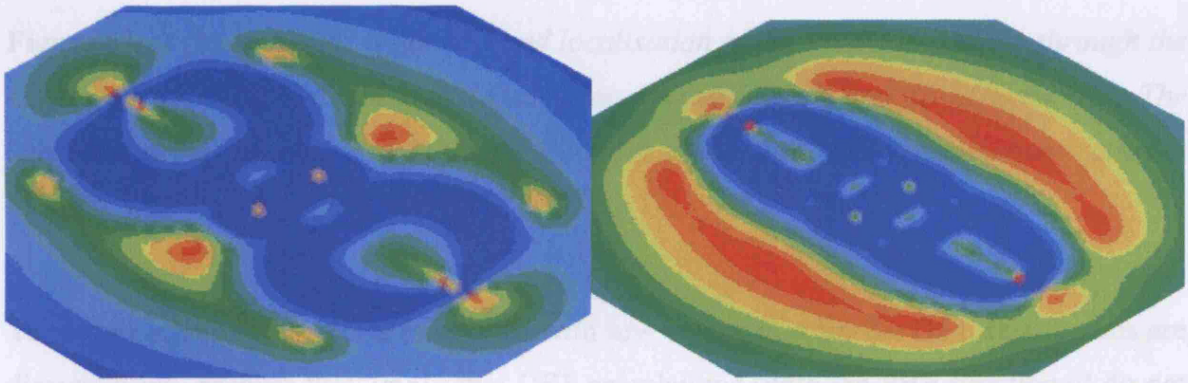

(a) UO_2^{2+} σ_g LOL **(b) UN_2 σ_g LOL**

Figure 68(a)-(b). *Electron localisation of the σ_g MO in a plane through the UO_2^{2+} and UN_2 axis from DFT calculations; (a) LOL for UO_2^{2+} and (b) LOL for UN_2. The maximum value for the LOL is 1 (red) and the minimum value 0 (blue).*

Figure 69 presents $\rho(\sigma_g)$ and the LOL of the σ_g MO in a plane through the UN_2 axis; the QM calculations are at the CCSD level of theory. Both $\rho(\sigma_g)$ and the LOL values look much more like the results of the σ_g MO from the DFT calculation for UO_2^{2+} than the results of the σ_g MO from the DFT calculations for UN_2. These results are more similar to sigma bonds in molecules of lighter atoms.

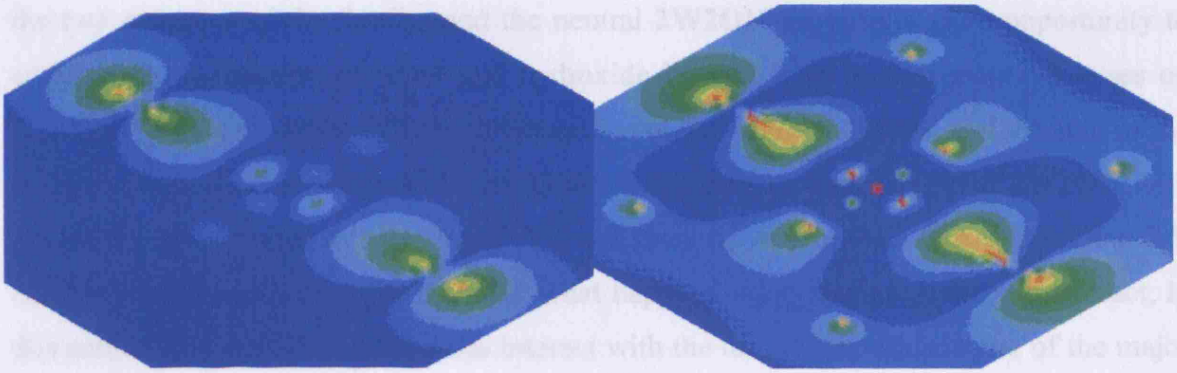

(a) UN_2 $\rho(\sigma_g)$ **(b) UN_2 σ_g LOL**

Figure 69(a)-(b). *$\rho(\sigma_g)$ (e^-/Bohr^3) and localisation of the σ_g MO in a plane through the UN_2 axis from CCSD calculations; (a) electron density for UN_2 and (b) LOL for UN_2. The maximum values of $\rho(\sigma_g)$ and LOL are 0.3 (red) and 1 (red) and the minimum values 0 (blue).*

The localisation of the σ MOs in regions with low values of ρ for the DFT calculations are disappointing, because they imply that DFT calculations (with the PBE functional) do not provide an accurate description of actinides in general, and UN_2 in particular. Localisation analysis of individual MOs is more promising than the same analysis of the whole density, as the bad description of the σ MOs in the DFT calculations "contaminate" the total electron density, which therefore shows localisation in areas with low values of ρ. It is, however, possible that the LOL works better on larger actinide systems. Introducing equatorial ligands, for example, increases the HOMO – LUMO gap (and therefore reduces non-dymamic correlation). I will therefore continue probing LOL on larger actinide systems in the following sections.

5.4 Another Look at Selected Species in the $[UO_2(H_2O)_m(OH)_n]^{2-n}$ (m+n=5) Family of Compounds

Studying localisation in the $[UO_2(H_2O)_m(OH)_n]^{2-n}$ (m+n=5) family is a natural step from the investigation of UO_2^{2+} and analogues. I especially focus on the $[UO_2(H_2O)_5]^{2+}$ (**5W**), $UO_2(H_2O)_2(OH)_2$ (**2W2OH**), and $[UO_2(OH)_4]^{2-}$ (**4OH**) species, as **5W** and **4OH** represent

the two extremes of the family, and the neutral **2W2OH** provides a good opportunity to compare the interaction of water and hydroxide ligands. This section mainly focuses on $\Delta\rho$; $\Delta\rho$ is calculated as the difference between ρ of the whole molecule, and the sum of the ρ values of all the fragments of the molecule. It is useful to compare $\Delta\rho$ of **2W2OH** with $\Delta\rho$ of the neutral complexes in chapter 3; I will show $\Delta\rho$ of those complexes in section 5.5. $\Delta\rho$ is a valuable tool, because it shows what happens when fragments start to interact, in this case when the equatorial ligands interact with the uranyl ion – this is one of the major questions discussed in chapter 2. It is useful to illustrate the results with isosurfaces, because the compounds in this section are larger and less symmetric than uranyl and its analogs.

I will present electron localisation analysis on **5W**, **2W2OH**, and **4OH** in this section, and electron density differences and localisation for the complexes in chapter 3 in section 5.5.

5.4.1 Electron Density Differences of 5W, 2W2OH, and 4OH

I divide the target molecules in two fragments each – the equatorial ligands and the uranyl unit. $\Delta\rho$ between the whole molecule and the two fragments are results of the interaction between the fragments.

Figure 70 shows all compounds from the side with the uranyl unit in the middle, and Figure 71 the same picture but from another angle to show more detail (Figure 13 in chapter 2 shows the geometries of all complexes). The red areas are isosurfaces of negative $\Delta\rho$ values, i.e. lower values of ρ in the complex compared with the sum of the fragments; the blue areas correspond to positive $\Delta\rho$ values, i.e. these areas have higher values of ρ in the whole complex than in the sum of their fragments. An interpretation of this is that electrons flow from red to blue areas when the fragments start to interact.

5W in Figure 70(a) and Figure 71(a) has large red areas in the equatorial plane around the uranyl unit. I call these areas "the lone pair regions" of the water ligands; the two small red areas above and below them are located close to the hydrogen atoms. The largest blue area is in the bonding region of the equatorial plane, between uranium and the water ligand that

has its hydrogen atoms rotated 90 degrees compared with the other ligands. The interaction with this ligand is different compared with the other ligands; electrons flow to the blue region, thereby creating a stronger and more covalent bond. The two smaller blue regions on the top and bottom of Figure 70(a) are located close to the O_{yl} atoms.

Figure 70(b) and Figure 71(b) show that the hydroxide ligands donate electrons when they start to interact with uranyl; the blue isosurface stretches towards the bonding region in the equatorial plane. ρ decreases in the lone pair region of the water ligands upon interaction with uranyl in **5W** and **2W2OH**. One also finds electron depletion just above and below the uranium nucleus, while electrons accumulate around O_{yl} and away from uranium in **2W2OH** and **4OH**. This indicates that the uranyl bond becomes more ionic as it starts to interact with hydroxide ligands. The non-symmetric distribution of the accumulated electron density around O_{yl}, but away from uranium, suggests hydrogen bonding between O_{yl} and the hydrogen atoms on the hydroxide ligands. **4OH** shows similar interaction as **2W2OH** in the equatorial plane, but the symmetric distribution of the ligands in **4OH** prevents the illustration of the hydrogen bonds.

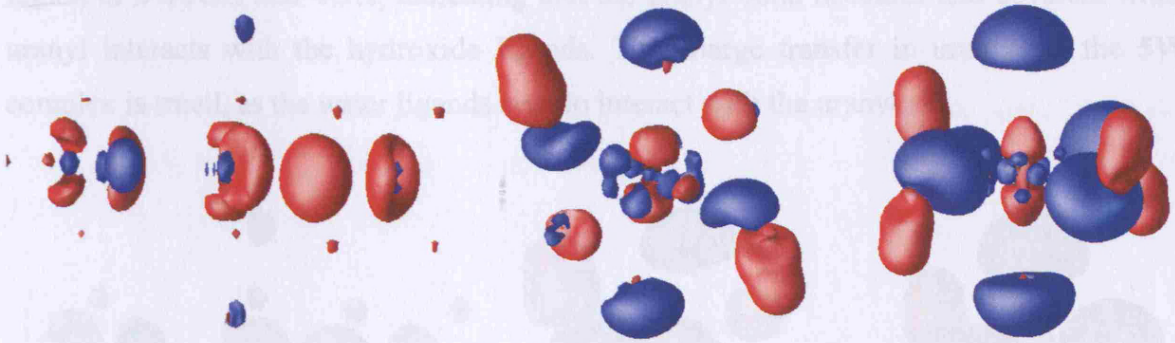

(a) 5W **(b) 2W2OH** **(c) 4OH**

Figure 70(a)-(c). *Side view of isosurfaces of $\Delta\rho$ (e^-/Bohr^3) in (a) **5W**, (b) **2W2OH**, and (c) **4OH** from DFT calculations. The fragments are UO_2^{2+} and the equatorial ligands. The isosurface values are -0.025 (red) and 0.025 (blue).*

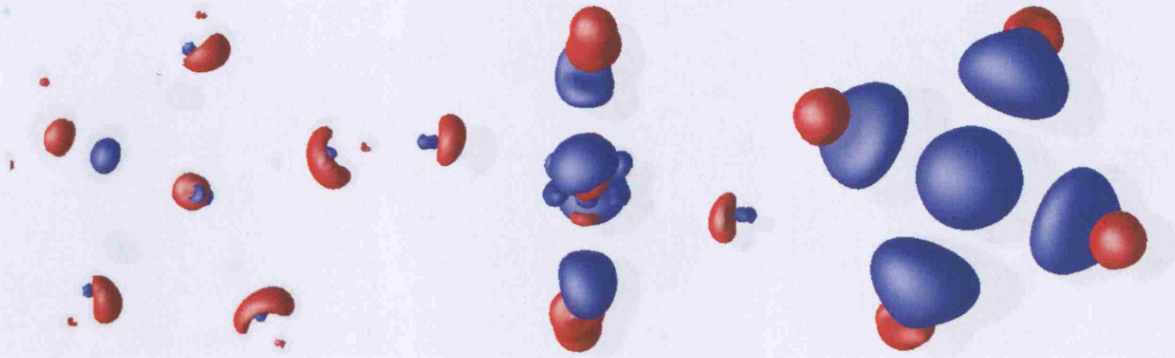

(a) 5W **(b) 2W2OH** **(c) 4OH**

Figure 71(a)-(c). *View from above of isosurfaces of Δρ (e^-/Bohr^3) in (a)* ***5W****, (b)* ***2W2OH****, and (c)* ***4OH*** *from DFT calculations. The fragments are UO_2^{2+} and the equatorial ligands. The isosurface values are -0.025 (red) and 0.025 (blue).*

Figure 72 and Figure 73 show $\Delta\rho$ for the same species as Figure 70 and Figure 71, but with lower isosurface values. These figures clearly show that ρ decreases in the uranyl bonding region of **2W2OH** and **4OH**, indicating that the uranyl bond becomes less covalent when uranyl interacts with the hydroxide ligands. The charge transfer in uranyl for the **5W** complex is small, as the water ligands start to interact with the uranyl ion.

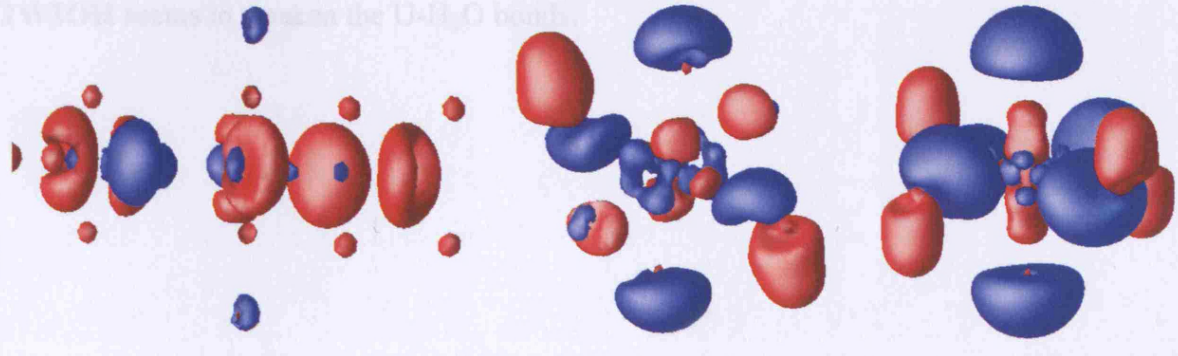

(a) 5W **(b) 2W2OH** **(c) 4OH**

Figure 72(a)-(c). *Side view of isosurfaces of Δρ (e^-/Bohr^3) in (a)* ***5W****, (b)* ***2W2OH****, and (c)* ***4OH*** *from DFT calculations. The fragments are UO_2^{2+} and equatorial ligands. The isosurface values are -0.02 (red) and 0.02 (blue).*

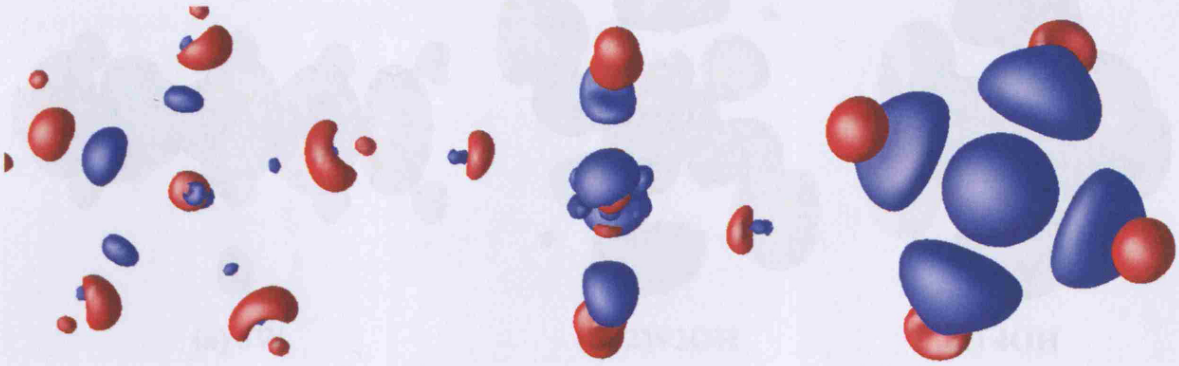

(a) 5W (b) 2W2OH (c) 4OH

Figure 73(a)-(c). *View from above of isosurfaces of Δρ (e^-/Bohr^3) in (a)* ***5W****, (b)* ***2W2OH****, and (c)* ***4OH*** *from DFT calculations. The fragments are UO_2^{2+} and the equatorial ligands. The isosurface values are -0.02 (red) and 0.02 (blue).*

I lower the isosurface values to +-0.015 in Figure 74 and Figure 75; these figures show electron donation from the hydroxide ligands to the equatorial plane in **4OH**. The shape of the large red "lone pair region" area of the water ligands reveals interaction between the ligands for **5W** and **2W2OH**. The accumulation of electrons in the bonding region of the equatorial plane is larger for the water ligands of the **5W** compound, compared with the water ligands in the **2W2OH** compound. The competition from the hydroxide ligands in **2W2OH** seems to weaken the U-H_2O bonds.

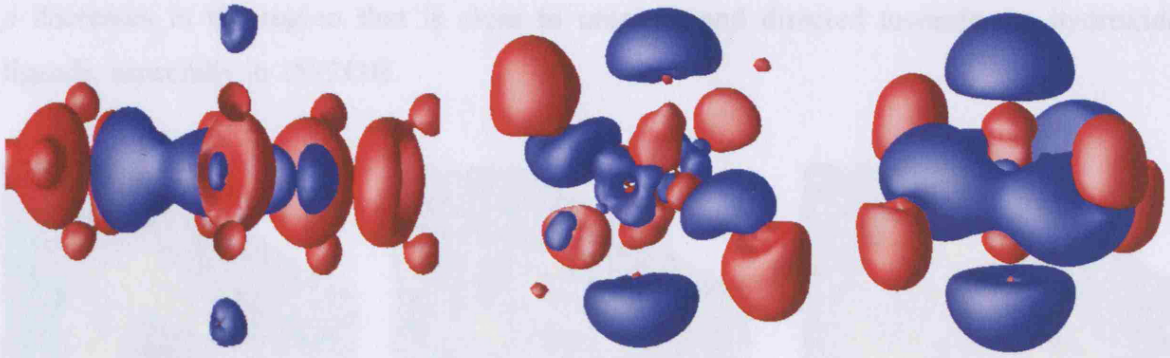

(a) 5W (b) 2W2OH (c) 4OH

Figure 74(a)-(c). *Side view of isosurfaces of Δρ (e^-/Bohr^3) in (a) **5W**, (b) **2W2OH**, and (c) **4OH** from DFT calculations. The fragments are UO_2^{2+} and the equatorial ligands. The isosurface values are -0.015 (red) and 0.015 (blue).*

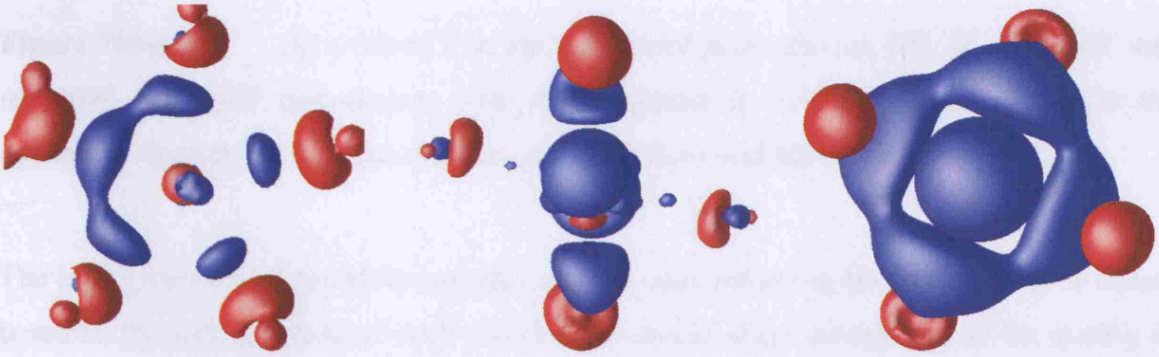

(a) 5W (b) 2W2OH (c) 4OH

Figure 75(a)-(c). *View from above of isosurfaces of Δρ (e^-/Bohr^3) in (a) **5W**, (b) **2W2OH**, and (c) **4OH** from DFT calculations. The fragments are UO_2^{2+} and the equatorial ligands. The isosurface values are -0.015 (red) and 0.015 (blue).*

Figure 76 shows Δρ in the equatorial plane; this provides a cleaner view of equatorial plane than do the isosurfaces. Red and blue colour represents positive and negative Δρ respectively in this figure – opposite to the previous figures. The interaction between the hydroxide ligands and uranium is clearly stronger than the interaction between the water ligands and uranium, although the water ligand that has its hydrogen atoms rotated 90 degrees compared with the other ligands in **5W** shows significant interaction with uranium.

ρ decreases in the region that is close to uranium and directed towards the hydroxide ligands, especially in **2W2OH**.

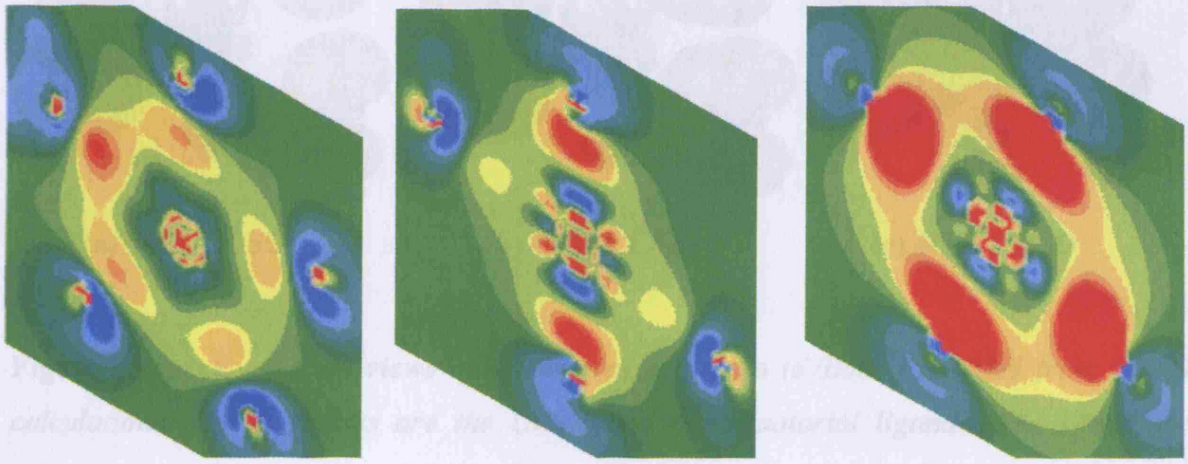

(a) 5W **(b) 2W2OH** **(c) 4OH**

Figure 76(a)-(c). *$\Delta\rho$ ($e^-/Bohr^3$) in the equatorial plane for (a) **5W**, (b) **2W2OH**, and (c) **4OH** from DFT calculations. The first fragment is UO_2^{2+}, and the second is the equatorial ligands. The maximum values are 0.03 (red) and the minimum -0.03 (blue).*

The high symmetry of the **4OH** complex renders calculations at the CCSD level of theory possible; the high accuracy of such calculations should allow assessment of the quality of the DFT calculations. Figure 77 presents $\Delta\rho$ from the CCSD calculations; their features are similar to the $\Delta\rho$ of the DFT calculations. ρ in the region around the oxygen atom of the hydroxide ligands generally decreases in the CCSD calculations, but electrons accumulate in the bonding region of the equatorial plane. As in the DFT calculations, electrons flow from U to O_{yl}, but the electron accumulation around O_{yl} is mainly on the side towards the uranium atom – the opposite side of the electron accumulation around O_{yl} in the DFT calculations.

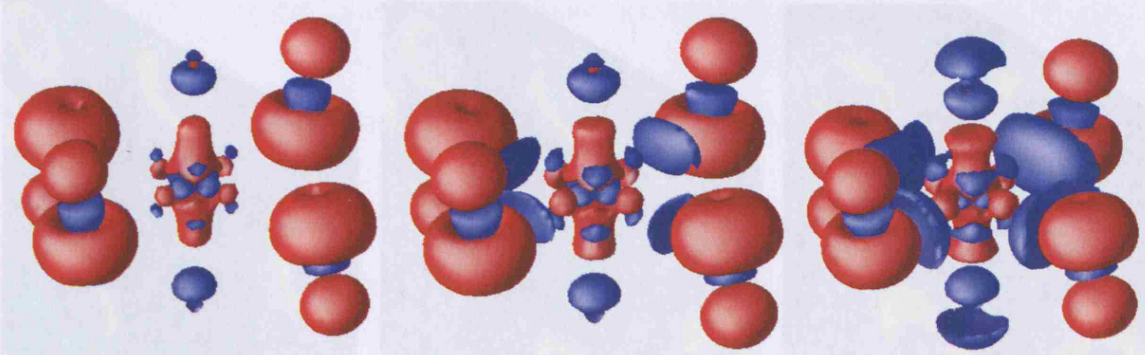

(a) 4OH CCSD (b) 4OH CCSD (c) 4OH CCSD

Figure 77(a)-(c). *Side views of isosurfaces of the Δρ (e^-/Bohr^3) in **4OH** from CCSD calculations. The fragments are the UO_2^{2+} and the equatorial ligands. The isosurface values are (a) -0.025 (red) and 0.025 (blue), (b) -0.02 (red) and 0.02 (blue), and (c) -0.015 (red) and 0.015 (blue).*

5.4.2 Electron Localisation in 5W, 2W2OH, and 4OH

Figure 78 and Figure 79 show the ELI and the LOL respectively in the equatorial plane taken from DFT calculations; both the ELI and the LOL describe similar and very ionic bonds for each species. The figures show the lone pair on the oxygen atom of the hydroxide ligands particularly well; especially for **4OH** (two of these regions are encircled). The large red areas in Figure 78(a) and Figure 78(b), and the yellow areas in Figure 79(a) and Figure 79(b) are hydrogen atoms.

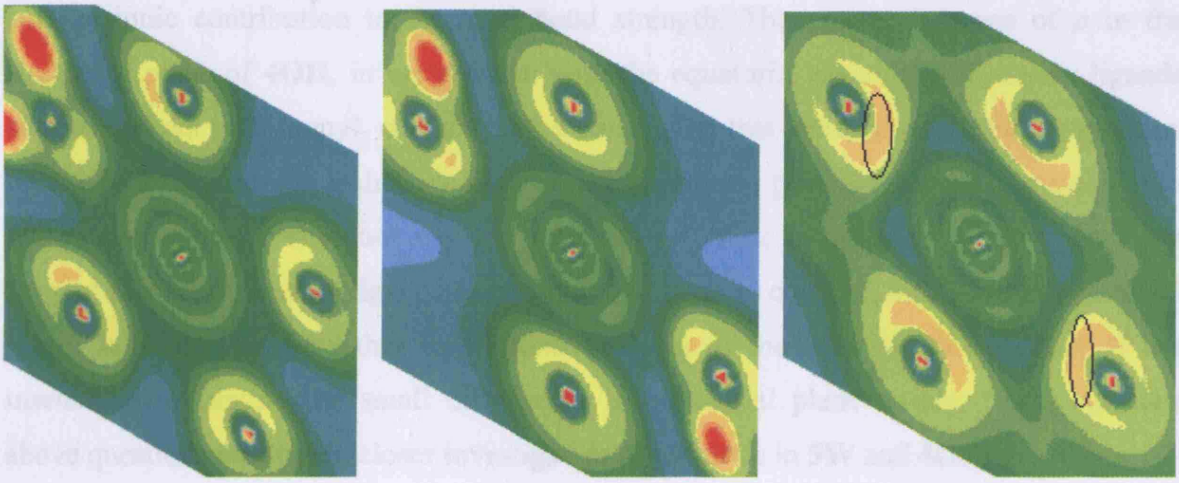

(a) 5W ELI **(b) 2W2OH ELI** **(c) 4OH ELI**

Figure 78(a)-(c). *Electron localisation in the equatorial plane from DFT calculations; (a) ELI for **5W**, (b) ELI for **2W2OH**, and (c) ELI for **4OH**. The maximum values are 2.5 (red) and the minimum 0 (blue).*

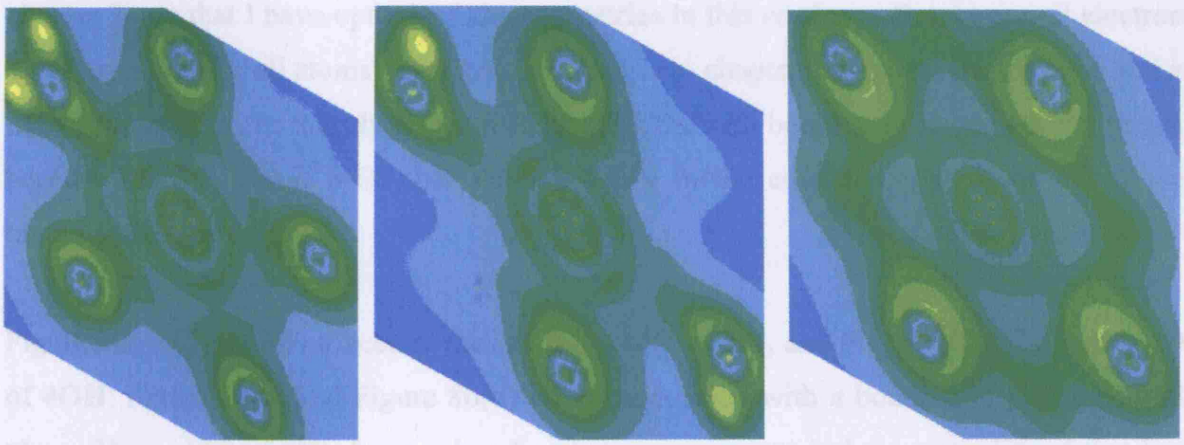

(a) 5W LOL **(b) 2W2OH LOL** **(c) 4OH LOL**

Figure 79(a)-(c). *Electron localisation in the equatorial plane from DFT calculations; (a) LOL for **5W**, (b) LOL for **2W2OH**, and (c) LOL for **4OH**. The maximum values are 1 (red) and the minimum 0 (blue).*

The $\Delta\rho$ investigation shows that the uranyl bonds become less covalent and more ionic as hydroxide ligands replace water ligands. This contradicts the conclusion from the charge analysis in chapter 2, which states that the increased uranyl bond distance is due to a

smaller ionic contribution to the total bond strength. The greater increase of ρ in the equatorial plane of **4OH**, in comparison with the equatorial plane of **5W,** as the ligands start to interact with uranyl, challenges the conclusion that there is very little competition for the 6*d* AOs from the hydroxide ligands. It is, however, possible that the increasing ρ in the equatorial plane does not overlap with the 6*d* AOs; localisation analysis does not support that the hydroxide ligands form significantly more covalent bonds in the equatorial plane. It is also possible that localisation analysis of the total electron density is too insensitive to capture the small differences in equatorial plane covalent bonding. The above questions motivate a closer investigation of the MOs in **5W** and **4OH**.

5.4.3 Molecular Orbitals and Their Localisation in 5W and 4OH

The aim of this section is to perform localisation analysis on the MOs with equatorial bonding character, to investigate differences in the water-uranyl and hydroxide-uranyl interaction. The differences between the orbital analysis in this section, compared with chapter 2, are that I have optimised the geometries in this section with a larger all electron TZ2P basis set (for all atoms), and that the analysis in chapter 2 focus on the uranyl σ and π MOs. The analysis in this chapter considers all MOs with bonding in the equatorial plane, because the non-uranyl MOs that show bonding in the equatorial plane can affect the uranyl MOs indirectly.

Figure 80(a) shows isosurfaces of the uranyl σ_u MO of **5W**, and Figure 80(c) the same MO of **4OH**; Figure 80(b) and Figure 80(d) show other MOs with π bonding in the equatorial plane. The σ_u MO of **5W** shows π bonding between uranium and the water ligand that has its hydrogen atoms rotated 90 degrees compared with the other water ligands. This is different from the σ_u MO of **4OH** that shows an antibonding interaction between the hydroxide ligands and uranium. The MO of **5W** with the most significant π-bonding in the equatorial plane is the HOMO-8 (Figure 80(b)). Figure 80(d) shows π-bonding in the equatorial plane for **4OH**. The amount of π-bonding in the equatorial plane looks quite similar for **5W** and **4OH**. The shapes of the MOs suggest that the major uranium contributions come from the 5*f* AOs.

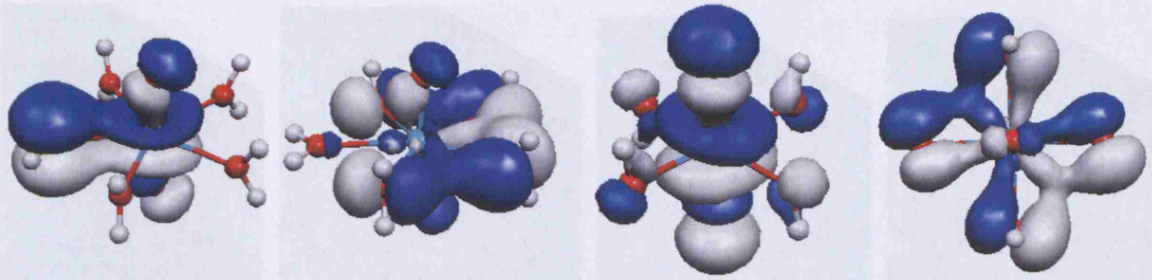

(a) 5W σ_u (b) 5W HOMO-8 (c) 4OH σ_u (d) 4OH HOMO-4

Figure 80(a)-(d). *Orbitals with π bonding (or potential for it) in the equatorial plane, from DFT calculations; (a) σ_u (HOMO-2) of **5W**, (b) HOMO-8 of **5W**, (c) σ_u (HOMO-3) of **4OH**, and (d) HOMO–4 of **4OH**. The isosurface values are 0.03 for all MOs.*

Figure 81(a) visualises ρ(HOMO-8) of **5W**, Figure 81(b) ρ(HOMO-4) of **4OH**, Figure 81(c) the LOL of the HOMO-8 of **5W**, and Figure 81(d) the LOL of the HOMO-4 of **4OH**. The HOMO-4 of **4OH** has higher values of ρ around the uranium atom compared with the HOMO-8 of **5W**; this suggests that the **4OH** MO has more 5*f* character than the MO of **5W**. The LOL suggests that the electrons in the **4OH** MO are slightly more localised in the bonding region than the MO of **5W**. The LOL indicates some interaction between the ligands for the MOs of both **5W** and **4OH**.

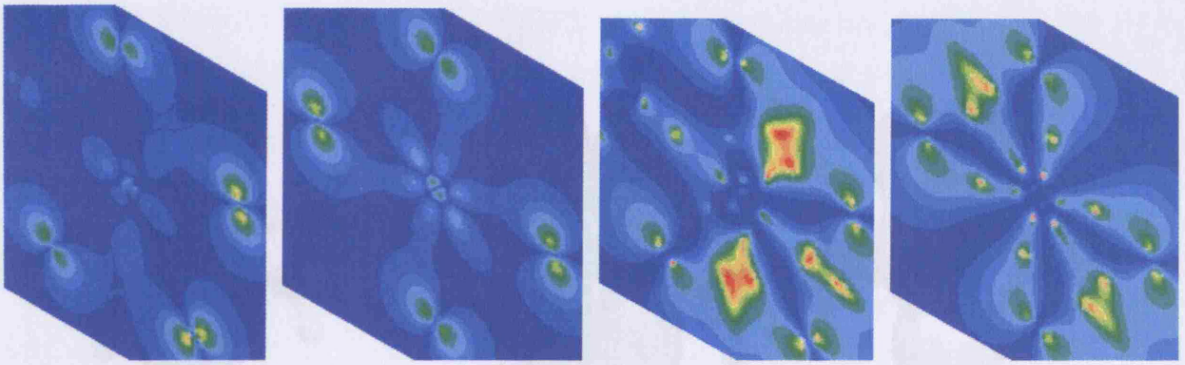

(a) 5W ρ(HOMO-8) (b) 4OH ρ(HOMO-4) (c) 5W LOL HOMO-8 (d) 4OH LOL HOMO-5

Figure 81(a)-(d). *(a) ρ(HOMO-8) (e^-/Bohr^3) in **5W** and (b) ρ(HOMO-4) (e^-/Bohr^3) in **4OH**, and electron localisation of the (c) HOMO-8 in **5W** and (d) HOMO-4 in **4OH**, in a plane through the equatorial plane, from DFT calculations. The maximum values of ρ and LOL are 0.3 (red) and 1 (red) and the minimum values 0 (blue).*

I also find σ-bonding in the equatorial plane for both **5W** and **4OH** (not shown), but the difference between them is insignificant, and hence give similar contribution to the covalent bonding.

The π_g MOs of **5W** and **4OH** in Figure 82, on the other hand, appear to interact with the ligands differently. The π_g MOs of **5W** are non-degenerate, while the π_g MOs of **4OH** are degenerate (the π_g MOs of **5W** should strictly be termed π_g-like, but I call them π_g for convenience); the degeneracy is due to the symmetric ligand field. The π_g MO in **5W** that has the highest (least negative) energy does not have any interaction with the equatorial plane, but the π_g MO that has the lower energy forms a π-bond with the water ligand that has its hydrogen atoms rotated 90 degrees compared with the other ligands. The contribution from the uranyl's and hydroxide's AOs to the π_g degenerate MOs of **4OH** are of the wrong symmetry to form π-bonds in a similar way as in **5W.** The π_g MO of **4OH** overlaps between uranyl and the hydroxide ligands by "bending" the π-bond towards the hydroxide ligands that have the same sign of the wavefunction (Figure 82(c)). The π_g MOs of **4OH** show more interaction between uranyl and its ligands, compared with the same MOs in **5W**, because all equatorial ligands in **4OH** form bonds to uranyl in the π_g MOs, while the equatorial bonding in the π_g MOs of **5W** only involves one ligand.

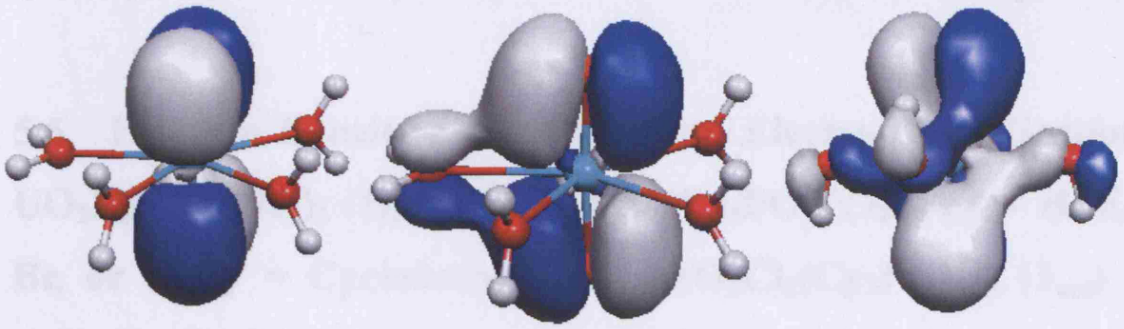

(a) 5W π_g (b) 5W π_g (c) 4OH π_g

Figure 82(a)-(c). *Uranyl π_g MOs from DFT calculations; (a) HOMO-9 for **5W**, (b) HOMO-10 for **5W**, and (c) HOMO-3 for **4OH**. The isosurface values are 0.03 for all MOs.*

The degenerate π_g MOs of **4OH** resemble the $\Delta\rho$ isosurfaces of **4OH** in Figure 70(c) - Figure 75(c); these figures show electrons flowing to the equatorial plane. Hence, the main conclusion from analysing $\Delta\rho$, electron localisation, and selected MOs is that electrons flow to the equatorial plane to a greater extent in **4OH** and are slightly more localised there in comparison with **5W**. This weakens the uranyl bond in **4OH** by decreasing ρ in the bonding region; the uranyl bond distance therefore increase. Both the water and hydroxide ligands form σ- and π-bonds in the equatorial plane, but the equatorial π-bonds of **4OH** are stronger, in particular the degenerate π_g MOs of **4OH** show greater interaction with the equatorial ligands, compared with the same MOs in **5W**. The difference between these MOs partly explains the greater flow of electron density to the equatorial plane for **4OH**.

This analysis modifies the conclusions in chapter 2 regarding the hypothesis of Clark *et al.*, which suggested that hydroxide ligands and O_{yl} compete to donate electrons, resulting in increased r(U-O_{yl}) in **4OH**. This now seems correct. The competition, however, does not originate from π-bonding in the equatorial plane, because the contributions from the hydroxide ligands to the uranyl π_g MO are of the wrong symmetry to form π-bonds with the uranium 6*d* AOs. The hydroxide ligands instead form bonds that can be described as combinations of π- and σ-bonds (Figure 82(c)). The hydroxide ligands also show greater interaction with the 5*f* orbitals through π-bonding in the equatorial plane, compared with

the water ligands in **5W**. Clark's hypothesis is based on D_{4h} symmetry; the lower symmetry of my calculations probably causes the distorted π-interaction in Figure 82(c).

5.5 Electron Density Differences and Electron Localization in $UO_2Z_2(Cy_3PNH)_2$ (1_{hal}) and $UO_2Z_2(Cy_3PO)_2$ (2_{hal}) (Z = H, F, Cl, Br, or I; Cy = Cyclohexyl), and $AcO_2Cl_2(Cy_3PNH)_2$ (1_{act}) and $AcO_2Cl_2(Cy_3PO)_2$ (2_{act}) (Ac = U, Np, Pu, or Am)

5.5.1 Electron Density Differences of the cis and trans Isomers of $UO_2Cl_2(Cy_3PNH)_2$ (1) and $UO_2Cl_2(Cy_3PO)_2$ (2) (Cy = Cyclohexyl)

In this section, I seek to find more information regarding the interaction between uranium and its ligands, in particular the equatorial U-N and U-O bonds and their effect on the uranyl bonds. I therefore calculate $\Delta\rho$ for **1** and **2** by dividing the molecules into two fragments: UO_2^{2+} and the equatorial ligands. I only show the uranium atom and its directly coordinated atoms, because it is too computationally demanding to accurately represent ρ on a grid for the whole molecule (ρ is, however, accurately represented in the DFT calculation). The orientation of the molecule is different from previous figures; Figure 83 shows the orientation of $\mathbf{1}_{trans}$ and $\mathbf{1}_{cis}$ in this section. The chlorine ligands are on the top and at the bottom of the figures in the *trans* isomers; the *cis* isomer has the first Cl-ligand above uranium, and the second behind and to the left of uranium. The first O_{yl} atom is in front and to the left of uranium, and the second is behind and to the right of uranium; the uranyl bond axis is the large red area in Figure 84. The O-donor and N-donor ligands locate the first ligand in front and to the right, and the second behind and to the left of uranium in the *trans* isomer, and the first in front and to the right, and the second below uranium in the *cis* isomer.

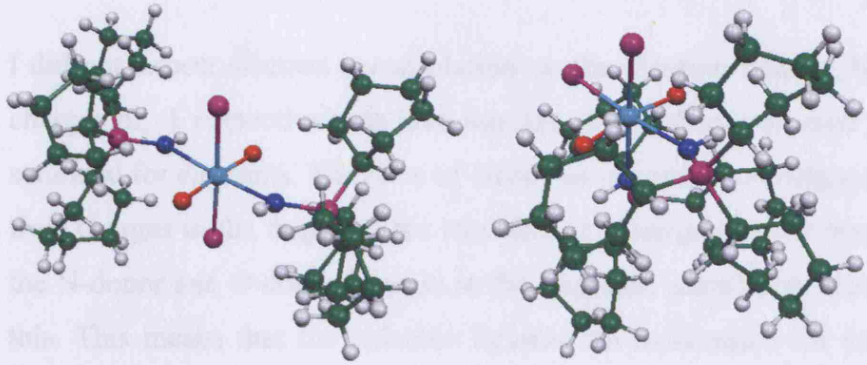

Figure 83(a)-(b). *Orientation of (a) $\mathbf{1}_{trans}$ and (b) $\mathbf{1}_{cis}$ in the Figure 84 below. The other compounds have similar orientations. The atoms have the following colours: O = red, U=cyan, N=blue, and Cl=purple.*

Figure 84 shows isosurfaces of $\Delta\rho$ for both isomers of **1** and **2**; it shows that electrons flow toward the chlorine ligands and to the lone pair regions of the O_{yl} atoms, as the fragments start to interact. The uranyl bond weakens in all complexes, more in the *trans* than the *cis* isomer, and more for N-donor ligands than O-donors. ρ increases in the bonding region of the equatorial plane between the N-donor ligands and uranium, and between the O-donor ligands and uranium. The electron accumulation in the equatorial bonding region between the N-donor ligands and uranium is slightly greater and closer to the uranium atom in comparison with between the O-donor ligands and uranium, in $\mathbf{1}_{trans}$ and $\mathbf{2}_{trans}$ respectively.

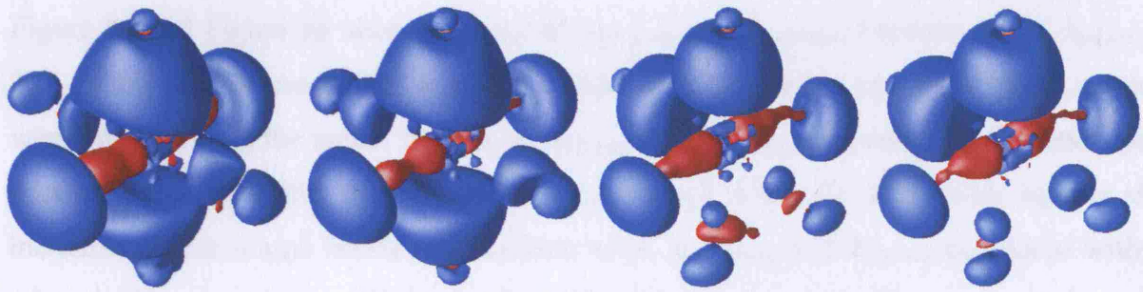

(a) $\mathbf{1}_{trans}$ **(b) $\mathbf{2}_{trans}$** **(c) $\mathbf{1}_{cis}$** **(d) $\mathbf{2}_{cis}$**

Figure 84(a)-(d). *Isosurfaces of $\Delta\rho$ ($e^-/Bohr^3$) in (a) $\mathbf{1}_{trans}$, (b) $\mathbf{2}_{trans}$, (c) $\mathbf{1}_{cis}$, and (d) $\mathbf{2}_{cis}$, from DFT calculations. The fragments consist of UO_2^{2+} and the equatorial ligands; the isosurface values are -0.02 (red) and 0.02 (blue).*

I did not expect electron accumulation on the chlorine ligands, because they have formal charges of -1 respectively as free ligands. If the charge of each Cl-ligand is -1, they are saturated for electrons. The flow of electrons towards the Cl-ligands therefore suggests that their charges in the fragment are less than -1. Charge transfer from the chlorine ligands to the N-donor and O-donor ligands in the fragment calculation is a possible explanation for this. This means that the chlorine ligands are unsaturated for electrons, and accumulate more electrons than the N-donor and O-donor ligands when the ligands start to interact with the uranyl ion. The larger electron accumulation in the equatorial bonding region between the N-donor ligands and uranium for $\mathbf{1}_{trans}$, and the greater weakening of the uranyl bond for **1** confirm the result in chapter 3: the softer N-donor ligands form stronger and more covalent bonds to uranyl in comparison with the harder O-donor ligands. The ligands' interaction with uranyl magnifies the dipole moment of the *cis* isomer, as the transfer of electrons to the chlorine ligands is larger than to the N-donor and O-donor ligands. It is also clear from the shape of the electron accumulation regions on the O_{yl} atoms that the dipole moment of the *cis* isomer redistributes electrons on the O_{yl} atoms towards the side of the O-donor and N-donor ligands. This is most likely the cause of the smaller bond angles of uranyl in the *cis* isomers.

5.5.2 Electron Density Differences of $\mathbf{1}_{hal,trans}$ and $\mathbf{2}_{hal,trans}$

Figure 85 and Figure 86 show only $\Delta\rho$ of $\mathbf{1}_{hal,trans}$ and $\mathbf{2}_{hal,trans}$, because $\Delta\rho$ of $\mathbf{1}_{hal,cis}$ and $\mathbf{2}_{hal,cis}$ show similar trends. The size of the blue isosurface in the equatorial plane increases when one traverses the halide ligands of $\mathbf{1}_{hal,trans}$ and $\mathbf{2}_{hal,trans}$. ρ around the fluorine ligands decreases slightly as they start to interact with uranyl, while all other halide ligands show increased ρ. The uranyl bonds also weaken more in $\mathbf{1}_{F,trans}$ and $\mathbf{2}_{F,trans}$, compared with the other halide complexes, although the differences are small. There are only minor differences between equatorial U-O and U-N interactions; $\mathbf{1}_{trans}$ and $\mathbf{2}_{trans}$ show the greatest differences regarding this interaction. The shapes of the blue isosurfaces at the nitrogen atoms are slightly more spherical than the same isosurfaces of the equatorial oxygen atoms. This is a potential sign of the σ character of the U-N bond.

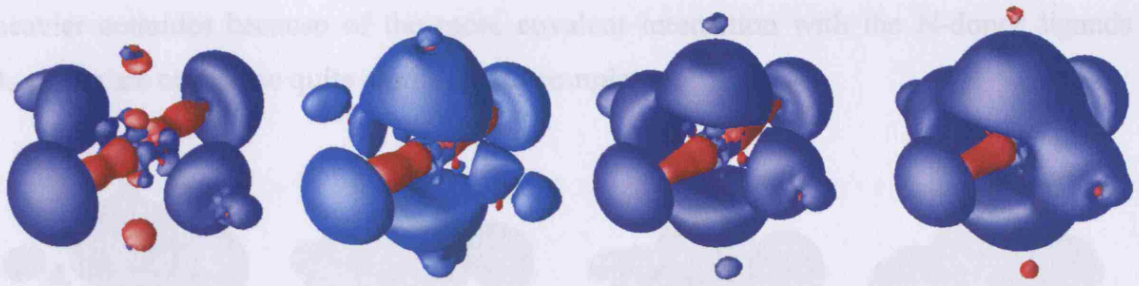

(a) $\mathbf{1}_{F,trans}$ (b) $\mathbf{1}_{trans}$ (c) $\mathbf{1}_{Br,trans}$ (d) $\mathbf{1}_{I,trans}$

Figure 85(a)-(d). *Isosurfaces of $\Delta\rho$ ($e^-/Bohr^3$) in (a) $\mathbf{1}_{F,trans}$, (b) $\mathbf{1}_{trans}$, (c) $\mathbf{1}_{Br,trans}$, and (d) $\mathbf{1}_{I,trans}$ from DFT calculations. The fragments are UO_2^{2+} and the equatorial ligands. The isosurface values are -0.02 (red) and 0.02 (blue).*

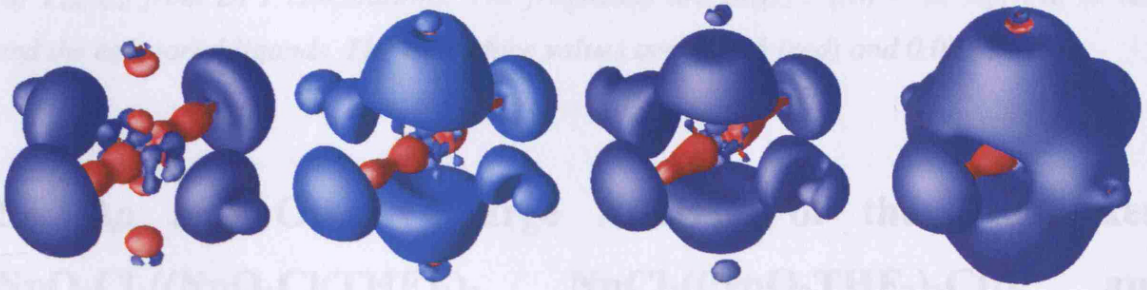

(a) $\mathbf{2}_{F,trans}$ (b) $\mathbf{2}_{trans}$ (c) $\mathbf{2}_{Br,trans}$ (d) $\mathbf{2}_{I,trans}$

Figure 86(a)-(d). *Isosurfaces of $\Delta\rho$ ($e^-/Bohr^3$) in (a) $\mathbf{2}_{F,trans}$, (b) $\mathbf{2}_{trans}$, (c) $\mathbf{2}_{Br,trans}$, and (d) $\mathbf{2}_{I,trans}$ from DFT calculations. The fragments are UO_2^{2+} and the equatorial ligands. The isosurface values are -0.02 (red) and 0.02 (blue).*

5.5.3 Electron Density Differences of $\mathbf{1}_{act,trans}$ and $\mathbf{2}_{act,trans}$

Figure 87 shows isosurfaces of $\Delta\rho$ in $\mathbf{1}_{act,trans}$. It reveals that the transfer of charge increases when going from $\mathbf{1}_{trans}$ to $\mathbf{1}_{Am,trans}$; ρ increases more in the equatorial plane in general, and around the N atoms in particular, and decreases more around the metal. This indicates greater ionic contributions to the bond between the actinide and the N-donor ligand. ρ decreases more in the actinyl bonding region of $\mathbf{1}_{trans}$, compared with $\mathbf{1}_{Am,trans}$; it is possible that ρ in the uranyl bonding region decreases more than in the actinyl bonding region of the

heavier actinides because of the more covalent interaction with the N-donor ligands in $\mathbf{1}_{trans}$. $\Delta\rho$ are otherwise quite similar in all complexes.

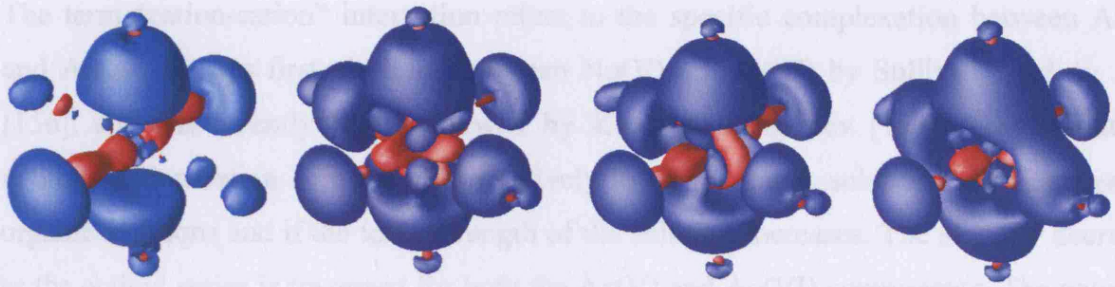

(a) $\mathbf{1}_{trans}$ (b) $\mathbf{1}_{Np,trans}$ (c) $\mathbf{1}_{Pu,trans}$ (d) $\mathbf{1}_{Am,trans}$

Figure 87(a)-(d). *Isosurfaces of $\Delta\rho$ ($e^-/Bohr^3$) in (a) $\mathbf{1}_{trans}$, (b) $\mathbf{1}_{Np,trans}$ (c) $\mathbf{1}_{Pu,trans}$, and (d) $\mathbf{1}_{Am,trans}$ from DFT calculations. The fragments are AnO_2^{2+} (An = U, Np, Pu, or Am) and the equatorial ligands. The isosurface values are -0.025 (red) and 0.025 (blue).*

5.6 $\Delta\rho$ and Other Charge Analysis of the Complexes: $NpO_2Cl_2((NpO_2Cl(THF)_3)_2$, $NpCl_3((NpO_2THF_2)_3Cl_4)$, and $((NpO_2)Cl_2THF)_n$.

My collaborators in Manchester have recently isolated crystals of the following complexes: $NpO_2Cl_2((NpO_2Cl(THF)_3)_2$ ($\mathbf{Np}_{tri}$), $NpCl_3((NpO_2)_3Cl_4THF_6)$ ($\mathbf{Np}_{tet}$), and $((NpO_2)Cl_2THF)_n$ ($\mathbf{Np}_{poly,exp}$). The two first complexes are prepared by allowing neptunyl(VI) solution in THF to stand for several weeks. They contain two and three neptunyl ions respectively that interact with each other by coordination of one and two O_{yl} atoms in the equatorial plane of the last neptunyl unit (i.e. "cation-cation" interaction). $\mathbf{Np}_{poly,exp}$ is prepared from $[NpO_2(OH)_2]_n$ in THF. I study here a piece of the polymer that contains three units, i.e. $((NpO_2)Cl_2THF)_3$ ($\mathbf{Np}_{poly}$). Np exists in three oxidation states in the complexes: Np(IV), Np(V), and Np(VI); all three complexes have several unpaired electrons ($\mathbf{Np}_{tri}$ has 5 unpaired electrons, $\mathbf{Np}_{tet}$ has 9 unpaired electrons, and $\mathbf{Np}_{poly,exp}$ has *n* unpaired electrons). The large size and the high number of unpaired electrons make the

complexes very computationally demanding; I therefore only perform single point calculations on the experimental crystal structures.

The term "cation-cation" interaction refers to the specific complexation between AnO_2^+ and AnO_2^{2+}. It was first observed between Np(V) and U(VI) by Sullivan *et al.* in 1961 [156], and has recently been reviewed by Krot and Grigoriev [157]. The stability of actinide cation-cation complexes is relatively low in aqueous solutions, but increases in organic solutions and if the ionic strength of the solution increases. The stability decreases as the actinyl series is traversed for both the Ac(V) and Ac(VI) components. The nature of the interaction is assumed to be mainly electrostatic, because the magnitudes of the positive charge of the actinide and the negative charge of O_{yl} decrease when going from UO_2^{2+} to AmO_2^{2+}. Cation-cation bonds in Np(V) compounds always form through a bridging O_{yl} atom of the NpO_2^+ ion, the bond length between the bridging O_{yl} atom and the Np(V) atom is 0.04 Å longer on average in the more than 20 cation-cation complexes that had been discovered by 2002 [157], in comparison with the NpO_2^+ complex without cation-cation interaction.

5.6.1 Geometries of Np_{tri}, Np_{tet}, and Np_{poly}

Figure 88 presents the geometries of $\mathbf{Np_{tri}}$, $\mathbf{Np_{tet}}$, and $\mathbf{Np_{poly}}$.

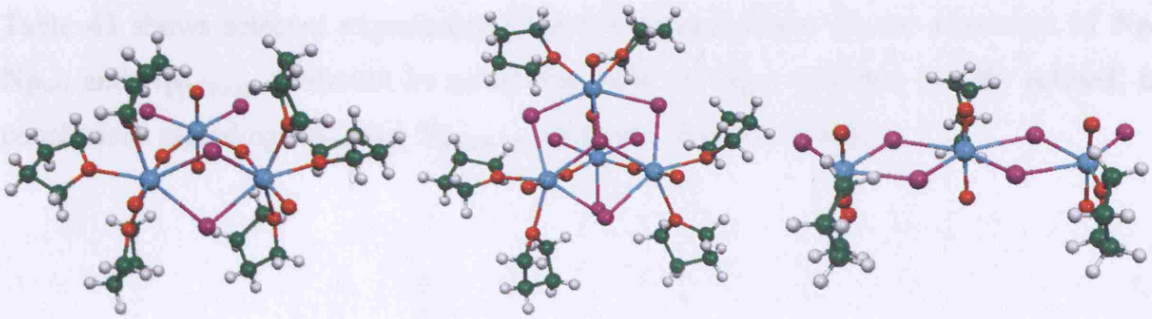

(a) $\mathbf{Np_{tri}}$ **(b) $\mathbf{Np_{tet}}$** **(c) $\mathbf{Np_{poly}}$**

Figure 88(a)-(c). *Ball and stick representation of the experimental crystal structures of (a) Np_{tri}, (b) Np_{tet}, and (c) Np_{poly}.*

The neptunyl unit in the back of Figure 88(a) consists of Np(1), $O_{yl}(1)$, and $O_{yl}(2)$. It coordinates two chlorine ligands (Cl(1) and Cl(2)) and two neptunyl units through their O_{yl} atoms ($O_{yl}(3)$ and $O_{yl}(4)$). The coordination of O_{yl} atoms of $[NpO_2]^+$ to the equatorial plane of an actinide in oxidation state VI has never been observed before. A chlorine bridge (the purple atoms in the middle of Figure 88(a)) connects those coordinating neptunyl units; these units also coordinate three THF ligands each. The first coordinating neptunyl unit consists of Np(2), $O_{yl}(3)$, and $O_{yl}(5)$, and the second of Np(3), $O_{yl}(4)$, and $O_{yl}(6)$. Np(1) is in oxidation state VI, and Np(2) and Np(3) are in oxidation state V.

The structure of $\mathbf{Np}_{tet}$ is quite similar to $\mathbf{Np}_{tri}$, the Np atom (Np(1)) in the back of Figure 88(b) coordinates three chlorine ligands (Cl(1), Cl(2), and Cl(3)) and three neptunyl units. All coordinating neptunyl units coordinate two THF ligands each, and they all have chlorine bridges between them. The crystal structure of $\mathbf{Np}_{tet}$ is close to C_{3v} symmetry; this makes the coordinating O_{yl} atoms ($O_{yl}(1)$, $O_{yl}(2)$, and $O_{yl}(3)$) in $\mathbf{Np}_{tet,large}$, the Np atoms (Np(2), Np(3), and Np(4)), and the additional O_{yl} atoms ($O_{yl}(4)$, $O_{yl}(5)$, and $O_{yl}(6)$) almost equivalent. Np(1) is in oxidation state IV, two of the Np atoms in the coordinating neptunyl units are in oxidation state V, and one in oxidation state VI.

$\mathbf{Np}_{poly,exp}$ is a polymer that consists of NpO_2THF units connected by chlorine bridges. Figure 88(c) shows three such connected units. The neptunium atoms in $\mathbf{Np}_{poly,exp}$ are in oxidation state VI.

Table 43 shows selected experimental bond distances of the crystal structures of $\mathbf{Np}_{tri}$, $\mathbf{Np}_{tet}$, and $\mathbf{Np}_{poly,exp}$. It should be noted that only the $\mathbf{Np}_{tri}$ structure is fully refined; my conclusions regarding $\mathbf{Np}_{tet}$ and $\mathbf{Np}_{poly,exp}$ are therefore preliminary.

Table 43. *Selected crystallographic bond lengths (Å) for complexes* $\mathbf{Np}_{tri}$, $\mathbf{Np}_{tet}$, *and* $\mathbf{Np}_{poly,exp}$.

$\mathbf{Np}_{tri}$		$\mathbf{Np}_{tet}$		$\mathbf{Np}_{poly,exp}$	
Np(1)-O_{yl}(1)	1.771(12)	Np(1)-O_{yl}(1)	2.23(3)	Np(1)-O_{yl}(1)	1.64(6)
Np(1)-O_{yl}(2)	1.793(10)	Np(1)-O_{yl}(2)	2.24(2)	Np(1)-O_{yl}(2)	1.93(6)
Np(1)-O_{yl}(3)	2.303(11)	Np(1)-O_{yl}(3)	2.25(2)		
Np(1)-O_{yl}(4)	2.317(11)	Np(1)-Cl(1)	2.575(9)		
Np(1)-Cl(1)	2.636(5)	Np(1)-Cl(2)	2.577(9)		
Np(1)-Cl(2)	2.626(5)	Np(1)-Cl(3)	2.605(10)		
Np(2)-O_{yl}(3)	1.912(11)	Np(2)-O_{yl}(1)	1.90(3)		
Np(2)-O_{yl}(5)	1.805(12)	Np(2)-O_{yl}(4)	1.79(2)		
Np(3)-O_{yl}(4)	1.885(11)	Np(3)-O_{yl}(2)	1.89(2)		
Np(3)-O_{yl}(6)	1.751(13)	Np(3)-O_{yl}(5)	1.76(2)		
		Np(4)-O_{yl}(3)	1.89(2)		
		Np(4)-O_{yl}(6)	1.77(3)		

r(Np(1)-O_{yl}(1)) and *r*(Np(1)-O_{yl}(2)) in $\mathbf{Np}_{tri}$ are similar to the analogous bonds in the Np-complexes discussed in chapter 3; the difference between the Np-O_{yl} bonds in $\mathbf{Np}_{tri}$ is more than 0.02 Å. *r*(Np(2)-O_{yl}(5)) and *r*(Np(3)-O_{yl}(6)) are also in the same range; the difference between these bonds is over 0.05 Å. *r*(Np(2)-O_{yl}(3)) and *r*(Np(3)-O_{yl}(4)) are about 0.1 Å longer than the other Np-O_{yl} bonds, because the O_{yl} atoms are also coordinating to the equatorial plane of Np(1). The coordination of the O_{yl} atoms in the equatorial plane show *r*(Np(1)-O_{yl}) of about 2.3 Å, similar to the equatorial *r*(U-O) in **4OH** (chapter 2).

r(Np-O_{yl}) in the three coordinating neptunyl units in $\mathbf{Np}_{tet}$ are similar to *r*(Np-O_{yl}) in the neptunyl units of $\mathbf{Np}_{tri}$. The coordination of O_{yl} atoms in the equatorial plane of Np(1) show shorter *r*(Np(1)-O_{yl}) than the equivalent equatorial coordination to Np(1) in $\mathbf{Np}_{tri}$. This is probably because the strong Np(1)-O_{yl}(1,2) bonds in $\mathbf{Np}_{tri}$ weakens all other bonds, in comparison with the Np(1) bonds in $\mathbf{Np}_{tet}$.

r(Np(1)-O_{yl}(1)) and *r*(Np(1)-O_{yl}(2)) in $\mathbf{Np}_{poly,exp}$ differ by almost 0.3 Å; this suggest that something is wrong with the crystal structure.

5.6.2 Charge Analysis

Table 44 shows Mulliken and Hirshfeld charges of $\mathbf{Np_{tri}}$ and its fragments.

Table 44. *Mulliken and Hirshfeld charges (e^-) in the gas phase for complexes Np_{tri}, $Np_{tri,large}$, and $Np_{tri,small}$.*

Mulliken	$\mathbf{Np_{tri}}$	$\mathbf{Np_{tri,large}}$	$\mathbf{Np_{tri,small}}$
Np(1)	1.55	-	1.36
Np(2)	1.72	1.53	-
Np(3)	1.75	1.56	-
Hirshfeld			
Np(1)	0.51	-	0.84
Np(2)	0.54	0.44	-
Np(3)	0.54	0.44	-

The Mulliken charges of the Np atoms are larger in $\mathbf{Np_{tri}}$ than in its fragments, i.e. Mulliken charges indicate that electrons move away from the Np atoms when the fragments start to interact. The Np atom in the small fragment has lower charge than the Np atoms in the large fragment – unexpected as Np(1) is in a higher formal oxidation state than Np(2) and Np(3). The differences between the charges of the Np atoms in $\mathbf{Np_{tri}}$ and its fragments are similar.

The large decrease between the Hirshfeld charges of Np(1) in $\mathbf{Np_{tri,small}}$ and in $\mathbf{Np_{tri}}$ is most likely because Np(1) coordinates six atoms in $\mathbf{Np_{tri}}$, but only four atoms in $\mathbf{Np_{tri,small}}$; Hirshfeld charges are very dependent on the number of coordinating ligands, because the integration volume changes drastically with the coordination number. The Hirshfeld charges are of lower magnitude than the Mulliken charges, and Np(2) and Np(3) have higher charge than Np(1) in $\mathbf{Np_{tri}}$.

Table 45 collects Mulliken and Hirshfeld charges of $\mathbf{Np_{tet}}$ and its fragments.

Table 45. *Mulliken and Hirshfeld charges (e^-) in the gas phase for complexes Np_{tet}, $Np_{tet,large}$, and $Np_{tet,small}$.*

Mulliken	$\mathbf{Np_{tet}}$	$\mathbf{Np_{tet,large}}$	$\mathbf{Np_{tet,small}}$
Np(1)	1.40	-	0.92
Np(2)	1.57	1.46	-
Np(3)	1.58	1.47	-
Np(4)	1.58	1.46	-
Hirshfeld			
Np(1)	0.49	-	0.68
Np(2)	0.51	0.47	-
Np(3)	0.51	0.47	-
Np(4)	0.50	0.47	-

The Mulliken charges of $\mathbf{Np_{tet}}$ are also higher than in its fragments. All Np charges are lower in $\mathbf{Np_{tet}}$ and its fragments in comparison with $\mathbf{Np_{tri}}$ and its fragments. The lower charge of Np(1) is expected, because Np(1) is in a lower oxidation state than the other Np atoms.

The magnitude of the Hirshfeld charges are also lower in $\mathbf{Np_{tet}}$ than in $\mathbf{Np_{tri}}$. The different coordination number of $\mathbf{Np_{tet}}$ and $\mathbf{Np_{tet,small}}$ is responsible for the large charge difference between them. The Hirshfeld charges are otherwise higher in $\mathbf{Np_{tet}}$ than in the large fragment, although the difference is not as large as in $\mathbf{Np_{tri}}$.

Table 46 presents Mulliken and Hirshfeld charges for $\mathbf{Np_{poly}}$ and its fragments.

Table 46. *Mulliken and Hirshfeld charges (e^-) in the gas phase for complexes Np_{poly}, $Np_{poly,mid}$, and $Np_{poly,side}$.*

Mulliken	$\mathbf{Np}_{poly}$	$\mathbf{Np}_{poly,mid}$	$\mathbf{Np}_{poly,side}$
Np(1)	1.42	-	1.47
Np(2)	1.42	1.47	-
Np(3)	1.42	-	1.47
Hirshfeld			
Np(1)	0.53	-	0.71
Np(2)	0.61	0.71	-
Np(3)	0.62	-	0.71

The Mulliken charges are slightly lower in $\mathbf{Np}_{poly}$ compared with in the fragments, opposite to $\mathbf{Np}_{tri}$ and $\mathbf{Np}_{tet}$. The magnitudes of the charges are similar to Np(1) in $\mathbf{Np}_{tet}$, but lower than all other Np atoms in $\mathbf{Np}_{tri}$ and $\mathbf{Np}_{tet}$.

The large charge difference between $\mathbf{Np}_{poly}$ and its fragments is due to the different coordination number in $\mathbf{Np}_{poly}$ and the fragments. The Hirshfeld charges are higher in $\mathbf{Np}_{poly}$ than in $\mathbf{Np}_{tri}$ and $\mathbf{Np}_{tet}$, opposite to the Mulliken charges. The charge difference between Np(1) and Np(3) in $\mathbf{Np}_{poly}$ is quite large.

5.6.3 Mayer Bond Orders

Table 47 contains MBOs of selected bonds in $\mathbf{Np_{tri}}$.

Table 47. *MBOs of selected bonds in the gas phase for the complex* $\boldsymbol{Np_{tri}}$.

Bond	MBO	Bond	MBO	Bond	MBO
Np(1)-O_{yl}(1)	2.01	Np(2)-O_{yl}(3)	1.54	Np(3)-O_{yl}(4)	1.58
Np(1)-O_{yl}(2)	2.01	Np(2)-O_{yl}(5)	2.08	Np(3)-O_{yl}(6)	2.08
Np(1)-O_{yl}(3)	0.41				
Np(1)-O_{yl}(4)	0.37				
Np(1)-Cl(1)	0.95				
Np(1)- Cl(2)	0.95				

The MBOs of the Np(1)-O_{yl}(1) and Np(1)-O_{yl}(2) bonds are slightly lower than the Np(2)-O_{yl}(5) and Np(3)-O_{yl}(6) bonds, while the Np(2)-O_{yl}(3) and Np(3)-O_{yl}(4) bonds show significantly lower MBOs. The coordination of O_{yl}(3) and O_{yl}(4) to the equatorial plane of Np(1) seems to weaken the neptunyl bonds of the coordinating O_{yl} atoms, but strengthen the neptunyl bonds of the uncoordinated O_{yl} atoms. The Np(1)-O_{yl}(3) and Np(1)-O_{yl}(4) bonds show much lower MBOs.

Table 48 contains MBOs of selected bonds in $\mathbf{Np_{tet}}$.

Table 48. *MBOs of selected bonds in the gas phase for the complex* $\boldsymbol{Np_{tet}}$.

Bond	MBO	Bond	MBO
Np(1)-O_{yl}(1)	0.45	Np(2)-O_{yl}(1)	1.44
Np(1)-O_{yl}(2)	0.47	Np(2)-O_{yl}(4)	2.10
Np(1)-O_{yl}(3)	0.48	Np(3)-O_{yl}(2)	1.47
Np(1)-Cl(1)	0.94	Np(3)-O_{yl}(5)	2.09
Np(1)-Cl(2)	0.97	Np(4)-O_{yl}(3)	1.45
Np(1)-Cl(3)	0.93	Np(4)-O_{yl}(6)	2.10

The MBOs of the neptunyl units in $\mathbf{Np}_{tet}$ are similar to the MBOs of the coordiniating neptunyl units in $\mathbf{Np}_{tri}$, although the MBOs between the Np atoms and the O_{yl} atoms that coordinates to Np(1) is about 0.1 smaller than in $\mathbf{Np}_{tri}$. The MBOs between Np(1) and the O_{yl} atoms are higher than the MBOs between Np(1) and the O_{yl} atoms in the equatorial plane of Np(1) in $\mathbf{Np}_{tri}$, indicating stronger bonds between Np(1) and the O_{yl} atoms in $\mathbf{Np}_{tet}$.

Table 49 provides MBOs for the neptunyl bonds in $\mathbf{Np}_{poly}$.

Table 49. *MBOs in the gas phase for the complex* $\mathbf{Np}_{poly}$.

Bond	MBO
Np(2)-O_{yl}(1)	2.12
Np(2)-O_{yl}(2)	2.10

The MBOs of $\mathbf{Np}_{poly}$ are similar to the non-coordinating neptunyl bonds in $\mathbf{Np}_{tri}$ and $\mathbf{Np}_{tet}$. Both bonds have similar MBOs, despite that the difference in r(Np-O_{yl}) is 0.3 Å.

5.6.4 *Electron Density Differences for $NpO_2Cl_2(NpO_2Cl(THF)_3)_2$*

Figure 89 shows isosurfaces of $\Delta\rho$ corresponding to different cutoff values in $\mathbf{Np_{tri}}$, and Figure 90 shows the orientation of the part of $\mathbf{Np_{tri}}$ that Figure 89 shows.

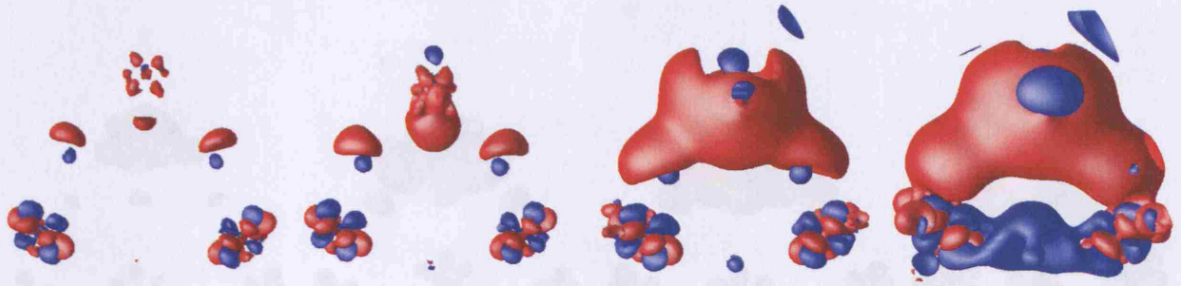

(a) $\Delta\rho$ $\mathbf{Np_{tri}}$ **(b) $\Delta\rho$ $\mathbf{Np_{tri}}$** **(c) $\Delta\rho$ $\mathbf{Np_{tri}}$** **(d) $\Delta\rho$ $\mathbf{Np_{tri}}$**

Figure 89(a)-(d). *Isosurfaces of $\Delta\rho$ ($e^-/Bohr^3$) of $\mathbf{Np_{tri}}$ with cutoff values: (a) +-0.015, (b) +-0.01 (c) +-0.005, and (d) +-0.002 from DFT calculations. The fragments are NpO_2Cl_2 ($\mathbf{Np_{tri,small}}$) and $(NpO_2Cl_2(THF)_3)_2$ ($\mathbf{Np_{tri,large}}$).*

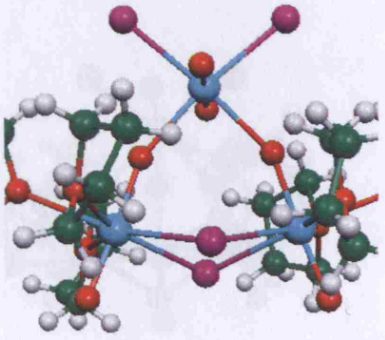

Figure 90. *Orientation of $\mathbf{Np_{tri}}$ in Figure 89.*

The main feature of Figure 89 is the electron transfer from the small fragment to the large fragment, as they start to interact. The electrons mainly accumulate in the region around the chlorine bridge. There is no electron accumulation between the O_{yl} atoms in $\mathbf{Np_{tri,large}}$ and the Np(1) atom in $\mathbf{Np_{tri,small}}$, but the decrease of charge in this area is smaller than

between the Np(1) – O_{yl} bonds (Figure 89a-b). ρ shows the largest decrease in the "lone pair region" of the two coordinating O_{yl} atoms ($O_{yl}(3)$ and $O_{yl}(4)$) in the large fragment. Some redistribution of electrons occurs around the Np atoms. $\Delta\rho$ is consistent with the Mulliken charges that are more positive in $\mathbf{Np_{tri}}$ than in its fragments.

Figure 91 shows isosurfaces of $\Delta\rho$ corresponding to different cutoff values in $\mathbf{Np_{tet}}$, and Figure 92 shows the orientation of the part of $\mathbf{Np_{tet}}$ that is shown in Figure 91.

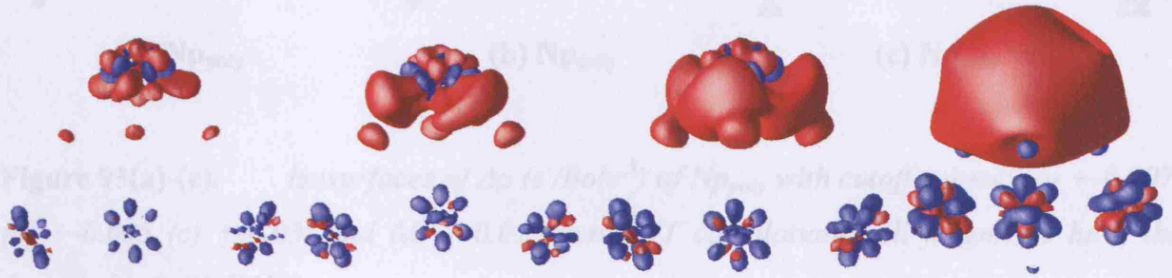

(a) $\mathbf{Np_{tet}}$ **(b) $\mathbf{Np_{tet}}$** **(c) $\mathbf{Np_{tet}}$** **(d) $\mathbf{Np_{tet}}$**

Figure 91(a)-(d). *Isosurfaces of $\Delta\rho$ ($e^-/Bohr^3$) of $\mathbf{Np_{tet}}$ with cutoff values: (a) +-0.05, (b) +-0.035 (c) +-0.03, and (d) +-0.01 from DFT calculations. The fragments are $NpCl_3$ ($\mathbf{Np_{tet,small}}$) and $(NpO_2THF_2)_3Cl_4$ ($\mathbf{Np_{tet,large}}$).*

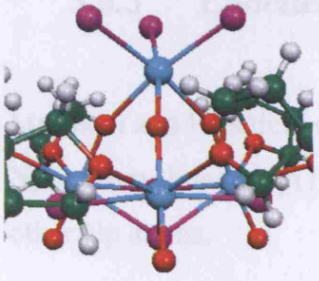

Figure 92. *Orientation of $\mathbf{Np_{tet}}$ in Figure 91.*

$\Delta\rho$ in Figure 91 possesses similar features as $\Delta\rho$ in Figure 89; the small fragment transfers electrons to the large fragment and ρ decreases in the bonding region between the fragments, although not quite as much as between the bonding regions between Np(1) and $O_{yl}(1\text{-}3)$.

Figure 93 shows isosurfaces of $\Delta\rho$ corresponding to different cutoff values in $\mathbf{Np}_{poly}$ and the orientation of the $\mathbf{Np}_{poly}$ in those pictures.

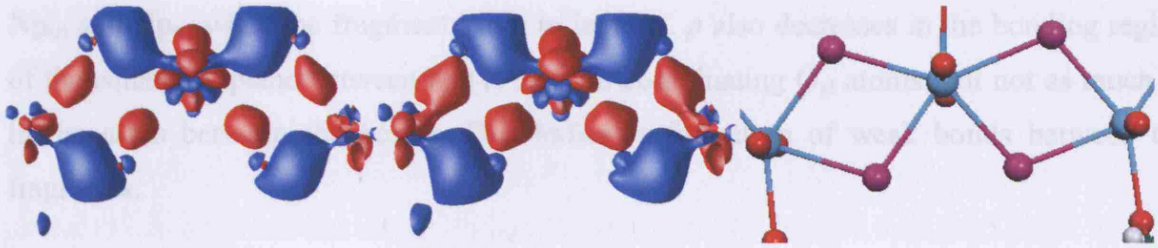

(a) $\mathbf{Np}_{poly}$ **(b) $\mathbf{Np}_{poly}$** **(c) $\mathbf{Np}_{poly}$**

Figure 93(a)-(c). *Isosurfaces of $\Delta\rho$ ($e^-/Bohr^3$) of $\mathbf{Np}_{poly}$ with cutoff values: (a) +-0.007, (b) +-0.005 (c) +-0.03, and (d) +-0.01 from DFT calculations. All fragments have the formula $NpO_2Cl_2(THF)$.*

The blue surfaces between the fragments correspond to bond formation between the Np and the Cl atoms and the red surfaces are bonds within the fragments that weaken, as the fragments start to interact and forming bonds between them.

5.6.5 Conclusions

Mulliken and Hirshfeld charges show lower charges in Np(1) than in the other Np atoms of $\mathbf{Np}_{tri}$, even though Np(1) is in oxidation state VI, compared with oxidation state V in the other Np atoms.

The coordination of the neptunyl units to the neptunium atoms in $\mathbf{Np}_{tri}$ and $\mathbf{Np}_{tet}$ increases r(Np-O_{yl}) between the coordinating O_{yl} atoms and the Np atoms in the coordinating neptunyl units, and decreases the MBOs of the same bond. This indicates a weakening of the bond. The MBOs of the neptunyl bonds that include the coordinating O_{yl} atoms are slightly lower in $\mathbf{Np}_{tet}$ in comparison with $\mathbf{Np}_{tri}$. The neptunyl bonds in the coordinating neptunyl units that include the non-coordinating O_{yl} atoms show higher MBOs than the

non-coordinating neptunyl unit in $\mathbf{Np}_{tri}$, possibly as a consequence of the weakening of the neptunyl bonds that include the coordinating O_{yl} atoms.

The general feature of the $\Delta\rho$ analysis is that electrons move away from the Np atoms in $\mathbf{Np}_{tri}$ and $\mathbf{Np}_{tet}$ when the fragments start to interact. ρ also decreases in the bonding region of the equatorial plane between Np(1) and the coordinating O_{yl} atoms, but not as much as in the areas between the bonds. This indicates formation of weak bonds between the fragments.

5.7 Conclusions

I have used electron localisation indicators on a range of actinide complexes with mixed results. Electron localisation is generally low in the bonding region, and the difference, in absolute numbers, between different actinide molecules is small. It is, however, more informative to calculate LOL on single MOs.

The extent to which analysis of $\Delta\rho$ yields insight depends on the complexes investigated. I find the results on the $[UO_2(H_2O)_m(OH)_n]^{2-n}$ ($m+n = 5$) most interesting, since they show a clear distinction between the interaction between water and hydroxide ligands. Electron density differences often contain information that is hard to obtain with for example analysis of MOs. Analysis of $\Delta\rho$ is therefore a good complement to MO analysis, and an extra "tool" for computational chemists to study bond formation. It is more difficult to draw any conclusions from the $\Delta\rho$ between the fragments of the Np-complexes that show cation-cation interaction, mainly because of the large charge transfer between the fragments.

5.8 Future work

The study in chapter 2 can be extended to include the neptunyl, plutonyl, and americyl ions.

A study of the relative stability of Cy_3PNH and Cy_3PO ligands in solutions would be useful to draw more compelling conclusions why Cy_3PNH ligands displace Cy_3PO ligands.

More work is required to better understand electron localisation in actinyl complexes, and whether the description of DFT is accurate enough for this purpose. An extension of the study on UO_2^{2+}, UNO^+, and UN_2 to include other xc-functionals and the effects of other approximations would be useful.

References

1. M. J. Sarsfield, M. Helliwell, and J. Raftery, *Inorg. Chem.* **43** 3170 (2004)
2. K. I. M. Ingram and N. Kaltsoyannis, *Recent advances in actinide science*; Royal Society of Chemistry, Cambridge, (2006).
3. D. L. Clark, *Los Alamos Science*. **26** 367 (2000)
4. *Chemical engineering news*. **23** 2085 (1945)
5. N. Kaltsoyannis and P. Scott, *The f elements*; Oxford University Press, Oxford, (1999).
6. N. Kaltsoyannis, *Inorg. Chem.* **39** 6009 (2000)
7. M. Pepper and B. Bursten, *Chem. Rev.* **91** 719 (1991)
8. C. K. Jørgensen and R. Reisfeld, *Struct. Bonding*. **50** 121 (1982)
9. K. Tatsumi and R. Hoffmann, *Inorg. Chem.* **19** 2656 (1980)
10. R. G. Denning, *J. Phys. Chem. A*. **111** 4125 (2007)
11. M. H. Klaproth, *Chem. Ann.* **II** 387 (1789)
12. E. Peligot, *J. Prakt. Chem.* **1** 442 (1841)
13. E. Peligot, *C. R. Acad. Sci.* **12** 735 (1841)
14. E. Peligot, *C. R. Acad. Sci.* **13** 417 (1841)
15. E. Peligot, *Ann. Chim. Phys.* . **3** 549 (1842)
16. E. Peligot, *Ann. Chim. Phys.* **3** 549 (1844)
17. G. T. Seaborg, L. R. Morss, and J. J. Katz, *The chemistry of the actinide elements vol 1*; London, (1986).
18. G. Gordon and H. Taube, *J. Inorg. Nucl. Chem.* **19** 189 (1961)
19. C. Nguyen-Trung, G. M. Begun, and D. A. Palmer, *Inorg. Chem.* **31** 5280 (1992)
20. E. M. McMillan and P. H. Abelson, *Phys. Rev.* **57** 1185 (1940)
21. G. T. Seaborg, E. M. McMillan, J. W. Kennedy, and A. C. Wahl, *Phys. Rev.* **69** 366 (1946)
22. A. Michaudon, *Los Alamos Science*. **26** 62 (2000)
23. R. S. Pepling. *Americium*. 2003 Available from: http://pubs.acs.org/cen/80th/americium.html.
24. Seaborg, James, Morgan, and Giorso, *National Nuclear Energy Series, Plutonium Project Record, Vol14b, The Transuranium Elements: Research papers, Paper No. 22.1*; McGraw-Hill Book Company, Inc., New York, (1949).
25. N. Bohr, *Philosophical Magaine*. **26** 1 (1913)
26. N. Bohr, *Philosophical Magaine*. **26** 476 (1913)
27. N. Bohr, *Philosophical Magaine*. **26** 857 (1913)
28. E. Schrödinger, *Annalen der Physik*. **79** 361 (1926)
29. E. Schrödinger, *Annalen der Physik*. **79** 489 (1926)
30. E. Schrödinger, *Annalen der Physik*. **79** 734 (1926)
31. E. Schrödinger, *Annalen der Physik*. **80** 437 (1926)
32. E. Schrödinger, *Annalen der Physik*. **81** 109 (1926)
33. E. Schrödinger, *Phys. Rev.* **28** 1049 (1926)
34. M. Born and R. Oppenheimer, *Ann. Physik*. **84** 457 (1927)
35. J. C. Slater, *Proc. Nat. Acad. Sci.* **13** 423 (1927)
36. P. M. W. Gill, *DFT, HF and the self-consistent field*; The Encyclopedia of computational chemistry, Wiley, New York, (1998).

37. D. R. Hartree, *Proc. Camb. Phil. Soc.* **24** 89 (1928)
38. V. Fock, *Z. Physik.* **60** 126 (1930)
39. N. C. Handy and A. J. Cohen, *Mol. Phys.* **99** 403 (2001)
40. F. Jensen, *Introduction to computational chemistry*; Wiley, Chichester, (1999).
41. W. Koch and M. C. Holthausen, *A chemist's guide to density functional theory*; Wiley, Weinheim, (2000).
42. E. Fermi, *Z. Phys.* **48** (1928)
43. L. H. Thomas, *Proc. Camb. Phil. Soc.* **23** 542 (1927)
44. P. A. M. Dirac, *Proc. Camb. Phil. Soc.* **26** 376 (1930)
45. C. F. Weizsäcker, *Z. Phys.* **96** 431 (1935)
46. N. H. March, *Int. J. Quantum Chem.* **101** 494 (2005)
47. P. Hohenberg and W. Kohn, *Phys. Rev.* **136** B864 (1964)
48. W. Kohn and L. J. Sham, *Phys. Rev.* **140** A1133 (1965)
49. F. M. Bickelhaupt and E. J. Baerends, *Reviews in Computational Chemistry.* **15** 1 (2000)
50. E. J. Baerends and O. V. Gritsenko, *J. Phys. Chem. A.* **101** 5383 (1997)
51. R. F. Bader, S. Johnson, T. H. Tang, and P. L. A. Popelier, *J. Phys. Chem.* **100** 15398 (1996)
52. A. D. Becke, *Phys. Rev. A.* **38** 3098 (1988)
53. A. D. Becke and K. E. Edgecombe, *J. Chem. Phys.* **92** 5397 (1990)
54. J. P. Perdew, A. Ruzsinszky, J. Tao, V. N. Stroverov, G. E. Scuseria, and G. I. Csonka, *J. Chem. Phys.* **123** 062201 (2005)
55. S. J. Vosko, L. Wilk, and M. Nusair, *Can. J. Phys.* **58** 1200 (1980)
56. J. P. Perdew and Y. Wang, *Phys. Rev. B.* **45** 13244 (1992)
57. A. D. Becke, *J. Chem. Phys.* **98** 5648 (1993)
58. L. A. Curtiss, K. Raghavachari, G. W. Tucks, and J. A. Pople, *J. Chem. Phys.* **94** 7221 (1991)
59. L. A. Curtiss, K. Raghavachari, P. C. Redfern, and J. A. Pople, *J. Chem. Phys.* **106** 1063 (1997)
60. J. Tao, J. P. Perdew, V. N. Staroverov, and G. E. Scuseria, *Phys. Rev. Lett.* **91** 146401 (2003)
61. D. C. Langreth and J. P. Perdew, *Phys. Rev. B.* **21** 5469 (1980)
62. J. P. Perdew, K. Burke, and M. Ernzerhof, *Phys. Rev. Lett.* **77** 3865 (1996)
63. J. P. Perdew, K. Burke, and M. Ernzerhof, *Phys. Rev. Lett.* **78** 1396 (1997)
64. A. D. Becke, *J. Chem. Phys.* **98** 1372 (1993)
65. V. A. Rassalov, M. A. Ratner, and J. A. Pople, *J. Chem. Phys.* **112** 4014 (2000)
66. A. D. Becke, *J. Chem. Phys.* **96** 2155 (1992)
67. A. D. Becke, *J. Chem. Phys.* **97** 9173 (1992)
68. A. D. Becke, *J. Chem. Phys.* **104** 1040 (1996)
69. A. D. Becke, *J. Chem. Phys.* **107** 8554 (1997)
70. J. P. Perdew, J. A. Chevary, S. H. Vosko, K. A. Jackson, M. R. Pederson, D. J. Singh, and C. Fiolhais, *Phys. Rev. B.* **46** 6671 (1992)
71. P. J. Stephens, F. J. Devlin, C. F. Chablowski, and M. J. Frisch, *J. Phys. Chem.* **98** 11623 (1994)
72. A. D. Becke, *J. Phys. Chem.* **98** 7 (1993)
73. I. Levine, *Quantum Chemistry*; Prentice Hall, New Jersey, (2000).
74. *ADF2004.01; SCM, Theoretical Chemistry, Vrije Universiteit.* 2004: Amsterdam, The Netherlands http://www.scm.com.
75. M. J. Frisch, G. W. Trucks, H. B. Schlegel, G. E. Scuseria, M. A. Robb, J. R. Cheeseman, J. A. Montgomery, T. J. Vreven, K. N. Kudin, J. C. Burant, J. M.

Millam, S. S. Iyengar, J. Tomasi, V. Barone, B. Mennucci, M. Cossi, G. Scalmani, N. Rega, G. A. Petersson, H. Nakatsuji, M. Hada, M. Ehara, K. Toyota, R. Fukuda, J. Hasegawa, M. Ishida, T. Nakajima, Y. Honda, O. Kitao, H. Nakai, M. Klene, X. Li, J. E. Knox, H. P. Hratchian, J. B. Cross, C. Adamo, J. Jaramillo, R. Gomperts, R. E. Stratmann, O. Yazyev, A. J. Austin, R. Cammi, C. Pomelli, J. W. Ochterski, P. Y. Ayala, K. Morokuma, G. A. Voth, P. Salvador, J. J. Dannenberg, V. G. Zakrzewski, S. Dapprich, A. D. Daniels, M. C. Strain, O. Farkas, D. K. Malick, A. D. Rabuck, K. Raghavachari, J. B. Foresman, J. V. Ortiz, Q. Cui, A. G. Baboul, S. Clifford, J. Cioslowski, B. B. Stefanov, G. Liu, A. Liashenko, P. Piskorz, I. Komaromi, R. L. Martin, D. J. Fox, T. Keith, M. A. Al-Laham, C. Y. Peng, A. Nanayakkara, M. Challacombe, P. M. W. Gill, B. Johnson, W. Chen, M. W. Wong, C. Gonzalez, and J. Pople, *Gaussian 03, Revision C02*. 2003, Gaussian: Pittsburgh PA.

76. X. Cao, M. Dolg, and H. Stoll, *J. Chem. Phys.* **118** 487 (2003)
77. E. Van Lenthe, E. J. Baerends, and J. G. Snijders, *J. Chem. Phys.* **99** 4597 (1993)
78. E. Van Lenthe, E. J. Baerends, and J. G. Snijders, *J. Chem. Phys.* **101** 9783 (1994)
79. E. van Lenthe, A. E. Ehlers, and E. J. Baerends, *J. Chem. Phys.* **110** 8943 (1999)
80. E. Van Lenthe, J. G. Snijders, and E. J. Baerends, *J. Chem. Phys.* **105** 6505 (1996)
81. E. Van Lenthe, R. van Leeuwen, E. J. Baerends, and J. G. Snijders, *int. J. Quantum Chem.* **57** 281 (1996)
82. P. A. M. Dirac, *Proc. Royal Soc. London.* **A117** 610 (1928)
83. M. Cossi, G. Scalmani, N. Rega, and V. Barone, *J. Chem. Phys.* **117** 43 (2002)
84. M. Cossi, N. Rega, G. Scalmani, and V. Barone, *J. Comput. Chem.* **24** 669 (2003)
85. A. Klamt, *J. Phys. Chem.* **99** 2224 (1995)
86. A. Klamt and G. Schüürmann, *J. Chem. Soc. Perkin Trans.* **2** 799 (1993)
87. J. L. Pascual-Ahuir, E. Silla, J. Tomasi, and R. Bonaccorsi, *J. Comput. Chem.* **8** 778 (1987)
88. J. L. Pascual-Ahuir, E. Silla, and I. Tunon, *J. Comput. Chem.* **15** 1127 (1994)
89. P. Scarlin, R. Battino, E. Silla, I. Tunon, and J. L. Pascual-Ahuir, *Pure & Appl. Chem.* **70** 1895 (1998)
90. M. Cossi and V. Barone, *European Summerschool in Quantum Chemistry 2005 - Book III: Solvent Effects by Effective Hamiltonian Model*; Chemical Centre Printshop, Lund, (2005).
91. V. Barone, M. Cossi, and J. Tomasi, *J. Chem. Phys.* **107** 3210 (1997)
92. R. S. Mulliken, *J. Chem. Phys.* **23** 1833 (1955)
93. R. S. Mulliken, *J. Chem. Phys.* **23** 2343 (1955)
94. G. te Velde, *PhD thesis*. 1990, Vrije Universiteit: Amsterdam.
95. F. M. Bickelhaupt, N. R. J. van Eikema Hommes, C. Fonseca Guerra, and E. J. Baerends, *Organometallics*. **15** 2923 (1992)
96. F. M. Bickelhaupt, C. Fonseca Guerra, J. W. Handgraaf, and E. J. Baerends, *in preparation*,
97. F. L. Hirshfeld, *Theoret. Chim Acta*. **44** 129 (1977)
98. K. B. Wiberg and R. R. B., *J. Comput. Chem.* **14** 1504 (1993)
99. G. Te Velde, F. M. Bickelhaupt, E. J. Baerends, C. Fonseca Guerra, S. J. A. van Gisenbergen, J. G. Snijders, and T. Ziegler, *J. Comput. Chem.* **24** 931 (2001)
100. P. Bultinck, *Personal communication*.
101. I. Mayer, *Chem. Phys. Lett.* **97** 270 (1983)
102. A. J. Bridgeman, G. Cavigliasso, L. R. Ireland, and J. Rothery, *J. Chem. Soc. Dalton Trans.*, 2095 (2001)

103. A. Savin, O. Jepsen, J. Flad, O. K. Andersen, H. Preuss, and H. G. von Schnering, *Angew. Chem. Int. Ed.* **31** 187 (1992)
104. A. D. Becke, *J. Chem. Phys.* **112** 4020 (2000)
105. H. L. Schmider and A. D. Becke, *J. Mol. Struct.* **527** 51 (2000)
106. M. Kohout, K. Pernal, F. R. Wagner, and Y. Grin, *Theor. Chem Acc.* **112** 453 (2004)
107. M. Kohout, *Int. J. Quantum Chem.* **97** 651 (2004)
108. M. Kohout, F. R. Wagner, and Y. Grin, *Int. J. Quantum Chem.* **106** 1499 (2006)
109. M. Kohout, *Program DGrid, version 4.2.* 2007.
110. *OpenDX: available free at : http://www.opendx.org.*
111. G. Schreckenbach and T. Ziegler, *Theor. Chem Acc.* **99** 71 (1998)
112. G. Schreckenbach, *Int. J. Quantum Chem.* **101** 372 (2005)
113. P. J. Wilson, R. D. Amos, and N. C. Handy, *Mol. Phys.* **97** 757 (1999)
114. A. M. Lee, N. C. Handy, and S. M. Colwell, *J. Chem. Phys.* **103** 10095 (1995)
115. K. Ruud, T. Helgaker, R. Kobayashi, P. Jorgenses, K. L. Bak, and H. J. A. Jensen, *J. Chem. Phys.* **100** 8178 (1994)
116. A. D. Becke, *Can. J. Chem.* **74** 995 (1996)
117. U. Wahlgren, H. Moll, B. Schimmelpfennig, L. Maron, V. Vallet, and O. Gropen, *J. Phys. Chem.* **103** 8257 (1999)
118. S. Tsushima and A. Suzuki, *J. Mol. Struct.* **529** 21 (2000)
119. P. J. Hay, R. L. Martin, and G. Schreckenbach, *J. Phys. Chem. A.* **104** 6259 (2000)
120. I. Grenthe, J. Fuger, R. J. M. Konings, R. J. Lemire, A. B. Muller, C. Nguyen-Trung, and H. Wanner, *Chemical Thermodynamics of Uranium*; North Holland, Amsterdam, (1992).
121. D. L. Clark, S. D. Conradson, R. J. Donohoe, D. W. Keogh, D. E. Morris, P. D. Palmer, R. D. Rogers, and D. Tait, *Inorg. Chem.* **38** 1456 (1999)
122. J. L. Sonnenberg, P. J. Hay, R. L. Martin, and B. Bursten, *Inorg. Chem.* **44** 2255 (2005)
123. T. Fujii, K. Fujiwara, H. Yamana, and H. Moriyama, *J. Alloys Comp.* **323-324** 859 (2001)
124. L. M. Toth and G. M. Begun, *J. Phys. Chem.* **85** 547 (1981)
125. F. Quilés and A. Burneau, *Vib. spectrosc.* **23** 231 (2000)
126. M. Gál, P. L. Goggin, and J. Mink, *Spectrochim. Acta, Part A* **48** 121 (1992)
127. R. G. Denning, *Struct. Bonding.* **79** 215 (1992)
128. K. I. M. Ingram, L. J. L. Häller, and N. Kaltsoyannis, *Daltons Trans.*, 2403 (2006)
129. J. Häller and N. Kaltsoyannis, *Recent Advances in Actinide Science*; Royal Society of Chemistry, Cambridge, (2006).
130. J. P. Perdew, *Phys. Rev. B.* **33** 8822 (1986)
131. V. Vallet, U. Wahlgren, B. Schimmelpfennig, H. Moll, Z. Szabó, and I. Grenthe, *Inorg. Chem.* **40** 3516 (2001)
132. S. Tsushima and T. Reich, *Chem. Phys. Lett.* **347** 127 (2001)
133. N. W. Alcock and S. Esperas, *J. Chem. Soc. Dalton Trans.*, 893 (1977)
134. M. Åberg, D. Ferri, J. Glaser, and I. Grenthe, *Inorg. Chem.* **22** 3986 (1983)
135. P. G. Allen, J. J. Butcher, D. K. Shuh, N. M. Edelstein, and T. Reich, *Inorg. Chem.* **36** 4676 (1997)
136. H. Moll, T. Reich, and Z. Szabó, *Radiochim. Acta.* **88** 411 (2000)
137. C. Clavaguéera-Sarrio, V. Brenner, S. Hoyau, C. J. Marsden, P. Millié, and J. P. Dognon, *J. Phys. Chem. B.* **107** 3051 (2003)
138. S. Spencer, L. Gagliardi, N. C. Handy, A. G. Ioannou, C. K. Skylaris, and A. Willetts, *J. Phys. Chem.* **103** 1831 (1999)
139. Y. Oda and A. Aoshima, *J. Nucl. Sci. Technol.* **39** 647 (2002)

140. G. Schreckenbach, P. J. Hay, and R. L. Martin, *Inorg. Chem.* **37** 4442 (1998)
141. V. Vallet, U. Wahlgren, B. Schimmelpfennig, Z. Szabó, and I. Grenthe, *J. Am. Chem. Soc.* **123** 11999 (2001)
142. V. Vallet, *personal communication.*
143. A. J. Bridgeman and C. J. Empson, *MAYER version 1.2.3.* 2004, University of Hull, Freely available on the worldwide web: http://www.hull.ac.uk/php/chsajb/mayer/.
144. A. J. Bridgeman and G. Cavigliasso, *Faraday Discuss.* **124** 239 (2003)
145. L. J. L. Häller, N. Kaltsoyannis, M. J. Sarsfield, I. May, S. M. Cornet, M. P. Redmond, and M. Helliwell, *Inorg. Chem.* **46** 4868 (2007)
146. G. Schreckenbach and T. Ziegler, *J. Phys. Chem.* **99** 606 (1995)
147. S. K. Wolff, T. Ziegler, E. van Lenthe, and E. J. Baerends, *J. Chem. Phys.* **110** 7689 (1999)
148. M. J. Sarsfield, H. Steele, M. Helliwell, and S. J. Teat, *Daltons Trans.*, 3443 (2003)
149. W. R. Wadt, *J. Am. Chem. Soc.* **103** 6053 (1981)
150. D. S. J. Arney and C. J. Burns, *J. Am. Chem. Soc.* **115** 9840 (1993)
151. D. S. J. Arney and C. J. Burns, *J. Am. Chem. Soc.* **117** 9448 (1995)
152. A. E. Vaughn, C. L. Barnes, and P. B. Duval, *Angew. Chem. Int. Ed.* **46** 6622 (2007)
153. M. Kohout, F. R. Wagner, and Y. Grin, *Theor. Chem Acc.* **108** 150 (2002)
154. L. Joubert, B. Silvi, and G. Picard, *Theor. Chem Acc.* **104** 109 (2000)
155. K. Stowe, *J. Alloys Comp.* **246** 111 (1997)
156. J. C. Sullivan, J. C. Hindman, and A. J. Zielen, *J. Am. Chem. Soc.* **83** 3373 (1961)
157. N. N. Krot and M. S. Grigoriev, *Russ. Chem. Rev.* **73** 89 (2004)